UNIVERSITY OF SOUTHAMPTON

FACULTY OF ENGINEERING AND THE ENVIRONMENT
AIRBUS NOISE TECHNOLOGY CENTRE

Advanced Computational Modelling for Aircraft Landing Gear Unsteady Aerodynamics

by

Sarah Premachandran

Thesis for the degree of Doctor of Philosophy

March 2017

UNIVERSITY OF SOUTHAMPTON

ABSTRACT

FACULTY OF ENGINEERING AND THE ENVIRONMENT
AIRBUS NOISE TECHNOLOGY CENTRE

Doctor of Philosophy

ADVANCED COMPUTATIONAL MODELLING FOR AIRCRAFT LANDING GEAR UNSTEADY AERODYNAMICS

by Sarah Premachandran

High-fidelity turbulence modelling techniques have been applied to simulate the flow field around a simplified landing gear bay geometry. Three-dimensional Detached Eddy Simulation (DES) simulations have been performed for a cavity with the front 2/3 covered, as is representative of a nose landing gear bay. Resonant modes were observed in the shear layer, with frequencies in good agreement with the Rossiter cavity modes. The side-walls of the cavity, when compared to quasi-two-dimensional simulations with infinite span, were found to suppress the presence of acoustic modes inside the cavity, as well as causing a greater degree of breakdown in the shear layer, and changing the dominant resonant modes.

The geometry was varied to incorporate a single strut, and (separately) open rear doors, to test their separate contributions to the flow field in the landing gear bay. Both were found to produce small, high-frequency vortex structures, which interacted with the cavity shear layer and caused higher resonant modes to be present than with the clean cavity.

A Large Eddy Simulation (LES) methodology has been developed and improved using the in-house solver software. An improved subgrid-scale model has been implemented, and the sensitivity of the solution to a variety of settings has been tested. Using a method for efficiently simulating flat-plate turbulence by tripping the flow using a small step, realistic wall-bounded turbulence has been modelled, with mean and turbulent quantities in good agreement with the literature for flat plate boundary layer flows.

The best-practice guidelines from this study were then applied to a turbulent flat plate upstream of the cavity with LES. The boundary layer turbulence structures were found to disrupt the coherence of the shear layer vortices, and lengthwise acoustic modes dominated inside the cavity in most cases. The sensitivity of this baseline simulation to several different parameters was investigated. These included the condition and thickness of the upstream boundary layer, the geometry around the lip of the cover, the turbulence modelling technique, and the spanwise length of the domain. The most significant difference was obtained by adding side walls, which was found to promote the development of shear layer resonance. Lower-mode tones were observed, with the associated pressure fluctuations being imposed and amplified inside the cavity.

Contents

List of Figures

List of Tables

Declaration of Authorship

I, Sarah Premachandran, declare that the thesis entitled "*Advanced Computational Modelling for Aircraft Landing Gear Unsteady Aerodynamics*" and the work presented in the thesis are both my own, and have been generated by me as the result of my own original research. I confirm that:

- this work was done wholly or mainly while in candidature for a research degree at this University;
- where any part of this thesis has previously been submitted for a degree or any other qualification at this University or any other institution, this has been clearly stated;
- where I have consulted the published work of others, this is always clearly attributed;
- where I have quoted from the work of others, the source is always given. With the exception of such quotations, this thesis is entirely my own work;
- I have acknowledged all main sources of help;
- where the thesis is based on work done by myself jointly with others, I have made clear exactly what was done by others and what I have contributed myself;
- Parts of this work have been published as described in Section 10.2.

Acknowledgements

I would like to thank my supervisors at the Airbus Noise Technology Centre (ANTC), Doctor Zhiwei Hu and Professor Xin Zhang, for providing steady guidance and support, and sharing their expertise with me, throughout the course of my PhD.

This work was jointly funded by the Engineering and Physical Sciences Research Council (EPSRC) (under award reference number 1417785), and by DST Group Australia. I would like particularly to thank Doctor Matteo Giacobello, my supervisor at DST Group, for his help and support throughout this process.

Computational analysis was performed using the IRIDIS High Performance Computing Facility at the University of Southampton. The use of this facility, and the support of the associated staff, were critical components in completing this study.

I would also like to thank my colleagues at the University of Southampton and the ANTC group for their help and technical discussions throughout the course of this project. Special thanks go to Meng Wang, Ryu Fattah, James Gill, and Utsav Oza.

Finally, thank you to my husband, my parents, and my friends and family for always believing in me and supporting me.

Nomenclature

α	Phase lag constant from Rossiter equation; $\alpha = 0.25$
$\alpha_F, \alpha_B, \beta_F, \beta_B$	Coefficients in spatial discretisation scheme
α_j	Filter coefficients
Δx_{LE}	Cell size in x at the leading edge of the cavity (open section).
Δx_{TE}	Cell size in x at the trailing edge of the cavity.
Δy_1	Height of the first cell from the wall (where y is the wall-normal direction)
Δy_{floor}	Cell size in y on the floor of the cavity.
Δz	Separatation distance in z direction
Δ	Grid/filter scale
δ, δ_{99}	Boundary layer thickness based on $0.99 * U_\infty$
δ^*	Displacement thickness of the boundary layer
δ_{ij}	Kronecker delta function
Δ_{max}	Maximum cell dimension
Δ_{Shur}	Hybrid LES lengthscale proposed by Shur et al [126], Equation 7.2
Δ_{wn}	Cell size in wall-normal direction
γ	Ratio of specific heats for an ideal gas
$\hat{\nu}_t$	Modified turbulent viscosity variable from the Spalart-Allmaras model
κ	Convection ratio constant from Rossiter equation
κ_C	Scaled cut-off wavenumber in implicit filtering scheme
κ_{vK}	von Kármán constant, $\kappa_{vK} = 0.41$
$\mathbf{\hat{U}}$	Vector of all solution variables, after buffer-zone modifications
$\mathbf{U_{target}}$	Target value of solution variable vector, for buffer-zone boundary condition

μ	Dynamic viscosity
μ_{SGS}	Sub-grid-scale (turbulent) viscosity
ν	Kinematic viscosity, μ/ρ
ν_{SGS}	Sub-grid-scale (turbulent) kinematic viscosity, μ_{SGS}/ρ
$\overline{p}$	Mean pressure
$\overline{q}$	RANS-averaged value of a variable q
$\overline{u}$	Mean value of variable u
ρ	Density
τ_w	Wall shear stress
τ_{ij}	Reynolds stress
θ	Momentum thickness of the boundary layer
$\widetilde{d}$	DES hybrid length scale
$\widetilde{q}$	LES-filtered value of a variable q
A^+	van Driest damping constant
a_B, b_B, c_B, d_B, e_B	Coefficients in spatial discretisation scheme
a_F, b_F, c_F, d_F, e_F	Coefficients in spatial discretisation scheme
B	Constant
c_0	Freestream speed of sound
C_p	Pressure coefficient, $C_p = (p - p_\infty) \,/\, \left({}^1\!/_2 \rho U_\infty^2\right)$
C_{DES}	DES model constant, $C_{DES} = 0.65$
$C_{f,x}$	Skin friction coefficient
C_{SGS}	Constant in Smagorinsky SGS model
D	Depth (cavity)
D_i	Spatial derivative of some function at point i
d_w	Normal distance to nearest wall
D_{strut}	Diameter of strut
e_T	Total energy
f	Frequency

f_d	DDES function
f_m	Frequency of mode m
f_{am}	Frequency of the acoustic mode inside the cavity
H_{12}	Shape factor; the ratio of the boundary layer displacement thickness δ^* to the momentum thickness θ; $H_{12} = \delta^*/\theta$.
k	Turbulent kinetic energy
k_{cutoff}	Cut-off wavenumber in implicit filtering scheme
L	Length
L_2	Modified lengthscale for cavity with strut; distance between the cavity leading edge and the upstream wall of the strut
L_{bz}	Length of buffer zone
L_{open}	Length of the open section of the cavity
m	Resonant mode number
M, M_∞	Freestream Mach number
N_x, N_y, N_z	Acoustic mode numbers (0, 1, 2...) in the x, y and z directions (length, depth and span)
p	Pressure
p'	Perturbation pressure; $p' = p - \overline{p}$
p_∞	Freestream pressure
q_j	Heat flux
$R(\Delta z)$	Correlation coefficient of a given variable across a spanwise separation of Δz
R^+, R^-	Riemann invariants
r_d	argument to DDES function
Re	Reynolds number, $Re = U_\infty * L/\nu$
Re_θ	Reynolds number based on momentum thickness θ
Re_D	Reynolds number based on strut/cylinder diameter D_{strut}
Re_x	Reynolds number based on distance x from plate leading edge
S_{ij}	Strain rate
St	Strouhal number, $St = fL/U_\infty$

T^*	Reference time period based on U_∞ and a reference length
$T_{ij}^{(\nu)}$	Viscous stress tensor
u, v, w	Cartesian velocity components
u^+, v^+, w^+	Dimensionless Cartesian velocity components, scaled with friction velocity
U_∞	Freestream velocity in x-direction
u_τ	Friction velocity based on wall shear stress
u_i, u_j, u_k	Cartesian velocity components (index notation)
v_n	Velocity component normal to boundary
W	Width (cavity)
x, y, z	Cartesian co-ordinates
x^+, y^+, z^+	Dimensionless Cartesian coordinates, scaled with u_τ and ν
x_i, x_j, x_k	Cartesian co-ordinates (index notation)
x_{bz}	Distance to the inner boundary of the buffer-zone region
x_{LE}	Streamwise (x) co-ordinate of the leading edge (upstream side) of the open section of the cavity
x_{TE}	Streamwise (x) co-ordinate of the trailing edge (downstream wall) of the open section of the cavity
$\mathbf{U}$	Vector of all solution variables
ANTC	Airbus Noise Technology Centre
DDES	Delayed Detached Eddy Simulation
PSD	Power Spectral Density
SGS	Sub-grid-scale
SISM	Shear-Improved Smagorinsky Model
SotonCAA	In-house computational aero-acoustic solver

Chapter 1

Introduction

In this section, the background of this area of research is reviewed and the practical motivation for this study is explained. The objectives of the study are also explained, and an outline of this report is presented.

1.1 Background

The rapid growth of civil air travel in the past few decades has led to increasing levels of aircraft-related noise near airports. This noise is problematic for nearby residents, which has led to increasingly stringent airport noise restrictions [1], as illustrated in Figure 1.1. These restrictions affect the profitability of airline operators. Therefore, there is an increasing demand for quieter aircraft. For example, the Advisory Council for Aeronautics Research in Europe (ACARE) has set a goal to reduce aircraft noise by 10 dB by 2020 [2].

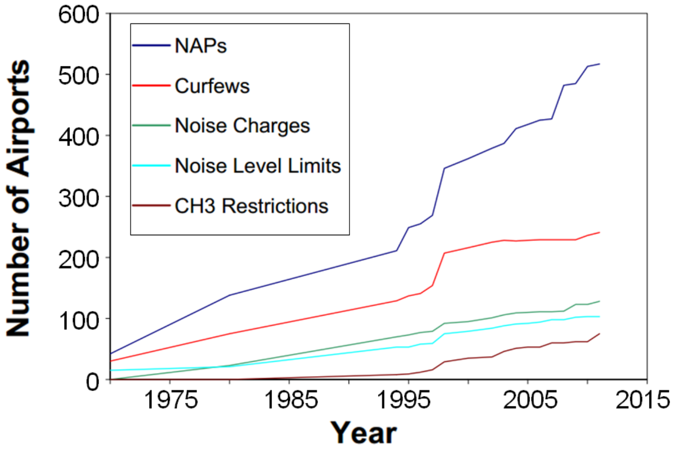

Figure 1.1: Growth in airport noise restrictions, adapted from [3].

Aircraft noise is particularly relevant in the take-off, landing and approach-to-land configurations, when the aircraft is closest to the ground. In the landing configuration, the engines are generally operating at a reduced power, and in fact the airframe itself is one of the most significant sources of noise [2]. The exposed landing gear arrangement is a major component [4], comparable to the noise from the high-lift devices on the wing [4,5]. In fact, landing gear noise can be the main contributor to airframe noise, especially for large-capacity and long-range aircraft [6,7], and for wide-body style aircraft (e.g. the Airbus A350 XWB), which require large (and perhaps additional) landing gear supports [8]. Hence it naturally follows that any attempt to reduce airframe noise (such as the ACARE 10dB target) should target landing gear unsteady aerodynamics.

Noise restrictions lead to a requirement to be able to accurately predict noise levels for certification purposes. Noise is generally quantified in decibels (dB), related to the measurement of the unsteady pressure. Certification may depend "on a fraction of a dB", whereas prediction accuracy to within 2 dB is currently considered "impressive" [9]. Noise prediction, in turn, depends on having an accurate prediction of the unsteady flow field which is the source of the acoustic field.

Additionally, the unsteady flow around the landing gear also produces unsteady forces on the local components. This can cause damage to the landing gear over the aircraft's operating lifetime. In some situations, the unsteady forces may even induce vibrations which are transmitted through the airframe to an unacceptable degree [10]. Therefore, there is a clear need to accurately model the unsteady flow around a landing gear.

Computational Fluid Dynamics (CFD) is emerging as a lower-cost alternative to experimental methods, which gives users the ability to measure all areas of the flow-field, and can be used at higher speeds and larger scales than many experimental facilities may permit. Not only will this be useful for certification purposes, but an accurate CFD methodology can also be used in the design stage in order to reduce or eliminate these undesirable unsteady flow features. Previous studies have indicated that there is certainly scope for aeroacoustic improvement in landing gear design. It has been speculated that noise reductions of the order of 2-6 dB could be achieved in this manner [6], and that many of the high-frequency noise components, which are generally linked to smaller geometric details, may be eliminated with streamlining [11].

Figure 1.2: Image of the Airbus A350 XWB landing gear, reproduced from the Airbus A350 website [12].

Accurately modelling the unsteady flow around a landing gear is a difficult task. An example of a landing gear geometry is pictured in Figure 1.2, illustrating the complexity of the geometry and the range of sizes of components. This leads to two major issues. First, it is not easy to create a computational model which captures all the smaller components and can accurately resolve the flow around them. One option is to drastically simplify the geometry by removing all these components. However these small-scale geometries have been found to play a significant role in generating high-frequency sound, to which the human ear is especially sensitive; Guo et al [13] found that predictions based on over-simplified geometries can underpredict the EPNL by around 8 dB. Secondly, even the large-scale components (for example the main strut, wheels, door and cavity) produce separated flows and unsteady shear layers. (The features of these components are described in more detail in Section 2.2.) The highly turbulent flow in these regions is difficult to model, due to the wide range of scales of fluid motion. Furthermore, it may be necessary to have an accurate estimate of the incoming boundary layer flow developing over the upstream fuselage, which is also turbulent. This is especially relevant in cavity flow, where the sound pressure level (SPL) can vary by up to 3 dB [14] due to the upstream boundary layer condition, as discussed in Section 2.4.

The highest level of accuracy would be obtained by fully resolving the flow field (including all of the relevant small-scale turbulent structures), a process referred to as Direct Numerical Simulation (DNS). However the limitations of current computing power make it impossible to perform DNS at speeds and lengthscales relevant to landing gear. Several CFD methods exist for simplified modelling of the effects of turbulence, as will be detailed in Section 3.3. Relatively low-fidelity methods, such as Reynolds Averaged Navier Stokes (RANS) modelling, make more assumptions about the turbulent behaviour; this makes it feasible to model more complex geometries while still obtaining a reasonable estimate of mean-flow features, but the small features and unsteady characteristics are not resolved. Higher-fidelity methods such as Large Eddy Simulation (LES) resolve more of the energetic turbulent motions, only modelling the more homogenous small eddies, leading to a more accurate result but requiring greater computing power.

An intermediate level of accuracy can be obtained by using Detached Eddy Simulation (DES), where RANS is used in the attached boundary layer regions and LES is used elsewhere, as will be detailed in Section 3.3. This approach has been widely used in simulations of landing gear geometries (e.g. [9, 10, 15, 16]), often with good results in the separated flow field, and has the advantage of allowing relatively coarse resolution in the attached region. However DES does have some significant drawbacks; in particular, it is unable to resolve the details of the developing turbulence within a boundary layer, due to the time-averaging approach embedded in RANS. This is likely to affect the ability to accurately model cavity flow, which is sensitive to the condition of the upstream boundary layer. Fully-resolved LES has been applied in the past to simple cavities (e.g. [17, 18]), but not, to the author's knowledge, to the more complicated geometries associated with landing gear bays, due to the significant additional computational cost of resolving the boundary layer. A comparative assessment of these two methods, for the purposes of predicting the flow around a landing gear geometry, would therefore be of practical interest for the future development of high-fidelity landing gear simulations.

Of the various geometric components to a landing gear, the bay is selected as the particular focus of this work. The flow over such a cavity can cause strong resonant vibrations, which produce significant noise as well as unsteady aerodynamic loads on the surrounding components, as will be discussed in more detail in Section 2.4. Therefore, tools for accurately and efficiently modelling the cavity resonant response are of particular interest in the process of improving landing gear design. One method for optimizing the efficiency of cavity numerical modelling is to simplify the geometry to a 2D or quasi-2D (i.e. 3D but periodic in the span direction) configuration, as the primary resonance mechanism develops along the length of the cavity. Some existing studies (as will be reviewed in Section 2.4.4) have been able to well replicate the main trends of experimental measurements with this approach, but others have found that the side walls cause a significant difference in the characteristics of the cavity resonance. In terms of the computational modelling approach, the sensitivity of the landing gear bay flow to the span boundary condition is of interest, in order to draw conclusions as to the usefulness of 2D or spanwise-periodic 3D simulations. From a physical perspective, examination of the interaction between the cavity flow and the side walls also contributes towards understanding of the underlying flow mechanisms.

1.2 Research Objectives

The goal of this project is to investigate the application of high-fidelity computational methods to simulate the unsteady flow around landing gear components, with increasing complexity, in an attempt to investigate the possibility of full LES for practical landing gear configurations. As mentioned in the previous section, the choice of CFD method is currently limited by computing power and reasonable timeframes. It is not yet possible to apply high-fidelity methods to a full, complex landing gear model, with a satisfactory level of grid resolution, and obtain a result in a reasonable timeframe. However, with recent advances in both available computing power and in efficient high-accuracy methods (see Section 3.4), it is becoming more feasible to apply a method like LES to a simplified version of a landing gear, or to individual components. The component selected for study in this thesis is the nose landing gear bay, simplified to a partially-covered cavity to account for the effect of the closed front doors. The characteristics of the flow field will be explored using DES, with particular attention towards the spanwise effects and the interaction with other components. The methodology will then be extended to consider LES. It is predicted that computing power will continue to increase [19], and it stands to reason that high-fidelity methods will thus become more affordable for increasingly complex applications. Therefore it is expected that the lessons learned from this study will form a useful foundation for future research into the complexities of modelling landing gear flow. The overall objectives of this study are:

- **To explore the unsteady characteristics of the cavity flow field.** Using DES, the features of the partially-covered cavity at subsonic speeds are investigated, including its mean, turbulent and resonant characteristics. The geometry is also extended to incorporate the effects of the strut and the closed rear doors, to investigate how the interaction with these components affects the cavity flow field.

- **To develop an efficient LES methodology for resolving a turbulent boundary layer.** An LES model is implemented into the in-house solver, enabling transitional flow simulations. Using established data on a turbulent flat plate boundary layer as validation, the effect of various simulation parameters are investigated, and a few simple tripping methods are compared, in order to synthesize a single set of guidelines for efficiently modelling resolved boundary layer turbulence. This methodology may then be extended to more complicated geometries.

- **To explore the effect of upstream turbulence and boundary layer characteristics on the cavity flow.** The developed LES methology is applied to a partially-covered resonating cavity, similar to the geometry investigated with DES, but with a fully-resolved turbulent boundary layer upstream. The sensitivity of the flow to the upstream boundary layer is explored by varying the thickness of the upstream boundary layer, the condition (laminar or turbulent), and the turbulence modelling method.

- **To explore the sensitivity of the cavity flow to the modelling in the span direction.** The effect of the side walls on the flow physics is investigated by comparing fully-3D simulations against modelled geometries that are periodic in the span. The dependency of a periodic-span simulation on the spanwise width is also considered. This comparison is performed with both DES and LES, as the difference in modelling of the turbulence is likely to affect the shear layer flow features and therefore the span effects. The effect of the modelling method (DES vs. LES) on the development of span effects in the cavity flow is also investigated by comparing the outcomes from the two methods.

1.3 Original Contributions

Some of the main original contributions from this thesis are as follows:

- **Analysis of spanwise modelling effects on flow for a partially-covered cavity using DES.** The cavity was observed to develop resonance in the shear layer, with the dominant modes being dependant on whether or not side walls were present. The amplitude of the pressure fluctuations inside the cavity were also found to be strongly dependant on the presence of the side walls. This study was presented at the 46th AIAA Fluid Dynamics Conference in June 2016; details will be presented in Section 10.2.

- **Analysis of span effects in the modelling of partially-covered cavity, with particular emphasis on the difference between LES and DES.** The effect of span width with the periodic-span configuration was investigated. With DES, an unphysical degree of spanwise coherence was observed, whereas using LES with a wall-resolved boundary layer was found to give more consistent behaviour between the different span widths, due to the effect of the small-scale structures in the upstream boundary layer. The LES analysis method was therefore found to be more robust in this sense. A fully-3D geometry was also compared against the periodic-span configuration, and the addition of solid side walls was found to cause a similar change in dominant modes with both LES and DES. An AIAA paper discussing the LES simulations is being developed and in is currently under internal review.

- **Examination of the effect of the main central strut, and of the closed rear doors, on the physical flow field of the partially-covered cavity**. Using DES, the additional components were added separately to the partially-covered cavity geometry. The effect of the interaction between the components and the cavity was therefore isolated, and the net effect on the flow field was compared between the two cases.

- **Analysis of the sensitivity of the partially-covered cavity to changes in the upstream boundary layer.** The effect of the upstream boundary layer (laminar vs. turbulent) is contrasted using wall-resolved LES, as well as the effect of the boundary layer thickness and the turbulence modelling method. An AIAA paper discussing these results is being developed and in is currently under internal review.

- **Development of a methodology for using the in-house code for modelling an LES-resolved turbulent boundary layer.** An improved turbulent viscosity model from the literature was implemented into the in-house solver “SotonCAA” (as described in Section 3.3.2), in combination with a step tripping mechanism from the literature (Section 2.3.3). The guidelines regarding mesh independance and the parameters of the solver, as presented in this thesis, may be of use for general future users of LES for resolved boundary-layer flow. In addition, the modified code and test cases are made available within the Airbus Noise Technology Centre at the University of Southampton for future researchers to build upon.

1.4 Thesis Outline

The structure of this thesis is as presented below. A summary of the conclusions drawn in each Chapter is provided at the end of the Chapter.

- Chapter 2 presents a review of the literature relevant to this study, including a more detailed discussion of landing gear simulations, cavity flows and turbulence effects, as relevant to the objectives discussed in Section 1.2.

- Chapter 3 details the methods that were used in this work. This project was entirely computational, performed using an in-house solver, so the emphasis is on the numerical schemes used by the solver, as well as the techniques used to model the effect of turbulence. The turbulence modelling techniques considered in this study are DES (Detached Eddy Simulation) and LES (Large Eddy Simulation). DES is a lower-fidelity method in terms of the modelling of the upstream boundary layer; however it is already well established for application to landing-gear geometries. DES will be used in Chapters 4-6. LES allows more accurate, but more computationally expensive resolution of boundary layer flows, and will be used in Chapters 7-9.

- In Chapter 4, a few validation cases are presented for DES. The DES methodology described in Chapter 3 is applied. As well as validating the code, the resulting grid and parameter independance studies are also used to synthesize a single set of meshing guidelines. These guidelines are applied in the following Chapters 5 and 6, as the grid sizes for those geometries make a systematic grid refinement study unfeasible.

- In Chapter 5, the DES methodology is applied to simplified partially-covered cavity, focusing on effects of the span boundary. This ties in with the objective of exploring the span boundary effects of the partially-covered cavity, which is of interest both from a numerical modelling perspective and to understand the spanwise features of the flow field.

- Chapter 6 extends the fully-3D simulations using DES from Chapter 5 to introduce other geometric components. The effect of the interaction between these components and the cavity is useful from a practical perspective to understand the characteristics of the landing gear bay.

- Chapter 7 investigates the use of the LES methodology discussed in Chapter 3 with the in-house solver, testing with a tripped turbulent flat plate boundary layer geometry for validation, and best-practices guidelines are developed. The purpose of this chapter to is to establish a methodology for the use of LES to resolve boundary layer turbulence, with the aim of applying this methodology to a partially-covered cavity and exploring the boundary layer effects.

- In Chapters 8 and 9, these guidelines are applied to perform a LES analysis of a partially-covered cavity with a fully wall-resolved incoming turbulent boundary layer. These chapters form the most significant part of this thesis. Chapter 8 focuses on the span effects, considering both the spanwise length and the effect of side walls. Similar to the geometries that were studied in Chapter 5 with DES, this Chapter explores how the use of LES (instead of DES), and the corresponding resolved upstream boundary layer turbulence, affect the span-wise characteristics of the flow.

- Chapter 9 tests the sensitivity of a baseline LES simulation to various parameters. From a numerical modelling perspective, the effect of tripping the upstream boundary layer, and the sensitivity of the simulated flow-field to the turbulence modelling technique, are compared. From a physical perspective (to inform future landing gear bay design efforts), the effect of the upstream boundary layer thickness, the covered section, and the geometry around the lip of the cover, are all investigated.

- An overall set of conclusions is provided in Chapter 10, along with some recommendations for future work.

Chapter 2

Literature Review

2.1 Overview

This section presents a review of the existing literature pertinent to the prediction of landing gear noise relating to the bay and the bay door. The features of landing gear geometries, and some relevant findings from previous studies on the aerodynamics and aeroacoustics of full landing gear geometries, are summarized in Section 2.2. Section 2.3 describes turbulent flows over zero-pressure-gradient flat plates, and some of the challenges and techniques used to simulate turbulence. This is relevant to the aims of the study because the incoming flow to the landing gear, from the fuselage upstream, may be simplified as a turbulent flat-plate flow. The upwash near the nose is small - of the order of 0.15° [10] - so the zero-pressure-gradient simplification is reasonable for the upstream condition into the landing gear cavity. The open landing gear doors may also be simplified as flat plates. Section 2.4 summarizes the current state of understanding of cavity flows. This includes some exploration of the effect of upstream flow conditions, geometric variations such as doors (open and closed), and items submerged in the cavity.

2.2 Landing Gear

A typical landing gear arrangement, as shown in Figure 1.2, is composed of the following major components: the wheel/bogie arrangement; the main strut; supporting structures such as the torque link; the wheel bay (i.e. the cavity); the door; and numerous small components which are generally referred to as "dressings" [20]. This complex geometry generates a considerable amount of noise when exposed to oncoming flow at take-off/approach speeds of Mach 0.2-0.3. It has been suggested that the high-frequency noise components may be significantly reduced with streamlining [11], and that there is potential to reduce broadband noise by up to about 10dB [21].

Geometric modifications to reduce landing gear noise are not straightforward. For example, one solution for the high-frequency components would be to shield the complex structures from the oncoming flow by using fairings; however, fairings have been shown to increase the flow speeds on adjacent components [21, 22], and therefore increase the noise from those components. Other modifications, which have been shown to be promising in reducing overall noise, include changing the bogie angle to a “toe-down” configuration, and adjusting the spacing between the wheels and wheel caps [21–24].

Previous studies have found the wheels to be the largest source of noise [6, 7, 25], as expected, since they have the largest area exposed to the flow. The main strut was also found to be a significant noise source [6, 25], producing regular vortex shedding as is characteristic of its cylindrical shape [7]. A horseshoe-vortex type structure has also been observed in the junction between the strut and the inboard wheel [26]. The landing gear bay (cavity) was also found to be an important source of noise, based on the in-flight measurements of Tam et al [27], particularly during the approach-to-land phase. Discrete noise components were observed, characteristic of resonant cavity oscillations (detailed in Section 2.4).

The landing-gear side-door has been found to be a relatively low noise source [6], contributing only about 1dB to the overall noise in the study of Humphreys et al [25], due to its streamlined shape to a straight oncoming flow. However the interaction with the rest of the gear causes strong unsteady forces on the door itself, which need to be accurately modelled in the design stage to ensure the strength of the structure. The door also has a significant effect on the rest of the landing-gear flow field; vortices are shed from the edges and can interact with other components, and the presence of the door can affect the symmetry of the vortex shedding from the wheels [5]. The position of the door can also strongly affect the acoustics of the strut; changing the angle of the door can suppress the cylindrical vortex shedding [16], thereby reducing the generated noise. The strut itself may also produce a velocity deficit on the outboard side of the wheel [11].

Therefore, there is obviously a complex and nonlinear interaction between the turbulent flow from the various landing gear components. In fact the noise measurements of Lazos [11] found that sources were not directly correlated with particular components, suggesting that the total “developed flow structure” needs to be considered. On the other hand, Smith & Chow [20] tested a simplified prediction model based on combining the effects of various components, and found that with the parameters of the model correctly tuned, it could predict experimental data to within approximately 3dB. Those authors suggest that therefore the noise sources are “essentially independant”, and therefore CFD of separate components can be used to build up a more comprehensive model.

Ultimately, certification will require accuracy to within a fraction of a decibel [9], so high-fidelity simulations of multiple interacting components is desirable. However in the meantime, as computing processing power builds to the point where this is possible, it is still very informative to consider the flow features of individual components and interactions of small groups. Of particular interest are the landing gear cavity (Section 2.4), the wall-bounded turbulence upstream of the cavity (Section 2.3), the door, and the main strut.

2.3 Turbulent Flat Plate Aerodynamics

2.3.1 Boundary Layer Thickness and Growth

The thickness of a turbulent boundary layer may be characterized in different ways [28]. The simplest to implement is the wall-normal distance by which the velocity has reached 99% of the freestream velocity U_∞, which is often denoted δ_{99} or simply δ for brevity; in this thesis, δ will be used to refer to the 99% boundary layer thickness. Other useful measures are the displacement thickness δ^* and the momentum thickness θ, which are calculated based on the distance the wall would have to be displaced to produce an equivalent effect on the outer inviscid flow, in terms of mass and momentum flux loss respectively, as defined in Equation 2.1. When the Mach number is low (around $M \leq 0.3$), the density ρ can often be neglected.

$$\delta^* = \int_0^\infty \left(1 - \frac{\rho u}{\rho_\infty U_\infty}\right) \mathrm{d}y, \quad \theta = \int_0^\infty \frac{\rho u}{\rho_\infty U_\infty} \left(1 - \frac{u}{U_\infty}\right) \mathrm{d}y \tag{2.1}$$

The shape factor $H_{12} = \delta^*/\theta$ (the ratio of the boundary layer displacement thickness to the momentum thickness) is another useful parameter. The shape factor has often been used to gauge whether or not a boundary layer can be classified as a fully-developed turbulent boundary layer (e.g. [29–31]). High-fidelity simulations performed by Schlatter et al [29] gave a very good agreement with the correlation proposed by Monkewitz et al [32] for the development of H_{12} against Re_θ, and this form will be used for validation of H_{12} in this thesis for turbulent boundary layers. For a laminar boundary layer, experimental data [33] has found $H_{12} = 2.59$.

The development of the skin friction coefficient C_f along the length of a plate can be estimated from the Schlichting skin friction equation [28], Equation 2.2. Throughout this thesis the Cartesian x co-ordinate is used to denote the flow direction, and the y co-ordinate denotes the wall-normal direction.

$$C_{f,x} = \left[2\log_{10}\left(Re_x\right) - 0.65\right]^{-2.3} \qquad for\ \ Re_x < 10^9 \tag{2.2}$$

where

$$C_f = \frac{\tau_w}{\dfrac{1}{2}\rho U_\infty^2}, \qquad \tau_w = \mu \left(\frac{\partial u}{\partial y}\right)_{y=0}$$

2.3.2 Boundary Layer Velocity Profiles

The mean velocity profile through the thickness of the boundary layer has been found [28, 34, 35] to be well described using the following nondimensionalizations, referred to as 'inner' scaling, based on the wall shear stress τ_w:

$$y^+ = \frac{u_\tau y}{\nu}, \qquad u_\tau = \sqrt{\frac{\tau_w}{\rho}}$$
$$u^+ = \frac{u}{u_\tau}$$

The exact form of the boundary layer profile is a subject of ongoing debate, especially with the degree of scatter in experimental measurements on flat plates, which is most likely due to variations in transition at low Reynolds numbers [36].
The classic theory [28,32] is that the boundary layer may be considered as being composed of three sections:

- The viscous sub-layer, where velocity u^+ varies linearly with y^+. It is generally expected [28] that this inner region follows a universal function, unaffected by the details of the external flow field. DNS data of zero-pressure-gradient turbulent flat plates has been shown [34] to collapse fairly well on $u^+ = y^+$ in this region, up to $y^+ \approx 10$. At the top of the viscous sub-layer, there is then a small 'buffer' region between the viscous sub-layer and the logarithmic region.

- The logarithmic region, which extends from approximately $y^+ \approx 10$ to $y^+ \approx 100$ for $Re \sim 2000$ [34], and the velocity is generally accepted to scale with a logarithmic profile of the form [28]:
$$u^+_{log} = \left(\frac{1}{\kappa_{vK}}\right) \ln(y^+) + B \tag{2.3}$$
where $\kappa_{vK} = 0.41$ and $B = 5.2$ [34].

- The outer, "wake" region. The velocity here is modelled in terms of the velocity defect, $(u_\infty - u)/u_\tau$. Unlike the inner region, this velocity function is likely to be dependant on the particular flow [28], and so is more difficult to generalize.

A more sophisticated composite profile has been suggested [32], where the inner region is modelled using the sum of two Padè approximants for the derivative, and the velocity in the wake region is fitted as the product of an Euler exponential integral function and a hyperbolic-tangent function. This function was validated against experimental data for H_{12} against Re_θ. However for the purpose of this study, the relatively simple profiles will be used for validation, as they have still been shown to give good agreement with with DNS data [37,38].
The distribution and form of the unsteady flow structures through the boundary layer are also of interest. In the near-wall region, streaks of turbulence are observed with length and spacing $\approx 1000 \times 120$ in wall units [34]. These streaks lift up from the wall [34]; and throughout the boundary layer, hairpin-shaped vortex structures have been found in numerous studies, e.g. the DNS of Wu and Moin [38], where this pattern is seen clearly. The amplitude of the turbulent fluctuations, as quantified by the Reynolds stresses (as defined in Section 3.3.1), are generally found to peak near the beginning of the log region [34,36].

The unsteady flow structures may also be quantified in terms of their RMS (root-means-square) velocities. The distributions of the RMS velocity components have been presented using inner scaling by the DNS simulations of Spalart [37], Wu et al [38] and Schlatter et al [34], all showing good agreement with each other. These results also agree with the empirical profile proposed by Marusic and Kunkel [39], which was based on wind tunnel measurements. Those authors suggested that the outer section of the boundary layer (log-layer and above) is composed of geometrically-similar attached eddies, and that the inner (viscous) region reacts to the forcing from this outer region.

Velocity profiles may also be quantified in terms of 'outer' scaling, where the reference lengthscale and velocity scale are δ and U_∞ respectively. One advantage of this scaling is that the results are not as sensitive to small details in the near-wall region, the way that u_τ is. The experiments of Probsting et al [40] measured the mean and turbulent velocity components of a low-Mach number boundary layer with $Re_\theta = 730$, using tomographic PIV, with the results presented in outer scaling. Those authors also performed a corresponding DNS simulation at $Re_\theta = 1000$, and found good agreement between the simulation and the experiment.

2.3.3 Modelling Methods for Transition to Turbulence

Overview of Methods

In a natural flow over a flat plate, the boundary layer transitions from laminar to turbulent after a certain Reynolds number is reached (generally around $Re \approx 5 \times 10^5$ [28], where Re is based on the freestream velocity and the distance downstream from the plate's leading edge). Instabilities, such as Tollmein-Schlichting waves in a Blasius boundary layer, appear and grow at an exponential rate until the flow has reached a state of full turbulence [28]. However, in practical experiments and simulations it is not generally considered feasible or necessary to model this entire process. The development length (i.e. domain size), flow time and resolution requirements are prohibitive, and the computational cost is generally better spent improving the simulation in the turbulent region of interest. Therefore, in order to accelerate this process it is useful to force some form of "bypass transition", which denotes any form of transition that bypasses the primary instability mechanism [35].

Several different methods exist for numerically simulating bypass transition. The simplest is to superimpose a white noise on the steady inflow velocity profile [41], but this requires a long simulation time and development length to evolve towards realistic turbulence [42]. In some cases, random white noise may even decay so quickly that the flow becomes laminar again [14]. This method can be improved by adding more realistic perturbations based on a stability analysis, but this complicates the flow process and is ideally best suited to low-Reynolds-number flows [41].

Scaling methods are also a fairly common technique [41, 43]. In this method a 'recycling' plane is designated where the turbulence from this stage is fed back into the inflow with some scaling modifications. This artificially allows the turbulence to develop over a longer length. However, this method requires particular care as the mean profile is still prone to drift [41]. Additionally, it imposes an artificial periodicity to the flow (i.e. in the streamwise direction, related to the distance to the recycling plane [42]). Furthermore the use of scaling arguments may not be ideally suited to examining the behaviour of wall-bounded turbulence, as the scaling behaviour may still be considered a subject of ongoing debate, and the use of these methods imposes a bias in the scaling behaviour [38]. It is also not a method that can be easily extended to imposing geometric modifications downstream of the developed boundary layer, which is the main interest of this study.

Turbulent-type inflow perturbations may also be developed from a set of random data, in the digital filtering method as proposed by Klein, Sadiki and Janicka [44]. The random data set is filtered so that the correlations and statistics have the desired distributions (i.e. based on realistic turbulence) to feed into the flow field. A modification to this method was proposed by Xie and Castro [45], based on an exponential form for the correlation function rather than a Gaussian form. Random data is generated over a 2D slice aligned with the inlet plane, and a filtered variable is defined as a linear function of the random points. The filter coefficients are determined so that the spatial correlation function matches the desired exponential form as closely as possible. A new set of random data is generated at each timestep, spatially filtered, and then averaged with the previous timestep (with weights from an exponential correlation function). The artificially generated turbulence is therefore temporally and spatially correlated. Test cases were performed using this method for near-wall turbulent flow, and the results were generally found to be in good agreement with a streamwise-periodic technique. With this method, length scales of the spatial correlation function do need to be specified, but tests on channel flows suggested that the flow statistics further downstream are not highly sensitive to this value [45].

Data from an experiment or auxiliary simulation may also be used [14, 41, 42]. The DNS study of Wu and Moin [38] periodically fed in 'slabs' of isotropic turbulence (based on a precursor DNS study). These slabs were imposed above the boundary layer, to avoid distortion of the developing boundary layer profile; hence the mesh resolution requirements of this method are high, and may not be feasible for an LES study. The additional cost of the auxiliary simulation, and the computational cost of interpolating and imposing the data from the precursor simulation (or experiment), should also be considered. If an auxiliary simulation is used, the added turbulence needs to be updated every timestep [42].

Aside from the computational cost, the addition of inflow perturbuations also generates artificial noise, which is undesirable for simulating flow fields which may later be used for aeroacoustic analysis. Chicheportiche & Gloerfelt [35] tested several artificial-turbulence generation methods for flow over a cylindrical cavity. They first used artificial perturbations based on random Fourier modes, generated using the kinetic energy spectrum; although this successfully produced turbulence, the unphysical noise from this method was found to be of the order of the cavity noise. Reducing the amplitude of the perturbations reduced the noise, but at the expense of a severe attenuation of the turbulent activity. A more sophisticated method of turbulence generation was also tested, using Gaussian-type spots with second-order moments imposed based on a Reynolds stress tensor, and still the spurious noise levels were found to be unacceptable for a reasonable amount of generated turbulence.

Chicheportiche et al [35] also tested a 3D simulation with a prescribed analytical inlet boundary layer profile, based on the idea that having an inflectional profile accelerates the transition to turbulence (as discussed in Section 2.3.3). They used a combination of a Blasius profile and a hyperbolic-tangent profile, and it was found that with careful tuning of the velocity parameters, transition time could be shortened. They imposed perturbations based on a linear local stablity analysis of the mean flow with some small amplitude ϵ. The perturbations were also scaled with a sinusoidal modulation in the span, of the form $\sin(2\pi mz/L_z)$, where m is a given number of spanwise modes.

Tripping with Backwards-Facing Step

Another method, as proposed by Berland & Gloerfelt [46] and Gloerfelt & Robinet [42], instead uses a small step to trip the transition to turbulence. The flow over the step introduces a local deceleration, changing the velocity profile in the boundary layer so that it contains a point of inflection, and it has been shown [42] that inflectional boundary-layer profiles are more susceptible to short-wavelength instabilities and are more likely to undergo bypass transition. Thus the growth of instabilities should be highly amplified, and therefore, crucially, there is no need for strong added disturbances to trigger turbulent behaviour. In fact, the added disturbances may be quite weak [42], and therefore the noise associated with the added disturbances will also diminish.

There are several ways to implement this method. Gloerfelt et al [42] used a stability analysis of a 2D simulation to identify the most unstable modes, then trimmed the step from the domain and imposed the modes on a 3D simulation. Chicheportiche et al [35] used the step method in an auxiliary 2D simulation, and found that the perturbations could be triggered with random noise, and that the spurious noise from the step was very low. Berland et al [46] performed 3D LES with the step remaining in the domain. A laminar Blasius [28] profile with a given boundary layer thickness δ was imposed at the inlet, and the step was introduced slightly downstream (at $x/\delta = 11$) with length 4δ and height 0.14δ. It was found that the step alone was not enough to guarantee transition to turbulence, so the initial flow field was modified to include random fluctuations upstream of the step. The simulation was found to give very good agreement in the mean and RMS velocity profiles against reference DNS data. Analysis of the acoustic field showed that the step created an additional narrow high-frequency peak, at a Strouhal number which corresponded to the wavelength of the pressure-field fluctuations downstream of the step. However, other than this peak, the overall acoustic spectrum was in reasonably good agreement with the power specturm as predicted by Tam [47].

2.4 Cavity Flow

2.4.1 Overview of Landing Gear Cavities

It has been widely observed [35, 48, 49] that air flow over an open cavity can cause an unsteady acoustic resonance. On aircraft, flow over cavities and surfaces has been known [50] to produce discrete tonal and broadband noise and significant pressure oscillations. Burst-disk type cavities on the fuselage can generate a whistling noise during the landing phase [35]. Noticeable acoustic and vibrational phenomena have also been observed inside the cavity of a nose landing gear [10].

There are several forms of cavity flow, depending on the Mach number M and the relationship between the cavity's length (L), depth (D) and width (W). These parameters determine whether an acoustic resonance is likely to occur, as well as the features of the flow field, such as whether the shear layer attaches to the floor, and the mode shape of the pressure oscillations [48]. For the take-off and approach-to-land phases of civil aircraft, when airframe noise is most important, the Mach number is generally in the range $M = 0.2 - 0.3$ [50].

The aerodynamics of a landing gear bay depends on the location of the doors, whether they are open or closed, and on the gear itself; incoming flow can be severely disrupted by the landing gear, especially while it is in the process of being deployed or retracted [50]. The effect of these geometric variations will be discussed in Section 2.4.5. The standard 'clean' cavity configuration is where the cavity geometry is a simple rectangle, with no modifications or submerged items. This configuration has already been well studed in the literature (e.g. [14, 48]). Furthermore, from the study of Bliss and Hayden [50], which examined landing gear and cavities for the Boeing 727 and McDonnell-Douglas DC-9, it was found that a simple rectangular cavity can in fact be a reasonable representation of the landing-gear bay. For example, for approximately 10 seconds while the main landing gear is deploying, the doors are open and the fuselage cavity exposed to the flow is essentially rectangular [50].

Those authors also performed measurements on the Boeing 727 landing-gear cavities in various door configurations, and found the L/D and L/W ratios to generally be in the vicinity of unity; for the main landing gear cavity it was $L/D = 1.2$, and for the nose landing gear cavity with the door closed $L/D = 1.5$, $L/W = 1.3$. Similar observations may be made for a range of aircraft. For these values, based on extensive experimental work on rectangular cavities in the past [48], it is expected that the flow-field will be characteristic of an "open" cavity [14], as is discussed in Section 2.4.2.

The scale of the cavity may be quantified using a Reynolds number Re based on a reference length, often the cavity length L. However, a number of past studies on resonating open-cavity flow in the subsonic regime have found that the flow field is fairly insensitive to this parameter [14, 48]. Experiments have been performed holding the geometry constant and varying the flow conditions to alter Re, where M and the various $L/D/W$ ratios are fixed [30, 48]. As long as the measured frequencies of the aeroacoustic response of the cavity (f) are appropriately scaled using the Strouhal number $St = fL/U_\infty$, and the pressure output is suitably normalized for the freestream kinetic pressure, it was found that the tonal response of the cavity (as described in Section 2.4.2) is largely unchanged in all respects (frequencies, amplitudes and bandwidth). This means that experiments and simulations may be performed on a smaller scale, while still being able to capture the main features of the flow physics. Good agreement has been observed between simulation and experiment with the Reynolds number varying by over one order of magnitude [14]. Therefore, it is expected that the Reynolds number will not be a particularly significant factor for the cavity flows under investigations.

2.4.2 Characteristics of a Clean 'Open' Cavity flow

A schematic of a typical open cavity flow is shown in Figure 2.1. The shear layer from the upstream boundary layer separates at the leading-edge of the cavity, beginning to form Kelvin-Helmholtz instabilities and unsteady structures [28]. This unsteady shear layer spans the length of the cavity, begins to break down into unsteady turbulence, and impinges on the upper corner of the aft wall [14]. This interaction between the unsteady shear layer and the wall creates acoustic waves at the trailing edge of the cavity. These acoustic waves propagate upstream and are scattered by the leading edge, generating instability waves which are amplified by the shear layer, leading to a cycle of resonance [51], which is further discussed in Section 2.4.4.

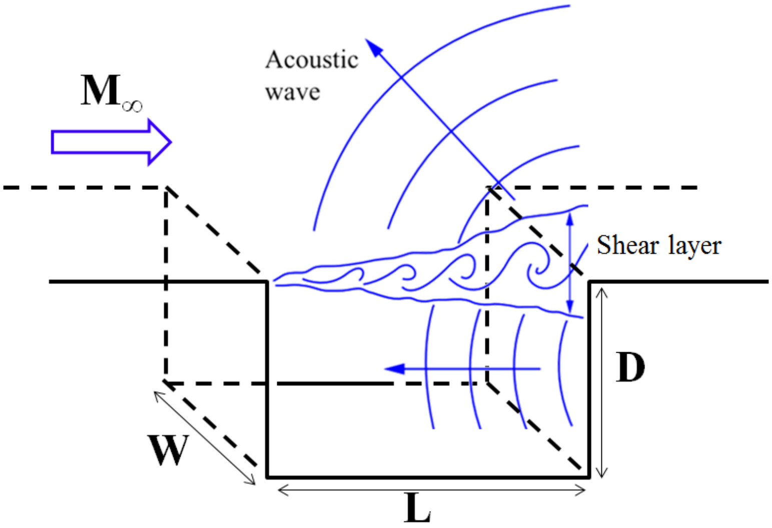

Figure 2.1: Schematic of open-cavity resonance mechanism, based on [48].

The experimental measurements of Roshko [52] on a cavity with $L/D = 1$ suggest that inside a cavity, a single large, stable vortex is found. Pressures on the cavity walls, at locations corresponding to this large vortex, were found to be steady. The same characteristics were observed when the velocity was increased (corresponding to $M = 0.2$, assuming the tunnel was at standard atmospheric conditions). Other experimental visualisations had also observed this vortex, as well as smaller additional "roller bearing" type vortices in the corners [52]. The PIV measurements of Murray et al [53], albeit on a shallower cavity, also showed that the open cavity flow is characterised by a large vortex structure across most of the depth of the cavity. This feature has also been reproduced computationally [17] using LES. Vortices have also been observed in the shear layer [54], growing in size as they are convected downstream, until they reach the cavity trailing edge. The numerical analysis of Gloerfelt et al [31] found that for a $L/D = 1$, $L/W = 0.5$ configuration with a laminar flow upstream, the shed vortex 'rolls' decelerated as they approached the trailing edge of the cavity, causing an interaction with the next-upstream vortex. The two vortices were observed to rotate about each other (as is expected for the strain field of two vortices) and begin to merge helically before being bifurcated at the impingement corner, with one portion being swept into the re-attaching boundary layer and the other being convected downwards into the cavity. [31]. On the floor of the cavity, the pressure coefficient is generally low, positive and near-uniform along roughly the first half of the cavity length, rising towards the end [14, 48].

2.4.3 Mach Number Effects

Most previous studies have focused on supersonic or at least high-subsonic flows for military applications; however, within the typical landing gear regime of $M = 0.2$-0.3, it can be expected that similar open-cavity resonance characteristics are present [50]. For example, Tam & Block [27] performed experimental measurements on cavities of $L/D = 0.78$-2.3 and $M = 0.05$-0.4, for the purpose of providing a validation database for landing gear bay noise. They found that for $M > 0.15$, the feedback instability mechanism described above was observed, with resonant tones observed at discrete frequencies. The aeroacoustic mechanism was only found to change at Mach numbers below this. To understand the characteristics of a landing gear bay, it is therefore of interest to consider the $M = 0.20 - 0.30$ regime. Many of the cavity flow studies to date have been performed at $M = 1$ and supersonic flow due to weapon bay applications [14, 49, 55], but the presence of shocks and other transonic/supersonic phenomena are not relevant to the prediction of landing gear flow fields. Cavity studies have also been performed at much lower freestream speeds ($M < 0.10$) or using incompressible solvers [56–58]; however these also have limited applicability to the landing gear regime, as there is a difference in the development of resonance within the cavity. As discussed by Tam and Block [27], for $M < 0.20$ the tonal response is generally dominated by acoustic modes inside the cavity instead of shear layer resonant modes. These resonance mechanisms are discussed in more detail in Section 2.4.4. The aeroacoustic response of the cavity is important both in terms of its contribution to the noise of the landing gear, and the development of unsteady loads on the surrounding components. Therefore it is important to study the characteristics of the landing gear bay using the correct Mach number range $M = 0.20 - 0.30$, which has not been as widely studied in the context of cavity flows.

2.4.4 Resonant Mechanism and Frequency Models

Shear Layer Feedback Resonance

The pioneering work of Rossiter [51] provided a framework for understanding the cavity resonance phenomenon and predicting the frequency. It was proposed that large vortical structures from the shear-layer breakdown are convected downstream at some fraction κ of the freestream velocity, typically $\kappa = 0.4$-0.6. The acoustic wave from the downstream edge travels upstream in time L/c_0, where c_0 is the freestream speed of sound. The acoustic energy reaches the leading edge (point of shedding), exciting stability waves which develop along the shear layer, creating a feedback loop [59] that causes resonance. Therefore the period of the m^{th} resonant mode, with frequency f_m, must be an integer multiple of the sum of these two time-scales. Adjusting to allow a phase lag α to reflect the influence of cavity depth, as was observed in the experiments, gives the model known as Rossiter's formula for the nondimensional Strouhal number St:

$$St = \frac{f_m L}{U_\infty} = \frac{m - \alpha}{\dfrac{1}{\kappa} + M_\infty}, \quad m = 1, 2, ... \tag{2.4}$$

From Rossiter's experimental database, which covered a range M between 0.4 to 1.2 and L/D between 4 and 10, $\alpha = 0.25$ was found to give the best fit.
The strength of the modes was found to be dependant on the L/D of the cavity; in shallow cavities the random pressure fluctuations dominated, while in deeper cavities the periodic components were significant, where 'deep' referred to $L/D < 2$ [51]. Therefore for dimensions typical to landing gear cavities (Section 2.4.1), it is expected that strong periodic components will be observed.
The aeroacoustic measurements of Tam & Block [27] support this hypothesis. The range of those experiments encompass the $L/D = 1$, $M = 0.2$-0.3 cases, and the resultant data exhibited peak frequencies which fell into clear bands of St against M. Plotted with the data from Rossiter [51], the general trends were found to match down to $M = 0.15$; therefore it can be expected that the same mechanism is occuring in the landing-gear case, and that Equation 2.4 should give a reasonable approximation of the resonant frequency. Another experimental study, conducted by Murray et al [53], on $M = 0.19$-0.73 but a shallower cavity of $L/D = 6$, also observed the same behaviour with tones observed for $M >$ 0.19, with frequencies in good agreement (to within 5-10%) with Equation 2.4.
This equation was later modified by Heller et al [60] to cover a wider range of Mach numbers and to correct for the higher speed of sound in the cavity. Based on their experimental database, which covered a range M from 0.8 to 3.0 and L/D from 4 to 7, the following relationship was derived, which is still in use today [14]:

$$St = \frac{m - \alpha}{\dfrac{M_\infty}{\sqrt{1 + \dfrac{\gamma - 1}{2} M_\infty^2}} + \dfrac{1}{\kappa}} \tag{2.5}$$

It was found that $\kappa = 0.57$ and $\alpha = 0.25$ gave the best fit to their data. However it should be noted that at lower Mach numbers the data began to show a dependancy on L/D, which is not captured in either Equation 2.4 or Equation 2.5. The range of L/D explored in [60] was also well above the $L/D \approx 1$ cases relevant to landing-gear bay applications, so there may be some margin for error.
Furthermore, in a more recent study [61] the Mach number effects on a subsonic cavity of $L/D = 4$ was explored, varying M between 0.2 and 0.65 in small increments. It was found that the convective velocity ratio κ is not in fact constant, but decreases systematically with Mach number. This may be a factor for the low Mach numbers involved in landing gear flow.
The mode number m is related to the spacing of the vortex structures [62]. Experimental studies have shown that when higher modes are dominant, the flow-field is characterised by multiple structures across the shear layer [53]. Rossiter [51] posited that the number of structures should coincide with the mode number. Alternatively, based on the analysis of Heller et all [60], it has been shown [62] that Equation 2.5 may be rewritten in terms

of the wavelength λ of a vortical disturbance:

$$\frac{\lambda}{L} = \frac{1}{m-\alpha}\left[1 + k\frac{M_\infty}{\sqrt{1+\frac{\gamma-1}{2}M_\infty^2}}\right] \tag{2.6}$$

Equation 2.6 can be used to estimate the spacing (and therefore number) of the vortices across the cavity mouth for a given mode m.

The prediction of which m will be the dominant mode is complex, as it has been shown that energy is constantly being exchanged between the modes [14]. Experiments on cavities with $L/D = 2$ and 4, at M between 0.2 and 0.6 [62], demonstrated the amplitude of the modes varies in time as energy is exchanged. Therefore the "dominant" mode is the one whose amplitude is large more often than the other modes. This mode-switching behaviour has been shown to have some sensitivity to Reynolds number [55]. Where multiple Rossiter modes exist, the flow-field can exhibit features of all of them. The experiments of Murray et al [53] found that at $M = 0.3$ with an $L/D = 6$ cavity, mode 3 was dominant. For the same Mach number but with $L/D = 2$, the experiments of Kegerise et al found mode 2 to dominate, with mode 4 being the second-highest in amplitude [62]. Sun et al [55] computationally studied $L/D = 2$ cavities with laminar incoming boundary layers, and found mode 1 to dominate for $M < 0.50$. There is an open question, therefore, about which mode is dominant for the case considered in the present study when $L/D = 1$, but it is likely to be one of these lower modes.

Acoustic Resonance within the Cavity

It is also possible for acoustic resonance to develop within the cavity, independant of the Rossiter shear layer feedback mechanism. These resonances are caused by the vibration of the air inside the cavity volume, causing a standing wave pattern; in cavity-flow literature these are often referred to as "normal modes" or "acoustic modes" [63, 64]. This study will refer to them as "acoustic modes", to distinguish from the Rossiter shear layer modes (which are a combination of vortex propagation and acoustic feedback).

The presence of these standing waves was observed in some shallow cavities by Rossiter [51]. Modes may theoretically develop in the length-wise, depth-wise or span-wise directions in the cavity (denoted x, y and z respectively in present study). Shaw, Bartel and McAvoy [63] performed experiments on cavities with the top mostly covered, save for a small opening. They treated the top wall as being solid, neglected spanwise modes, and estimated the acoustic mode frequencies based on:

$$f_{am} = \frac{c}{2}\sqrt{\left(\frac{N_x}{L}\right)^2 + \left(\frac{N_y}{D}\right)^2} \tag{2.7}$$

N_x, N_y, N_z denote the mode numbers in the x, y and z directions, where the mode number denotes the number of half-waves (based on a sine wave) in that direction. This equation gave good agreement with the measured frequencies from their experiments. The local speed of sound in the cavity c can be estimated from c_0 based on $c = c_0\left(1 + 0.2M^2\right)^{0.5}$.

(For $M \leq 0.30$, the difference is less than 0.1%, and so this distinction may be neglected for landing-gear bay applications.)

For cavities where the top is open, this equation can be expanded by treating the top 'wall' as a pressure-release surface [30, 64, 65], giving Equation 2.8. If the top wall is partially covered, there is an open question as to which form is more appropriate to calculate the depth-mode frequency. However they give the same result for longitudinal modes, which are expected to dominate for $L/D \geq 1$ [66]. The spanwise modes (N_Z) have not been generally observed for cavity configurations that have been studied in the past [63, 65].

$$f = \frac{c}{2}\sqrt{\left(\frac{N_x}{L}\right)^2 + \left(\frac{N_y}{2D}\right)^2 + \left(\frac{N_z}{W}\right)^2} \tag{2.8}$$

It is quite possible for these acoustic modes to co-exist with the shear layer modes, as has been observed by multiple studies [51, 63, 65]. When this occurs, the strongest resonances develop where the frequency of the acoustic mode is near the frequency of a Rossiter mode [30, 63, 65]. This suggests a positive interaction between the two mechanisms, where the shear layer oscillations 'lock on' (so to speak) to the acoustic modes, thereby exciting and reinforcing the pressure oscillations at that frequency.

Modelling Requirements in the Span Direction

Since the shear layer resonance develops along the length of the cavity, and the spanwise (N_z) acoustic mode is not common, there is a question about the extent to which it is necessary to model the spanwise effects of the cavity. Limiting the geometry to a 2D domain, or a narrow quasi-2D domain with periodic boundary conditions applied in the span, is one way to reduce the computational cost. From a design persective, this would make it possible to explore a broader parameter space while still using high-fidelity turbulence modelling. Examples of spanwise-periodic cavity simulations include the DNS study of Bres and Colonius [67], and the LES simulations of Chang et al [18, 56], where the mean flow features were found to be in good agreement with experimental data. Gloerfelt et al [68] also used periodic boundary conditions in the span, and obtained good agreement for the frequency response against experimental data from a very wide ($L/W = 0.03$) cavity. The acoustic response of a wide cavity, in terms of the measured sound pressure level (SPL) spectrum, has also been well predicted using a 2D compressible direct numerical simulation [69] compared to benchmark data. However, other studies have observed that a fully-2D approach can interfere with the development of the recirculating zone [68]. A 2D approach is also unable to simulation realistic turbulence (e.g. in the shear layer), which is necessarily three-dimensional.

The flow inside the cavity can show a high level of three-dimensionality [17, 67]. A 2D or spanwise-periodic simulation should however give a reasonable first estimate of the flow features, since for $W/L > 1$, the far-field acoustics are fundamentally representative of the 2D flow, and the width may not directly affect the resonant frequencies [70]. The width has been shown to have no effect on whether or not resonance develops for $W/L > 1$ [30, 57]. Some experimental data [30] has indicated that as W/L approaches unity, the amplitude of the acoustic tones tends to asympote, so that $W/L = 1$ may be considered 2D. However, other studies [70] have suggested that the width can effect the tonal amplitude. Bres et al [67] performed a DNS analysis of a compressible cavity flow with $W/D = 2$, $L/D = 2$ and 4, and they observed the presence of a spanwise mode with wavelength of the order of the cavity depth and frequency about one order less than the 2D resonant acoustic frequency (Section 2.4.4). It was concluded that this spanwise mode was primarily associated with the primary vortex in the cavity; hence the wavelength scales with D, and the frequency is related to the speed of advection of disturbances around the vortex. This mode was found to be largely independant of M for $M < 0.6$, but strongly dependant on Re and the incoming boundary layer thickness.

The specific effect of the side walls on the flow should also be considered. Larcheveque et al [17] compared periodic boundary conditions against viscous and inviscid side walls for $M = 0.8$ and $L/W = 0.42$ and found that the walls caused a difference in the dominant Rossiter modes. Li et al [71] compared periodic span boundary conditions against inviscid side walls for $L/W = 5$ and in the transonic regime ($M = 1.2$). Both configurations were found to give overall good agreement between the simulated SPL spectra against reference experimental data, with the side walls improving the agreement. To the author's knowledge, there is no previous work investigating the effect of side walls for a landing gear bay type cavity geometry at $M = 0.20 - 0.30$.

2.4.5 Variations on the 'Clean' Cavity Configuration

Practical landing-gear bays have several features which differ from the standard 'clean' geometry: the cavity itself is disrupted by the doors, struts and braces, with their associated dressings; the leading edge may have significant overhang and the length may not be constant; for the main landing gear, one end of the cavity opens into a much larger volume in the fuselage; and flow upstream of the cavity may be substantially altered by wing leading-edge devices (in the case of the main landing gear) or other components [50]. These modifications will interfere with the aerodynamics of the 'clean' cavity. The effect is often to attenuate the amplitude of the resonant aeroacoustic oscillations [50], and perhaps even to suppress them entirely.

Upstream Conditions

Several studies on cavity flow have highlighted the importance of the upstream boundary layer conditions. Differences in δ/L or δ/D (where δ refers to the upstream boundary layer thickness) can change the cavity response from the 'open' configuration described in Section 2.4.2 to a 'wake-mode' type oscillation, with large-scale vortex shedding and St independant of M [72]. Existing discrepancies between experimental and numerical data may be attributable at least in part to differences in the upstream boundary layer [14]. Past studies have considered D/δ over a wide range (0.5-10, [73]), and although the role of the boundary layer thickness is not yet fully understood, it is known that it can affect the resonant frequencies, the amplitude of the oscillations, and even the existance of the resonant mechanism itself [48].

Even when acoustic resonance is not present, the near-wall coherent structures of an incoming turbulent boundary layer have been observed to influence the characteristics of the shear-layer structures [18]. Grace, Dewar, and Wroblewski [57] experimentally compared laminar and turbulent incoming boundary layers for a low-M flow ($M = 0.022-0.045$) with $L/D = 4$ and $L/W = 0.1$, where the cavity flow is non-resonating. They observed that the upstream-laminar case had a higher maximum Reynolds shear stress $\langle uv \rangle$ in the shear layer, with a slightly higher vertical location of the peak value. Inside the cavity, the laminar case had a stronger main vortex, with the maximum vorticity about 30% higher than in the turbulent case. This stronger vortex pushes the shear layer outwards, thereby raising the location of the peak Reynolds shear stress. The lifting of the shear layer also means that the laminar case has less interaction between the shear layer and the cavity trailing-edge walls, as the higher streamlines are abl to reattach on the other side more smoothly. The authors suggest that the difference is due to the turbulent shear layer allowing more fluid from the cavity to enter the shear layer. This entrainment causes a more diffusive - and therefore weaker - vortex inside the cavity. The vortex streamlines inside the cavity were also different, with the strong vortex in the laminar case inducing a secondary vortex in the upstream half, whereas in the turbulent case the whole cavity is filled with the main vortex. The laminar shear layer was observed to transition to turbulence about halfway across the length of the cavity. Velocity and u_{RMS} slices in the downstream half of the cavity are therefore more similar between the two cases.

Kang and Sun [74] experimentally studied an incompressible flow with a turbulent boundary layer for the case of a non-resonating cavity. They characterised the incoming boundary layer by its momentum thickness θ. For $L/D = 1$, $Re_\theta > 1410$ and $\theta/L < 0.025$, broadband peaks were observed in the spectra at $St = 0.48$-0.65. The average velocities and turbulent quantities were found to be largely independant of L/θ, and this it was concluded that these broadband peaks were induced soley by the developing shear layer, and not caused by cavity resonance. The same behaviour was observed at $L/D = 4$, with slightly different conditions for developing this broadband peak. They concluded that in this particular case, where compressibility effects are not present and the flow is not resonating, the incoming boundary layer condition is not as important.

The boundary layer thickness and condition can also determine whether or not the cavity develops shear layer resonant modes. For a laminar boundary layer with low Mach number, studies have indicated that the cavity will not resonate if the boundary layer is too thin or too thick. Gharib and Roshko [75] performed an experimental study on an axisymmetric cavity, and found that resonance was observed for $0.0065 < \theta/L < 0.0125$. However experiments by Grace et al [57] with $\theta/L = 0.0076$ showed no resonance in the shear layer, which conflicts with these guidelines. Another criteria, proposed by Sarohia [76], is that for $D/\delta \geq 2$, resonance will not occur if $(L/\delta)(Re_\delta)^{0.5} < 290$ [76]. Their results showed this cut-off to be fairly constant over their range of data (D/δ up to 25), for laminar upstream boundary layers, even when imposing different pressure gradients ahead of the cavity. The condition of the shear layer also plays a role; they found that the cavity shear layer remains laminar as long as $\theta/L > 0.01$; for a longer cavity, the shear layer began to transition to turbulence and the periodic signal was no longer observed. These experiments were performed at $M = 0.015$, which is quite low, so the applicability of these results to the $M \approx 0.3$ regime is questionable. Still, the authors did note that when tones were observed, they were due to the amplification of shear layer disturbances, not acoustic-mode resonance from inside the cavity. Also, the tones were at frequency bands of $St = 0.5$-0.6, 0.8-0.95 and 1.3-1.5. Using the Heller equation (Equation 2.5) the calculated frequencies are $St = 0.42$, 0.99 and 1.5, which is not far from the measured tonal bands, especially considering that the equation is calibrated for higher-speed flows, and so would be less accurate in this regime.

Grace et al [57] performed experiments at a similar low Mach number range ($M = 0.022 - 0.045$) with $\theta/L = 0.0052$ and 0.0076, and $(L/\delta)(Re_\delta)^{0.5} = 932$ and 1613. According to the criteria of Gharib et al [75], one of the cases should resonate; but according to the $\theta/L > 0.01$ criteria of Sarohia [76], neither should resonate. In practice, both experiments were found to be non-resonating. They also observed that the shear layer fully transitioned to turbulence about halfway across. Those authors concluded that the guidelines of Sarohia [76] were a better prediction of laminar resonance conditions. However they also cited an earlier water tunnel experiment with a much thicker boundary layer where only partial transition was observed, so there are some open questions about the conditions for shear layer transition, which is an important factor in the development of resonance.

Despite the suppressing effect that shear-layer transition appears to have on the development of tones in an upstream-laminar flow, it is quite possible for a fully turbulent upstream boundary layer to still produce resonant tones over a cavity. The criteria for resonance in this situation is, however, different. This was investigated by Ahuja and Mendoza [30], who performed experiments at $M = 0.4$, which is near the range of interest for landing gear applications. For a cavity with $W/L = 2$ (effectively 2-D for the purposes of determining whether resonance occurs) and $L/D = 3.75$, they found that increasing the boundary layer thickness reduced the tendency to develop resonance. At $\delta/L = 0.038$, four strong resonant modes were observed; at $\delta/L = 0.045$ only one mode was observed, although its amplitude had increased. Increasing the boundary layer thickness further to $\delta/L = 0.066$, no peaks were observed at all. It was concluded that cavity resonance with a turbulent boundary layer requires $\delta/L < 0.066$. This is supported by the experiments of Grace et al [57] (albeit at a much lower Mach number), for a turbulent boundary layer with $\delta/L = 0.127$, where no resonance was observed.

For a cavity that is resonating, the aeroacoustic response is still highly sensitive to the condition of the boundary layer upstream [53, 64]. The turbulence in the shear layer partially determines the width of the tonal peaks [50], and the boundary layer upstream will in turn affect the characteristics of the shear layer. When the upstream boundary layer is completely laminar, the acoustic field is stronger and less diffusive [70] with more intense oscillations and louder tones [30, 50]. The overall sound pressure level can be up to 3-5dB higher than for a cavity with a turbulent boundary layer upstream [14, 31]. It has been suggested [35] that the laminar boundary layer profile slightly raises the vorticity structures in the separated shear layer, and in this case this results in a stronger acoustic response from the impact on the downstream cavity edge. Alternatively, this difference has been attributed to the way the unsteady fluctuations in a fully-turbulent boundary layer have been observed to“break ... the coherence” of the shear-layer shed vortices [56], as was observed in the computational analyses of Chang et al [56] and Gloerfelt et al [31]. Those authors observed that the presence of fluctuations upstream of the cavity (whether through artificial imposition of inflow fluctuations or genuine resolution of the boundary layer turbulent structures), caused a “jittering” of the boundary layer. This resulted in a larger range of turbulent structures inside the cavity [14, 56], as well as a reduction in the amplitude of the shear-layer fluctuations, and therefore a reduction in acoustic emissions [31, 56, 77]. Simulations with a laminar boundary layer upstream were found to significantly overestimated the first tonal peak; tripping the boundary layer in the simulation was found to give much better agreement with experimental data [56, 77]. Additionally, the scale of the larger structures in the shear layer may be correlated with the thickness of the incoming turbulent boundary layer [48].

Therefore it is important to accurately capture not only the condition of the upstream boundary layer, but also its mean profile and the unsteady structures. This requires a high level of numerical fidelity (see methods discussed in Section 3.3). Low-fidelity RANS-based methods, applied to cavity aerodynamics, can model the large-scale structures and low frequencies reasonably well; but they are ill-suited to resolving the small scales, high frequencies and broadband noise [14]. The method of turbulent generation is also of interest. Earlier studies tended to use simple methods such as addition of synthetic turbulence or random perturbations [56]. More recently, some studies have used an auxiliary high-fidelity simulation to generate the upstream turbulence [18, 56] and interpolate onto a lower-resolution mesh and method for the cavity itself. Gloerfelt et al [31] generated turbulence by superposing Fourier modes on a turbulent mean flow and used a near-wall corrected model to resolve the boundary layer (the Smagorinsky model with van Driest damping; see Section 3.3.2). However, that analysis was performed on a $M = 0.80$ cavity; and the simulations of Chang et al [18, 56] were performed in the incompressible regime. Therefore, for the $M = 0.20 - 0.30$ regime of interest, there is scope for futher work exploring the relationship between cavity structures and incoming boundary-layer turbulence.

Bay Doors

Landing gear geometries come with different types of doors; most commonly, either a single pair of doors opening from the middle, or two sets of doors - front and rear - to allow extra room while the gear is being deployed (e.g. [50]). In the latter case, generally one of the sets of doors will be closed and the other open while the gear is deployed. This scenario is shown in Figure 2.2 for an Airbus 380 nose landing gear, with the front doors closed and the rear doors open.

Langtry and Spalart [10] studied a cavity geometry more representative of a landing gear bay, with the rear doors closed, front doors open and gear partially retracted, as they had found that to be a case of significant practical interest, where strong vibrations had been observed during flight tests. The cavity geometry also had a rear wall that protruded further into the freestream than the front wall, on account of the curvature of the nose-fuselage section it was built within. Examination of the flow pattern through a cycle showed the following behaviour [10]:

Figure 2.2: Image of the Airbus A380 nose landing gear with gear deployed, front doors closed and rear doors open; reproduced from [78].

- The shear layer, following the freestream orientation, is directed into the inside of the cavity.
- The shear layer impingement on the rear wall creates a high-pressure wave, which propagates upstream inside the cavity.
- As the pressure wave reaches the leading edge, it begins to force the shear layer away from the cavity.
- The full length of the shear layer, up to the leading-edge of the rear doors, is lifted away from the cavity.
- High-pressure fluid inside the cavity begins to flow out.
- The pressure inside the cavity reduces; the pressure suction brings the shear layer back to its original position.

In spite of the geometric complexity, the measured frequency of the cavity tone was found to be a fairly good match to the Rossiter-type mode, as predicted using the model of Heller [60] (Equation 2.5), based on the length of the front doors. The main effect of the closed rear doors was to effectively shorten the cavity. The additional space inside the rear section did not seem to have a primary effect on the aerodynamic mechanism; only the leading-edge of the rear doors appeared to strongly interact with the shear layer.

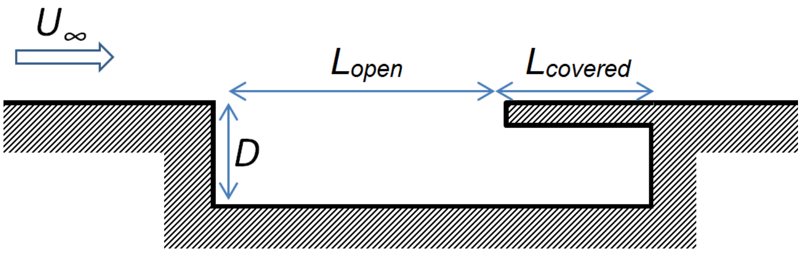

Figure 2.3: Schematic of an extended cavity geometry, adapted from Wittich et al [79].

The effect of closed rear doors was studied more systematically by Wittich et al [79], using an experimental setup where the cavity has an open section of length L_{open} upstream, and a covered section downstream of length $L_{covered}$; see Figure 2.3. A series of experiments were performed varying $L_{covered}/L_{open}$. They assumed that the acoustic waves were created at the downstream edge of the open section, then propagated first down to the downstream end of the closed section, then back up to the leading edge of the cavity; therefore, the addition of the closed section changes the acoustic propagation length from L_{open} to $2L_{covered} + L_{open}$, leading to the following modification of the Rossiter formula, described as the 'long-path' model:

$$St = \frac{m - \alpha}{M_\infty + 2M_\infty \dfrac{L_{covered}}{L_{open}} + \dfrac{1}{\kappa}} \tag{2.9}$$

From their experimental database, which covered a range of M across 0.3 - 0.7 and $L_{covered}/L$ between 0 and 1.4, they found the best fit to Equation 2.9 was with $\kappa = 0.54$ and $\alpha = 0.13$. The peak frequencies from the experiment were found to be in good agreement with Equation 2.9.

The present study is more concerned with the effect of closed front doors, as shown in Figure 2.2, where the open section is at the downstream end of the cavity. As mentioned in Section 2.4.4, Shaw et al [63] performed experiments with a mostly-covered cavity, with only a small aperture exposed to the flow. This opening was located in the centre-span and near the downstream edge of the cavity. The dimension ratios were $L/D = 0.26$-0.33 (depending on the geometry) and $W/D = 1$ for the whole cavity; for the opening, $L_{open}/L = 0.33$, $W_{open}/W = 0.2$. Using L_{open} as the reference length, the calculated Rossiter-mode frequencies were found to be in fairly good agreement with the experimental data, despite the strong presence of acoustic modes in this configuration. For the lowest Mach numbers (0.4-0.50) no tonal response was observed; for $M = 0.60$, the strongest response was observed for the second length-wise acoustic mode ($N_x = 2$).

A variety of covered-cavity simulations were investigated experimentally by Bartel et al [65]. Again, the open section of the cavity was located at the downstream end, and the Rossiter mode frequencies were calculated based on L_{open}. The same tendency was observed for the Rossiter mode frequency to 'lock on' to the acoustic-mode frequency developing inside the cavity.

Heo et al [80] performed 2D simulations on a $M = 0.50$ cavity with $L_{total}/D = 2$ and various configurations of the covered section. They found that with symmetric covers upstream and downstream, increasing the cover-lengths caused a decrease in St due to a decrease in the vortex convection velocity (κ in Equation 2.5). Using their modified κ as directly computed from the flowfield, the frequency (St) was found to be in good agreement with the Rossiter modes as predicted by Equation 2.5. Once the length of the cover plates reached $0.375L_{total}$ each (i.e. the mouth is 75% covered in total), no unsteadiness was observed in the shear layer. The flow inside the cavity consisted of a large vortex under the open section (induced by the shear-layer velocity) with a second, counter-rotating vortex upstream, induced by the first vortex. On comparing the effect of having covered sections either upstream, or downstream, or symmetrically at both ends, those authors found that in all cases the frequencies correspond to the Rossiter modes, but the modes varied with different configurations, with mode 3 dominant for the symmetric configuration and mode 2 for the others. Considering the effect of the cover-plate thickness, it was found that increasing the thickness caused a decrease in κ, due to the thick plates interfering with the cavity vortex and suppressing its circulation. (It is not clear whether the same trends from this 2D study would occur in the presence of fully-resolved turbulence and spanwise variation.)

Nishimura et al [58] performed an experimental wind-tunnel study on a cavity with symmetric (upstream and downstream) cover plates, with $L_{total}/D = 2.85$ and $L_{open}/D = 1.32$, in the very low-subsonic regime ($M = 0.07$, effectively incompressible). Taking measurements of velocity magnitude at the leading edge of the downstream cover (i.e. the point of impact for the unsteady shear layer), they observed the presence of a small spectral peak at around $St = 1.37$ (based on the freestream velocity and L_{open}). Syed et al [59] performed a 3D DES simulation at $M = 0.85$ for a cavity with $L/D = 5$ and $W/D = 1$, with and without symmetric cover plates of length $1.75D$ each. They found that the open-section shear layer exhibited acoustic-resonance behaviour, but the frequencies were not in agreement with the Rossiter modes, and no explanation was presented for the discrepancy. However, evaluating Equation 2.9 for the flow configuration in [59], neglecting the upstream covered section, produces frequency estimates that are within 5-10% of the simulation results for most of the peaks. Thus overall there have been several studies on the effect of cavity covers, but it appears that there is still a void for the case of a upstream-covered cavity in the $M = 0.20$-0.30 regime with proper consideration of the 3D effects, which is of significant interest in the analysis of landing-gear aerodynamics.

Considering now the aerodynamic effect of the open doors along the side of the cavity: for a single set of open doors along the sides of a rectangular cavity, to the author's knowledge, there has been no study at subsonic speeds. Murray and Jansen [49] conducted experiments with $M = 1.5$, $L/D = 9$ and $W/D = 5$, exploring the effects of open doors against cases with one door open and one closed. (The effect in the landing-gear regime may vary significantly from this high-aspect-ratio supersonic case). They found that with both doors open, the resonant tones inside the cavity were entirely suppressed. With one door open and one closed, however, the resonant tone was dominant. Compared to the case with no doors, the acoustic peaks were found to be higher, narrower (i.e. less spread), and occurring at slightly higher frequencies. They further analyzed the data by estimating the Rossiter model parameters using the process described in [81]. They found that the presence of the closed side door both increases the shear-layer convection κ and decreases the phase lag α. They suggested this was due to an increased efficiency of the acoustic generation and propagation, due to the closed door generating edge tones, and because the acoustic waves should be able to propagate more easily through the sheltered flow in the closed half of the cavity.

Effect of Other Geometric Components within the Cavity

The literature on blockages inside the cavity has tended to focus on weapon release configurations, i.e. high-subsonic/transonic Mach numbers and shallower cavities. The presence of a weapon geometry inside a cavity has been found to potentially reduce the intensity of the fluctuation [14]. Experimental studies on the effect of the weapon's location on the aeroacoustics found that when it was fully submerged in the cavity, the frequency spectrum was not significantly affected. As it was moved out, the magnitudes of the resonant peaks reduced; when the weapon reached the free-stream flow, the resonant peaks were indistinguishable from the background noise [14]. Obstructions in the shear layer therefore disrupt the development of the shear layer resonance.

The effect of landing-gear type geometries in appropriate cavities for civil aircraft has been much less studied. The computational study of Langtry et al [10] simulated a retracted nose landing gear scenario, although their landing gear geometry was considerably simplified, with emphasis mainly on ensuring the correct volume inside the cavity. A reference clean cavity was not simulated to isolate the effect of the retracted gear. However, from the fact that the cavity tones were found to be very similar to the Rossiter modes (Equation 2.4), it may be inferred that in this case the effect of the gear on the cavity noise response was small. This is consistent with the findings from weapon-bay applications, as the gear was fully retracted inside the cavity, away from the shear layer. The same study [10] also added a small baffle to the geometry, downstream of the gear and close to the shear layer. It was found that this had a substantial effect on the total cavity noise. The baffle prevented the shear layer flow from entering the cavity, deflecting it towards the outer side of the rear doors. This repressed the development of the pressure oscillation mechanism described in Section 2.4.2; measurements of the acoustic pressure confirmed a major reduction in the amplitude of the primary tone. Therefore this study, in agreement with the weapon-bay studies, illustrates that both the position and the size of the object are important in determining its effect on the aeroacoustic cavity flow field.

2.5 Summary

Several studies have been performed in the past using DES to simulate landing gear geometries with simple to moderate complexity, with good results. However the partially-covered cavity with the upstream section covered, relevant to many nose landing gear bay applications has not, to the author's knowledge, been systematically investigated. The present thesis seeks to expand this knowledge by investigating the characteristics of such a cavity, and its interaction with other landing gear components (the open rear doors, and the main strut), using DES.

In the previous literature, the characteristics of a simple cavity geometry have been well studied, especially at high Mach numbers or for $M < 0.1$ (incompressible). The upstream boundary condition has been identified as significant to the cavity flow, and some studies have been performed comparing laminar and turbulent boundary layers. However there is a shortage of studies in the $M = 0.20 - 0.30$ regime, where compressibility effects are still expected to play a part (through the development of Rossiter shear layer resonance). Studies that have resolved the upstream boundary-layer turbulence also have not, to the author's knowledge, been extended to varying cavity geometries more representative of cavity landing gear bays. The aims of the present thesis include the development and implementation of a wall-resolved upstream turbulence modelling method for a bay-type partially-covered cavity at $M = 0.25$, which will therefore address this void. Part of this requires the contrasting of turbulence modelling methods (which will be discussed in more detail in the next Chapter, Chapter 3), as DES and LES differ in their approach to modelling the upstream boundary layer.

Some open questions also exist about the necessity of resolving the spanwise boundary, with some studies in the past obtaining good results with 2D and quasi-2D (spanwise-periodic) simulations, and others finding that the side walls affect the resonant mode dominance. The sensitivity of the modelled flow field to the span boundary condition, and to the spanwise extent with periodic boundary conditions, will therefore be investigated, in the context of the partially-covered cavity with different turbulence modelling methods.

Chapter 3

Governing Equations and Numerical Methods

3.1 Overview

This section provides an overview of the methods used to predict the unsteady aerodynamic flow field around the simplified landing gear components. First, the governing equations of the flow field are summarized (Section 3.2). These equations may be discretized in time and space and simulated directly, through a process called DNS (Direct Numerical Simulation). However for most practical applications where the flow becomes turbulent, the associated grid and temporal resolution requirements become so high that DNS is not feasible with the current state of computing power. Therefore, several different methods have been developed to simplify these governing equations, in order to ease the computational requirements while still capturing most of the flow physics of interest. The appropriateness of these methods depends on the scale and type of the flow-field under consideration, and the degree of accuracy that is required. The principles of analyzing the turbulent flow around the body of interest are described in Section 3.3. The process of discretising the geometry in time and space is also important, as it plays a significant role in the accuracy and computational efficiency of the solution. This is discussed in Section 3.4.

3.2 Governing Equations

For all conditions of practical interest, the motion of fluids in a co-ordinate system x_i $(i = 1, 2, 3)$ is governed by the following fundamental equations:

$$\frac{\partial \rho}{\partial t} + \frac{\partial}{\partial x_i}(\rho u_i) = 0$$

$$\frac{\partial}{\partial t}(\rho u_i) + \frac{\partial}{\partial x_j}\left(\rho u_i u_j + p\delta_{ij} - T_{ij}^{(\nu)}\right) = 0 \tag{3.1}$$

$$\frac{\partial}{\partial t}(\rho e_T) + \frac{\partial}{\partial x_j}\left[\rho u_j e_T + u_j p + q_j + u_i T_{ij}^{(\nu)}\right] = 0 \tag{3.2}$$

where e_T denotes the total energy, q_j denotes the heat-flux and the viscous stress tensor $T_{ij}^{(\nu)}$ takes the form:

$$T_{ij}^{(\nu)} = \mu \left(\frac{\partial u_i}{\partial x_j} + \frac{\partial u_j}{\partial x_i} - \frac{2}{3} \left(\frac{\partial u_k}{\partial x_k} \right) \delta_{ij} \right) \tag{3.3}$$

These relations are referred to as the Navier-Stokes equations, and they are based on the Newtonian principles of conservation of mass, momentum and energy. The variables p, μ and δ_{ij} represent the pressure, dynamic viscosity and Kronecker delta function, respectively.

3.3 Modelling of Aerodynamics and Turbulence

3.3.1 RANS modelling

RANS modelling is based on the principle that the flow quantities (u, v, w, ρ and p) may be split into a mean component (here denoted with the overbar, $\overline{q}$) and fluctuation component *q'*. This process is known as the Reynolds decomposition. This approach is based on the idea that there is a fundamental disparity between the time scales of random turbulent fluctuations, and the deterministic time scales of interest for engineering applications [70]; therefore, it should be possible to average-out the motions of the former and still produce a reasonable estimate of the latter.

The Reynolds decomposition is substituted into the Navier-Stokes equations given in Eq. 3.1, and ensemble-averaging is applied to the whole equation, to arrive at the Reynolds averaged Navier-Stokes (RANS) equations. The RANS equations has a form similar to the original equations, but with one crucial difference; in the momentum equation the viscous stress $T_{ij}^{(\nu)}$ is replaced with $T_{ij}^{(\nu)} + \overline{\rho u_i' u_j'}$, where the second term represents the effect of the fluctuations on the mean flow. This is referred to as the Reynolds stress τ_{ij}.

Some sort of closure equation is therefore required to model the Reynolds stresses. Most RANS models use the Boussinesq hypothesis, which relates the Reynolds stresses to the turbulent kinetic energy $k = 0.5(u'^2 + v'^2 + w'^2)$, a turbulent viscosity μ_t, and the mean velocity gradients:

$$\tau_{ij} = \mu_t \left(\frac{\partial \overline{u}_i}{\partial x_j} + \frac{\partial \overline{u}_j}{\partial x_i} - \frac{2}{3} \frac{\partial \overline{u}_k}{\partial x_k} \delta_{ij} \right) - \frac{2}{3} \rho k \delta_{ij} \tag{3.4}$$

This simplifying assumption is used to model the turbulence at all scales. Therefore, it may be difficult to get an accurate solution for geometrically-complex problems. It also relies on certain assumptions: (i) that changes in the flow direction are slow enough for the turbulent production and dissipation to be in balance; and (ii) that turbulence structures are isotropic [82]. Neither of these can be guaranteed in a complex unsteady flow. RANS models are also often calibrated with ‘standard’ thin shear flows, and so are likely to fail when the dominant eddies are highly influenced by the specific geometry [83]. However RANS modelling has been shown to give good results for steady flows, and produces a reasonable approximation for time-averaged values of unsteady flows. RANS techniques are also useful in generating an initial solution as a springboard for the more sophisticated techniques, which may be less numerically stable. The turbulence model which will be used in this thesis is the one-equation Spalart-Allmaras model [84], which solves a transport equation for a modified turbulent viscosity variable $\hat{\nu_t}$. The original turbulent viscosity ratio ν_t/ν can be recovered using $\hat{\nu_t}/\nu$ and the model constants. The full mathematical details of the model are given in [85]. It has been used in several studies (e.g. [9, 86, 87]) and has been shown to be generally well suited for aircraft applications.

3.3.2 LES modelling

Fundamentals of LES modelling

Large Eddy Simulation (LES) is a different approach to the same problem; that is, the prohibitive cost of resolving all the scales of motion in a turbulent flow. LES uses a spatial filtering approach to separate the flow into large and small structures. This allows a more direct treatment of the structures, which is better suited to massively-separated flows and complex geometries.

Explicit LES filtering generally takes the form of a integration in space of the original function multiplied by the filter function [82], which is characterized by a cutoff width Δ. The field may also be considered "implicitly" filtered, so to speak, by treating the grid-resolved variables as the filtered variables, as will be done in this thesis. The filtered version of any variable q is denoted $\widetilde{q}$. Structures larger than the filter size are computed directly using the filtered Navier-Stokes equations; only the structures smaller than the filter size are modelled. This allows a much more accurate treatment of the larger structures and their transient nature. Also, it is expected that the large scales carry most of the energy and are more directly related to the geometry; small scales tend to be more homogenous and universal [88]. Therefore a simplified modelling approach is more likely be successful with these small scales. Additionally, as the small scales carry only a small proportion of the total kinetic energy, it is expected that simplifications here should not unduly affect the large-scale structures [89].

Applying the filtering operation to the Navier-Stokes equations produces terms relating to the "small" (unresolved) structures, which take the form of stresses and are generally referred to as subgrid-scale (SGS) stresses $T_{ij}^{(SGS)}$ [82]. The filtered continuity equation takes the same form as the original, and the filtered momentum equation (from Equation 3.1) is given in Equation 3.5.

$$\begin{aligned} \frac{\partial}{\partial t}\left(\widetilde{\rho}\widetilde{u}_i\right) + \frac{\partial}{\partial x_j}\left(\widetilde{\rho}\,\widetilde{u}_i\widetilde{u}_j + \widetilde{p}\delta_{ij} + \widetilde{T_{ij}^{(\nu)}} + T_{ij}^{(SGS)}\right) = 0 \\ T_{ij}^{(SGS)} = \widetilde{\rho u_i u_j} - \widetilde{\rho}\widetilde{u}_i\widetilde{u}_j \end{aligned} \tag{3.5}$$

SGS stresses allow the resolved flow to adapt to the effect of the unresolved turbulence [90]. Several SGS models exist for modelling this stress. This project uses the Smagorinsky-Lilly model [82], which is based on the Boussinesq hypothesis (Equation 3.4), and suggests that the SGS stresses are proportional to the local large-scale strain rate:

$$T_{ij}^{(SGS)} = -\mu_{SGS}\left(\frac{\partial \widetilde{u}_i}{\partial x_j} + \frac{\partial \widetilde{u}_j}{\partial x_i}\right) - \frac{1}{3}T_{ii}^{(SGS)}\delta_{ij} \tag{3.6}$$

The sub-grid-scale turbulent viscosity μ_{SGS} (or $\nu_{SGS} = \mu_{SGS}/\rho$) may then be estimated from one of many available models.

The Smagorinsky SGS model

One of the simplest and most robust SGS models is the Smagorinsky model, which relates μ_{SGS} to the grid scale (quantified by the cutoff filter) and the stress tensor of the resolved flow S_{ij}:

$$\nu_{SGS} = (C_{SGS}\Delta)^2\sqrt{2S_{ij}S_{ij}}, \tag{3.7}$$

$$S_{ij} = \frac{1}{2}\left(\frac{\partial \widetilde{u}_i}{\partial x_j} + \frac{\partial \widetilde{u}_j}{\partial x_i}\right)$$

$$|S| = (2S_{ij}S_{ij}) \tag{3.8}$$

The tilde denotes the variable from the filtered flow field. The constant C_{SGS} is generally set at 0.16 [82, 91], but it has shown some tendency to be flow dependant and require adjusting for different applications [82, 89].

The Smagorinsky model is based on the assumption that in the small scales, kinetic energy production and dissipation are in balance. Energy transfer between the scales is only permitted from large scales to small scales; that is, it does not permit backscatter of energy to large scales. It may not be well suited to properly modelling the reduction in scale near a wall [14], which is problematic for boundary-layer applications. It also has a tendency towards excessive damping [89]. For example, in the viscous sublayer of the turbulent boundary layer the local flow is essentially laminar, and thus the SGS viscosity should theoretically be zero (as there are no smaller turbulent scales to be modelled). However, the velocity gradient in the wall-normal direction produces a non-zero mean shear strain and therefore - according to Equation 3.7 - a non-zero ν_{SGS}. This artificially inflates the viscosity beyond what is physical, and therefore excessively damps the flow field. A variety of more sophisticated LES models have been developed to combat such effects, and are described in Section 3.3.2.

The cutoff grid size Δ used in the filtering operation is generally related to the grid size. In this thesis, it is set to equal to the cube-root of the volume of the cell, which is a fairly common approach [82]. It also allows the cutoff width to be reduced near the wall, where the cell size is generally smaller, so that the small near-wall turbulent eddies may be properly resolved.

For simple turbulence that conforms to Kolmogorov's theory of self similarity, the modelled stress component has been shown [92] to be proportional to the grid size, which makes the conventional RANS notion of grid-independance more complicated. LES is also highly sensitive to the grid quality; stretched grids have been shown to produce false numerical noise in the high-frequency range [90]. Furthermore, numerical errors caused by discretization can, if not properly managed, even be so large as to swamp the SGS stresses [82]. Therefore grid generation of particular importance for LES simulations. For fully wall-resolved LES, typical values of dimensionless grid sizing which have been used in past studies for a variety of applications [93] are: $\Delta y_1^+ < 1$, $50 < \Delta x^+ < 150$, and $15 < \Delta z^+ < 40$.

Variations on the SGS model

Various modifications to the standard Smagorinsky models have been proposed to address these shortcomings. One of the most straightforward is the addition of van Driest damping. This is a relatively simple modification to the Smagorinsky model, which imposes artificial damping to allow the turbulent viscosity to approach zero near the walls. The Smagorinsky constant C_S is multiplied by the van Driest damping factor:

$$1 - e^{\left(y^+/A^+\right)} \tag{3.9}$$

In general, the van Driest damping constant is taken as $A^+ = 25$ [94]. This model has been applied in many studies and is well verified (e.g. [43, 88, 95, 96]). The van Driest model is effective at imposing zero viscosity near the wall, but the existance of the constant A^+ requires some degree of tuning. Also, its dependance on wall-normal units make it inherently less suitable for application to complex geometries with non-standard boundary layers, where such units may be difficult to define. A modified LES model which only depends on the local flow would be more robust and useful for landing-gear applications.
Another option is the dynamic Smagorinsky model. This method uses a second level of filtering in order to estimate the SGS model constant (C_S as in the standard Smagorinsky model) dynamically, by computing it from the larger-scale structures [89]. In addition to the standard filter (generally the grid) separating the grid-scale from the sub-grid scale, an additional test filter (usually twice as large as the grid filter) is implemented. The difference between the sub-grid-scale stresses and the sub-test-scale stresses is used to evaluate the model constants, often with averaging over a small time interval [82]. This method has also been extensively tested (e.g. [43, 89]) and is generally accepted to be more accurate than the standard Smagorinsky model in the near-wall area. The main disadvantage is the additional computational burden of the test-filter stage, which may significantly increase the time required for a simulation.

The standard Smagorinsky model was the only LES model which had previously been implemented in the in-house solver used in this thesis. In deciding which additional SGS model would be best to introduce, the following factors were considered: it should have minimal additional computational expense, as landing-gear geometries are complex and likely to require large meshes; it should allow the turbulent viscosity to vanish near the wall for accurate results in the boundary layer, and in laminar flow; it should have minimal tunable constants, in order to be robust across different flow types; and, ideally, it should not depend on a strict definition of wall distance etc., as this may become problematic with more complex geometries.

Such a model was proposed by Leveque et al [91], called the Shear-Improved Smagorinsky Model (SISM). Instead of defining the turbulent viscosity as directly proportional to the total strain rate, they use an 'adjusted' strain rate with the mean-strain removed:

$$\nu_{SGS} = (C_s\Delta)^2 \left(|S| - |\langle\overline{S}\rangle|\right) \tag{3.10}$$

The angle brackets in the term $|\langle\overline{S}\rangle|$ denote an averaging procedure to obtain a mean shear; this may be a time average, an ensemble average (if there is a homogenous direction in the flow-field), or both. Those authors [91] posit that near the wall, the large velocity gradients should dominate the shear strain; thus the averaged $|\langle\overline{S}\rangle|$ will be comparable to the local $|S|$, reducing the right-hand side term and allowing ν_{SGS} to approach zero in the steady viscous sublayer, as desired. Far away from the wall the mean shear is expected to be weak (close to zero), and therefore $|S| \gg |\langle\overline{S}\rangle|$, allowing Equation 3.10 to recover the standard Smagorinsky model. The SISM model was tested for a channel flow with periodic boundary conditions in the spanwise and streamwise directions, and was found to give good agreement with DNS data [91].

As the turbulent viscosity is calculated from the local strain with the shear strain subtracted, and the local strain may fluctuate slightly due to the turbulent nature of the outer flow, it is possible that Equation 3.10 may occasionally yield negative values of ν_{SGS}, which is not physical. It is unlikely for this to have a major effect on the flow field, as the mean strain rate will be only be significantly non-zero in the near-wall region, where the turbulent fluctuations are expected to be small within the viscous sublayer. However, both previous studies have imposed a limiting on the viscosity to force it to be non-negative (i.e. negative values are set to 0). This can be applied either to the total viscosity (as in [91]), or specifically to the SGS viscosity (as in [97]). In this work, the standard implementation of the SISM model has the clipping applied to the SGS viscosity. When applying this model to a geometry that is periodic in the span direction, the averaged term $|\langle\overline{S}\rangle|$ is composed of both an ensemble-average in the spanwise (z) direction, and a time-average, updated at the end of each time iteration. The ensemble average in z is a simple average through the full span for a given (x, y) location. (This part of the algorithm was later removed when extending this approach to a fully three-dimensional geometry). For the time-averaging, to avoid the computational expense of retaining the strain field through a range of timesteps, an exponential averaging technique is used, as recommended by Boudet et al [97]. The averaging takes the form [97]:

$$\langle q\rangle^t = (1 - c_{exp})\,\langle q\rangle^{t-1} + c_{exp}q^t, \quad c_{exp} = 1 - 0.05^{\Delta t/T_{cutoff}} \tag{3.11}$$

The value of T_{cutoff} determines the effective window of the time average; data older than T_{cutoff} will have a cumulative influence of less than 5% on the total average. In this thesis, T_{cutoff} was selected to be half of the total domain flow-through time, and c_{exp} was calculated accordingly from Equation 3.11.

3.3.3 DES modelling

Due to the substantial decrease in scale near a wall, LES is not always affordable for wall-bounded flows. For this reason a hybrid between LES and RANS was developed, called Detached Eddy Simulation or "DES" [85].

The formulation of DES is based on the parallels between the formulation of the RANS and LES models. In the RANS model, the destruction term for the modified eddy viscosity ν_t is dependant on a lengthscale d, which is the distance to the closest wall [85]. The term ν_t is found to scale with d^2 and the strain rate S_{ij}, as defined in Equation 3.7. For the LES formulation, as given in Equation 3.7, the sub-grid-scale eddy viscosity ν_{SGS} also scales with strain rate, and with the square of a lengthscale, in this case based on Δ which varies with the grid spacing. Therefore, the definition of the lengthscale determines whether the SGS model or the Spalart-Allmaras model is being used, and the two formulations may be linked in this way.

The standard DES model [85] uses the following hybrid lengthscale:

$$\widetilde{d} = \min\left(d_w, C_{DES}\Delta\right) \tag{3.12}$$

The model constant C_{DES} is of order 1; the commonly used value is $C_{DES} = 0.65$, which has been used with good results in past studies (e.g. [56, 59]). When $d \ll \Delta$, the model acts as a Spalart-Allmaras RANS model; when $d \gg \Delta$, it is effectively LES [85]. In other words, it allows the treatment of the turbulence to be dependant on the grid. In regions where the grid is fine (and therefore Δ is small), where it may be assumed that the energetic motions can be captured in the resolved grid-scale, LES is used; in other regions, Reynolds-averaging is used [83]. Generally the mesh is configured such that LES regions coincide with regions where the flow is separated and complex turbulent structures are expected. Therefore it is expected that modelled stresses are dominant in the RANS region, and are small relative to the resolved stresses in the LES region, for a grid with adequate resolution in the separated regions [92].

DES has been used successfully in bluff-body aerodynamics, and has been shown to give the correct features of complex flows such as separated cylinder flow [83] where unsteady RANS does not. For landing-gear applications, DES simulations can resolve the small-scale turbulence and the downstream propagation of the structures (which is relevant for component wake interaction) much more accurately than RANS [92]. DES analysis of landing gear cavity has been shown to give agreement with experiment to within 4dB in the overall sound pressure level [10].

Although this is good by current standards of landing gear noise computation, a 4dB error corresponds to a 60% error in the unsteady forces, and therefore there is significant room for improvement. For other cavity simulations DES has been found to under-predict the broadband noise and over-predict the amplitude of the tonal peaks [14]. Its high dependance on grid quality and the uncertainty in the region where the behavior switches from RANS to LES can be an issue for landing-gear applications [98]. Several modifications to the DES formulation have been proposed and used with some success for complex geometries and landing gear flow (see for example [26, 98, 99]).

Delayed Detached Eddy Simulation (DDES)

In this thesis, all DES simulations were performed using the extension to the DES model proposed by Spalart et al [100], referred to as Delayed Detached Eddy Simulation (DDES). This modification seeks to improve the transition between the RANS modelling and the LES modelling. The standard formulation (Equation 3.12) uses only the grid to determine whether the LES or RANS model is selected. In regions where the flow is attached, but the wall-parallel grid spacing is smaller than the boundary-layer thickness δ_{BL}, this can cause problems. This situation can be caused by the thickening of the boundary layer (such as in the presence of an adverse pressure gradient), or by grid refinement near an edge (which is relevant for the case of a thick boundary layer approaching a cavity lip). Equation 3.12 would follow the LES branch in this situation, despite the fact that the boundary layer is still attached and the resolution is insufficient for LES. The LES formulation has a lower ν_t than the RANS, which means a reduction in modelled Reynolds stresses; and the resolved Reynolds stresses are unable to compensate, due to the insufficient LES resolution [100]. The modified DDES model utilizes a parameter r_d, which is related to the ratio between a lengthscale and the wall distance:

$$r_d = \frac{\nu_t + \nu}{\sqrt{\frac{\partial u_i}{\partial u_j}\frac{\partial u_i}{\partial u_j}}\kappa^2 d^2} \tag{3.13}$$

The value of r_d is 1 in a logarithmic boundary layer and drops to 0 towards the edge of the boundary layer. Therefore in the LES region, $r_d \ll 1$. This is used to define the DDES hybrid lengthscale [100], according to:

$$\widetilde{d} = d - f_d \max\left(0, d_w - C_{DES}\Delta\right), \text{ where } f_d = 1 - \tanh\left([8r_d]^3\right) \tag{3.14}$$

The function f_d controls the switching between the RANS and LES branches of the model. In the boundary layer r_d is close to 1, therefore $f_d \approx 0$ and the RANS model is activated ($\widetilde{d} = d_w$). Outside the boundary layer, and in regions of massive separation, f_d increases from 0 to 1; where $f_d = 1$, the standard DES lengthscale (Equation 3.12) is recovered. Because the hybrid lengthscale is now dependant on the flow field, it is able to discern whether a point is within the boundary layer (based on the value of r_d), and resist the switch from RANS to LES mode even if the grid is ambiguous. Furthermore, the switch from RANS to LES behaviour was found [100] to be sharper using the DDES formulation, with less of the uncertain area between the branches. This model has been tested on several applications [100], including a multi-element airfoil and a backwards-facing step (which is particularly relevant for the sharp separation expected in a cavity application), and was found to give good results. The constants 8 and 3 in the definition of f_d were derived by Spalart et al [100] from tests using the Spalart-Allmaras model, which is the same RANS model used in this thesis, and therefore are expected to be suitable values. The implementation of this DDES model in SotonCAA has previously been used with good results [16].

3.4 Discretisation and Numerical Methods

The governing equations and numerical models given in Section 3.3 need to be discretized in both time and space in order to arrive at a solution. This project utilizes an in-house code called SotonCAA, from the Airbus Noise Technology Centre (ANTC) at the University of Southampton. SotonCAA has been developed over many years, and has been used successfully in previous studies (e.g [7,101,102]). Recent improvements to SotonCAA have been described by Wang, Fattah, Angland and Zhang [103,104] and Gill, Fattah and Zhang [105]. This code utilizes high-order discretization methods in order to maximize computational efficiency and flow resolution for a given mesh size. The software solves the compressible Navier-Stokes equations in full conservative form.

3.4.1 Spatial Discretisation

SotonCAA is a finite difference solver, requiring a structured grid. This allows relatively simple implementation of high-order schemes, to improve accuracy and resolution requirements.

The finite difference scheme used in SotonCAA is the optimized prefactored compact scheme as proposed by Ashcroft and Zhang [106], based on the original compact scheme by Lele [107]. Compact schemes define the derivative function for one point using the derivatives from neighbouring points. Unlike explicit spatial schemes, where the spatial derivative at some point is a function of a certain fixed ‘stencil’ of other points, compact schemes (also known as ‘implicit’ schemes) implicitly use the values at all the other points in the domain. A linear system of equations must be solved simultaneously to obtain the spatial derivatives at any point. This creates complexity in the implementation but a higher level of interdependancy of the spatial points, and allows significant improvements in the resolution of high-wavenumber components, compared to an equivalent explicit scheme [107]. The Lele scheme is given by [107]:

$$\begin{aligned}\beta\left(D_{i-2}+D_{i+2}\right)+\alpha\left(D_{i-1}+D_{i+1}\right)+&D_i \\ &= c\frac{f_{i+3}-f_{i-3}}{6\Delta x}+b\frac{f_{i+2}-f_{i-2}}{4\Delta x}+a\frac{f_{i+1}-f_{i-1}}{2\Delta x}\end{aligned} \tag{3.15}$$

where D_i denotes the spatial derivative of the function f at point i and Δx is the spacing between points. The coefficients a, b, c, α and β may be obtained by matching the coefficients of the corresponding Taylor series expansion of f about f_i [107]; the formal truncation error is determined by the number of terms matched to the Taylor expansion. The Ashcroft & Zhang scheme builds on this, dividing the process into forward and backwards operators, D_i^F and D_i^B respectively. The general form is given by:

$$
\begin{aligned}
D_i &= \frac{1}{2}\left(D_i^F + D_i^B\right), \\
\alpha_F D_{i+1}^F + \beta_F D_i^F &= \frac{1}{\Delta x}\left(a_F f_{i+2} + b_F f_{i+1} + c_F f_i + d_F f_{i-1} + e_F f_{i-2}\right), \\
\beta_B D_i^B + \beta_B D_{i-1}^B &= \frac{1}{\Delta x}\left(a_B f_{i+2} + b_B f_{i+1} + c_B f_i + d_B f_{i-1} + e_B f_{i-2}\right)
\end{aligned}
\tag{3.16}
$$

Additional constraints are imposed to ensure the scheme is symmetric and therefore non-dissipative [106], and that the derivative vanishes to zero in zero-gradient regions of the flow:

$$
\begin{aligned}
\beta_B = \beta_F, \gamma_B = \alpha_F \\
a_B = e_F, b_B = -d_F, c_B = -c_F, d_B = -b_F, e_B = -a_F \\
a_F + b_F + c_F + d_F + e_F = 0
\end{aligned}
\tag{3.17}
$$

The closure of the remainder of the coefficients is based on a combination of two methods: first, the Taylor-series expansion matching as used in the Lele scheme, which determines the formal accuracy; and second, an optimization process to improve resolution over a wider range of wavenumbers. The optimization process is based on first finding the numerical wavenumber of the scheme, by taking the Fourier transform of the stencil. An integrated error measure is then defined, calculated from the weighted difference between the numerical and actual wavenumber, over a certain range. The error is then minimized by finding the derivative of the error with respect to the coefficients, and setting this to zero. Therefore, instead of defining the constants entirely from the Taylor expansion process, some of those constraints are substituted with the constraints from the error minimisation process. This sacrifices some formal accuracy of the scheme, but in return improves its ability to resolve wave propagation characteristics over a higher range of wavenumbers [106].

The particular scheme used in this thesis is the “8/4” scheme [106], which is an optimised 4^{th}-order prefactored compact scheme using a three-point stencil. The name refers to its having a theoretical maximum 8^{th}-order accuracy but an actual 4^{th}-order accuracy due to the constraints allowed to the optimisation process. The coefficients of the scheme are given in Table 3.4.1, reproduced from Table 1 in [106]. Those authors’ analysis of the scheme, based on the criteria that the slope of the numerical wavenumber to the actual wavenumber should be within 0.5% of unity, found that the minimum points-per-wavelength required to accurately resolve a wave is 4.49.

At internal block boundaries, ghost points from the neighbouring block are used to retain the same scheme. Near the external boundary points, where central schemes are not possible, the numerical implementation switches to biased schemes. As described in [106], third-order biased explicit stencils are used, using the four points closest to the boundary. Coefficients of the stencils are obtained by matching the Taylor series expansions of the derivatives.

Table 3.1: Coefficients of 8/4 Compact Scheme; reproduced from [106]

α_F	0.36469246438579827
β_F	0.68337354822981936
a_F	0.0
b_F	0.80189188343264239
c_F	-0.53899133241291931
d_F	-0.27962697285647092
e_F	0.01672642183674783

3.4.2 Temporal Discretisation

SotonCAA uses the time-stepping approach as put forth by Li et al [108] to solve the governing equations plus the perfect-gas equation of state. This is considered an 'implicit' temporal approach, as the variables at the next timestep t_{i+1} are estimated using the other variables at t_{i+1}, insteading of the 'lagged' values at t_i. This method avoids having to time-lag any terms by using a Newton-like subiteration method based on a 'pseudo-time' τ.

Beginning from the solution at time t, a pseudo-time derivative of the dependant variables is added to the governing equations, and is discretised using a backwards first-order accurate time-differencing method. A flux-splitting technique is then used to evalute the fluxes for each cell, the convective flux is linearized about the pseudo-time level, and the matrices are decomposed into lower and upper matrices (LU decomposition) for use in the numerical algorithm. The solution is thus iterated forward through pseudo-time levels until the unsteady residual in the solution converges to zero, and the solution stabilizes (referred to in [108] as the 'pseudo steady state'). The subiterations in τ allow the solution to converge at each timestep before proceeding to the next timestep.

This method has been found [108] to perform better than conventional explicit time-stepping for a number of cases. For example, when tested on an unsteady fuselage flow at $M = 0.20$, this technique was found to obtain a converged result where the Runge-Kutta method had failed, using the same timestep. Overall this strategy was found to be reliable, robust and accurate [108]. Using implicit time stepping also allows longer timesteps to be used than an explicit method would require. This is useful for oscillating flows where a large time-sample is required to resolve lower-frequency content.

3.4.3 Filtering

The high-order nature of these discretization methods allows a high degree of accuracy. Unfortunately, it also means that numerical and dispersive errors are able to propagate through the domain, and may grow to the point of compromising the solution. This is particularly likely when the geometry is complex or the flow is highly turbulent [109]. These numerical errors tend to occur in the high-frequency portion of the spectrum [110]. For very high wavenumbers, at spatial scales beyond the minimum that can be adequately resolved by the grid and spatial scheme, the predicted velocities of waves can be grossly inaccurate, leading to contamination of the flow-field [111]. Therefore some form of filtering is required to remove this erroneous and numerically destabilizing content, without

Table 3.2: Coefficients of Explicit Filters

	α_0	α_1	α_2	α_3
4^{th}-order scheme	$\frac{5}{8}$	$\frac{1}{4}$	$-\frac{1}{16}$	-
6^{th}-order scheme	$\frac{11}{16}$	$\frac{15}{64}$	$-\frac{3}{32}$	$\frac{1}{64}$

excessively interfering with the legitimate components of the flow.

Two methods will be used in this thesis. The first is a discrete, explicit filtering function, as developed by Vasilyev, Lund and Moin [110]. The purpose of this process is to damp the energy in the high-frequency range, where the numerical error is dominant [110]. For a central scheme, the function f_i (which represents any of the conserved variables at some point i) is related to the filtered function $\hat{f}_i$, according to:

$$\hat{f}_i = \sum_{j=-m}^{j=m} \alpha_j f_{i+j} \tag{3.18}$$

The filtering is accurate to $2m$-order. The filter coefficients α_m were developed [110] such that they satisfy constraints based on the filter moments (for minimal commutation error), and to allow the Fourier transform of the filter to be zero at the cutoff frequency. The fourth-order and sixth-order symmetric filters (that is, $\alpha_{-j} = \alpha j$) have been chosen for this thesis. The coefficients are given in Table 3.2. At the boundaries, biased stencils are used. The coefficients are as described in [110], and derived in the same manner as central scheme coefficients. The 6^{th}-order filter uses four-point third-order accurate biased schemes for the three points nearest each boundary, while the 4^{th}-order filter uses three-point, second-order accurate, biased stencils for the two boundary points.

The second method is an implicit filter function. Implicit filtering differs from the explicit method in that it is formulated with the filtered variable $\hat{f}_i$ being a function of not only the unfiltered variable f, but also the filtered variable at other points. Similar to the compact formulations used in the spatial discretization, this requires a linear system of equation to be solved for each point, and is more numerically complex to implement. However, it also allows a greater sensitivity of the filtered variable to the wider flow-field. The implicit filtering method can therefore be more accurate and provide greater resolution for the same stencil size [109].

The implicit filter used in SotonCAA is taken from the study of Kim [109]. It is based on a symmetric seven-point stencil, of the form:

$$\begin{aligned} &\beta\hat{\Delta}f_{i-2} + \alpha\hat{\Delta}f_{i-1} + \hat{\Delta}f_i + \alpha\hat{\Delta}f_{i+1} + \beta\hat{\Delta}f_{i+2} \\ &\qquad = \sum_{m-1}^{3} a_m \left(f_{i-m} - 2f_i + f_{i+m}\right), \qquad \hat{\Delta}f_i = \hat{f}_i - f_i \end{aligned} \tag{3.19}$$

The coefficients in Equation 3.19 were derived [109] to satisfy the requirements for formal sixth-order accuracy according to the Taylor series expansion. Additional constraints were imposed on the filter transfer function to ensure desirable smooth filtering behaviour in the high wavenumber domain. The nominal cut-off scaled wavenumber for filtering κ_C may be imposed by the user, where κ_C is related to an actual cutoff wavenumber k_{cutoff} according to $\kappa_C = k_{cutoff}\Delta/\pi$, where Δ is the grid size in a given direction. The filter coefficients are determined from κ_C from the following [109]:

$$\begin{aligned}
\alpha &= -\frac{30\cos(\kappa_C\pi) + 2\cos(2\kappa_C\pi)}{A(\kappa_C\pi)}, \\
\beta &= \frac{18 + 9\cos(\kappa_C\pi) + 6\cos(2\kappa_C\pi) - \cos(3\kappa_C)}{2A(\kappa_C\pi)}, \\
a_1 &= \frac{30}{A(\kappa_C\pi)}\cos^4\left(\frac{\kappa_C\pi}{2}\right), \quad a_2 = -\frac{2a_1}{5}, \quad a_3 = \frac{a_1}{15} \\
&\text{where } A(\kappa_C\pi) = 30 - 5\cos(\kappa_C\pi) + 10\cos(2\kappa_C\pi) - 3\cos(3\kappa_C\pi)
\end{aligned} \tag{3.20}$$

Values of κ_C can range between 0.4996 and 0.99999 [109]. The largest resolvable wavenumber for a uniform grid is equal to π/Δ [112], equivalent to $\kappa_C = 1$. The higher the value of κ_C, the less of the solution is being filtered. Past experience with SotonCAA has indicated that κ_C must be below 0.90 for a steady solution, and $\kappa_C \approx 0.80$ should allow most of the physical oscillations to be retained. Estimating the dissipation from the method described in [112], using values typical of the boundary layers in the LES of in Chapter 7-9, $\kappa_C = 0.8$ gives $k_{cutoff}\eta = 1.4 \times 10^{-2}$ (where η is the Kolmogorov length scale). Compared to the Kolmogorov energy spectra for similar applications in the literature [113], this places the cutoff wavenumber in the inertial range of the spectrum, as is desired [112].

Near the edges of the domain, where the central scheme cannot be used, a boundary formulation is implemented following Kim et al [109]. Fourth-order polynomials are used to extrapolate data from the interior to the boundary nodes, and the derived coefficients are functions of the interior-scheme coefficients [109]. Therefore the overall numerical implementation of the scheme is determined by the single parameter κ_C. User experience has indicated that the solution performs best if the boundary-stencil value of κ_C is slightly smaller than the main value.

3.4.4 Boundary Conditions

Wall boundaries in this thesis are, unless otherwise specified, modelled as rigid no-slip walls with no flux of mass, momentum or energy through the boundary. All velocity components are set to zero. In some cases a slip wall is used near corners, where only the velocity component normal to the wall is set to zero, and the gradients normal to the wall are also zero. In the span direction, periodic boundary conditions are used to model the flow across an infinite span, by effectively tiling the solution in the periodic direction (generally, the z direction). The variables in the vicinity of each periodic boundary are copied across as ghost points to the other boundary, so that the flow structures across the boundary are perfectly coherent.

For uniform inflow conditions, the variables are prescribed at freestream values. However most of the LES simulations (Chapters 7-9) use a spatially-varying prescribed inflow profile which is described in those sections. The LES turbulent viscosity ν_{SGS} is calculated from the inflow velocity field; and the DES turbulent viscosity ν_t is, unless otherwise specified, set such that $\hat{\nu_t}/\nu = 5$, in accordance with the recommendation of Spalart and Rumsey [114], which equates to $\nu_t/\nu = 1.3$.

Outflow Boundary Condition

The standard outflow boundary condition used in this thesis is formulated according to the far-field pressure boundary condition proposed by Jameson and Schmidt [115]. This boundary condition is non-reflective, i.e. it minimizes the reflection of acoustic waves back into the domain. Freestream values are specified at the boundary, and the nodes adjacent to the boundary are modified using the Riemann invariants R^+ and R^-. These are defined according to Equation 3.21, where γ is the ratio of specific heats for an ideal gas, v_n denotes the magnitude of the velocity component normal to the boundary, the subscript $_\infty$ denotes freestream values, and $_i$ denotes variables from the adjacent interior node.

$$R^+ = v_{n,\infty} - \frac{2c_\infty}{\gamma - 1} \tag{3.21}$$

$$R^- = v_{n,i} + \frac{2c_i}{\gamma - 1} \tag{3.22}$$

The tangential component of the velocity, and the entropy s, are interpolated from the interior. Values of v_n, c, pressure p and density ρ at the boundary are calculated according to:

$$c = \frac{\gamma - 1}{4}\left(R^+ - R^-\right) \tag{3.23}$$

$$v_n = \frac{1}{2}\left(R^+ + R^-\right) \tag{3.24}$$

$$s = p/\rho^\gamma, \qquad c = \gamma p/\rho \tag{3.25}$$

3.4.5 Buffer Zone Boundary Condition

Some simulations in this thesis also the buffer zone boundary condition of Richards et al [116]. The solution variables at the end of each timestep $\mathbf{U}$ are explictly forced to evolve to target values $\mathbf{U_{target}}$ over the buffer zone region. The modified variables $\hat{\mathbf{U}}$ are calculated according to: [116]

$$\hat{\mathbf{U}} = \mathbf{U} - 1\left(1 - \frac{L_{bz} - x_{bz}}{L_{bz}}\right)^3 (\mathbf{U} - \mathbf{U_{target}}) \tag{3.26}$$

This allows a smooth transition between the physical flow variables (at the flow-interior sides of the buffer zone) and the prescribed values at the exterior boundary ($\mathbf{U_{target}}$), which has been shown to reduce reflections of numerical noise back into the simulation domain [116]. The DDES simulations use this boundary condition with the target values set to the freestream values. The LES simulations in later chapters used a modification to this where the U_{target} values were obtained directly from the developing mean-flow values at a small distance inside of the boundary, and updated regularly throughout the simulation, in order to minimize the disturbance caused by this boundary condition. Buffer-zone widths of 2, 5, and 10 cells were tested, and the smaller zones were found to produce better results, so a buffer width of 2 was selected for those simulations.

3.4.6 Alterations to In-House SotonCAA Solver

Node-Centred vs. Cell-Centered

The version of SotonCAA available at the beginning of this PhD project used a node-centred formulation. This version was used in the square-cavity simulations in Section 4.4, and the unsteadiness the cavity flow-field was found to cause stability issues, requiring the use of the explicit filters, as described in that Section. However, the code was later updated to a cell-centred formulation by Wang, Fattah et al [103], which was found to be more stable. All other simulations used this updated version, and the improved stability allowed the 6^{th}-order implicit filter to be used throughout, so long as the κ_C variable was correctly tuned.

Contributions from this Thesis

At the beginning of this thesis, the available version of the in-house solver had an LES module with the standard Smagorinsky model, but it had not been tested or validated. Part of the work in this thesis was to assess and modify the implementation of the LES solver. Several errors in this part of the code were identified and fixed.

Additionally, the shear-improved Smagorinsky model [91] was implemented into the code for the first time, including the time-averaging and ensemble-averaging required to calculate the mean shear strain. Rigorous tests were performed to ensure that the solver calculated the turbulent viscosity correctly, and that the model was able to regain the standard Smagorinsky formulation away from the wall.

Also, the implementation of the outflow buffer-zone boundary condition was modified. The original formulation used the freestream values as the target values. This was undesirable as the flow near the no-slip wall boundary layer was also forced to evolve towards uniform freestream values. Instead, the new version of the boundary condition obtained the mean variables from the interior of the flow field, at a slice parallel to the boundary and near the boundary, and used these values as target values. This allowed the boundary layer to develop relatively uninterrupted up to the buffer-zone boundary face, reducing the influence on the flow upstream.

Chapter 4

DES Validation Cases

4.1 Overview

The purpose of this chapter is to synthesize a set of guidelines for the application of DES to partially-covered cavity geometries at $M = 0.2 - 0.3$. The simulations in the following two chapters (Chapter 5 and Chapter 6) require large grids, so it was not deemed feasible to perform separate systematic grid independance studies for each case. Also, no single validation case was found in the literature for the case of a partially-covered cavity in the Mach number range of interest. Therefore, the validation is built up by considering separate validation cases for various aspects of the case of interest. Section 4.2 deals with a simple zero-pressure-gradient flat plate at $M = 0.20$ where the flow is fully attached; essentially a test of the RANS modelling in the boundary layer from DES. Section 4.3 is a validation case for a partially-covered cavity at a low Mach number ($M < 0.1$), for which experimental velocity measurements are available. Section 4.4, the third validation case, is a generic subsonic ($M = 0.3$) square cavity, for which the development of Rossiter modes is expected, and may be compared to the trends observed from the literature. The purpose of these studies is to validate the code, and to investigate mesh and simulation guidelines for the case of interest - a partially-covered cavity at low-subsonic speeds - which is a combination of these validation cases. The DES simulations in Chapter 5 and Chapter 6 are conducted according to gridding and simulation parameter guidelines based on the outcomes of these validation studies.

4.2 2D RANS Validation Benchmark Case

This section tests the ability of the code to correctly model the features of an attached boundary layer, by validating against a standard zero pressure gradient flat plate. Since DES uses RANS in the attached region, and the whole flow field is attached in this simple case, this is essentially a validation of the implemented RANS model, which is the same Spalart-Allmaras model used with the DDES.

The validation case selected is the $M = 0.2$ turbulent flat plate study in the NASA validation archive [117]. The freestream pressure and temperature are close to standard atmospheric conditions: 101.3 kPa and 294 K; with the Reynolds number Re (based on

U_∞ and plate length L) reaching up to Re_L of $12{\times}10^6$, and u-velocity profile (where x is aligned with the freestream velocity) taken at $Re_x = 7.6 \times 10^6$. A schematic of the domain is shown in Figure 4.1. The floor of the main section of length L is set to a no-slip wall condition to simulate the plate. Upstream and downstream of the plate, small slip-wall sections of $0.025L$ were added to allow the flow to relax towards the inflow and outflow conditions. At the inflow, a uniform freestream velocity profile was prescribed; downstream of the plate a small free-slip wall was applied, and the outflow condition set to match the freestream condition. The total height of the domain was $0.25L$ for this initial simulation.

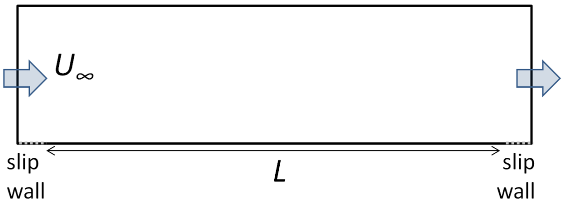

Figure 4.1: Schematic of computational domain for 2D flat-plate turbulent boundary layer

The 2D mesh was generated using rectangular cells. Along the plate, the x-spacing was set to $0.001L$ with additional clustering near the leading and trailing edges (see Figure 4.2). In the wall-normal (y) direction 300 grid points were used, clustered towards the wall to give $y_1 = 1.6{\times}10^{-6}L$, which should equate to $\Delta y_1^+ = 1$ (estimated using the standard turbulent flat plate empirical profiles in Pope [28]). This is sufficient to resolve the boundary layer, and consistent with the Δy_1^+ used in the computational study in the validation case [117]. The corresponding spacing in the free-stream direction was $\Delta x^+ \approx 600$, which (although high for most applications) is expected to be sufficient for this simple case, especially as the CFD study in [117] was able to obtain quite good agreement with 10 times few nodes in the x-direction.

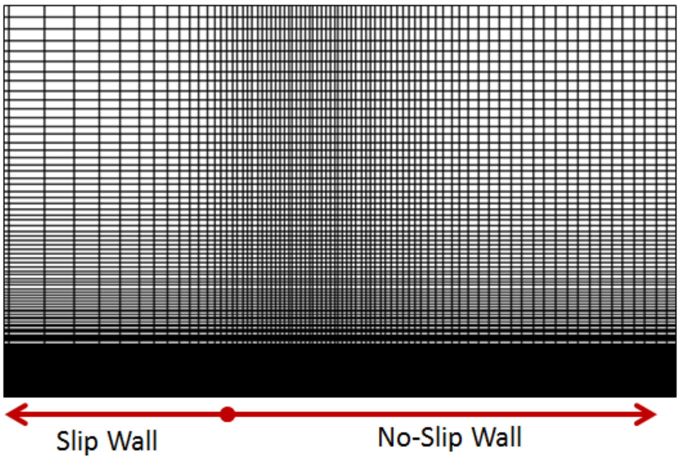

Figure 4.2: Close-up of 2D mesh at leading edge

The final flow field was obtained by iterating the simulation forward in time until the measured flow field had been observed to settle to a steady solution. The timestep used equated to CFL = 3. The implicit time marching scheme described in Section 3.4 was used, with cutoff wavenumber $\kappa_C = 0.80$ for the interior scheme and 0.78 for the boundary. (Since the flow field is steady, less aggressive filtering could be used than in Section 4.3 without causing instability. However, increasing κ_C further above this level was found to cause stability issues.) Defining a reference time $T^* = L/U_\infty$, a steady solution was obtained after $t/T^* \approx 1.0$.

The comparison between the SotonCAA result and the validation data is given in Figure 4.3, along with data from a refined mesh with the x-spacing halved, and the Schlichting turbulent skin friction profile from Equation 2.2. The SotonCAA result is an excellent fit to the Schlichting profile. It is also a very good fit to the validation data, aside from a small offset, which may have to do with the freestream conditions or inaccuracies in digitizing the data from [117]. Also, there is no significant difference in the solution from having doubled the x-resolution. Therefore we may conclude that the SotonCAA simulation is set up and implemented correctly, and the RANS model is able to correctly predict the characteristics of a turbulent flat plate.

The effect of inflow turbulent viscosity was also tested. The simulations in Figure 4.3 used a turbulent viscosity ratio $\hat{\nu}_t/\nu = 5$, equivalent to $\nu_t/\nu = 1.3$, which is fairly common practice [114]. A much lower value of $\hat{\nu}_t/\nu$ =0.3 was also tested, following the recommendation of Spalart and Rumsey [114], where excessively high eddy viscosities had been found to "contaminate" the flow-field, producing unphysical results. In the present case, the solution was found to be identical. This is consistent with the observations from [114], where it was noted that $\hat{\nu}_t/\nu = 5$ may be considered low, and that the flow field only becomes affected at around $\hat{\nu}_t/\nu = 500$. Those authors also note that $\hat{\nu}_t/\nu$ values of 3 or 5 are "well-placed" to allow a fully-turbulent boundary layer where the Reynolds number is reasonably high, as is generally the case for landing gear applications. Therefore, $\hat{\nu}_t/\nu = 5$ is retained as the inflow condition throughout the rest of this thesis.

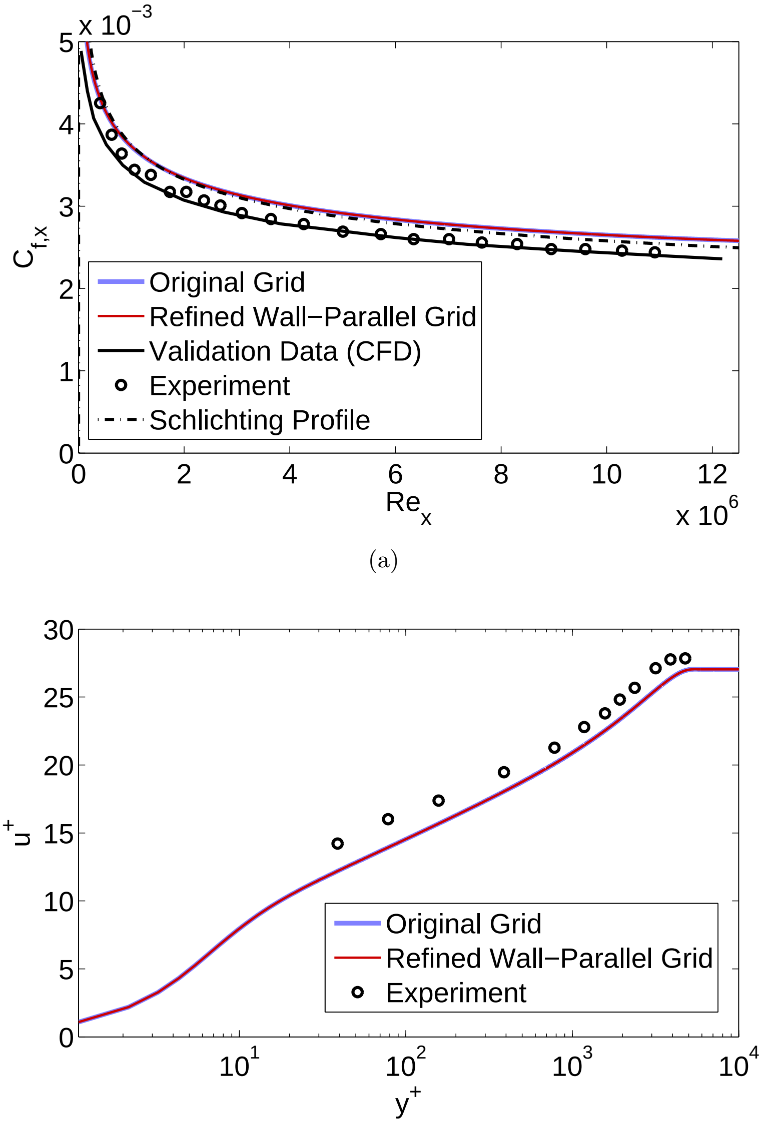

(a)

(b)

Figure 4.3: Comparison of 2D RANS simulation with validation data from [117] and Equation 2.2: (a) skin friction distribution; (b) velocity profile at $Re = 7.6 \times 10^6$

4.3 Low-Subsonic Partially Covered Cavity

4.3.1 Overview and Geometry

A landing gear bay geometry will typically have a covered section either upstream (if the front doors close while the gear is deployed) or downstream (if the rear doors close while the gear is deployed). The case study here investigates the effects of having covered sections at both ends. The simulation is set up to match the partially-covered cavity experiment performed by Nishimura, Goto and Kimura [58]. As well as providing an additional validation case for the CFD methodology, the results of this study will also be useful for investigating the flow features of a partially-covered cavity, and how this differs from the standard square cavity described in Section 4.4.

The numerical method uses the in-house SotonCAA solver as described in Section 3.4. The turbulence is modelled with DES, specifically the Spalart-Allmaras-based DDES model as described in Section 3.3.3. The 6^{th}-order implicit filter is used, with $\kappa_C = 0.52$ in the interior and 0.50 at the boundary nodes.

The geometry of the cavity is illustrated in Figure 4.4, based on the setup used in the experiment [58]. A freestream velocity is imposed in the x-direction, travels over a flat plate (developing a boundary layer), and then over a cavity. At the leading edge of the cavity, denoted x_{LE}, the Reynolds number Re_x is equal to 5.3×10^5. The cavity is partially covered from both sides: based on the cavity depth $D = 0.207$m, the covered sections are of length $0.76D$, and the open section L_{open} is $1.32D$; the cavity lip itself is of thickness $0.1D$. The shear layer impacts the lip of the downstream covered section, so this area is expected to have the greatest degree of unsteadiness and therefore is of particular interest. Mean velocity and RMS-velocity probes are placed at points around the lip of the downstream cover, as shown in Figure 4.5, to match the locations of the hot-wire probes used in [58].

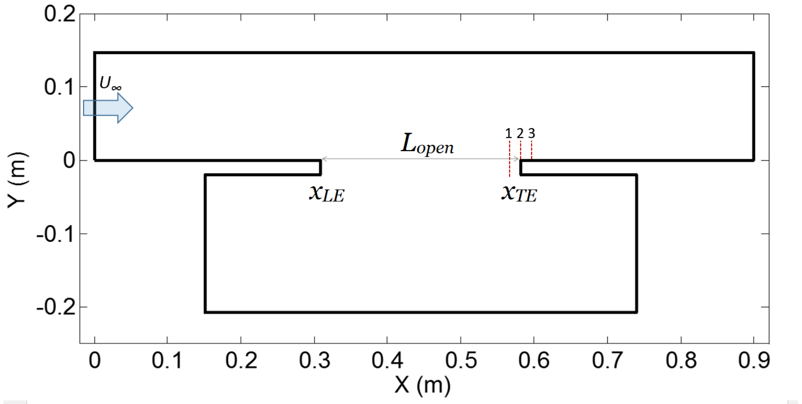

Figure 4.4: 2D view of geometry for covered-cavity case of Nishimura et al [58]; at x_{LE}, $Re_x = 5.3 \times 10^5$.

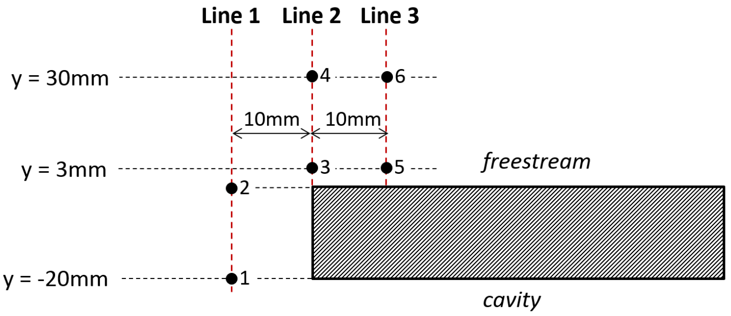

Figure 4.5: Close-up of measurement lines from Figure 4.4, and monitor points

4.3.2 Boundary Conditions

The inflow is modelled with the freestream velocity $U_\infty = 25$ m/s ($M_\infty = 0.0735$). As discussed in Section 4.2, the inflow turbulent viscosity is set to $\hat{\nu}_t/\nu = 5$, equivalent to $\nu_t/\nu = 1.3$, as will be used for all further DES simulations in this thesis. The first 0.02m after the inflow, as well as the last 0.02 before the outflow, are modelled as a free-slip wall to avoid numerical instabilities in the corner; the rest of the plate, the top wall, and the cavity are all no-slip walls, to match the tunnel walls used in the experiment. The x and y directions denote the freestream and wall-normal distances.

In the spanwise (z) direction, the experimental setup [58] had a tunnel width of 0.1m, ending in perforated plates with cloth covering the holes, in order to be acoustically transparant. The effect of this boundary on the flow is not clear, as measurements were not taken to show the variation in the span. Additionally, those authors also did not specify the spanwise location of the hotwire probes. A preliminary simulation was performed with $L_z = 0.1$m and with no-slip walls at the ends. The mesh is shown in Figure 4.6, and a plot of u_{RMS} at the x-plane equivalent to Line 1 (Figure 4.4) is shown in Figure 4.7. There is clearly a strong variation in the z-direction caused by the influence of the no-slip wall conditions; velocity probes will be highly dependant on the z location. To avoid these uncertanties in the CFD setup, periodic boundary conditions were used instead for the z walls (so that the flow has a theoretically infinite span), and the mean velocity is averaged through the span. The same $L_z = 0.1$m is used, to allow similar development of flow structures in the span.

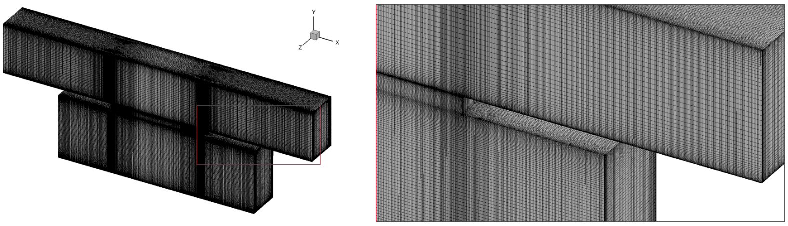

Figure 4.6: 3D mesh used in initial simulation, with no-slip side-walls

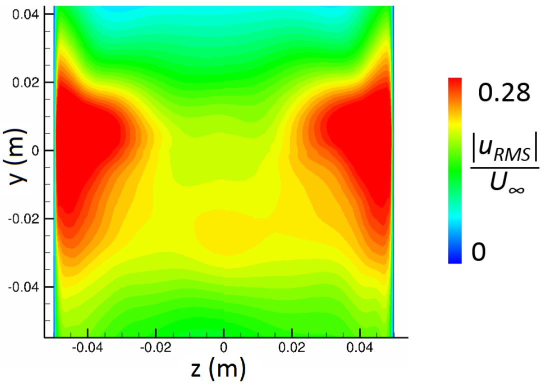

Figure 4.7: u_{RMS} at $x = 0.572$m (corresponding to Line 1 in Figure 4.4, evaluated using fully-3D geometry

4.3.3 Resolution

$X - Y$ Resolution and Timestep

Two meshes were tested to gauge the sensitivity of the simulation to the $X-Y$ resolution. The coarser mesh is shown in Figure 4.8. The baseline Δx is 1.3mm ($0.005L_{open}$), with additional resolution near x_{LE} and x_{TE} (cell size reduced to $0.002L_{open}$). In the y-direction, the mesh has 60 cells above the cavity and 30 cells across the cavity lip, again clustered towards the edges, with a minimum y-distance of $0.001D$. The 2D mesh has 94,000 cells, which was then extruded across L_z with 40 cells in the z-direction, yielding a final mesh with 3.8M cells. From the initial analysis this corresponds to $\Delta x^+ = 17 - 46, \Delta y_1^+ = 7$ and $\Delta z^+ = 89$.

The finer $X - Y$ mesh is shown in Figure 4.9. The resolution in the unsteady shear layer region is significantly increased: the number of points across the open section is nearly doubled (from 230 to 400); N_Y across the lip is increased from 30 to 50; the first cell height (y_1) is halved to $0.0005D$; and the smallest cells inside the cavity are reduced by 40% in both the X and Y directions. Overall, the 2D mesh size is increased to 157,000 cells. The 3D mesh is generated using the same spanwise extrusion of 40 cells, yielding a total mesh size of 6.3M cells.

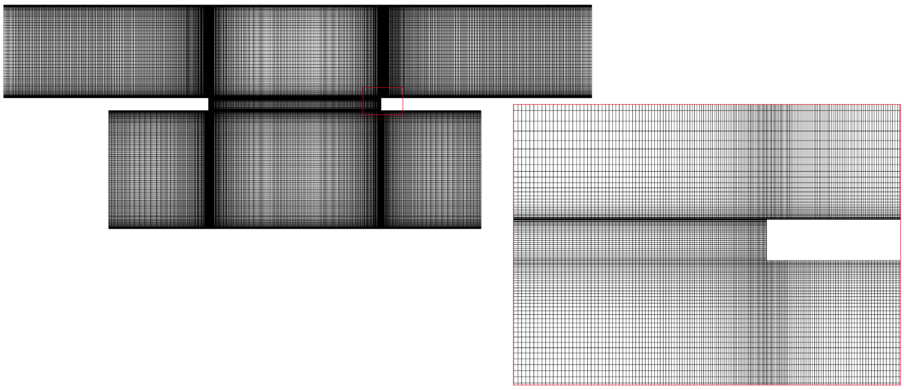

Figure 4.8: $X - Y$ resolution - Mesh 1 (coarser)

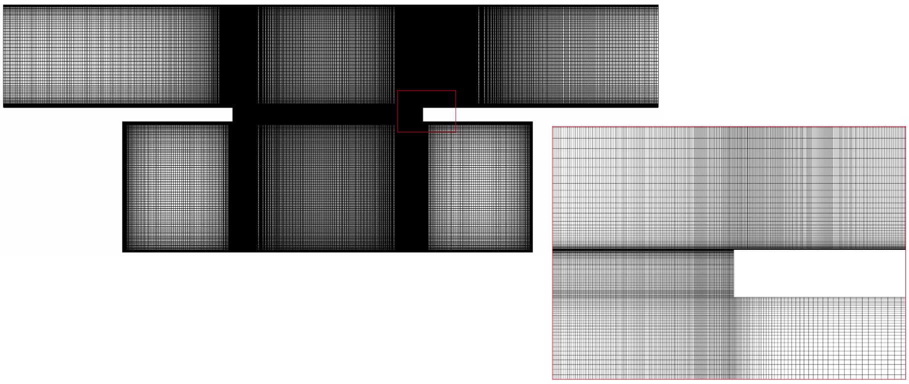

Figure 4.9: $X - Y$ resolution - Mesh 2 (finer)

The baseline timestep used was equivalent to $T^*/\Delta t = 3700$, where T^* is based on L_{open} and U_∞. This equates to a CFL number of 5, which is high but still stable with the implicit time advancement scheme used in the code, and allows sufficient resolution of the highest frequency components expected based on the experimental data. However with the finer $X - Y$ mesh, the same physical timestep results in a higher CFL number, and was found to cause stability issues. Therefore the finer $X - Y$ mesh also used a finer timestep: the timestep was halved, $T^*/\Delta t = 7400$, to give the same CFL ≈ 5. The effect of the finer $X - Y$ mesh and the finer timestep are therefore tested together. An example of the comparison between the two results is shown in Figure 4.10. The difference is fairly small. Both use the coarsest z-resolution, which may be the cause of some of this scatter. It may be concluded that in terms of the overall trends in the data, significantly increasing the $X-Y$ resolution and halving the timestep does not cause a substantial change in this flow field. Therefore, for computational efficiency, the coarser mesh and timestep are used for the remainder of this validation case.

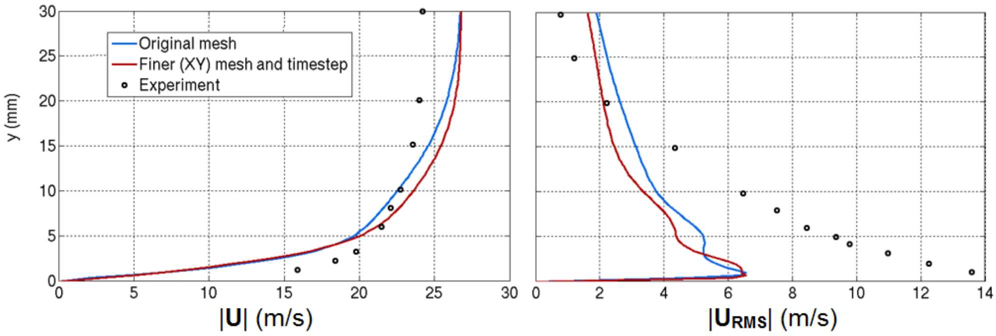

Figure 4.10: Comparison of mean and RMS velocity between coarser and finer $X-Y$ meshes at Line 3

Z Resolution

The effect of the resolution in the z direction was investigated using the coarser $X-Y$ mesh and the same $L_z = 0.1$. Three spanwise resolutions were tested; $\Delta z/L_{open} = 0.01$ (the baseline), $\Delta z/L_{open} = 0.006$, and $\Delta z/L_{open} = 0.0037$. (In inner units this corresponds to $\Delta z^+ = 89$, 61, and 36). An example of the difference produced in the flow field is shown in Figure 4.11. There is a clear increase in the RMS velocity going from $\Delta z/L_{open} = 0.01$ to 0.006, and no significant difference in reducing the value further. It may therefore it can be concluded that at $\Delta z/L_{open} \approx 0.006$, the simulation result is grid-independant.

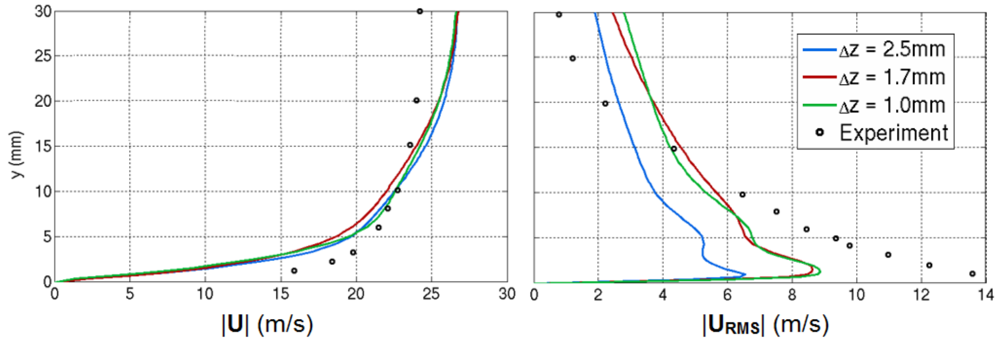

Figure 4.11: Comparison of mean and RMS velocity between coarser and finer Z meshes

4.3.4 Comparison with Experimental Data

The computed velocity magnitudes with this optimal grid are compared across the three downstream measurement stations in Figure 4.12. The overall trends are reasonably well captured. At Line 1 and Line 3 the velocity magnitude from the CFD is generally within

$0.1U_\infty$ of the hot-wire measurements. The location of the velocity minimum around the lip in Line 1 ($y < 0$, the only measurements inside the cavity) is especially well matched.

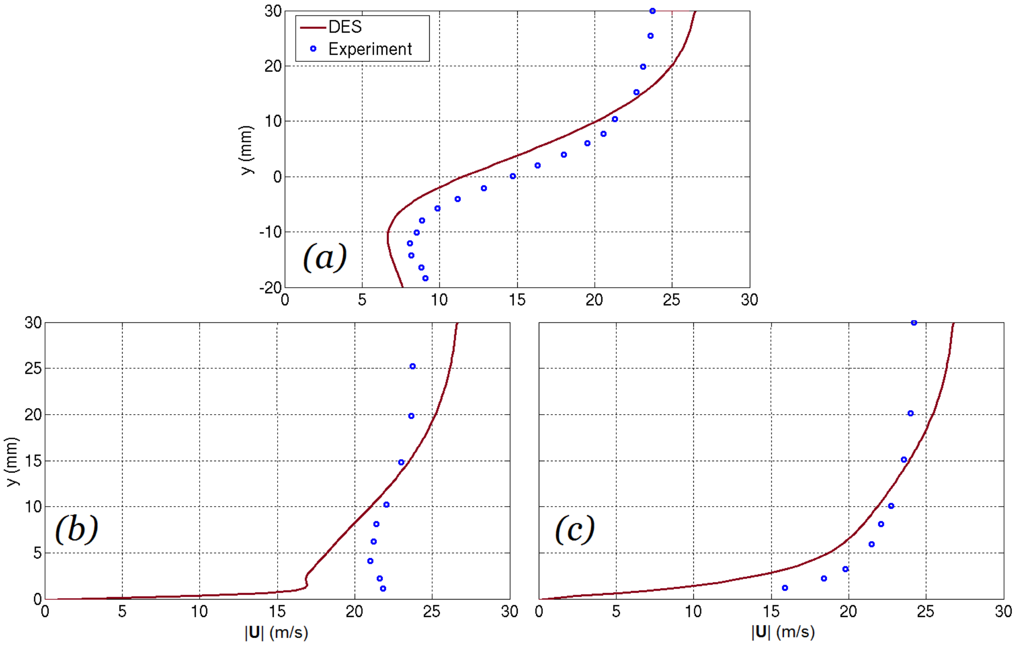

Figure 4.12: Comparison of mean velocity profiles between current DES simulation and experimental data from [58], at locations indicated in 4.4: (a) Line 1; (b) Line 2; (c) Line 3

RMS velocities were also recorded in the experiment, but unfortunately were not well predicted by the current simulation, as indicated in Figure 4.10 and 4.11. The simulation tends to significantly under-predict the peak values of $|U_{RMS}|$. This is attributed to the difference in the upstream boundary layer. In the experiment, the cavity was placed near the beginning of the test section of the tunnel. In the simulation, the flow coming into the test section (i.e. at the $x = 0$ point) was modelled as a uniform flow with the freestream velocity, as shown in Figure 4.4. The length of the plate upstream of the cavity is matched to the experiment. However, Figure 4.13 compares the mean and RMS velocity at the leading edge of the cavity, x_{LE} (i.e. the start of the open section, where the shear layer separates). The experiment has a thinner boundary layer, which could account for some of the discrepancies in Figure 4.12. Significantly, DES substantially under-predicts the RMS velocities in this region, compared to the experiment, which explains the under-prediction of the RMS velocities at the downstream locations. The under-prediction of RMS velocity may be related to the omitted spanwise-end plates, as Figure 4.7 illustrated that the walls in the z-direction have a tendency to increase the turbulent intensity. In terms of the modelling assumptions in the streamwise direction, at the inlet to the test section ($x = 0$ in Figure 4.4), the simulation assumes that the flow is steady; however, $x = 0$ corresponds to the edge of the converging nozzle in the wind tunnel setup. Therefore it is possible that the flow is still settling at the upstream cavity edge, which would contribute to increased RMS velocity in the experiment and the difference in the boundary layer profile. Probably the most significant factor, however, is that the DES uses unsteady RANS in the upstream boundary layer, which is only capable of modelling very low-frequency unsteadiness, and therefore cannot correctly model the kinetic energy in the upstream boundary layer. The $|U_{RMS}|$ levels shown by the DES at x_{LE} in Figure 4.13 are caused by the proximity to the cavity; further upstream in the boundary layer, $|U_{RMS}|$ in the DES is effectively zero, since the flow is attached, so the RANS-modelled boundary layer is effectively steady. This is a fundamental shortcoming of DES analysis, which is therefore unable to model the unsteady boundary layer turbulence upstream, which feeds into the cavity shear layer and therefore is very likely to affect the results downstream in the cavity. The wall-resolved LES modelling approach for a turbulent boundary layer described in Chapter 7, and the application of that methodology with a partially-covered cavity downstream in Chapters 8 and 9, seek to address this deficiency in the modelling approach.

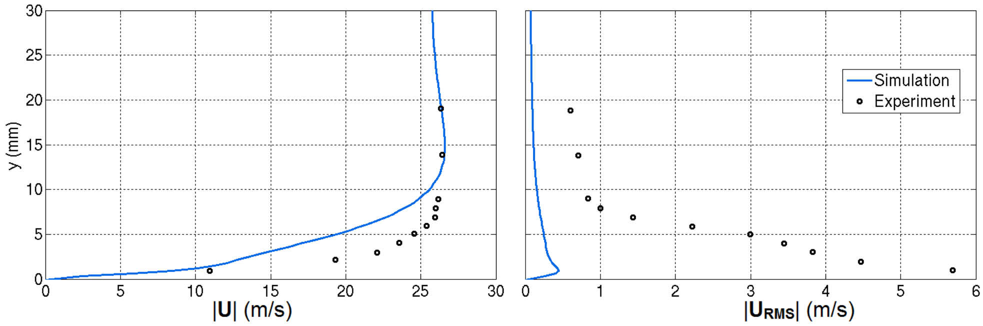

Figure 4.13: Comparison of computational results (($\Delta z = 1.7$mm grid) with experimental measurements at the upstream edge of the cavity

4.3.5 Frequency analysis

The hot-wire measurements taken in the experiment were also used to calcuate the spectra of the turbulent intensity at the points show in in Figure 4.5. Using the final grid described in Section 4.3.3, the time history of the velocity magnitudes were recorded at the same points at every timestep. This time series data was subdivided into nine windows with 50% overlap, a fast-Fourier transform was performed on each window, and the resultant power spectral density (PSD) distributions were averaged together. This method has been shown to be a reliable way of smoothing sampling noise out of a spectral analysis [118].The resultant spectra shown in Figure 4.14. The minimum resolvable frequency with this windowing was 4.8Hz, which is well below the range shown in the figure (which is based on the range of the experimental spectra), therefore the simulation sampling time can be considered sufficiently long. Even with the coarser timestep, the highest maximum resolvable frequency was also well above the range of the experiment. Comparing the DES result with the experiment, the spectral 'hump' at about 125Hz is well captured. At higher frequencies, the CFD drops off more quickly than the experiment, which is not uncommon for numerical methods (e.g. [46]). At the lower frequencies, the points highest above the edge exhibit a drop-off with decreasing frequency in the experiment that was not replicated in the CFD. Since the CFD sampling window provided sufficient resolution at low frequencies, it is unclear why this feature could not be modelled; it may be related to the previously-described differences in the upstream condition. Regardless, at Points 1 (upstream of the impact edge), 3 and 5 - the points closest to the wall - the experimental spectra does not drop off at low frequencies, so the shape is fairly well matched by the DES; and at Points 3 and 5 (dowstream of the lip, closest above the surface of the cavity cover) the DES spectra is a very close match to the experiment up to $f = 250$Hz. Furthermore, the experimental spectra exhibits a higher peak for the points closest to the surface, and the CFD result shows the same trend. Therefore overall, the DES simulation is able to replicate the major features of the turbulent intensity spectra for this case.

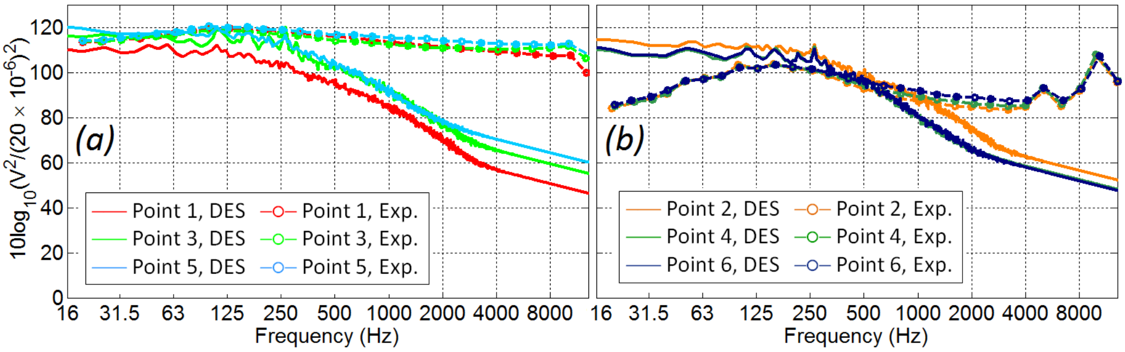

Figure 4.14: Computed velocity magnitude spectra at monitor points (Figure 4.5) compared with experimental measurements from [58]: (a) Points near the wall (Points 1, 3 and 5); (b) points further from the wall (Points 2, 4 and 6)

4.3.6 Flow features

Having validated the quantitative measurements to a reasonable degree of accuracy, the CFD simulation may now be used to further investigate the flow features of this cavity beyond the variables that were measured in this experiment. The vorticity structures in the cavity region are illustrated using the Q-criterion in Figure 4.15. The plot shows the shedding of regular vortex structures from x_{LE} across the shear layer. These structures start to break down as they travel over the open section, and then impact on the upstream edge of the downstream lip (x_{TE}), where the measurements were taken. The small unsteady features in the shear layer and downstream are indicative of turbulence. Inside the cavity the structures are also chaotic; but there is a clear region of higher velocity underneath x_{TE} and then back upstream along the bottom wall. This suggests that some of the higher-velocity flow in the shear layer is diverted downwards by the downstream lip, and forms a vortex inside the cavity.

This is more clearly illustrated by the mean (time-averaged) velocity vectors, as shown in Figure 4.16. A large, strong vortex is formed underneath the open section of the cavity, with two weaker, lower-velocity counter-rotating vortices forming under the two covered sections on either side. The 3D streamlines show that the mean-flow vortices are quite orderly, with little variation in the span direction (as is expected due to the spanwise-periodic boundary condition), and minimal interaction between the three vortices. The unsteady pressures are shown in Figure 4.17 for a representative z-slice in the centre of the domain. The RMS pressure is characterized by a band across the shear layer, increasing in width with distance from the upstream lip (corresponding to the increasing unsteadiness

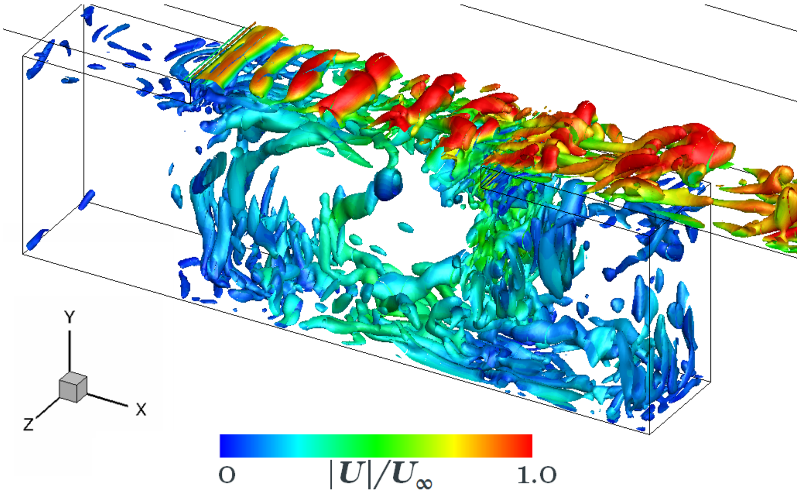

Figure 4.15: Iso-surfaces of the Q-criterion, coloured by velocity magnitude

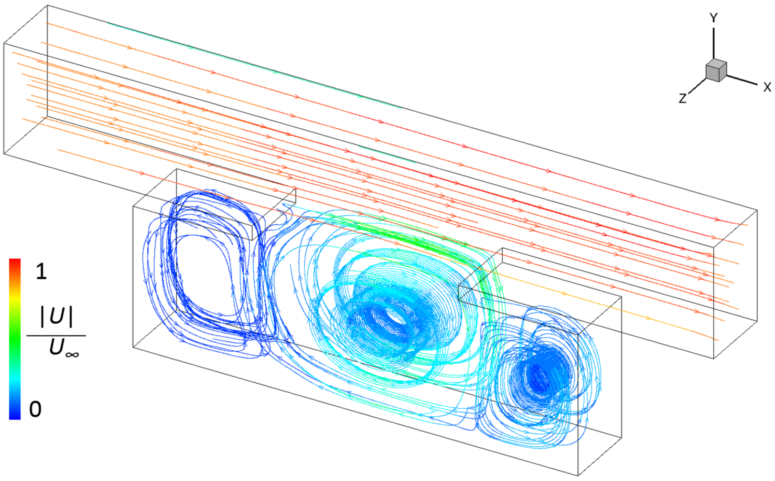

Figure 4.16: Streamtraces of mean velocity, coloured by mean velocity magnitude

of the shear layer after it is shed from the upstream boundary layer), and culminating in a maximum region at the point of impact with the downstream lip. The instantaneous fluctuation pressure, shown in Figure 4.17, exhibits the pattern of alternating high-pressure and low-pressure regions that is characteristic of vortex shedding.

From all this, it may be concluded the cavity covers (which would be representative of closed landing-gear bay doors) have the effect of dividing the flow inside the cavity into sections of counter-rotating vortices, with the strongest vortex being underneath the open section of the cavity. Outside the cavity, the shear layer exhibits common characteristics of an open cavity; the shear layer separates at x_{LE} and reattaches at x_{TE}.

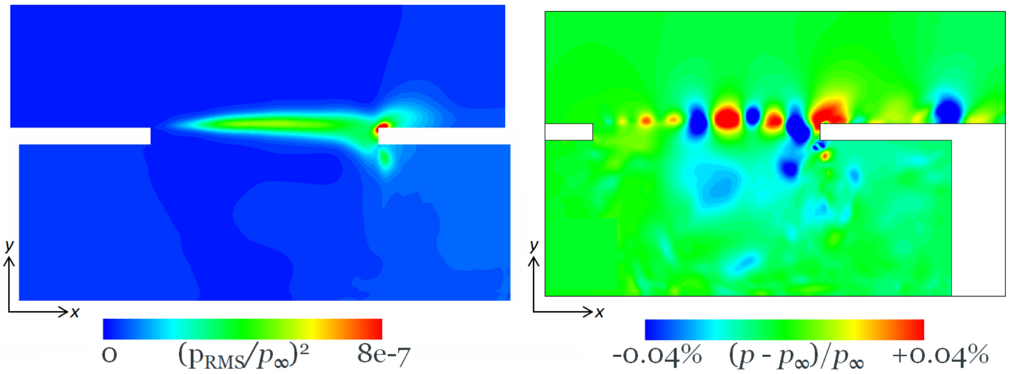

Figure 4.17: Contours of pressure at plane $z/L_z = 0.25$: (a) RMS pressure across cavity mouth, averaged in z; (b) instantaneous pressure fluctations

4.4 Square Cavity

4.4.1 Overview

This chapter describes a series of simulations on a basic square cavity configuration at subsonic speeds. This case provides an additional validation for the code, particularly the frequency response of the cavity, which can be predicted for this simple configuration by the equations described in Section 2.4.

4.4.2 Geometry and Scaling Parameters

The $X - Y$ domain consists of a $L/D = 1$ cavity in a flat plate of length $4L$ upstream of the cavity and L downstream of the cavity. The domain extends above the cavity and plate by height L. At the upstream and downstream ends of the plate, additional sections of $0.1L$ are added with a free-slip condition, to allow the flow to relax to the freestream conditions as show in Figure 4.18. (The downstream extent of the domain was extended in later geometries, in order to rule out boundary interference.) This 2D mesh was extruded in the normal (z) direction by a distance of $0.075L$ with 15 uniformly-sized blocks of $\Delta z = 0.005L$ (the same as used in Section 4.3), so the cells in the centre of the cavity are cubic. The 3D mesh on the surfaces at the cavity leading edge is shown in Figure 4.20. The same boundary conditions are retained on the extruded surfaces on the new mesh. The new surfaces (the z-normal planes at the front and back) are assigned periodic boundary conditions.

The cavity and plate sections are all treated with standard no-slip wall boundary conditions. A freestream velocity in the x direction is imposed at the inlet, and freestream conditions are also imposed on the top wall. The outlet uses an earlier implementation of the buffer zone, where the target values are set to the freestream values, and a small free-slip wall (15 cells) is imposed at the downstream edge of the plate to allow this evolution.The freestream flow conditions used in these simulations are as follows: the Reynolds number, based on reference length L, is $Re_L = 3.1 \times 10^6$; temperature $T = 288$K and the Mach number is set at $M_\infty = 0.30$, towards the top end of the range of interest for landing gear applications, to ensure resonance develops. These parameters were used with

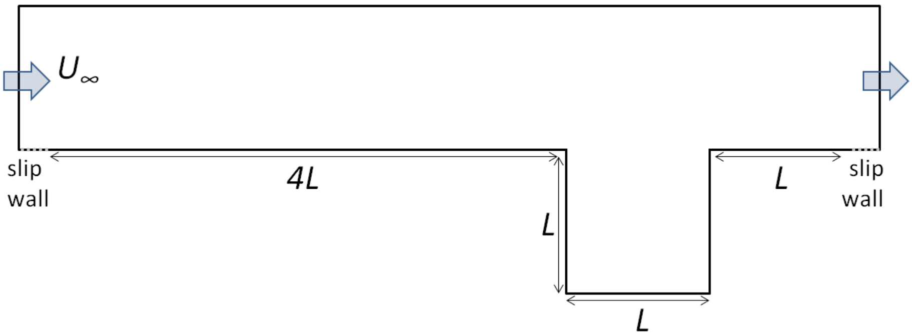

Figure 4.18: Schematic of cavity flow domain

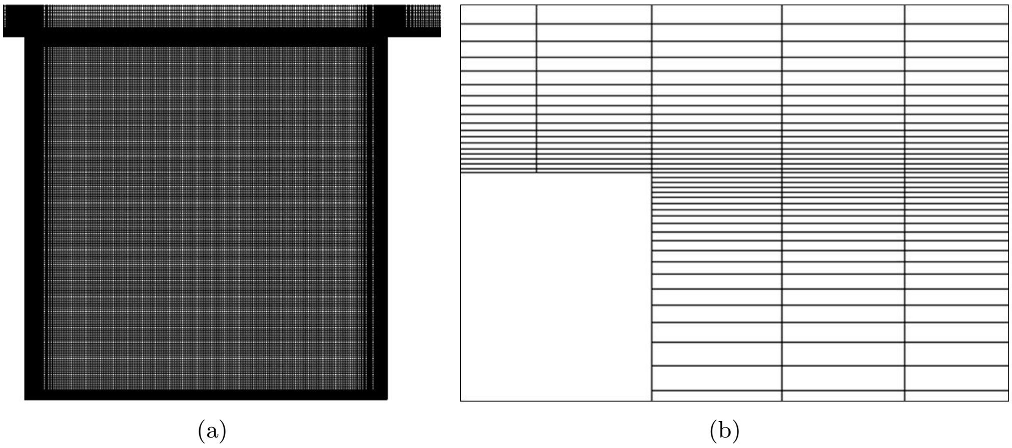

Figure 4.19: 2D cavity mesh: (a) whole cavity region (b) Close-up at leading-edge

Equation 2.5 to obtain the predicted Strouhal numbers of the cavity response. The dimensionless time T^* is based on U_∞ and L (i.e. the flow-through time over the mouth of the cavity).

4.4.3 Mesh

The flat plate sections of the mesh are based on the RANS analysis of a flat plate in Section 4.2. It contains 250 uniformly-distributed points per length L in the streamwise direction. Based on the turbulence properties in Section 4.2, this gives $\Delta x^+ \approx 63$. The wall-normal direction has 67 points clustered near the wall using a hyperbolic-tangent profile, such that the first cell height equates to $\Delta y_1^+ \approx 1$. The grid inside the cavity is based on a $\Delta_x = \Delta_y = 0.005L$ square spacing in the interior. At the cavity walls and across the mouth, the grid is refined in the x and y directions to match the spacing in the boundary layer mesh. This allows the mesh to maintain 1:1 blocking (as is currently required by SotonCAA), as well as eliminating skewness and sharp changes in grid size, both of which can affect the numerical accuracy of the solution. The mesh in the cavity, and a close-up at the leading edge of the cavity, are shown in Figure 4.19. Pressure monitors are placed across the mouth of the cavity, at distances x from the leading edge equivalent to $x/L =$ 0.05, 0.25, 0.5, 0.75 and 0.97.

The simulations in this section also use DDES with the SotonCAA solver. However the earliest node-centred version of the code was used in this study, which had a greater

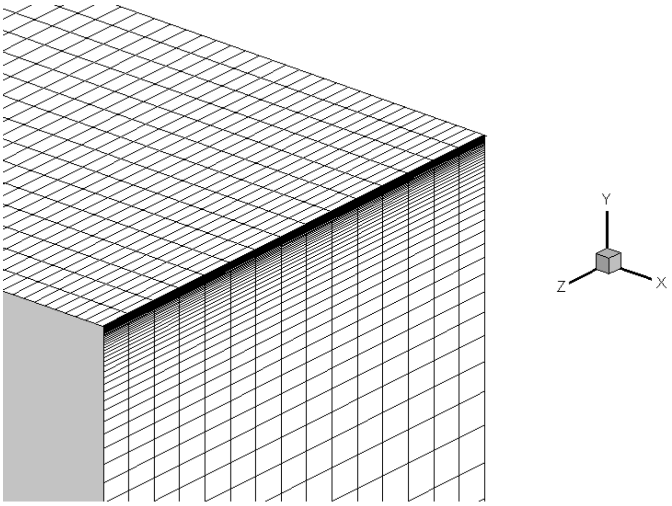

Figure 4.20: Close-up of 3D surface mesh at cavity leading edge

tendency towards divergence with unsteady cavity flow fields. This placed some limitations on the solver settings and timestep. The implicit filter could not be used; therefore the two explicit filters (4^{th}-order and 6^{th}-order) were tested. A base timestep of CFL = 3.2 was selected, equivalent to $T^*/\Delta t = 11,000$.

4.4.4 Results

Baseline simulation flow field characteristics

For the 4^{th}-order filter, after a simulated flow time of $t/T^* = 15$, the pressure and vorticity contours, and streamlines, are shown in Figure 4.21, where velocities are scaled with the freestream speed of sound c_0. The velocity lines clearly indicate a large, stable central vortex, with smaller "roller-bearing" type vortices in the corners, quite consistent with the flow features expected based on the literature summarised in Section 2.4.2 and the experimental observations of Roshko [52]. The vorticity distribution also highlights the existance of several smaller unsteady structures across the mouth of the cavity in the shear layer, with a spacing of $\lambda/L \approx 0.33$.

The FFT analysis of the pressure monitors is shown in Figure 4.22, along with frequencies of shear layer mode m, calculated using Equation 2.5. The start-up time (about $15T^*$) was discarded. The pressure was scaled with the freestream dynamic pressure, the remainder of the signal was subdivided into 3 time segments with 50% overlap, and the individual PSD distributions were then averaged together, following [118]. There is a sharp peak in very good agreement with the 4^{th}-mode resonance; the frequency agrees to within 1% of Equation 2.5. The vortex spacing for the 4^{th} mode instability with $M = 0.3$, calculated using Equation 2.6, is $\lambda/L = 0.32$; again in very good agreement with the observation from Figure 4.21. Therefore the simulation appears to be successfully capturing realistic cavity flow features.

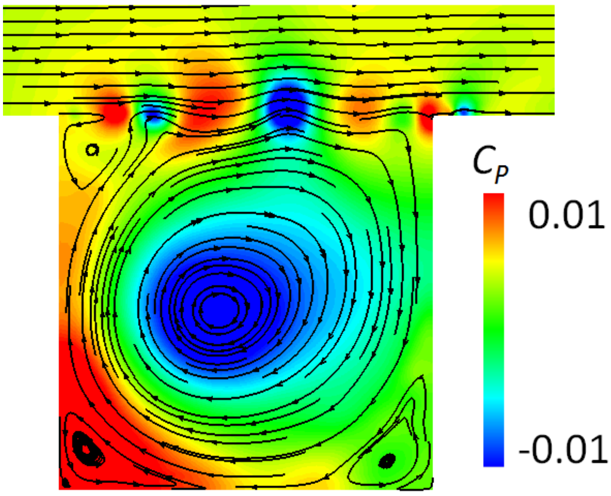

(a)

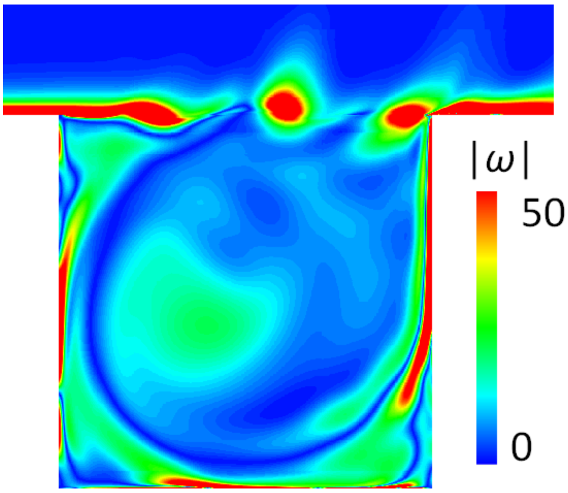

(b)

Figure 4.21: Instantanous contours at cavity midplane: (a) pressure coefficient, with velocity streamtraces overlaid; (b) vorticity magnitude, based on velocities scaled with freestream speed of sound c_0.

Sensitivity to filtering method

To improve accuracy, the solution from $t/T^* = 8$ was used to initialize a simulation using the 6^{th}-order explicit filter. This simulation was extended up to $t/T^* = 54$ to increase the temporal resolution for the lower-frequency components in the spectra. The pressure and vorticity fields are shown in Figure 4.23. It is evident that increasing the filter order has significantly increased the high-frequency and random content of the simulation. The higher-order filter produces a higher level of unsteady pressures; shown on the same scale, the pressure contours in Figure 4.23(a) saturate the scale over a much greater area than in Figure 4.21(a). The central-vortex streamlines are also more irregular, illustrating the influence of the small random structures inside the cavity. Figure 4.23(b) shows that the structures in the shear layer are more sharply defined with the 6^{th}-order filter. Estimating λ/L from Figure 4.23(b) gives a value of 0.31, still consistent with the estimate from Equation 2.6 for mode 4. Figure 4.23(b) also shows a number of vorticity structures inside the cavity, in sharp contrast to Figure 4.21(b), where the flow inside the cavity was fairly

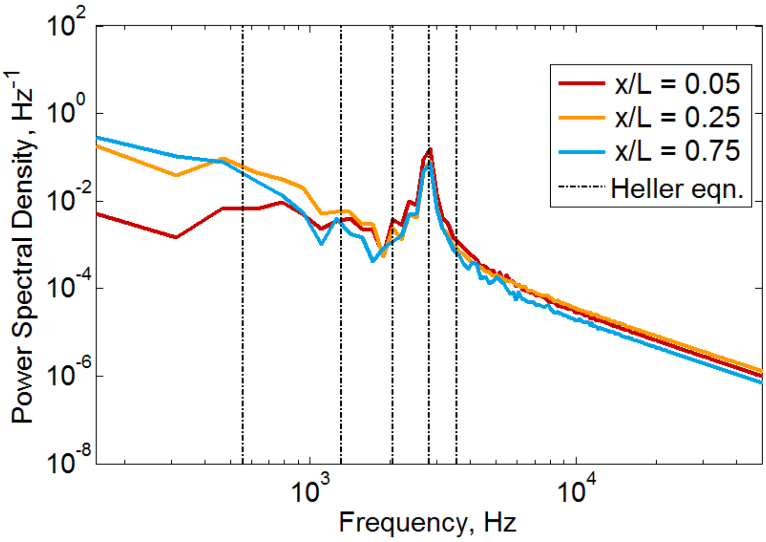

Figure 4.22: FFT of some pressure monitors across the cavity mouth, calculated using DDES with 4^{th}-order filter, along with mode frequencies from Equation 2.5.

simple. It appears the 4^{th}-order filter had damped out these smaller features. Thus overall, the higher-order filter is able to resolve much more of the unsteadiness in the flow.

An example of a comparison of the FFT of the pressure monitors is shown in Figure 4.24, for $x/L = 0.75$. The higher-order filter allows a greater level of small-scale structures to develop, which corresponds to higher broadband levels in the PSD results. The same $m = 4$ tone is observed to dominate, consistent with the vortex structures observed. The width of the peak is slightly broader, indicating that the flow is not as coherent. To investigate the mean flow features, a time-averaged flowfield was computed over the final $t/T^* = 14$. The average pressure and velocity pathlines are shown in Figure 4.25. The small unsteady structures are all negated in the averaging, and only the large central vortex and smaller "roller-bearing" type vortices are evident, which is consistent with the flow features described in the literature review in Section 2.4.2.

The results thus far have all been presented at the cavity midplane. It is expected that for the relatively small number of z-cells, and with spanwise-periodic boundary conditions, that the flow field will remain largely constant through the span. Figure 4.26 shows instantaneous iso-surfaces of the Q-criterion computed at $t/T^* = 54$. Overall the flow structures do indeed appear to be uniform in the span. The short spacing in the span direction ($L_z/L = 0.075$) prevents the development of instabilities and variations in the span direction, forcing the flow field to remain two-dimensional. Therefore these results may be considered a representation of the cavity's 2D characteristics.

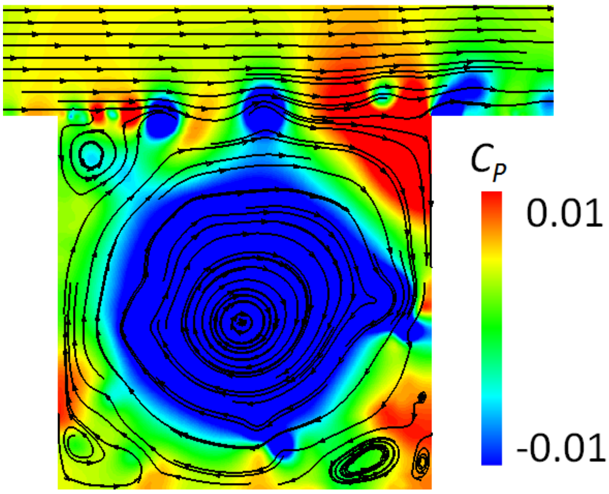

(a)

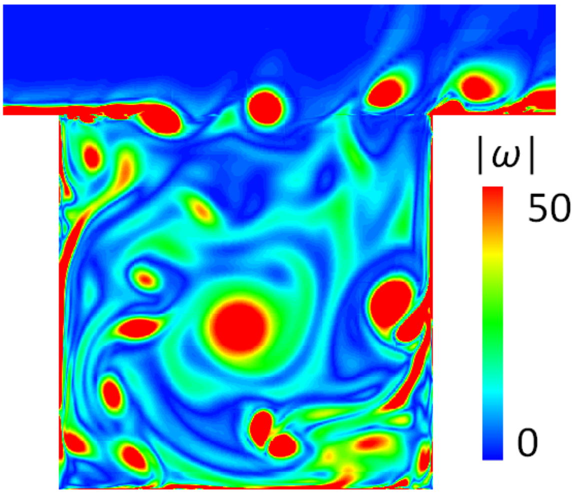

(b)

Figure 4.23: Instantanous contours at cavity midplane: (a) pressure coefficient, with velocity streamtraces overlaid; (b) vorticity magnitude, based on velocities scaled with c_0.

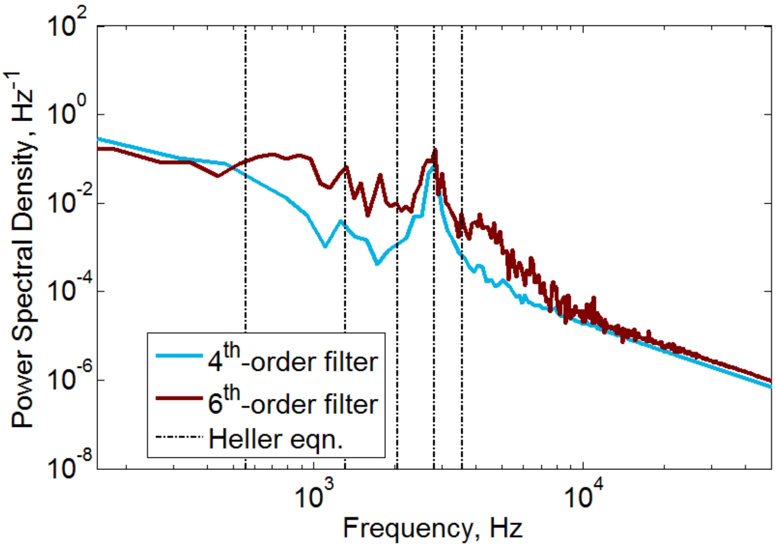

Figure 4.24: Comparison of FFT data at $x/L = 0.75$ between 4^{th}-order filter and 6^{th}-order filter

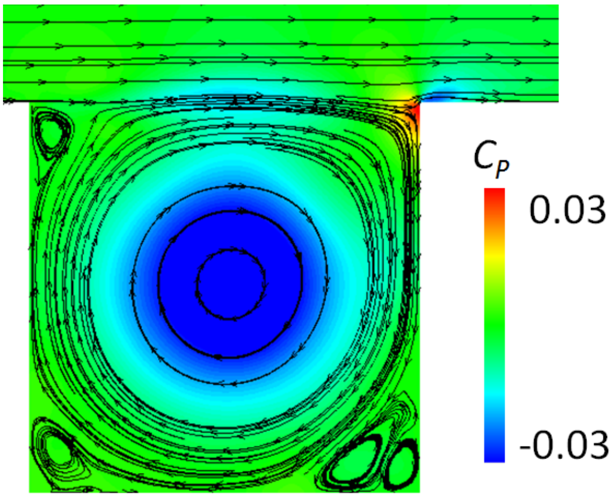

Figure 4.25: Pressure coefficient, with velocity streamtraces overlaid, computed using mean flow field

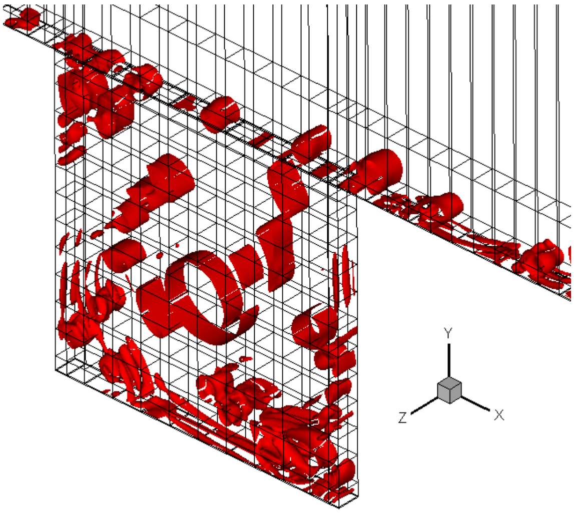

Figure 4.26: Iso-surfaces of Q-criterion = 100, computed using velocity field non-dimensionalised with c_0

4.5 Summary

Validation studies were performed using DES to model an attached turbulent boundary layer with RANS, a partially-covered cavity at low Mach number, and a cavity at $M = 0.30$ with shear layer resonance developing. In all cases the DES model with the in-house SotonCAA code was able to correctly predict the general trends of the flow-field. The mean velocity profile of the RANS-modelled flat-plate boundary layer was well-predicted, and the frequencies of the square-cavity shear-layer resonance agreed well with the correlations from the literature. A grid-independance study was performed for the partially-covered cavity, and the results will be used to sythesize meshing guidelines for the partially-covered cavity simulations in the next Chapters (Chapter 5 and Chapter 6). The DES simulations were found to under-predict the RMS velocity (linked to the turbulent kinetic energy) at the downstream edge of the cavity, which is likely to be attributable to the under-prediction of turbulent kinetic energy at the upstream edge of the cavity. This in turn is due to the shortcomings of the DES modelling approach, which models an attached boundary layer with URANS, and is therefore unable to fully resolve the boundary layer unsteady turbulence. This underlines the importance of developing LES with resolved upstream boundary layer turbulence for application to cavity flows, as is discussed in Chapters 7-9.

Chapter 5

DDES of Partially-Covered Cavity

5.1 Overview

In this Chapter, DES analysis will be performed to simulate a partially-covered cavity at $M = 0.25$, where the partially-covered cavity geometry is broadly representative of the bay from the Airbus A350 nose landing gear (NLG). The mesh and simulation settings are derived based on the outcomes from Chapter 4, and the same DDES methodology described in Section 3.3.3, and applied in Chapter 4, is used. The features of the partially-covered cavity flow from a physical perspective will be investigated, and compared with that of a rectangular cavity, in keeping with the first research objective about exploring the unsteady characteristics of the cavity flow field. This chapter also explores the sensitivity of the cavity flow field to the periodic-span boundary condition configuration, and compares the physical case (with side walls) against the simplified modelling configuration with no side walls. The sensitivity to span width in the absence of side walls will also be investigated, as part of the research objective about exploring the sensitivity of the cavity flow to span effects. This aspect of the study is of numerical interest, to determine to what extent the main flow features can be modelled without the expense of resolving the full span and side walls.

5.2 Geometry

The cross-section of the cavity geometry is simplified into a rectangular shape, as illustrated in Figure 5.1. The characteristic length $D = 0.12$m to match the 1/10.5 scale model. An upstream flat plate of length $4D$ is intended to mimic the development of an attached turbulent boundary layer over the upstream (nose) section of the fuselage. The cavity itself is of $L/D = 3$, with the first 2/3 of the cavity covered, to represent the closed front doors while the gear is deployed. The thickness of the covered section is $0.03D$, which approximates the thickness of the closed doors. The 'lip' of the covered section is a 45° sharp edge, which was found from initial testing to provide better numerical stability than a squared-off edge. (Since the attached flow separates from the top edge regardless, this geometric variation is not expected to significantly affect the result). The open section is of length D ($L_{open}/D = 1$), with the open rear doors omitted from the model for this case. The section $3D$ downstream and $3D$ above the cavity allow sufficient space from the geometry boundaries to avoid any undue interference.

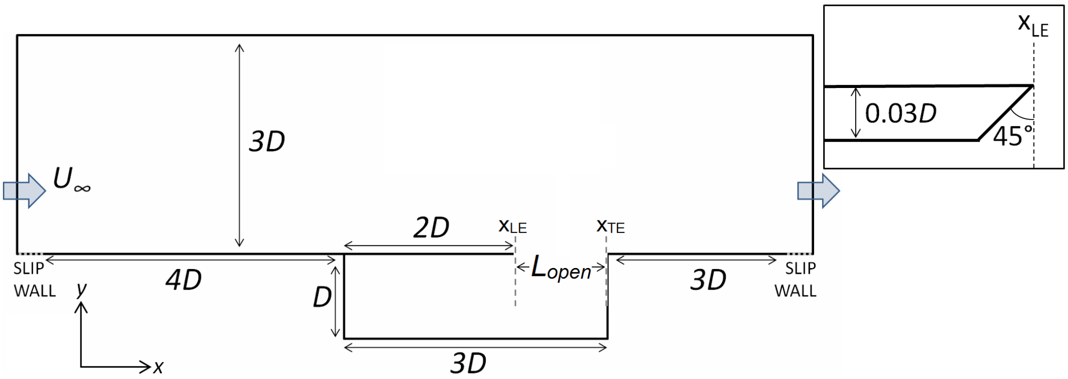

Figure 5.1: 2D geometry schematic (not to scale) for partially-covered cavity configuration; inset: close-up around leading edge, showing cover lip geometry

As the variation of the flow in the span direction is of interest, a few different geometric configurations in the spanwise (z) direction are compared. For landing gear bay applications, $L_Z/D = 1.0$ is the case of most interest. Simulations were performed using periodic boundary conditions in the span direction (which will be referred to as 'spanwise-periodic'), with $L_Z/D = 0.075$, 0.25 and 1.0. $L_z/D = 1$ is the full width of the cavity of interest; and since a major purpose of the periodic-span boundary condition is to significantly reduce the grid size, much smaller values of $L_Z/D = 0.075$ and 0.25 were selected for comparison. These three L_Z configurations will allow a more in-depth exploration of the effect of the domain width on the development of flow features. It is of interest to determine how these simulations compare against a fully 3D configuration. Therefore a fully 3D geometry was also created, with $L_Z/D = 1$ inside the cavity, and $L_Z/D = 3$ outside the cavity (see Figure 5.4). The z-extents inside the cavity have solid walls, unlike the spanwise-periodic simulations (i.e. with periodic boundary conditions in the span direction), which model an 'infinite' span. Therefore, the difference between the 3D simulation and the $L_z/D = 1$ spanwise-periodic simulation will illustrate the effect of the side-walls on the cavity.

5.3 Mesh and Boundary Conditions

The setup of the domain is similar to the method used in Section 4.4 and Section 4.3 for the other cavity simulations: an inflow condition is imposed upstream, with the freestream velocity $U_\infty = 85$ m/s ($M_\infty = 0.25$) specified across the height of the domain. As discussed in Section 4.2, the inflow turbulent viscosity is set to $\hat{\nu}_t/\nu = 5$, equivalent to $\nu_t/\nu \approx 1$, as will be used for all further DES simulations in this thesis. A small free-slip section is imposed upstream of the plate, as a buffer between the freestream inflow and the no-slip wall, and then the plate, cavity walls and downstream section of the plate are all modelled as no-slip walls. Downstream of the plate is another small free-slip section before the outlet boundary. In these simulations an outflow condition is used (the Riemann-based boundary condition described in Section 3.4.4), as this was found to give better resolution of the structures approaching the exit of the domain. Regardless, it is far enough away to avoid any influence on the region of interest. A free-slip (symmetry) condition is used on the top wall, where the flow is expected to have regained freestream conditions, and which is also far enough from the region of interest to avoid any undue influence.

Given the computational cost of the $W/D = 1$ simulations, it was not considered feasible to perform a comprehensive grid refinement study. Instead, a single set of meshing parameters was synthesized based on the guidelines from the cavity validation cases in Section 4.3 and Section 4.4.

Since the mesh will be used for a DES simulation, upstream of the cavity the boundary layer will be attached and therefore modelled with RANS. As the mesh requirements for RANS in this application are not intensive (as shown in Section 4.2), a relatively coarse mesh can be used in this region. Downstream of the cavity, high resolution is maintained for a length of $1D$ to resolve the structures coming out of the cavity region; the mesh is then allowed to grow in x-spacing until it reaches the outflow (Figure 5.2). This coarsening of the mesh allows the structures to begin to diffuse before they reach the boundary, further reducing the likelihood of any reflections. Similarly, in the y-direction the cell size also grows away from the cavity, as the y-scale of the structures is expected to be of the order of the shear layer thickness, and the coarser mesh away from this region helps to avoid reflection from the top boundary (Figure 5.2).

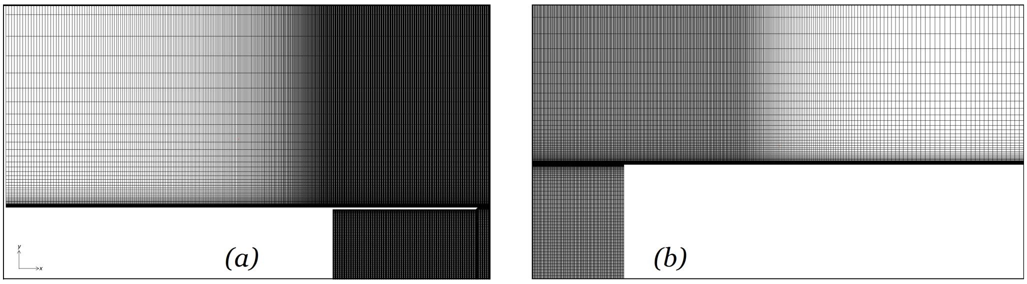

Figure 5.2: Coarsening of 2D mesh away from the cavity: (a) upstream; (b) downstream

Therefore the majority of the mesh resolution is in the cavity region. Across the open section of the cavity the grid is discretized to give 220 points, with $\Delta x/L_{open} = 0.005$ through most of the cavity and additional clustering towards x_{LE} and x_{TE}, similar to the grid-independant resolution from Section 4.3. In the y-direction, the inside of the cavity has 60 points, and in the boundary-layer/shear-layer the cell size is further reduced to give $\Delta y_1^+ = 1$, to ensure good resolution of the shear layer unsteadiness. The cell size inside the cavity was limited to a maximum $\Delta y/D = 0.025$ and $\Delta x/L_{open} = 0.005$, to allow a smooth and relatively uniform resolution of the flow features in this region, as illustrated in Figure 5.3. The lip of the cavity cover is resolved with the same resolution as the shear layer, as shown in Figure 5.3.

The points are clustered down to give a minimum $\Delta x^+ = 70$ (comparable to the Nishimura simulation which had $\Delta x^+_{min} \approx 50$).

In the spanwise direction, the spanwise-periodic simulations all use a mesh which is uniform in z. Based on Section 4.3, Δz is set as $\Delta z/L_{open} = 0.005$, equal to the maximum Δx in the cavity (so that most of the cells in the cavity are cubic). The square-cavity simulations indicated that Rossiter modes could develop from N_z as little as 15; hence the three

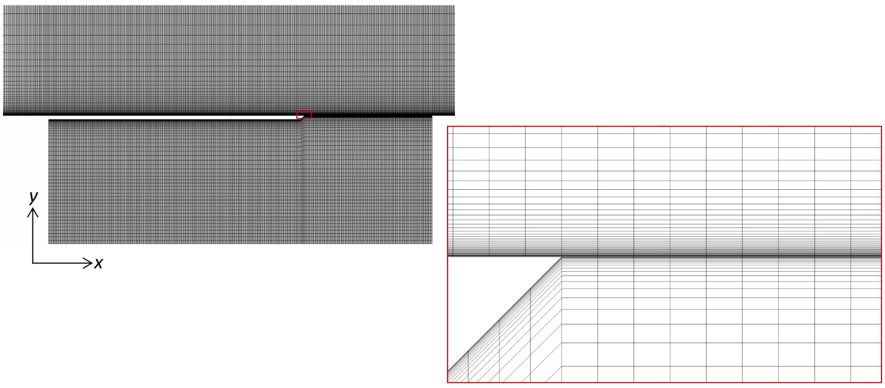

Figure 5.3: $X - Y$ mesh for covered cavity simulations; inset: close up of cover lip

spanwise extents were tested with $L_Z/D = 0.075$, 0.25 and 1.0, corresponding to $N_z =$ 15, 50 and 200 respectively.

For the fully-3D simulation with side-walls, $N_Z = 220$ inside the cavity; the same $\Delta z/D = 0.005$ is used at the centre, with additional clustering down to $\Delta z/D = 0.0028$ to better resolve any smaller features at the edges. (Since all previous results indicate that the flow inside the cavity is of low velocity and dominated by the vortex motion, it was not considered necessary to impose as fine a boundary-layer mesh as was used in the outside plate section). As shown in Figure 5.4, the plate extends not just upstream and downstream of the cavity, but also around the sides, with a length D on either side. In the x and y directions these outer sections have the same mesh as over the cavity plate (to maintain high-quality cells), but in the z-direction the mesh is allowed to grow from $\Delta z/D = 0.0028$ up to 0.03, as the unsteady flow features are expected to remain close to the cavity, and the additional width is primarily to allow sufficient space between the region of interest and the outer z boundaries of the domain. Spanwise-periodic boundary conditions are used at these outer boundaries. Preliminary test simulations confirmed that cavity flow structures do not extensively spill over in the z direction, and that the flow in the region of the spanwise-periodic boundary has settled down to being a simple RANS flat-plate boundary layer.

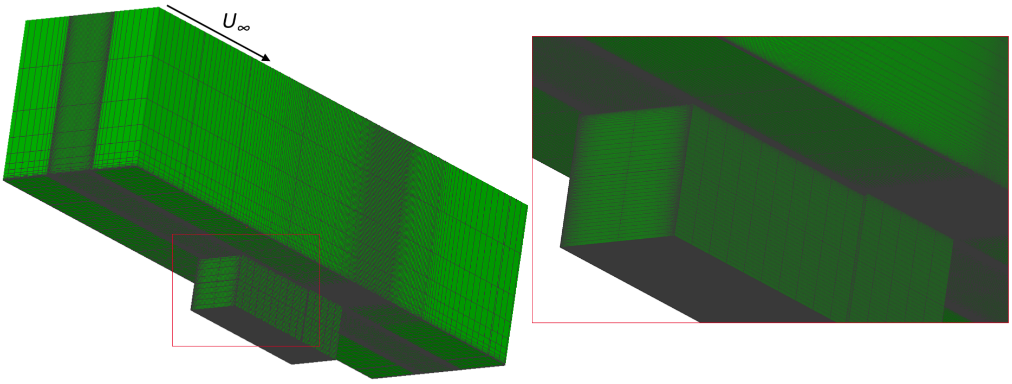

Figure 5.4: Geometry and mesh for the fully-3d cavity simulation

5.4 Simulation Parameters

The simulations were performed using SotonCAA and the DDES method. Due to the improved stability of the cell-centred formulation, the 6^{th}-order implicit filter of Kim [109] was used in this chapter, as discussed in Section 3.4.3. To maintain numerical stability, the cutoff wavenumbers were generally set to $\kappa_C = 0.72$ and $kappa_{C,boundary} = 0.70$. The mean flow-field was computed by sampling at every time step, with the start-up transient period discarded. Pressure monitors were also recorded at every timestep. In the mid-z plane of the cavity, the points are as shown in Figure 5.5, with an additional row of monitors in the shear layer near the z extent of the domain (Figure 5.5(b)).

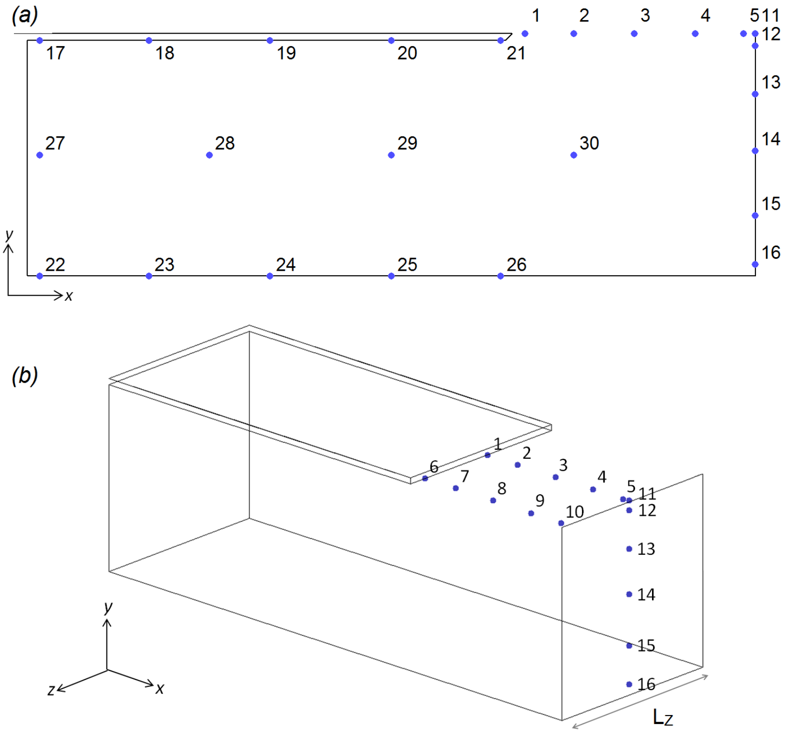

Figure 5.5: Monitor points in covered-cavity geometry; (a) in mid-z plane; (b) in the open section

The timestep was set to give a maximum CFL of 3.4, which is reasonable for the implicit time-stepping method in SotonCAA. Defining a relevant dimensionless time T^* based on $U_\infty = 85\text{m/s}$ and L_{open}, the timestep equates to $\Delta t = T^*/24,000$, which is expected to be sufficient to resolve even high-frequency flow structures for this application.

For the 3D simulation with side-walls, the simulation was initialized from an idealized hybrid field with quiescent flow inside the cavity and freestream flow outside the cavity, and uniform pressure throughout the domain. (From 2D tests, it was observed that initializing from $U = U_\infty$ throughout the domain caused numerical instabilities and divergence before a physical solution could evolve.) For the spanwise-periodic simulations, the 3D simulations were initialized from the final 2D simulation, which is described in Section 5.5. (The 2D simulation, in turn, was initialized with $U = U_\infty$ outside the cavity and $U = 0$ inside.) The flow-field was extruded uniformly in the z direction with no spanwise velocity components $w = 0$, and allowed to develop with time.

The DDES methodology described in Section 3.3.3 aims to ensure that the model applies RANS treatment in the boundary layer while quickly switching to LES treatment in the separated regions. The regions of RANS and LES can be identified by plotting the DDES function f_d, which is 0 in the RANS region (which should correspond to the boundary layer), and 1 elsewhere. A typical example of an instantaneous plot of f_d is shown in Figure 5.6. In the outer part of the upstream boundary layer there is a strip of $f_d = 1$. This behaviour has been observed in other DDES studies [119]. If the grid was coarser, the DDES function would retain the RANS option ($\widetilde{d} = d$) all the way through; the pocket of LES is caused by finer resolution than is needed for a RANS boundary layer. However, as noted by Spalart et al [100], $f_d > 0$ in the outer half of the boundary layer is not an issue since the Spalart-Allmaras turbulence model's destruction term is "negligible" here. Plots of ν_t confirmed that the turbulent viscosity is smooth across the boundary layer. At the separation of the shear layer across the cavity, Figure 5.6 shows that the value of f_d in the shear layer jumps to 1 within about $0.03D$ downstream of x_{LE}, which means that the LES mode is activated quite quickly, as desired. The LES treatment is applied throughout the cavity, except in the near vicinity of the walls, where a RANS boundary layer may be considered a reasonable treatment. A RANS region ($f_d = 0$) is also observed developing downstream of the cavity in the very near-wall region. Overall, the DDES method appears to be functioning correctly.

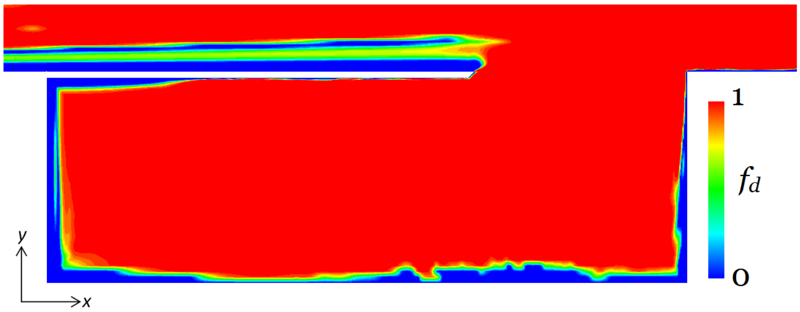

Figure 5.6: A typical instance of an instantaneous slice plot of DDES variable f_d, from $t/T^* = 49$

Given the large mesh size for the $L_z/D = 1$ simulation, it was thought that some simulation time might be saved by initializing it instead from the developed $L_z/D = 0.25$ solution, tiled 4 times in z and overlaid with a small w-velocity perturbation to break the periodicity. This initial field was generated, with the w-velocity perturbation taking the form of a sine wave across L_z with amplitude of 4 m/s ($0.012U_\infty$), overlaid with a random perturbation of mean amplitude 1.5 m/s. The pressure field was maintained as the tiled solution from the $L_z/D = 0.25$ simulation. Performing the simulation from this initial field, however, it was found that the periodicity in the boundary layer structures was visible until about $t/T^* = 15$. Furthermore, the pressure field retained a strong imprint of the sine wave in z even up to $t/T^* = 25$, although the velocity field and and $X - Y$ slice planes looked physical. This indicates that the addition of unphysical coherent perturbations in a high-order low-dissipation code such as SotonCAA, perhaps particularly in conjuction with the periodic boundary conditions, is not a suitable method for evolving a physical flow.

(The perturbations used later in the flat-plate LES analysis were found to damp out quite quickly, but this may be because they were random and therefore uncorrelated with the spanwise-periodic lengthscale.) Although the perturbations were fairly small and only applied to the initial field, they were still unable to diffuse out of the simulation after a considerable flow time. Therefore instead of using this method, the flow field was re-initialized from the 2D simulation with uniformity in z, as with the other spanwise-periodic simulations.

5.5 2D Simulation

Although the 2D simulation is primarily a start-off point for the 3D simulation, and 2D DES analysis is fundamentally questionable, it is still of interest to briefly consider the characteristics of the 2D flow-field, as a comparison point for the later 3D simulations.
For stability, the 2D simulation was initially run for $T/T^* = 29$ with the 6^{th}-order explicit filter until a stable flow-field had clearly developed, then switched to the 6^{th}-order implicit filter for a further $t/T^* = 27$. From the final solution field, contours of velocity magnitude with streamlines superimposed are shown in Figure 5.7. The shear layer is steady and spans the open length of the cavity without oscillations, which is evidence of the shortcomings of 2D DES, as oscillations in the shear layer are expected for this configuration. Instead, the 2D flow field is fundamentally steady. Inside the cavity, the flow exhibits one large vortex filling the square open region, as seen in the square-cavity simulations in Section 4.4. Underneath the covered lid a large counter-rotating vortex has developed, similar to the pattern observed in the covered-cavity simulations in Section 4.3. The vortex in the open-section has a velocity band at around $0.5U_\infty$, comparable to the velocity in the shear layer; the second, sheltered vortex has significantly lower velocity, close to zero. This suggests that the energetic flow in the shear layer contributes to the first vortex, likely through the diversion of some flow down the back edge of the cavity from the impact point; the highest velocities inside the cavity are in the downward flow along the downstream wall. Very little of this high-velocity flow is transmitted to the second vortex, and the streamlines are mostly separate. Figure 5.8 shows the same streamlines overlaid on the pressure field. There is a large region of lower pressure in the centre of the open-section vortex, consistent with the behavior of a strong, coherent vortex [28]. Spikes of high pressure are observed at the top edge of the cavity downstream wall, where the shear layer impacts, as expected. There are also small regions of high and low pressure around the lip of the cavity cover, where the shear layer separates.

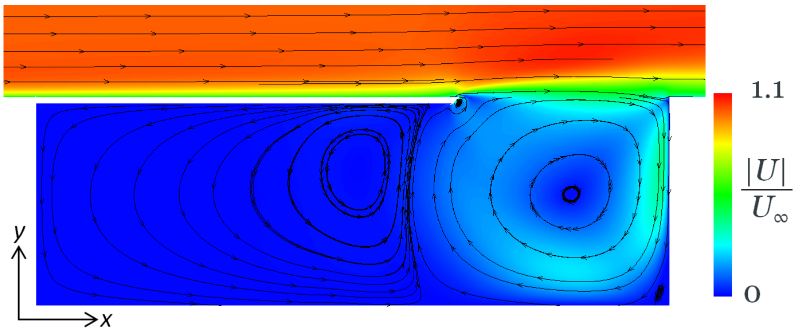

Figure 5.7: Contours of velocity magnitude from 2D simulation

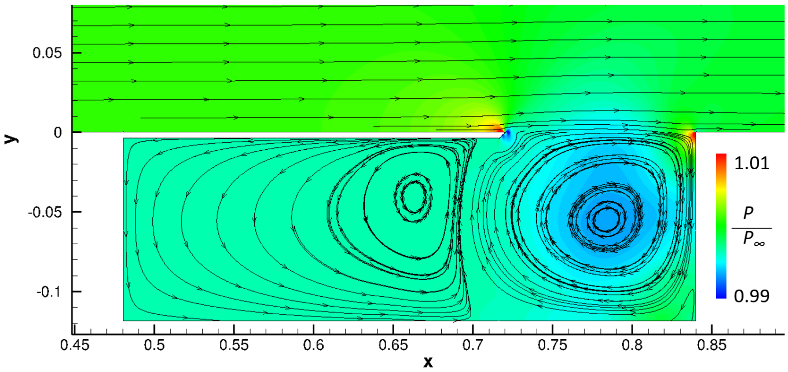

Figure 5.8: Contours of instantaneous pressure from 2D simulation

5.6 Spanwise-Periodic Simulations

5.6.1 Flow Features

Three spanwise-periodic simulations with $L_z/D = 0.075$, 0.25 and 1 are discussed in this section. Contours of the Q-criterion are compared in Figure 5.9. In all cases, unlike the 2D result, the shear layer exhibits breakdown into regularly-shed vortex structures, similar to the behaviour observed from the square-cavity case in Section 4.4. The shear layer in the thinnest simulation generates neat, regular vortex structures, uniform in the span. In $L_z/D = 0.25$ and 1 simulations the same structures show variation in the span and eventually start to break down as they approach the back edge of the cavity. This illustrates that the increased width of the simulation allows a degree of variation in z of the structures that was prohibited by $L_z/D = 0.075$. Visually, both latter cases appear to retain some coherence in the span even downstream in the shear layer. This is especially true of the $L_z/D = 1$ simulation, which shows a regular pattern in z. The $L_z/D = 1$ simulation also shows strong vortex structures developing right from the leading edge of the shear layer, and more unsteady vortex structures inside the open section of the cavity. The instantaneous and time-averaged mean velocity fields are compared in Figure 5.10 and 5.11 respectively. The mean flow field was computed by averaging from every time instance after the flow had been observed to settle. For the two narrower-span simulations, the start-up transients had disappeared by around $10T^*$; however for the $L_z/D = 1$ case, the flow remained in a persistent 2-D state until about $30T^*$, when the flow field switched to the pattern shown in Figure 5.9(c).

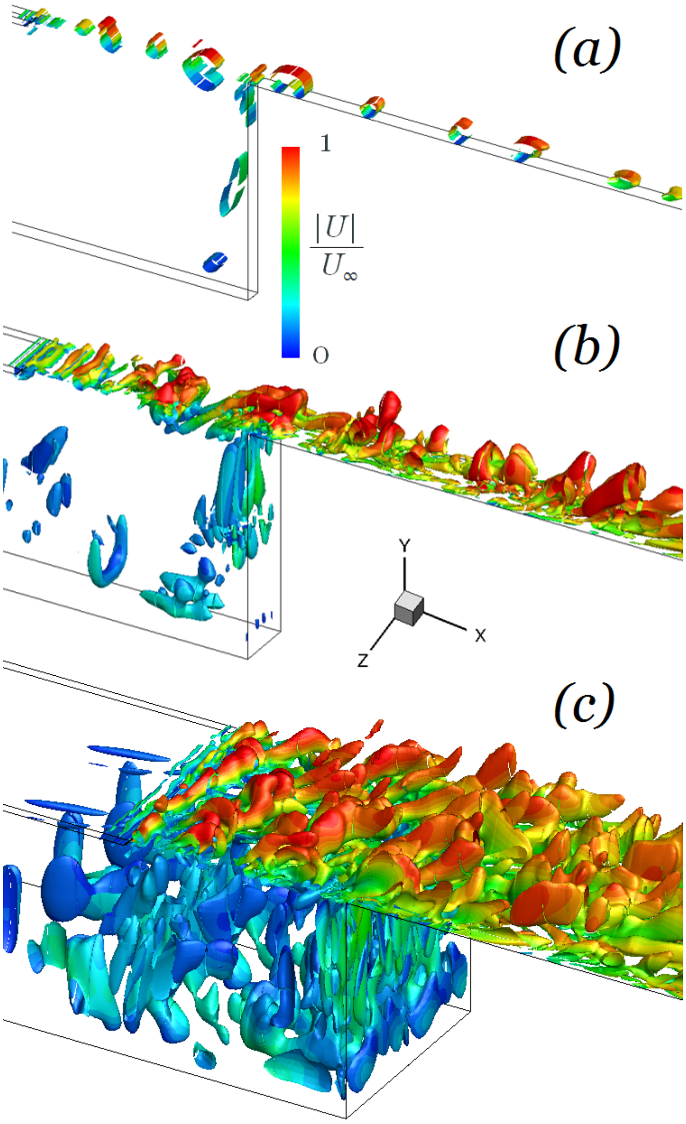

Figure 5.9: Iso-surfaces of the Q-criterion; (a) $L_z/D = 0.075$; (b) $L_z/D = 0.25$; (c) $L_z/D = 1$

Inside the cavity, a two-vortex structure is observed, similar to the 2D simulation; one large, stronger vortex in the open section, and a weaker counter-rotating vortex under the closed section. For the thinnest $L_z/D = 0.075$ case the streamlines are very regular and organized, indicating that the structures are smooth and coherent, and the instantaneous field is fairly similar to the mean field. In contrast, the vortex structure inside the cavity for the wider $L_z/D = 0.25$ simulation ($N_z = 50$) simulation is visibly less orderly. In the instantaneous flow-field the second (covered-section) vortex has almost completely broken down. In the mean field, the streamlines are still not as orderly as in the narrower-span simulation, with a smaller vortex developing in the open-section vortex, and the covered-section vortex being visibly distorted.

In all cases, the boundary layer thickness just upstream of the open section was measured to be $\delta_{99,upstream} \approx 0.09D$, which influences the thickness of the shear layer. Both of the narrower-span 3D simulations show the mean streamlines across the shear layer being

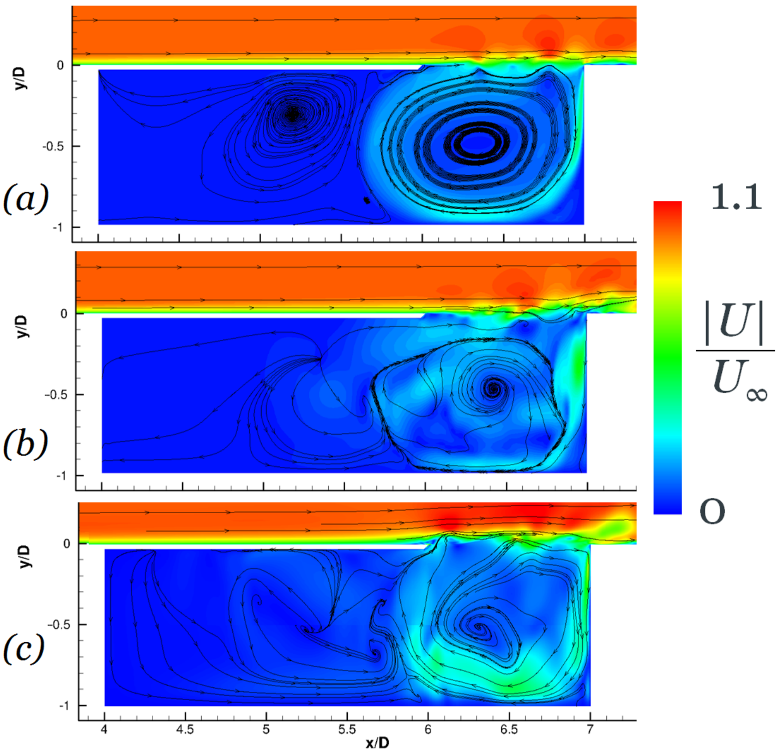

Figure 5.10: Contours of instantaneous velocity magnitude with streamtraces, evaluated at mid-z plane: (a) $L_z/D = 0.075$; (b) $L_z/D = 0.25$; (c) $L_z/D = 1$

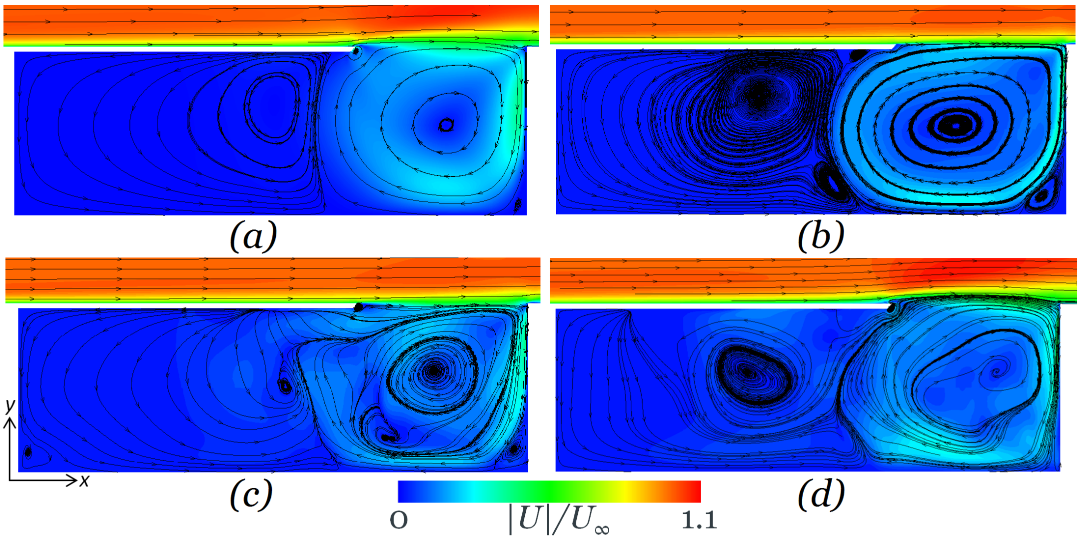

Figure 5.11: Contours of time-averaged velocity magnitude with streamtraces in the $X-Y$ plane: (a) 2D simulation (steady flow-field); (b) $L_z/D = 0.075$; (c) $L_z/D = 0.25$; (d) $L_z/D = 1$

largely level, with a small downward deflection for $L_z/D = 0.25$. The open-section vortex extends some $0.5D$ upstream under the cover; the streamlines coming up impact on the cover, and are then deflected horizontally. By the time the flow reaches x_{LE}, it has settled primarily into the $+x$ direction, parallel to the shear layer, and therefore allowing the shear layer to separate smoothly.

The $L_z/D = 1$ case, however, is completely different in this respect. Although the open-section vortex has a similar length along the floor of the cavity, it is visibly distorted and shortened in the top half. The upwards flow - which draws in some of the flow around the weaker covered-section vortex - impacts the shear layer at x_{LE} with an appreciable component of upwards ($+y$) velocity, thus driving the shear layer upwards. This accounts for the early development of vortex structures from x_{LE} seen in the Q-criterion plots. It is interesting to note that the upwards deflection of thes shear layer was also observed, to a slightly lesser extent, in the 2D simulation (Figure 5.11(a)), due to the open-section vortex only extending about $0.2D$ upstream of x_{LE}. However in the 2D case, the open-section vortex streamlines are more circular, and the vortex is largely symmetric about the cavity mid-depth, whereas the $L_z/D = 1$ case shows a distortion of the vortex core shape. In the bottom downstream corner of the cavity, the $L_z/D = 1$ case has the open-section vortex expanding almost to the wall. In contrast, both of the narrower-span 3D simulations show a smaller roller-bearing type vortex in this region, as does the 2D simulation to a lesser extent.

It is not immediately obvious why the increase in L_z should cause this change in behaviour. The tendency for the open-section vortex to deflect the shear layer upwards is more similar to the 2D simulation than to the narrower-span 3D simulations, which is a surprising trend. One possible explanation is that the length allows the open-section vortex to develop spanwise variations and instabilities (which is supported by the Q-criterion structures seen in the open section in Figure 5.9(c)). This weakens the coherence of the vortex, allowing the vortex core to be distorted as shown, which then leads to the deflection of the shear layer.

The RMS pressure variations are compared in Figure 5.12. The two narrower-span simulations show nearly identical distributions. The first third of the shear layer shows very little p_{RMS}; the band grows in the downstream shear layer as the structures develop. This is consistent with Figure 5.9 and Figure 5.10, which showed the shear layer initially separating steadily from the upstream edge, with vortex structures growing as they convect downstream. Inside the cavity, vertical bands of higher p_{RMS} are observed equi-spaced throughout the cavity, suggestive of an acoustic mode developing inside the cavity with $N_x = 2$ (two nodes). The differences observed in the instantaneous flow-field for the $L_z/D = 0.25$ simulation therefore do not seem to significantly affect the mean unsteady pressure field; the variations in z appear to average out in time.

The $L_z/D = 1$ simulation, in contrast, shows markedly different characteristics. The coherent shear layer vortex structures starting at x_{LE} cause a band of high p_{RMS} all the way across the cavity. The levels are not, however, as high as in the narrower-span simulations; nor do they show the same growth downstream, instead remaining at a largely constant thickness across the length, actually decreasing slightly near the trailing edge. The shear layer is also deflected upwards, as seen from the mean velocity. Inside the cavity, almost no RMS pressure is visible on this scale; the bands suggestive of $N_x = 2$ resonance are not present with the larger spanwise length.

The impingement of the shear layer on the trailing edge of the cavity is shown in Figure 5.13. Again, the two narrower simulations show very similar behaviour; the flow impinges on the downstream wall just below the top of the wall. Some of the flow is then

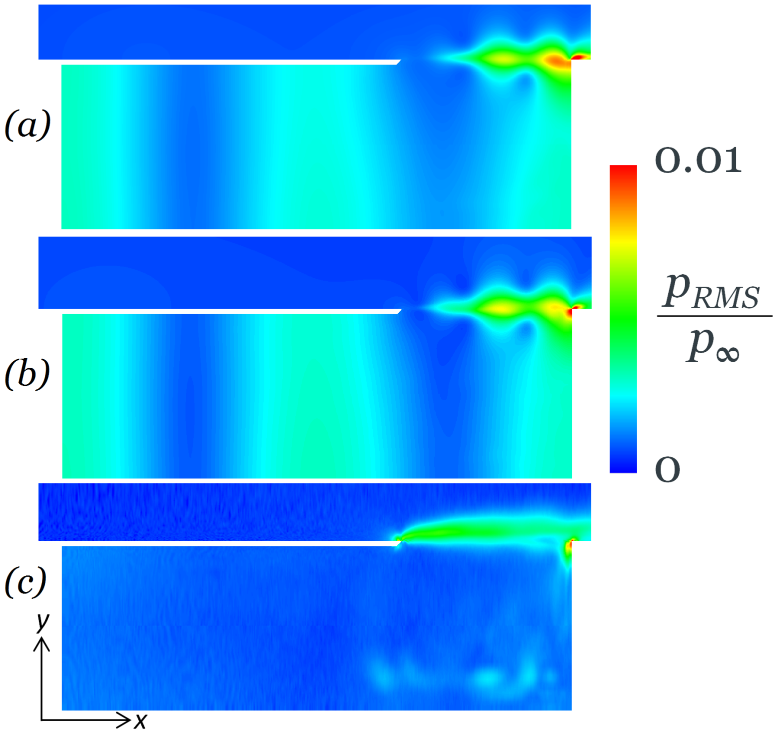

Figure 5.12: Contours of P_{RMS} in the $X-Y$ plane: (a) $L_z/D = 0.075$; (b) $L_z/D = 0.25$; (c) $L_z/D = 1$

diverted upwards before convecting downstream, forming a small recirculation bubble on the downstream surface of the plate. For the $L_z/D = 1$ simulation, however, the shear layer streamlines are visibly raised, causing a much smoother reattachment downstream and no recirculation bubble. The shear layer is also much thicker, due to the development of structures right from x_{LE}, which in turn is caused by the lifting of the shear layer by the open-section vortex.

5.6.2 Frequency analysis

Examples of the variation in the pressure monitors across the shear layer are shown in Figure 5.14 and Figure 5.15, at $x = x_{LE} + 0.25D$ and $x_{LE} + 0.75D$ respectively. The frequency analysis was performed using a fast-Fourier transform of the pressure monitors (normalized by the freestream dynamic pressure), with the start-up transient regions omitted, and the PSD results averaged using windows with 50% overlap [118]. Also shown are the frequencies obtained from the Heller equation for Rossiter-mode shear layer resonance (Equation 2.5), evaluated based on L_{open}. The peaks are well predicted by Equation 2.5. The modified ‘long-path’ equation for a cavity with the rear section covered (Equation 2.9) was also tested, and was found to give no improvement on the prediction of the resonant tones. This indicates that the frequencies of the shear-layer vortex shedding develop based only on the open section; the additional covered section does not have a significant impact in this respect. This is consistent with past experimental observations on partially-covered cavities with the open section downstream [63], where the unmodified Rossiter-mode equations were also found to give good agreement with the measured tonal peaks.

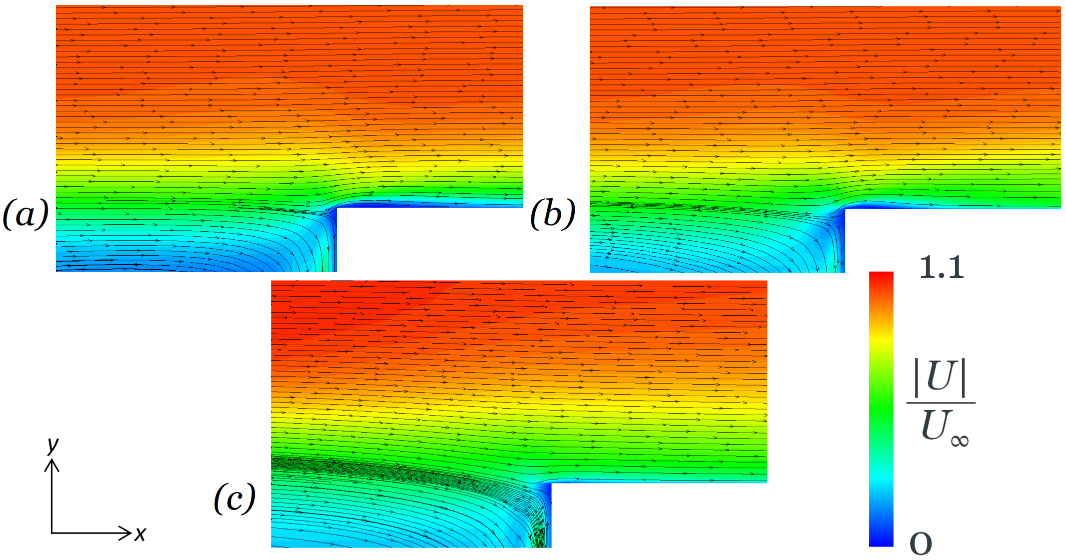

Figure 5.13: Contours of velocity magnitude and streamlines at the trailing edge of the cavity: (a) $L_z/D = 0.075$; (b) $L_z/D = 0.25$; (c) $L_z/D = 1$

Comparing the different cases, the two narrower simulations show dominant peaks that closely match the 3^{rd} Rossiter mode ($m = 3$) at both locations. The vortex spacing in Figure 5.9 is consistent with this as well, as the larger vortex structures are separated by about $\lambda/L_{open} \approx 0.4$, which matches Equation 2.6. The corresponding frequency for $m = 3$ is 0.97kHz. The second length-wise acoustic mode $N_x = 2$, which appears from Figure 5.12 to be present in these cases, has a frequency of 0.95kHz (computed from Equation 2.8). It therefore appears that the acoustic modes developing inside the cavity are 'locking on' to the closest shear layer mode, as described in Section 2 and observed by Rossiter [51]. At the downstream monitor, the peak amplitude of this tone is higher by approximately a factor of 6. The RMS pressure plots showed increasing p_{RMS} towards the trailing edge of the shear layer; it seems that this is due to the growth of the resonant structures. Also, a secondary peak is observed at 1.9kHz - almost exactly double the frequency of the first peak (0.95kHz) - which is therefore most likely a harmonic of this strong peak.

The $L_z/D = 1$ simulation, in contrast, shows very different behaviour. The mode at $m = 3$ is eliminated. Upstream, a tone is present at $m = 4$, but downstream, there are no strong tonal modes shown in the shear layer. Resonant-mode vortex structures are therefore not steadily growing across the shear layer, consistent with the RMS pressure plot. The RMS pressure plots for this case showed no evidence of acoustic modes inside the cavity, which is confirmed by the lack of acoustic-mode tones in the pressure monitors. The disruption of this acoustic resonance may be due to the interaction between the open-section vortex and the upstream shear layer. With the shear layer deflected upwards, there is less of an impact on the downstream wall, and therefore, less opportunity for acoustic waves to be emitted from the impact region. The acoustic waves are necessary to development of the shear layer resonance feedback loop.

Inside the cavity, the same basic trends are observed. Figure 5.16 shows the pressure monitors at Point 17 (near the top corner of the upstream wall, in the covered section; see

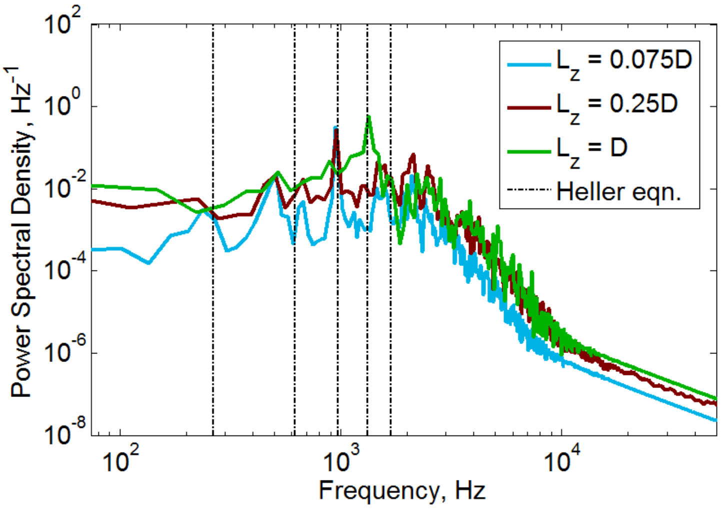

Figure 5.14: Frequency analysis of pressure monitors in the shear layer, $0.25D$ downstream of x_{LE}

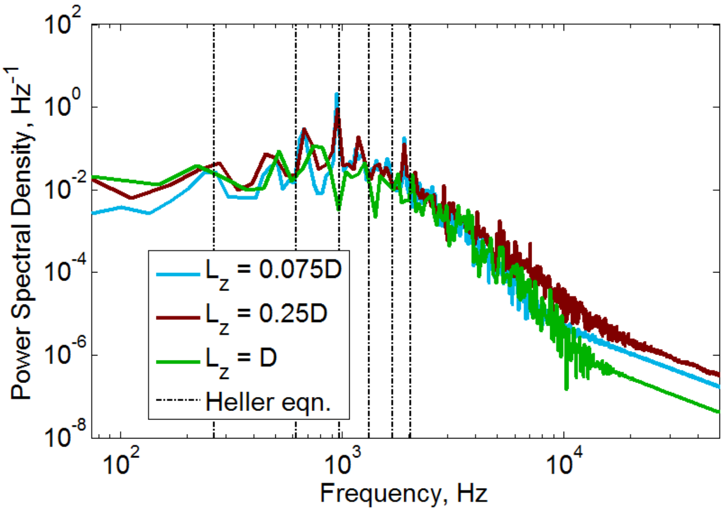

Figure 5.15: Frequency analysis of pressure monitors in the shear layer, $0.75D$ downstream of x_{LE}

Figure 5.5). An $m = 4$ resonance is observed with $L_z/D = 1$, but of a significantly weaker amplitude than the $m = 3/N_x = 2$ tone from the narrower-span cases. This is consistent with the trends from p_{RMS}, where the $L_Z/D = 1$ case had much lower values inside the cavity.

To explore the degree of correlation in the z direction, additional points were placed near the downstream edge of the cavity, at the same (x, y) locations as point 11 (Figure 5.5), but near the z-extents of the domain. The edge points are located one cell ($\Delta z/D = 0.005$) away from the periodic boundary condition. Figure 5.17 compares the pressure monitors at the two edge points and the centre point over a section of the flow time. For the $L_z/D = 0.075$ simulation the results are identical, as expected from the spanwise-uniformity of the flow structures, and the correlation coefficient is equal to 1 for all three pairings. With the $L_z/D = 0.25$ simulation there is more variation. The two edge points are strongly correlated (as expected, due to the fact that they are only separated by two points and

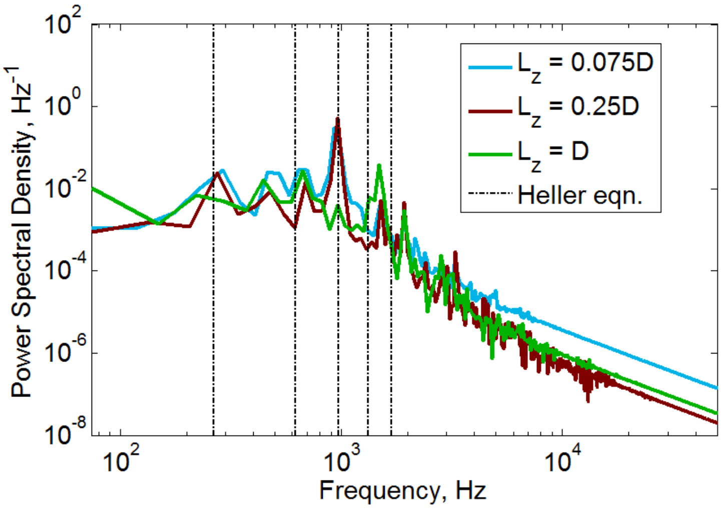

Figure 5.16: Frequency analysis of pressure monitors inside the cavity, at the upstream back wall (Point 17, as shown in Figure 5.5)

the periodic boundary condition). The correlation coefficient between the centre-plane point and the end points is 0.30. This is obviously much lower, but not quite negligible, suggesting that there is still some level of spanwise coherence still in the flow field.

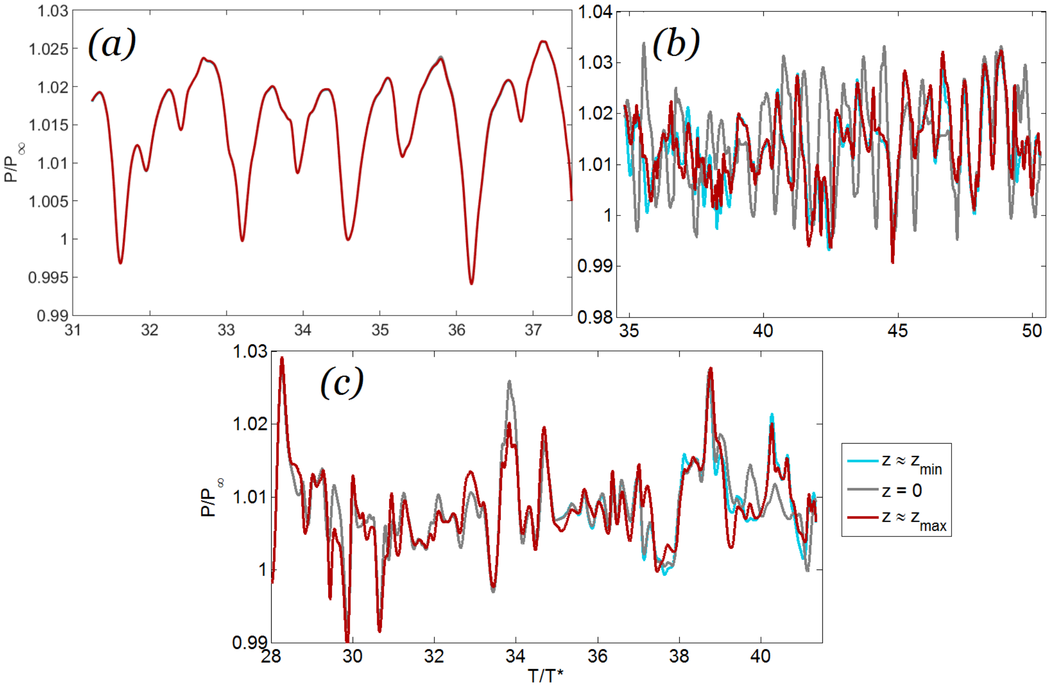

Figure 5.17: Comparison of pressure monitors at centre and edges of domain: (a) L_z/D = 0.075; (b) L_z/D = 0.25; (c) $L_z/D = 1$

It would be desirable, therefore, if increasing to $L_z/D = 1$ removed the correlation in the span altogether, and the differences between this simulation and the narrower-span simulations could be attributed to complete breakdown of the shear layer flow in this case. However the Q-criterion contours already suggest that this is not the case. In fact, Figure 5.17(c) shows that the pressures are still strongly correlated across the span, with correlation coefficients around 0.90. The degree of correlation is actually higher than in the $L_z/D = 0.25$ case. The highest degree of span-wise breakdown is therefore obtained with the $L_z/D = 0.25$ simulation.

A possible explanation for this is that with $L_z/D = 0.25$, the periodic boundary in the span introduces a periodic component to the flow field of wavelenth $\lambda/D = 0.25$. The vortex structures in the shear layer are of a similar scale, $\lambda/D = 0.4$. It may be, therefore, that the periodic component across the span length resonates with some instability in the vortices at this scale. Inside the cavity, the open-section vortex is of scale D, and the periodic boundary condition with $L_z/D = 1$ caused the most fluctuations in this region; perhaps a similar coupling is occuring between this vortex and this span scale.

5.6.3 Temporal Development of $L_z/D = 1$ Simulation

The development of the $L_z/D = 1$ simulation with time will be briefly discussed here, as the behaviour of this simulation was found to differ from the other simulations. As mentioned, the vortex structures in the shear layer shown in Figure 5.9 only developed after around $30T^*$, whereas the narrower-span simulations had settled into a stable state (i.e. no systematic transient effects) after $5 - 10T^*$. An example of the shear layer vortex structures at $20T^*$ is shown in Figure 5.18. The same upwards deflection of the shear layer was observed, but the shear layer is completely uniform in z. There are also very well-defined, coherent vortex structures with a spacing of $\lambda/L_{open} \approx 0.3$. The time histories of the pressure monitors in the shear layer up to this stage are presented in Figure 5.19. It would be easy to conclude from the pressure monitors that the flow field had settled into a stable state from $T^* = 10$. The regular, coherent shear layer flow field at $20T^*$ would thus be taken as the final state of the simulation, even though the level of spanwise uniformity shown in Figure 5.18 seems unlikely to be physical. Iso-surfaces of the Q-criterion showed the same basic behaviour between $t/T^* \approx 10 - 27$. This particular setup therefore has a particularly strong tendency towards retaining spanwise coherence (in fact, spanwise uniformity) in the shear layer, more so than with $L_z/D = 0.25$, and unlike the $L_z/D = 1$ simulation with side walls discussed in the next section.

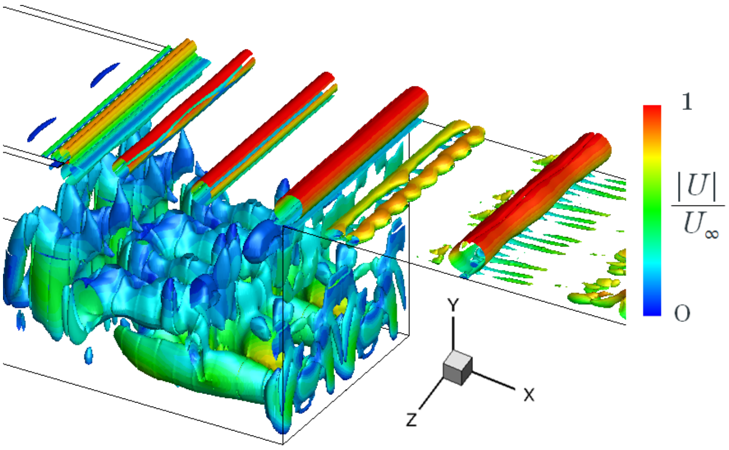

Figure 5.18: Iso-surfaces of the Q-criterion, coloured by velocity magnitude, from $L_Z/D = 1$ simulation at $t = 20T^*$

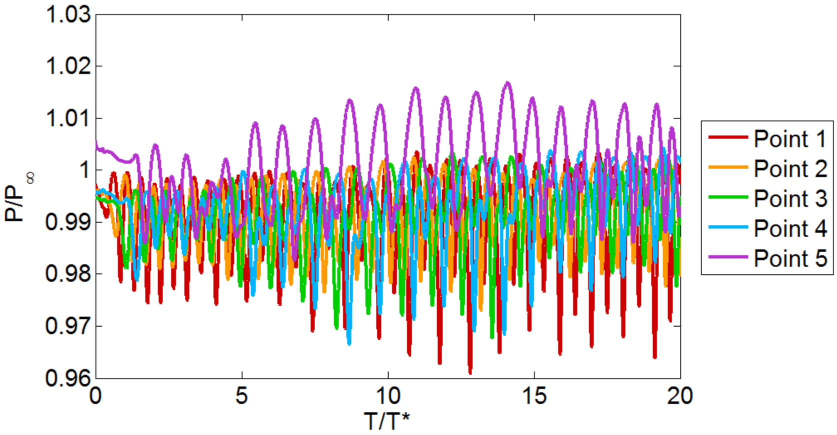

Figure 5.19: Time history of pressure monitors in the shear layer up to 20T* (monitor point locations are as indicated in Figure 5.5

In terms of the mean velocity field, the upward deflection of the shear layer, the mean pressure and even the turbulent kinetic energy, the eventual change in the shear layer structures did not significantly affect the flow field. The mean fields presented in this section are all clipped to begin averaging at $33T^*$, but compared with earlier measurements where the mean-field calculation covers the whole simulation time, the trends in the data for all those variables were fairly similar. As seen in the correlation plots, the flow is still highly correlated across the span, so it is not a true breakdown of the shear layer structures.

However the RMS pressure did changed significantly. Figure 5.20 shows p_{RMS} computed from a mean field averaged over the whole time period. Compared to the clipped p_{RMS} field in Figure 5.12(c), the levels are significantly higher. The spanwise-uniform vortex structures shown in Figure 5.18 produce much higher p_{RMS} in the shear layer, and the influence seems to extend to the structures swept down into the cavity and through the inside of the cavity. Pressure monitors in the shear layer also showed much stronger resonant modes at $m = 4$ (consistent with the λ spacing from the Q plot) and $m = 2$, suggesting some mode-switching over the time sample.

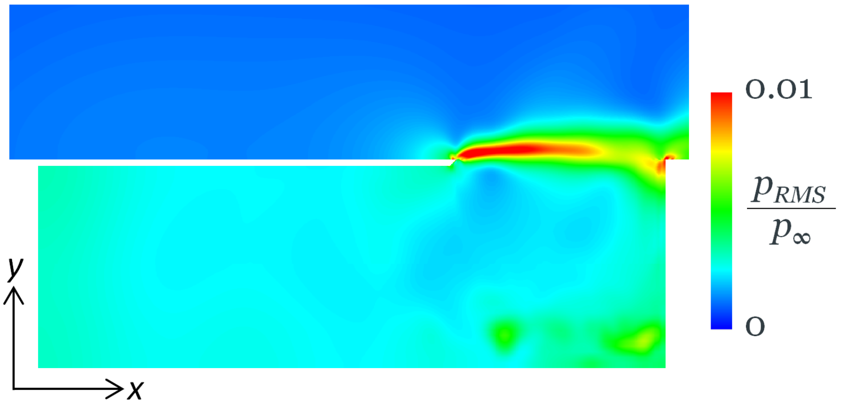

Figure 5.20: Contours of RMS pressure from $L_z/D = 1$ simulation with periodic boundary in the span, where RMS values are averaged starting from 0 instead of $33T^*$

This tendency towards spanwise coherence in vortex shedding, and inflated RMS pressures, has been observed in past studies using spanwise-periodic simulations in other applications. One example of this is the review of tandem cylinder simulations by Bres et al [120]. Although this is a fundamentally different application, both flow fields do involve periodic vortex shedding from a separated shear layer. The authors of [120] found that for a tandem cylinder setup with the same length in the span, the spanwise-periodic simulation produced higher RMS levels than the simulation with side-plates. In that study a fairly wide span was used in both cases, equivalent to $16D_{cylinder}$. The study concluded that the spanwise periodic boundary conditions caused enhanced coherence of the vortex shedding, and stronger spanwise uniformity [120, 121]. The side-plates represented the tunnel walls from that experiment, so that configuration was more representative of the true flow field, just as the side walls in the present cavity application is the more physically accurate case. The use of periodic-span boundary conditions is desired to replicate the main features of the unsteady flow field, at a lower computational cost. Since this enhanced coherence and spanwise uniformity was observed for separated shear layers even with a relatively wide span, it is likely to be an issue for cavity applications as well.

Therefore the use of spanwise-periodic boundary conditions in the cavity application is not ideal, as the separated shear layer has a tendency to maintain correlation in the z-direction beyond what would be expected from a physical flow field with side walls, and p_{RMS} is therefore prone to over-prediction. The setup in this particular case caused a change in the flow field late in time, breaking the spanwise uniformity of the shear layer, and ameliorating the over-prediction of p_{RMS} from the earlier data. Still this is not desirable behaviour in a CFD simulation, as it requires a much longer simulation time, and the results from the earlier times may be mis-interpreted.

5.6.4 Conclusions

A systematic trend in the flow fields was expected with increasing L_z, but this was not observed. The two narrower-span simulations showed the same resonance mechanisms (acoustic modes coupling with shear layer modes) and similar mean and RMS flow fields. The $L_z/D = 1$ simulation, however, showed different flow behaviour; the shear was deflected upwards by the open-section vortex, changing the dominant shear layer modes and suppressing the acoustic resonance inside the cavity. Increasing the spanwise length with this modelling setup did not cause a corresponding increase in the degree of breakdown of the shear layer. The vorticity structures in the shear layer were found to be correlated in the span in all cases, to an extent which does not seem likely to be physical. The $L_z/D = 0.25$ simulation showed the highest degree of breakdown in spanwise correlation, although this might be artificially induced by a coupling between the scale of the shear layer structures ($\lambda \approx 0.4D$) and the span width ($0.25D$).

It is therefore difficult to conclude which of these flow fields is the most representative of the 2-D characteristics of such a cavity, since the characteristics of the spanwise-periodic simulation depend on the span width in an unpredictable way. Going from $L_z/D = 0.25$ to $L_z/D = 1$ actually caused an increase in the degree of spanwise correlation in the shear layer, which indicates some issues with using this methodology in predicting realistic breakdown of shear layer structures. The periodic-span setup may be considered quasi-2D, and the steady RANS boundary layer upstream is perfectly uniform in the span. The introduction of some variation upstream to disrupt the spanwise uniformity may alleviate this problem. This could be achieved by resolving the upstream boundary layer turbulence, which is possible using LES (discussed in Chapters 8-9). The introduction of solid side walls, discussed in the next section, would also disrupt the spanwise uniformity.

In the absence of a conclusive trend in the flow field with L_z, the $L_z/D = 1$ simulation was retained for comparison with the fully-3D simulation. As well has having the widest domain, which should theoretically cause the least span-boundary interference, this also allows the width to be matched (as $W = 1$ with the side walls); so this is a direct comparison to isolate the effect of the side walls.

5.7 $L_z/D = 1.0$ Simulations: Effect of Side-Walls

5.7.1 Mean and RMS Flow Features

The development of the flow with the side walls was found to be much quicker than the spanwise-periodic setup with the same L_z. With the side walls, the start-up transients were no longer visually present by about $5 - 10T^*$, and the shear layer developed to a stable degree of variation in the span by around $15T^*$, as opposed to the $30T^*$ required by the periodic-span simulation to develop spanwise non-uniformity in the shear layer.

Figure 5.21 compares slices of the time-averaged mean velocity and streamlines across three span stations for the simulation with side walls, and the periodic span solution (which was the same at all z locations). Both cases show two large counter-rotating vortices inside the cavity, with the open-section vortex being stronger and having a higher velocity, similar to the observed flow-field from the 2D and narrower-span spanwise-periodic simulations. The side walls do cause some variation in the z direction, mainly in distortion of the covered-section vortex, but overall the location and the shape of the two large vortices are fairly constant across the span.

Significantly, the introduction of the side walls, instead of the periodic boundary condition, changes the shape of the open-section vortex. With the side walls, the open-section vortex extends upstream into the covered section (by about $0.3D$) at all span slices, and through nearly the full depth of the cavity. At x_{LE}, therefore, the vortex flow is horizontal, and the shear layer does not exhibit the upwards deflection seen in the spanwise-periodic configuration. At all three stations the streamlines in the shear layer are level, impacting slightly below the downstream wall of the cavity. That upward deflection may be a unique feature of the periodic-span configuration with $L_z/D = 1$, since in this respect, the mean streamlines with the side walls are actually more similar to the narrower-L_z cases than the $L_z/D = 1.0$ case. A small roller-bearing type vortex is even seen to develop at the bottom downstream corner, which was observed with $L_Z/D = 0.25$ but not with $L_Z/D = 1$ (Figure 5.21(a)).

It is also noted that in all cases with the covered-cavity configuration, the small "roller-bearing" type vortices described in the literature (Section 2.4) and observed in the square-cavity simulations (Section 4.4) are not observed in all the corners; mainly only in the

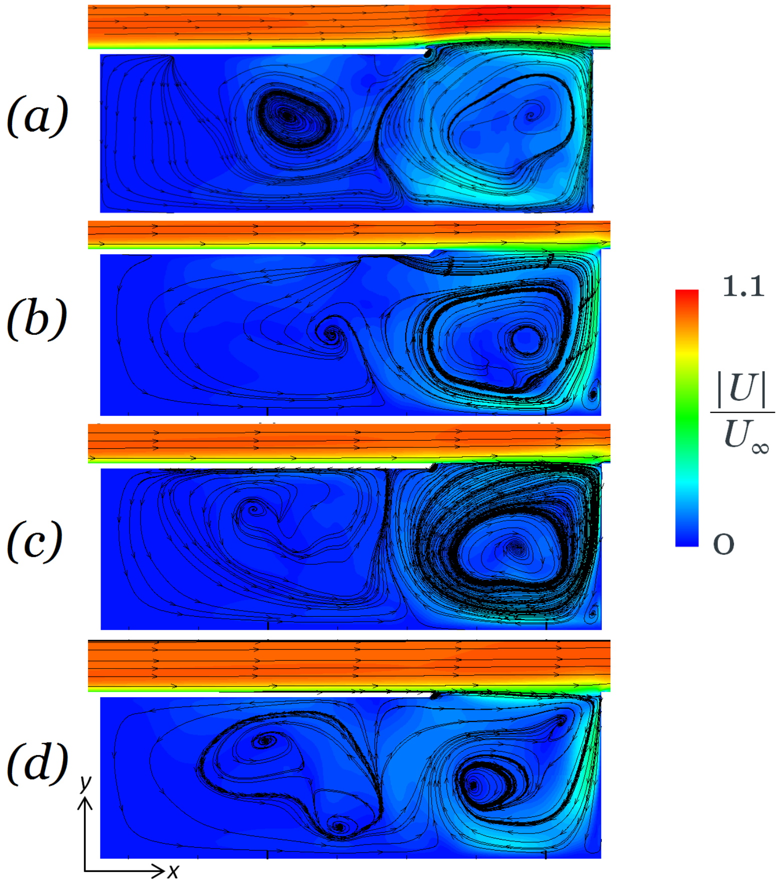

Figure 5.21: Mean velocity magnitude and $X - Y$ streamlines with $L_z/D = 1$: (a) spanwise-periodic; (b) side-walls, $z = 0$ (mid-span); (c) side walls, $z = 0.25D$; (d) side walls, $z = 0.475D$ (near the side)

bottom downstream corner. The presence of the cover appears to change the shape of the large vortices to fill most of the cavity area, with less space remaining to develop secondary vortices. The narrowest-span simulation had some small roller-bearing vortices developing between the two main vortices, due to having slightly more circular streamlines, but this was not observed with greater widths or the 3D walls. Therefore the width of the simulation domain is significant in determining the presence of these smaller structures.

Figure 5.22 shows a close-up comparison of the velocity slices at the mid-plane. For the spanwise-periodic configuration, the flow reattaches fairly smoothly at the trailing edge, with the shear layer streamlines coming down to align with the downstream plate. However in the simulation with side walls, the shear layer is slightly lower at the trailing edge, impinging on the back wall of the cavity, and causing a small recirculation bubble just downstream of the cavity. (Again this is qualitatively similar to the $L_z/D = 0.25$ configuration.) This suggests that with the side walls, there is a more of a tendency for flow from the shear layer to be directed into the cavity.

This behaviour is confirmed by the contours of mean pressure, shown in Figure 5.23. Both simulations show a small high-pressure region at the cavity trailing edge, but it is significantly larger in the simulation with the side-walls, due to the lower shear layer and therefore larger flow impingement region. Examination of the span-averaged pressure

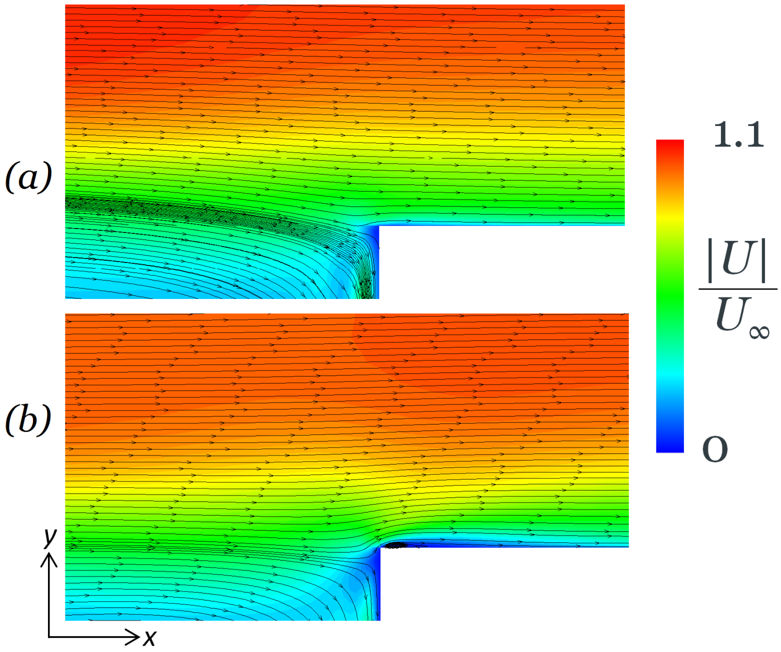

Figure 5.22: Close-up of mean velocity magnitude and $X - Y$ streamlines at the mid-span plane for the $L_z/D = 1$ cavity: (a) spanwise-periodic; (b) with side-walls

distribution on the downstream wall (Figure 5.24) showed that the side-wall simulation had higher mean pressure overall, with the peak (which denotes the impingement location) located about $0.007D$ lower than the spanwise-periodic simulation. The simulation with side walls also shows a negative-pressure region just downstream of the trailing edge, characteristic of the small recirculation zone shown in Figure 5.22. Inside the cavity, the spanwise-periodic simulation shows a region of low pressure in the open section, characteristic of the strong open-section vortex. In contrast, the simulation with side-walls shows a much higher level of mean pressure inside the cavity; almost ambient throughout. The frequency analysis in later sections showed a pattern of alternating build-up and release of pressure inside the cavity, which accounts for the averaged pressure being close to the ambient pressure. The simulation with side walls also has a greater tendency for flow from the shear layer to be directed into the cavity, causing a higher pressure peak on the bottom downstream corner of the cavity (where the flow directed downwards along the back wall impacts on the floor).

Contours of the turbulent kinetic energy k are shown in Figure 5.25. In the spanwise-periodic simulation there is a higher degree of k in the shear layer, due to the separated structures starting from the leading edge. In contrast, the shear layer from the side-wall simulation has low turbulent kinetic energy near the separation point, with the band steadily increasing in thickness and amplitude as the structures grow and convect downstream. This simulation also has a secondary region of high k downstream of the cavity trailing edge, due to the separation and recirculation region previously discussed. Inside the cavity, the shape of the turbulent kinetic energy region is broadly similar, but the periodic-span configuration has much higher peak k on the floor the cavity. With side walls, in the span direction, the cut plane in the middle of the open section (Figure 5.25(c))

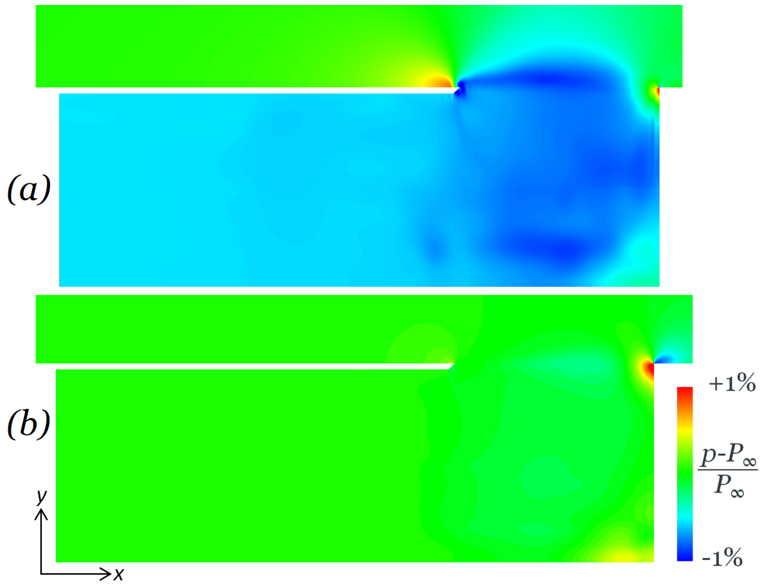

Figure 5.23: Contours of mean pressure in the mid-span plane for the $L_z/D = 1$ cavity simulations; top: spanwise-periodic; bottom: with side-walls.

shows an increase in k towards the sides of the cavity, with a small degree of overspill over the side walls.

5.7.2 Unsteadiness in the Shear Layer

Unsteady vortex structures, visualized through the Q-criterion, are compared across the two simulations in Figure 5.26. The periodic simulation shows large structures, beginning at the leading edge, with regular variations in the z direction. In contrast, the simulation with side walls separates smoothly from the leading edge. Vortices are shed, and grow as they convect downstream; initially, they are almost uniform in the span, but further downstream they start to break down in the span direction, forming smaller-scale structures than were observed in the periodic-span configuration (and in fact in any of the periodic-span configurations, even the $L_z/D = 0.25$ case which had a simialar mean velocity field). Therefore the presence of the side walls appears to disrupt the spanwise coherence of the vortex structures, forcing them to break down into smaller vortices. Small vortex structures are also visible developing along the top of the side walls of the cavity in the shear layer.

At the trailing edge, and downstream, even smaller vortex structures develop around the reattachment/recirculation-bubble region at the wall. Some of these take the form of hairpin vortices, which is consistent with observations from the literature in wall-bounded turbulence (Section 2). In the periodic-span setup, the structures in the shear layer and downstream are all fairly similar, due to the smoother reattachment. Inside the cavity, both simulations show a similar amount of vortex structures into the open section. With the side walls there are more small-scale structures, presumably swept into the cavity from the shear layer.

The RMS pressure variation is compared between the two simulations in Figure 5.27. In the shear layer, the trend is different to that shown by the turbulent kinetic energy. The

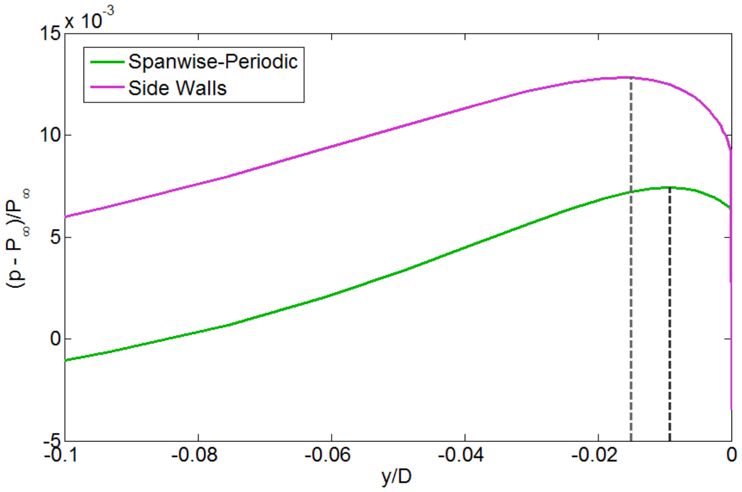

Figure 5.24: Comparison of mean pressure on the downstream wall of the cavity.

shed vortex structures in the periodic-span case had stronger k forming in the unsteady lifted shear layer; but the corresponding RMS pressures shows that the side walls develop higher levels towards the downstream end of the cavity. The stronger p_{RMS} is due to the development and growth of coherent resonant-mode vortex structures, which was not observed in the downstream half of the cavity for the spanwise-periodic setup with $L_Z/D = 1$. In this respect, again, the side wall simulation more closely resembles the narrower-span simulations.

More significantly, the introduction of the side walls causes significantly higher P_{RMS} throughout the covered section and towards the upstream $(-x)$ wall of the cavity. This was not observed in any of the periodic-span simulations, even the narrower ones. This suggests a structural change in the flow in the covered section. The difference is most likely due to the restriction of the flow in the span direction by the side walls, allowing fluctuating pressure to build up, especially in the covered section where the flow is most constrained. A 3D view, showing slice planes at the side wall ($z = -0.5D$), floor (y=$-D$) and downstream wall ($x = x_{TE}$) of the cavity, is shown in Figure 5.28. The pressure variation is largely uniform in the span and depth direction, and only increasing towards the upstream wall of the cavity (within around D of the covered-section wall). It is also noted that neither of these simulations show the vertical p_{RMS} bands associated with lengthwise acoustic modes (or any acoustic modes) inside the cavity.

5.7.3 Frequency Analysis

A fast-Fourier transform analysis was performed on the pressure histories, with the start-up transients omitted, and the resultant data further averaged using a windowing method with 50% overlap [118] as in all previous cases. An example of the results in the shear layer is shown in Figure 5.29, from $x_{LE} + 0.75D$. The simulation with the side walls shows significant peaks at modes 1 and 2. The presence of multiple Rossiter mode spikes in the frequency analysis generally indicates mode switching, so that both of these modes have dominated over the time sample. A smaller peak is also visible around mode 3. In spite of

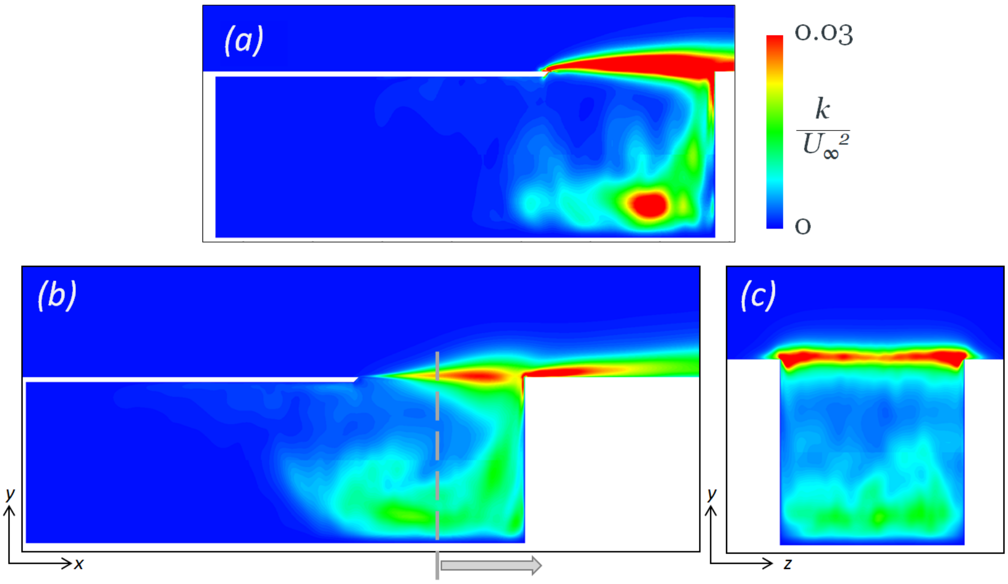

Figure 5.25: Contours of turbulent kinetic energy in the $L_z/D = 1$ cavity; (a) spanwise-periodic simulation, mid-span plane; (b) side-wall simulation, mid-span plane; (c) side-wall simulation, plane at mid-length of shear layer (as indicated in (b)).

the greater spanwise variation in the shear layer structures, the simulation with side walls is developing stronger resonance in the shear layer. This is consistent with the trends seen in the RMS pressure plots, where p_{RMS} in the side-walls simulation grows downstream, due to the growth of the resonant vortex structures. The dominance of modes 1 and 2 instead of mode 3 suggest that there is no coupling with a lengthwise acoustic mode inside the cavity (none of the N_x modes closely match f_1 or f_2). As indicated by the RMS pressure plots, no acoustic modes appear to be developing in this case.

The presence of the side walls was not found to cause much variation in the FFT data across the span. For example, Figure 5.30 compares the same $x = x_{LE} + 0.75D$ pressure monitor at the mid-span, with a monitor at the same x but close to the side wall. The same resonant peaks are observed, and the small differences are most likely due to sampling noise. Therefore it may be concluded that the frequency content does not vary with proximity to the side walls in this simulation.

Inside the cavity, the same modes are visible, but with the lower background noise the tones are much more prominent. The high p_{RMS} observed inside the cavity with the side walls can be directly attributed to these tones. Figure 5.31 compares the pressure monitor FFT data at the upstream wall of the cavity, where the side walls had the highest p_{RMS}. Both modes 1 and 2 are very strong here, with the mode 1 tone slightly stronger, and both much higher than any of the tones at this location from the simulation with the periodic span boundary (the strongest of which is at mode 4). In both cases the flow inside the cavity is ‘locking on’ to resonant modes in the shear layer, but it is particularly amplified in the simulation with side walls. This may be because the tones in the shear layer are stronger, but the increase towards the upstream covered section suggests that the restriction of the flow by the walls is also a contributing factor. (The periodic-span simulations are theoretically infinite in the span, and so have no span-wise constrictions

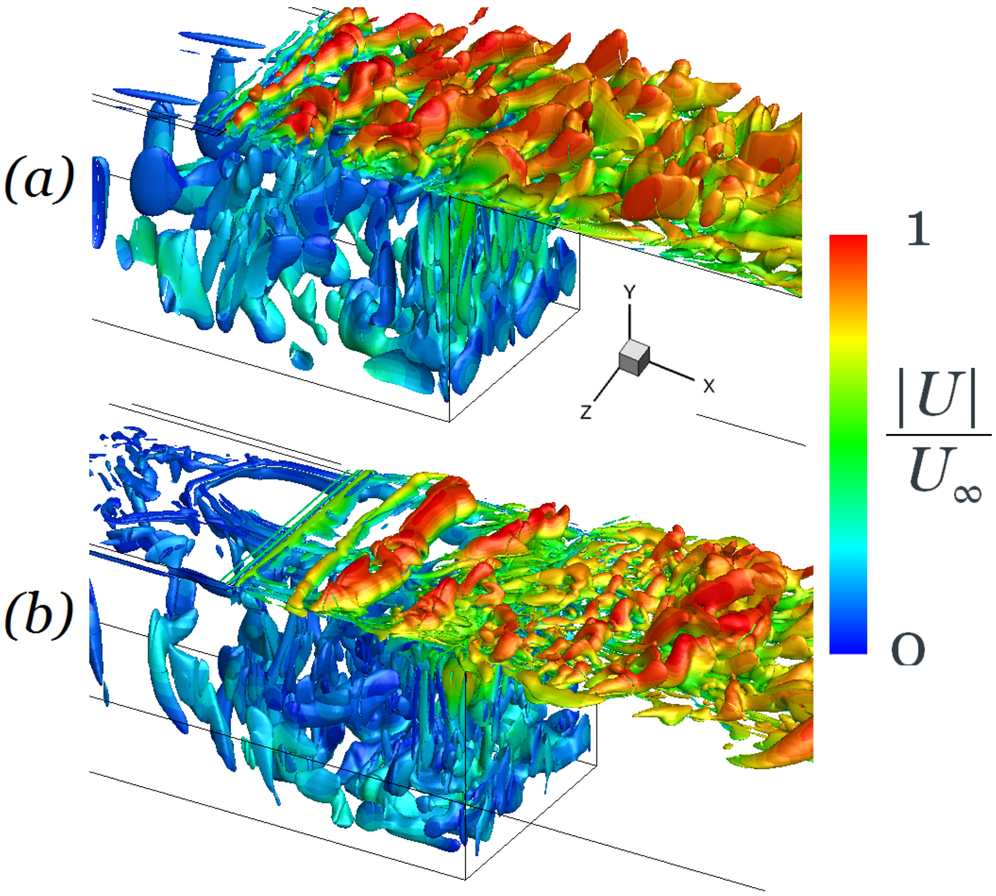

Figure 5.26: Instantaneous Iso-surfaces of the Q-criterion for the $L_z/D = 1$ cavity; (a) spanwise-periodic simulation; (b) simulation with side-walls

affecting the build-up of pressure.)

5.7.4 Unsteadiness Inside the Cavity with Sidewalls

A sample of the time history of the pressure monitors at the mid-span, mid-depth line is shown in Figure 5.32. The pressures exhibit a pattern of fairly regular oscillatory behaviour. The instantanous flow-field was sampled at the time instances indicated in Figure 5.32, covering a total time period equal to $1/f_1$ (i.e. one cycle of the mode 1 frequency), which is the dominant mode in this region. The corresponding instantanous wall pressures and streamlines are plotted in Figure 5.33.

Figure 5.33 shows that the unsteadiness in this region is characterized by large regions of alternatingly high and low pressure inside the cavity. There is some degree of spanwise pressure variation in the open section of the cavity, but towards the covered-section the pressure is largely uniform across the span and depth. The strongest pressure gradients are in the x (streamwise) direction, with the covered section often experiencing positive (relative to freestream) pressure when the open section has negative pressure, and vice versa. This explains why the mean pressure (Figure 5.23) showed an overall ambient pressure inside the cavity; these positive and negative pressure fluctuations cancel out over a long time period. The fluctuation pressures are largely uniform throughout the

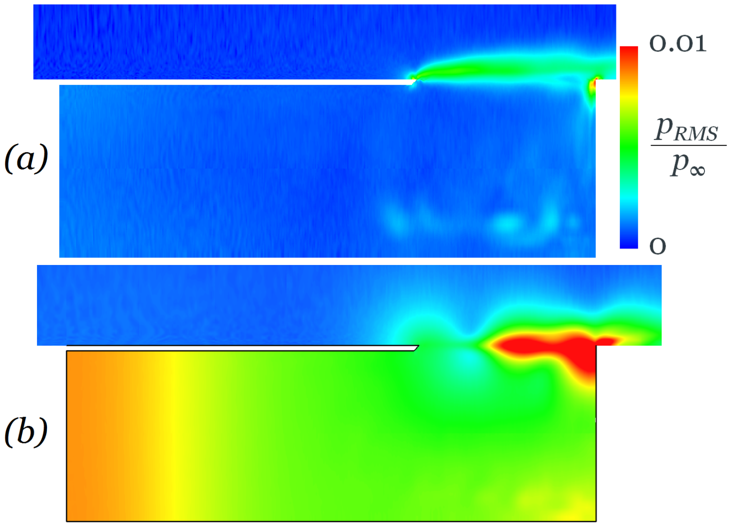

Figure 5.27: Contours of p_{RMS} at mid-z plane:(a) spanwise-periodic simulation; (b) simulation with side-walls

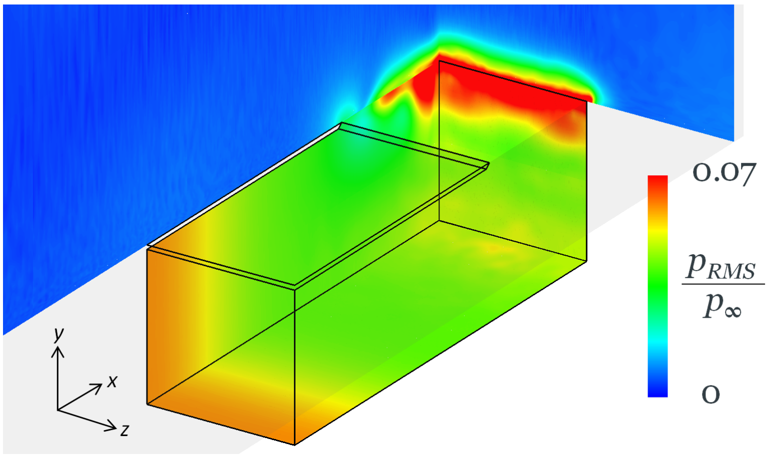

Figure 5.28: Slice planes of RMS pressure from simulation with side walls, at $z = -0.5D$, y=$-D$ and $x = x_{TE}$

depth and span of the cavity. Since the span width $W = D$ as well, this means that the spatial scale of these pressure fluctuations is of order D, much larger than the vortices in the shear layer.

The instantaneous streamlines exhibit a similar two-vortex trend to the mean streamlines (Figure 5.21). The vortex sizes appear relatively constant, but the streamlines are visibly distorted by local velocity perturbations. The open-section vortex in particular is sometimes compressed and sometimes expanded by the pressure oscillations in the shear layer, with flow entering and leaving the cavity at certain times, which is likely coupled with the large-scale pressure oscillations.

It seems, therefore, that the flow inside the cavity is 'breathing' so to speak, in time with the shear layer. Since the shear layer impacts below the top of the trailing edge wall, the amount of flow entering (or leaving) the cavity will vary based on the shear layer vortex structures, which in turn correspond to the resonant mode frequencies. Fluctuations in the shear layer induce a local fluctuation pressure in the open section. This in turn imposes

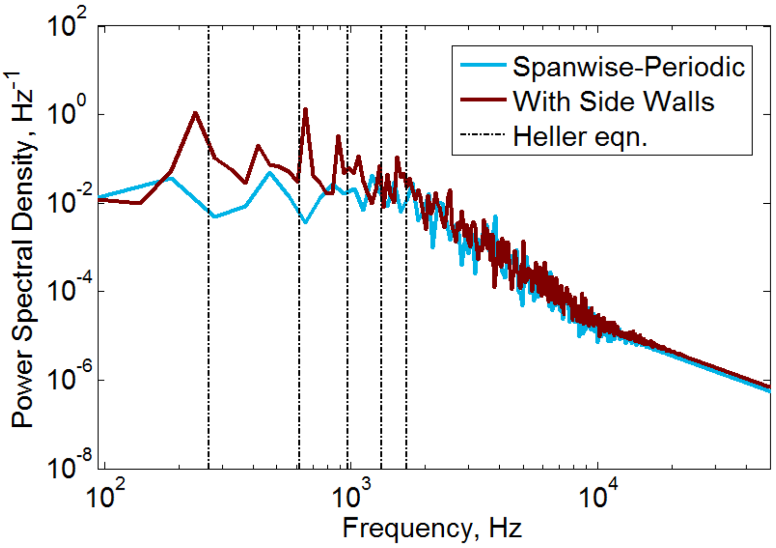

Figure 5.29: PSD of pressure at monitor Point 4 ($x_{LE} + 0.75D$ in the shear layer, location as indicated in Figure 5.5

a pressure variation in the covered section. There seems to be a phase lag between the two ends of the cavity; by the time a high-pressure signal from the shear layer has reached the upstream covered section, the next low-pressure signal is being imposed on the open section, so that the pressure is often opposite at opposite ends. The pressure disturbances are amplified inside the cavity by the presence of the side walls.

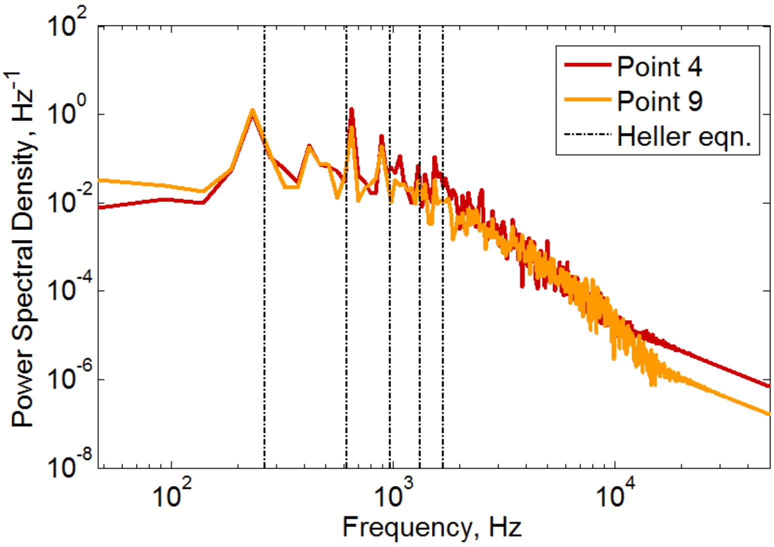

Figure 5.30: PSDs of pressure at monitor Point 4 and 9 (x_{LE}+$0.75D$, $z = 0$ and $z = 0.45D$ as indicated in Figure 5.5), from the simulation with side walls

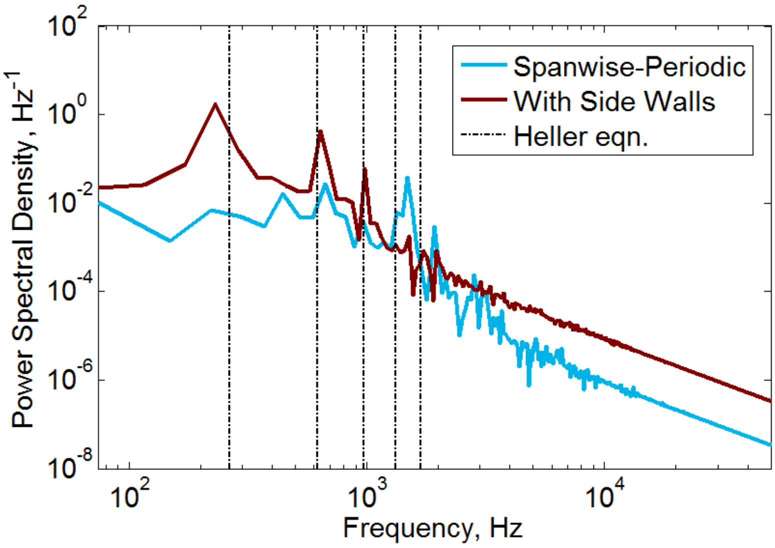

Figure 5.31: PSDs of pressure at monitors near top corner of upstream cavity wall (Point 17, as indicated in Figure 5.5

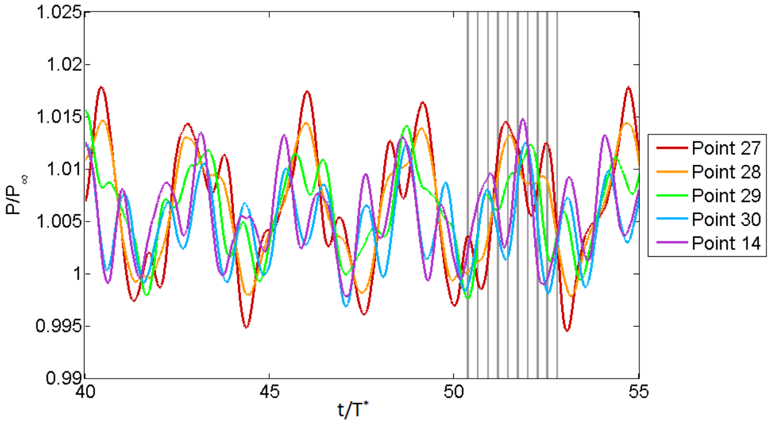

Figure 5.32: Time history of pressure monitors at mid-depth and mid-span of cavity from the simulation with side walls. Grey lines indicate sample times corresponding to Figure 5.33.

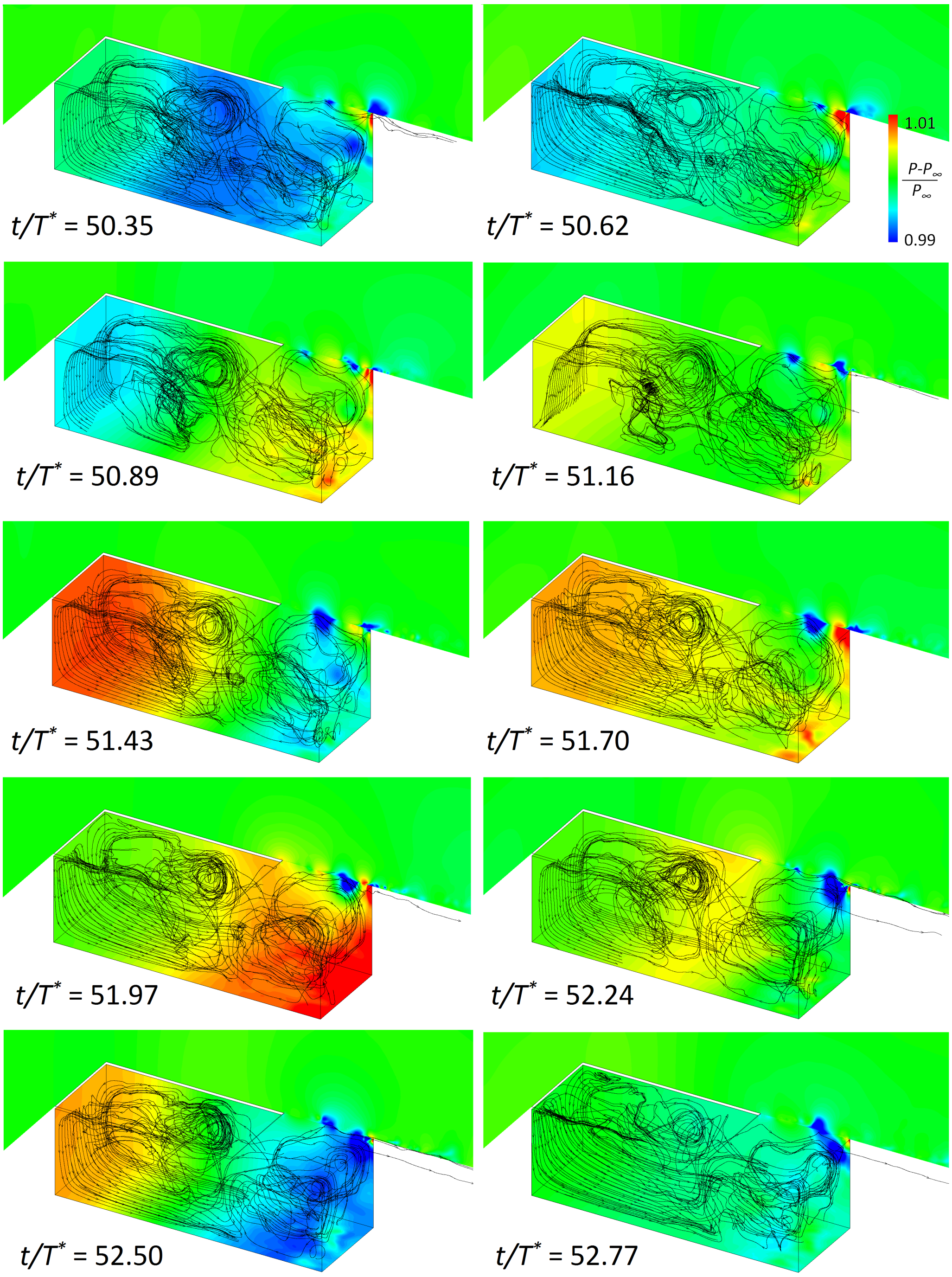

Figure 5.33: Instantaneous streamlines and pressure contours on the side, floor and upstream wall of the cavity from the simulation with side walls, at times corresponding to Figure 5.32.

5.8 Summary

DDES simulations were performed on a covered-cavity geometry of small widths and width $L_z/D = 1$, with and without side-walls at the spanwise extents. The periodic-span simulations with $L_z/D = 0.075$ and 0.25 showed similar resonant behaviour: the second length mode develops inside the cavity, and this couples with the third shear layer resonance mode, causing a strong tone. Increasing to $L_z/D = 1$ caused a distortion of the open-section vortex, which raised the shear layer, destroyed the acoustic-mode resonance, changed the dominant shear layer mode (to mode 4), and weakened the growth of the shear layer structures. Therefore, the periodic-span simulations did not show a systematic trend with increasing span width L_z. The shear layer structures remained correlated across the span in all cases, which does not seem to be physical behaviour, especially since the widest-span simulation $L_z/D = 1$ had a higher degree of correlation than the $L_z/D = 0.25$ case.

The addition of the side walls, compared to the $L_z/D = 1$ case, changed the dominant modes, and the lifting of the shear layer by the open-section vortex did not occur. Large pressure variations were observed, whose frequency corresponded to Rossiter mode 1. It is theorized that this is due to an alternating build-up and release of pressure, imposed by the shear layer fluctuations on the cavity, and amplified by the presence of the side walls. The side walls in a cavity of this configuration therefore play a significant role in determining the flow physics.

In some respects, the flow field from the simulation with side walls more closely resembled the $L_z/D = 0.25$ simulation than the $L_z/D = 1$ simulation; particularly in the mean velocity field in the shear layer, and in the trailing-edge impingement. This may suggest that the distortion of the open-section vortex in the $L_z/D = 1$ simulation is anomalous, and not truly representative of the 2D characteristics of the flow field. There is therefore still uncertainty about which spanwise length is 'best' with the periodic-span setup, in terms of being most representative of the 2D characteristics of the cavity flow.

These issues may be attributed to some extent to the shortcomings of using DES with spanwise-periodic boundary conditions to model cavity flow. DES cannot correctly model the boundary layer development upstream; the URANS model produces an effectively steady and spanwise-uniform boundary layer. The spanwise-periodic boundary condition also allows the flow to remain correlated in the span, so the combination of these methods could be allowing the simulation to retain spanwise coherence beyond what is physical.

From a modelling perspective, using LES with a wall-resolved incoming boundary layer should break up the uniformity in the span, allowing three-dimensionality to develop within the flow, and therefore addressing some of the issues with the overly-correlated shear layer structures. This will be explored in Chapters 8 and 9.

From a physical perspective, it is of interest to investigate the effect of the nearest other nose landing gear components on the development of the strong resonance developing inside the cavity in the fully-3D case with the side walls. This is the subject of the analysis in Chapter 6, where the geometry with side walls is extended to incorporate the main strut and open rear doors separately.

Chapter 6

DDES of Cavity with Landing-Gear Components

6.1 Overview

As a next step in complexity between the covered cavity described in Chapter 5 and the more realistic nose landing gear configurations described in Section 1.1, this chapter deals with the two components most likely to directly affect the landing gear bay flow-field: the main strut, and the opened rear doors. These components are added separately to the partially-covered cavity geometry studied in the previous chapter, so that the contributions of each to the flow field may be isolated. The purpose of this chapter is to use the methodology developed in the previous chapters to explore the physical effect of the strut and doors on the cavity flow field. This ties in with the objective of exploring the physical characteristics of the unsteady flow field, using the already-established DES methodology for landing gear geometries. The clean cavity with side walls discussed in Chapter 5 is used as a baseline case. The same DDES analysis techniques are used, and therefore the same simplification of the upstream boundary layer with RANS modelling.

6.2 Geometries

The geometry of the covered cavity with $W/D = 1$ and side walls is taken as a baseline for these simulations (see Figure 6.1). (The reference length D refers to the depth of the cavity, as used in Chapter 5). The length of the open section is $L_{open} = D$, with a total cavity length of $3D$. The leading and trailing edge of the open section of the cavity will be denoted x_{LE} and x_{TE} respectively ($x_{TE} = x_{LE} + D$), with the $y = 0$ plane denoting the top edge of the cavity (the surface of the upstream plate), and $z = 0$ denoting the mid-span of the cavity.

The geometry with rear doors is illustrated in Figure 6.2. The open rear doors are directly vertical (normal to the z-axis), of equal height $0.5D$ (i.e. half of the span), with thickness $0.03D$ (the same as the covered section), and squared edges. The inner face of the doors is flush with the side walls of the cavity, as shown in Figure 6.2(left). As with the standard covered cavity simulation, the flat plate extends by D on either side in the span, so as to

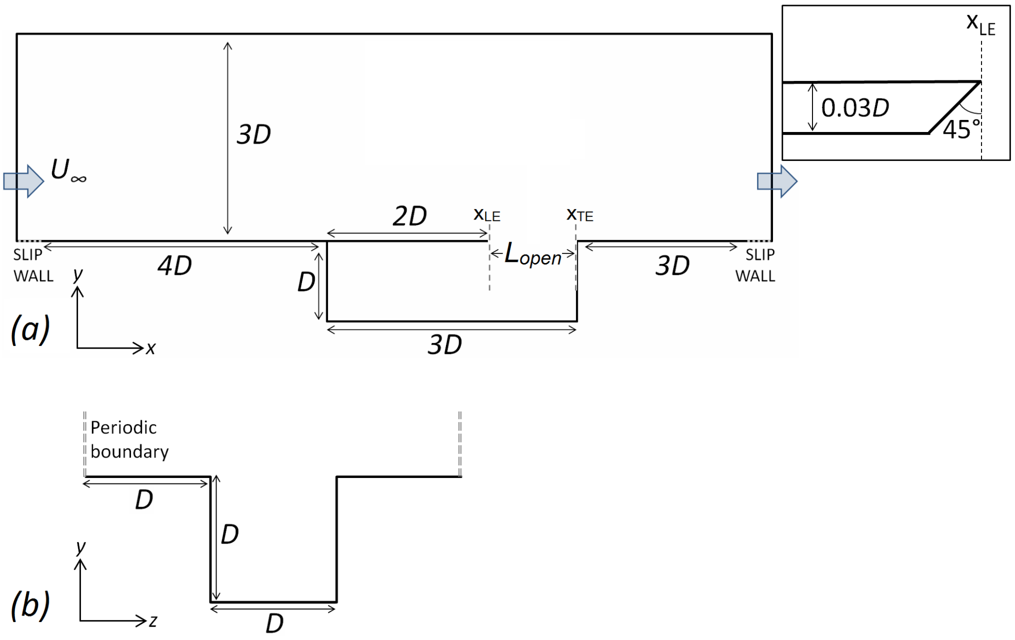

Figure 6.1: Schematic of baseline geometry (not to scale): (a) $X - Y$ plane, with inset showing close-up around leading edge and lip geometry; (b) $Y - Z$ plane slice through the open section of the cavity

avoid any interference with the boundary, and by $3D$ downstream of the cavity to avoid outflow interference.

The geometry with the strut is illustrated in Figure 6.3. A cylinder of diameter 0.02m was selected as being roughly representative of a landing gear strut on this scale, which results in $D_{strut}/D = 0.17$. For simplicity, the strut was located in the centre of the square open section of the cavity, aligned with the $z = 0$ plane. Inside the cavity, the strut extends all the way to the floor. Outside the cavity, in a realistic geometry, the strut would eventually terminate in the landing gear wheel bogey arrangement. To avoid any spurious effects from the edge of the cavity, the strut in this geometry was instead allowed to extend to the top of the domain, at a height of $3D$ above the cavity. Since the bogey arrangement is normally at a significant distance from the bay (at least $2D$ - see, for example, Figure 1.2 in Section 1.1), the effect of the strut on the cavity flow - independant of any end effects - is an important part of building up an understanding of the landing gear flow field.

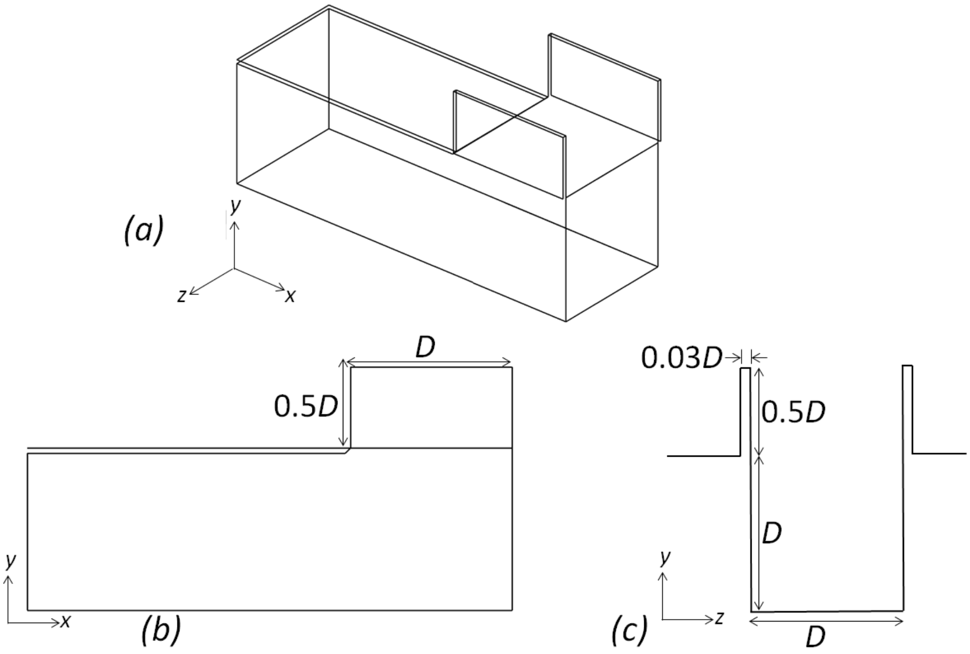

Figure 6.2: Close-up schematics showing the addition of the rear doors to the clean partially-covered cavity geometry: (a) 3D view; (b) schematic of $X-Y$ plane view; (c) schematic of $Y-Z$ view (not to scale). All other dimensions, and the domain away from the cavity, are as indicated in Figure 6.1.

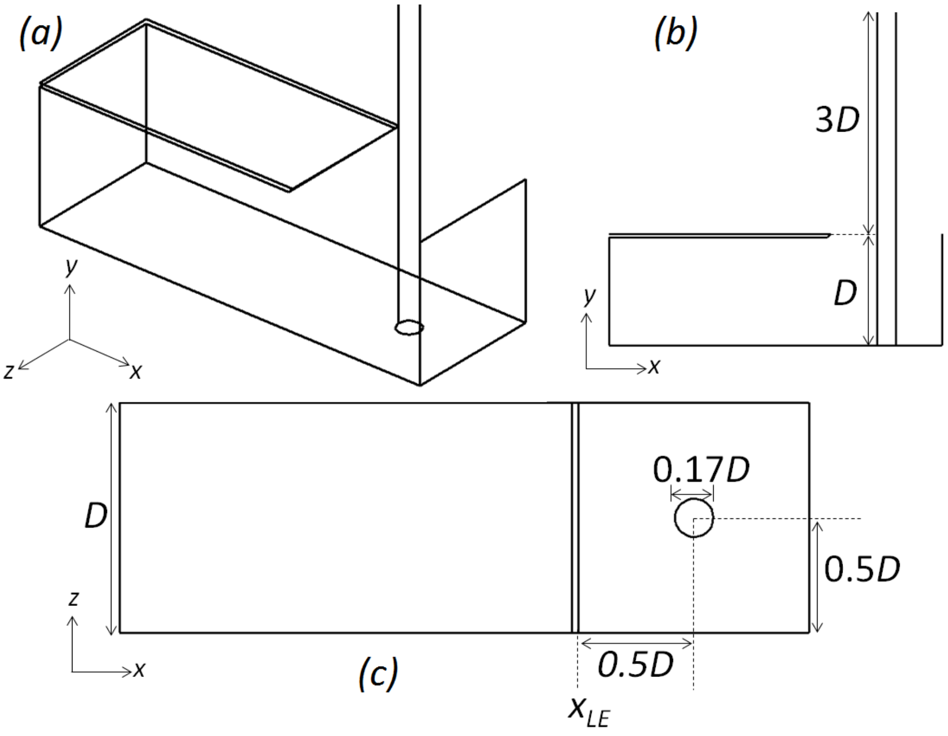

Figure 6.3: Close-up schematics showing the addition of the strut to the clean partially-covered cavity geometry: (a) 3D view; (b)$X-Y$ plane view (side view); (c)$X-Z$ view (top view). All other dimensions, and the domain away from the cavity, are as indicated in Figure 6.1.

6.3 Meshing

6.3.1 Cavity with Rear Doors

Slice planes of the mesh around the cavity with rear doors are shown in Figure 6.4. The mesh is fully structured with hexahedral cells and no skewness. Inside the cavity, and upstream, the resolution is similar to the mesh with side-walls in Chapter 5. The wall-normal resolution outside the open section is increased to resolve the anticipated smaller turbulent structures developing between the rear doors, with 142 points across the height of the doors, and additional clustering over the top edge to go down to down to $\Delta y^+ = 1$. Additional resolution is also provided near the spanwise and streamwise edges of the rear doors. The final mesh has 53×10^6 nodes; almost twice as many as the covered cavity without the rear doors from Chapter 5.

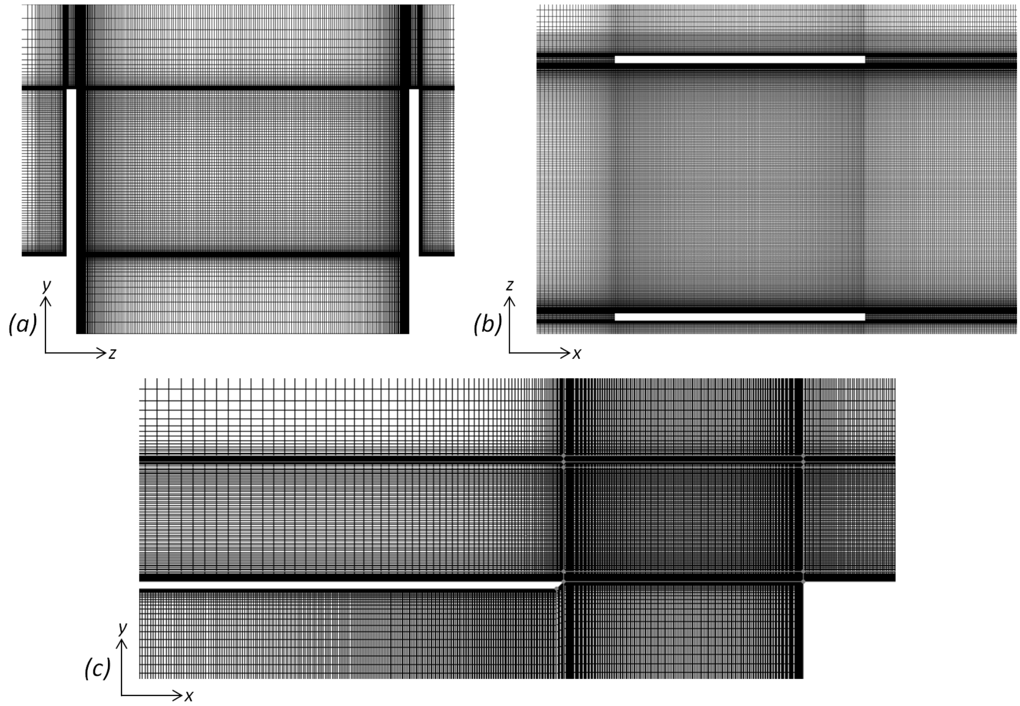

Figure 6.4: Slice planes from mesh of partially-covered cavity with rear doors; (a) X-plane in middle of open doors; (b) Y-plane at bottom of open doors; (c) Z-plane at mid-span.

6.3.2 Cavity with Strut

Again, the partially-covered cavity with side walls described in Chapter 5 is used as a base mesh, and the upstream and covered-section mesh resolutions are similar to that simulation. In the open section, where the strut is located, a typical slice in the $Y - Z$ plane is shown in Figure 6.5. The mesh topology was selected to optimize grid quality. The wall-normal resolution near the strut goes down to $\Delta^+ = 1.5$, and in the tangential direction the surface is resolved by 230 points, including additional clustering towards the downstream side of the cavity, as shown in Figure 6.5(a). This mesh is extruded in the Y-direction in accordance with the same wall-normal resolution used in Chapter 5, as shown in Figure 6.5(c).

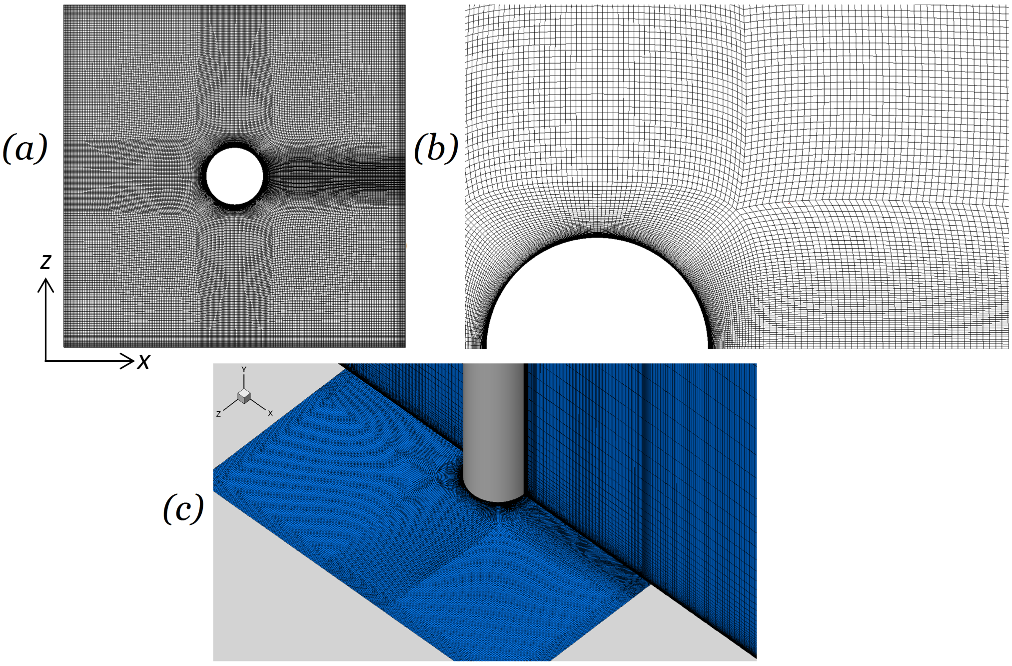

Figure 6.5: Mesh of partially-covered cavity with strut; (a) slice plane at $y = 0$ (i.e. surface of cavity); (b) close-up of (a); (c) 3-D view with mid-span plane.

6.4 Simulation Parameters

The boundary conditions used are similar to the basic covered-cavity simulations. No-slip walls are used for the flat plate, the cavity walls, and the rear doors and the strut. The plate extends by $4D$ upstream of the cavity and $3D$ downstream. Additional small free-slip wall sections are used upstream and downstream of the plate, with a freestream condition at the inlet and an outflow condition at the outlet. For the simulation with the strut, a finite volume method is used at the five-block junctions (Figure 6.5(c)), using the method implemented by Wang et at [103, 104], in order to minimize numerical noise from this region.

The simulations were performed using SotonCAA with a DDES modelling approach, the same methodology as described in Chapter 5. The 6^{th}-order implicit filter of Kim [109] was used , with cutoff wavenumbers set to $\kappa_C = 0.52$ and $\kappa_{C,boundary} = 0.50$. The same timestep was used as in Chapter 5, $\Delta\ t/ = T^*/24,000$, where T^* is based on $U_\infty = 85$m/s ($M_\infty = 0.25$), and the open length of the cavity $L_{open} = D = 0.12$m, resulting in a maximum CFL number of 3.4 (which is reasonable for this time stepping scheme, as mentioned in Section 3.4). The mean flow-field was computed by sampling at every time step, starting after the initial transient phase of the flow has finished. The presence of the start-up transients was judged based on the time history of the pressure monitors (also sampled at every time step). Cut-off times were set at $28T^*$ and $27T^*$ for the door and strut configurations respectively. For both cases, a simple idealized initial flow field was generated with quiescent flow inside the cavity and freestream flow outside the cavity, and uniform pressure throughout the domain.

Pressure monitors, as mentioned, were recorded at every timestep. For the simulation with the rear doors, the points are as indicated in Figure 6.6. The points inside the cavity and in the shear layer use the same locations and numbering scheme corresponding to the basic covered cavity (Figure 5.5), with additional points on the door surfaces and in the mid-plane. The pressure monitor locations for the cavity with the strut are illustrated in Figure 6.7, and again, Points 1-30 correspond to the locations in Figure 5.5 (except for Point 3, which has been shifted slightly downstream to allow for the strut). Frequency analysis is performed by taking a fast-Fourier transform of the pressure data (which is previously normalized by the freestream dynamic pressure), where start-up transient time is discarded and the remaining signal is divided into overlapping windows and averaged, as in the previous Chapter.

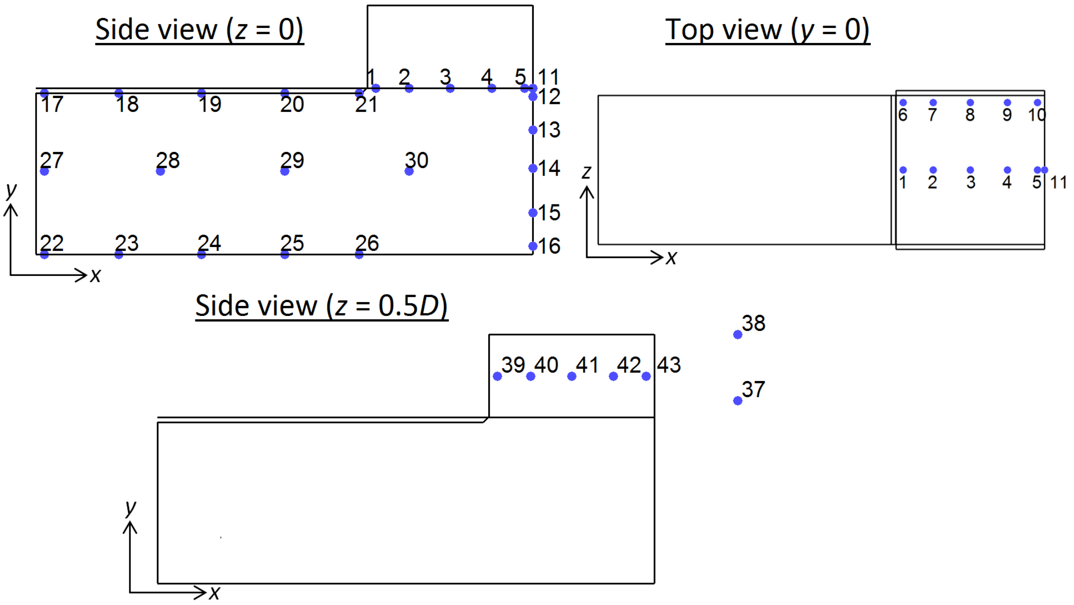

Figure 6.6: Monitor points in covered-cavity geometry with rear doors

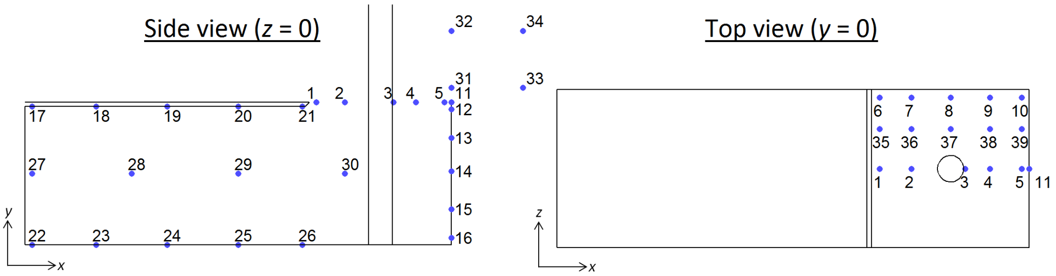

Figure 6.7: Monitor points in covered-cavity geometry with strut

6.5 Cylinder Pressure Validation

As a preliminary check, the pressure distribution around the strut at height of $2D$ above the cavity was extracted and is presented in Figure 6.8. At this distance from the cavity, it is expected that the flow around the strut is independant of the cavity effects, and therefore should follow the characteristics of normal cylinder flow. The RANS model in the attached boundary layer assumes that the flow is fully turbulent, regardless of the Reynolds number ($Re_{D,strut} = 1.1 \times 10^5$). The comparison against experimental measurements for turbulent cylinder flows from Travin et al [83] is presented in Figure 6.8. The mean pressure is in fairly good agreement, suggesting that the flow around the cylinder is adequately modelled. The strut shedding frequency downstream, measured from a pressure monitor $2D$ above the cavity and $0.5D$ downstream, was found to give a Strouhal number $St = fD_{strut}/U_\infty = 0.2$. $St \approx 0.2$ in this Reynolds number range has also been observed in the literature [122], so the present results are in good agreement.

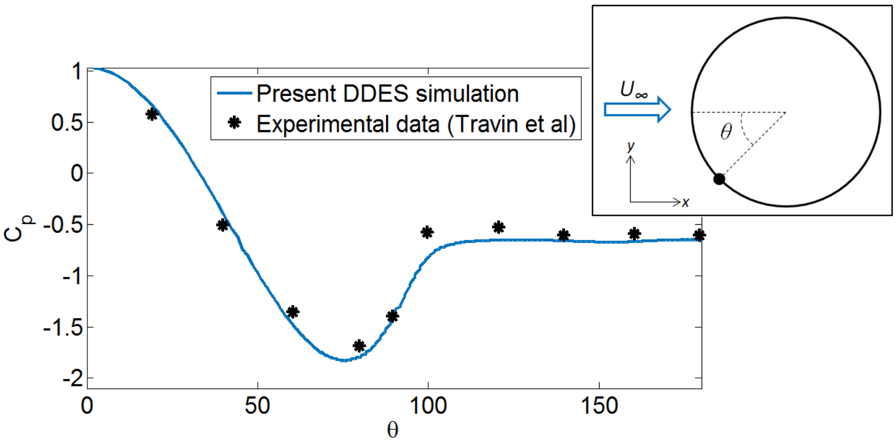

Figure 6.8: Mean pressure distribution around the strut at $2D$ above the cavity, compared with experimental results from Travin et al [83] for turbulent flow around a cylinder; inset: top of of strut and coordinate system, showing measurement direction for θ.

6.6 Effect of Geometry Modifications on Shear Layer

6.6.1 Overview

For both geometry modifications, the cavity flow field was still observed to develop Rossiter-mode resonance, with modes 1 and 2 dominant. The resonant characteristics inside the cavities were found to be broadly similar. The largest differences caused by the geometries were observed in the shear layer, and the differences within the cavity can be traced back to these shear layer effects. Therefore, the analysis of the results will be structured as follows: first, separate comparisons of the shear layer flow from each case (strut and door) with the baseline (clean) configuration; and then, a comparison of all three cases inside the cavity.

6.6.2 Interaction between Shear Layer and Rear Doors

An overview of the effect of the rear doors on the shear layer can be obtained from a comparison of instantaneous iso-surfaces of the Q-criterion, compared in Figure 6.9. Despite the flat surfaces being aligned with the freestream, the flow separates around the blunt front edge of the doors, both on the inner side (facing the cavity) and the outer side, as well as over the top. This causes the development of smaller structures which grow downstream, beginning to interact with the shear layer structures at about halfway across the open section. Small horseshoe-type vortices also appear to be developing around the base of the upstream ends of the doors. However, the structures in the shear layer - at least across the first half of the length - appear to be fairly similar to the baseline covered-cavity case.

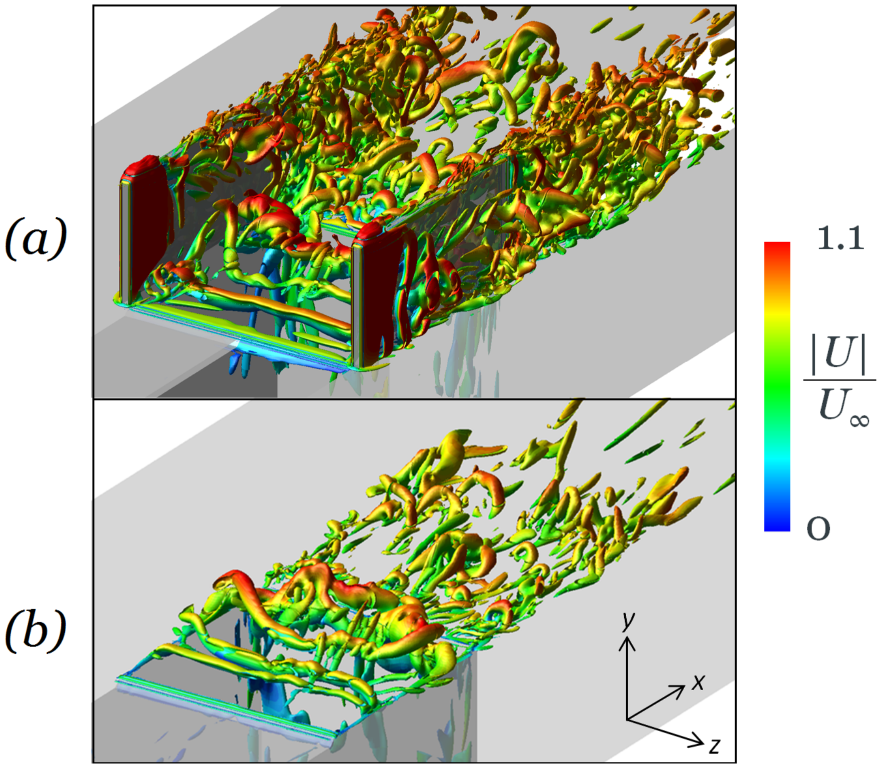

Figure 6.9: Iso-surfaces of the Q-criterion coloured by velocity magnitude; (a) covered cavity with rear doors; (b) baseline (clean) covered cavity

Near the leading edge of the shear layer, Figure 6.10 compares the frequency content of pressure monitors at $x = x_{LE} + 0.05D$, for $z = 0$ (mid-span) and $z = 0.45D$ ($0.05D$ from the side wall), against the clean configuration. (The spectral content from the clean cavity case was not found to vary significantly in the spanwise direction.) Compared to the clean cavity, the mode 2 frequency is slightly weakened, but still almost as strong. The mode 1 frequency, however, has been completely removed, and a new, significant resonant tone is observed at 3.5kHz at both z locations. This peak is slightly stronger at $z = 0.45D$ (i.e. nearer the door), but otherwise the two span stations give very similar frequency data, which was also observed with the clean cavity.

Monitors at $x_{LE}+0.25D$ and further downstream did not show this 3.5kHz peak as strongly (both for $z = 0$ and $0.45D$). However, pressure monitors located at the mid-height of the door and on the surface, as plotted in Figure 6.11, show this peak all the way along the length of the door, as well as the $m = 2$ peak. (These pressure monitors were recorded over a shorter simulation time, so the frequency resolution is coarser, but the peaks were observed to be consistent.) The 3.5kHz frequency corresponds quite well to Rossiter mode $m = 10$ (calculated from Equation 2.5), as shown in Figure 6.11.

The presence of such a high mode is, however, fairly unusual for a cavity flow in this

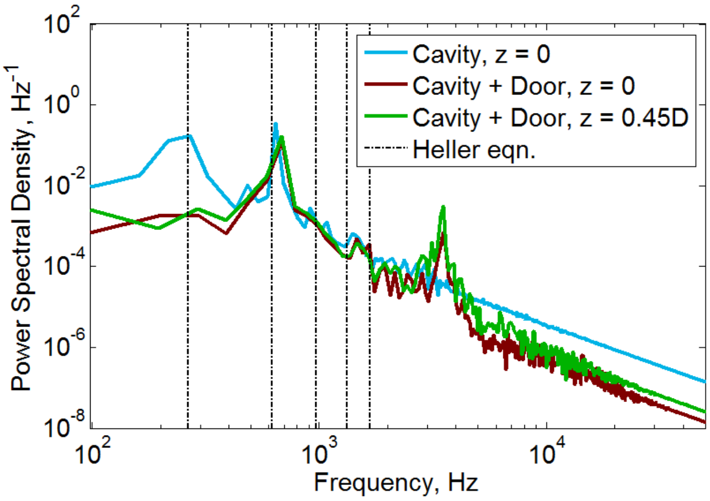

Figure 6.10: PSDs of pressure at monitors at Point 1 and 6 ($x_{LE} + 0.05D$, as shown in Figure 5.5)

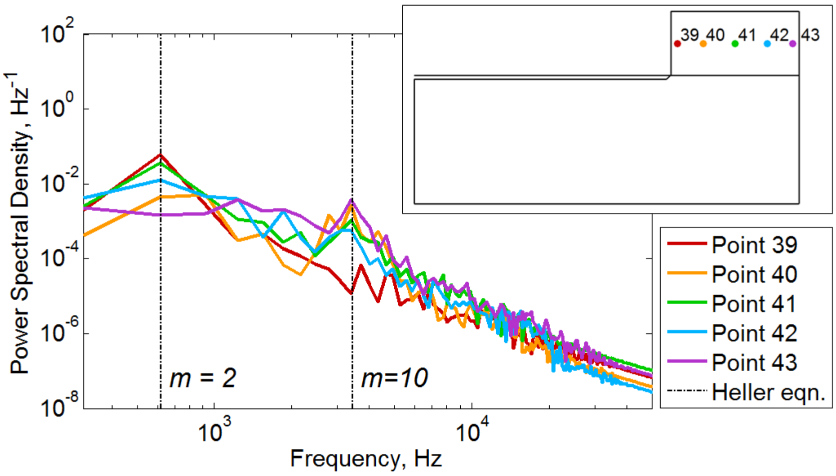

Figure 6.11: PSDs of pressure at monitors on inner surface of rear door, at $z = 0.5D, y = 0.25D$; inset: location of pressure monitors

Mach number regime, where $m = 1 - 4$ is most commonly observed (see Section 2). To explain this phenomenom, contours of the instantaneous perturbation pressure near the side of the cavity ($z = 0.47D$, $0.03D$ from the inner surface of the rear door) are shown in Figure 6.12. It is clear that the flow separation and vortex shedding around the front of the doors, visualized in Figure 6.9, creates pressure waves shedding from the upstream top edge of the door. The wavelength of this pressure wave can be estimated by measuring the distance between the successive low-pressure bands in Figure 6.12, which gives $\lambda/L_{open} \approx 0.115$. The shear layer mode $m = 10$, according to Equation 2.6, produces structures with a separation of $\lambda/L = 0.12$ - in very good agreement. The temporal evolution of p' over one cycle of 3.5kHz confirmed that this is roughly the time for one wave (positive and negative pressure) to be produced from the upstream top edge of the door. Presumably, the imposition of the high-frequency tone from this vortex shedding into the upstream shear layer, allows the signal to be carried down to the cavity trailing edge to produce the acoustic reinforcement necessary for shear layer resonance. (It is also possible that the oscillation of these door vortices is unrelated to the cavity at all, and the similarity between the frequency and f_{10} is coincidental. However, the fact that the pressure wavelength agrees with the Heller equation, and the presence of the tone in the shear layer, tend to support the idea that it is a high-mode Rossiter tone.)

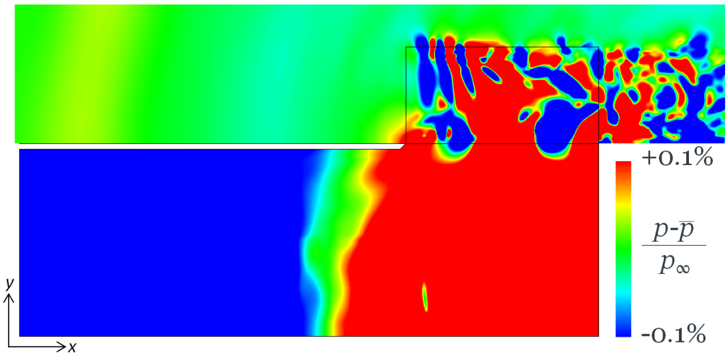

Figure 6.12: Contours of instantaneous perturbation pressure from plane at $z = 0.47D$ from simulation with rear doors

In terms of the spatial variation, Figure 6.12 shows that this $\lambda/L = 0.12$ structure is most clearly defined, and reaches furthest down towards the shear layer, at the upstream side of the door. This explains why the downstream pressure monitors at $y = 0$ did not pick up this tone, but the downstream monitors on the door at $y = 0.25D$ did. Instantaneous vorticity contours at the same location near the side edge (Figure 6.13) illustrate the vortex structures from the door, and how their region of influence grows and widens downstream until it interferes with the shear layer. Compared to the clean configuration, side doors promote the development of smaller structures in the shear layer. This may explain effect of the doors on the mode 1 frequency: if the small-scale structures produced by the side doors interact with the shear layer, this would favour higher shear layer modes, as they correspond to smaller structures. The first mode has the largest structures and the largest spacing between structures ($\lambda/L_{open} = 1.5$), so it would therefore be the most affected by any tendency of the door flow to 'break up' shear layer structures.

Another major difference observed in Figure 6.13 is that the rear doors appear to cause a lifting of the shear layer. A slice plane of the mean velocity at $x_{LE} + 0.5D$ (halfway across the open length of the cavity) illustrates this more clearly (Figure 6.14). Towards the centre-span, the shear layer height and thickness is fairly similar to the clean configuration. However within about $0.1D$ of the sides, the shear layer is clearly deflected upwards. In the clean configuration, mean streamlines in the $Y - Z$ direction showed no trends, since the w component is very small. However, with the side walls, there is a clear pattern. The separation of the flow along the doors produces a vortex along the inner surface of the door, extending in the flow direction ($+x$ or $-x$, depending on the side), and drawing the surround flow up around the doors. The pressure plot from the same region was observed to show low pressure at the centre of these streamlines, confirming the presence of coherent vortices. These vortices fill the region above the cavity between the doors, causing a net upwash velocity. The streamlines illustrate that the flow around these vortices comes mainly from inside the cavity, and towards the side walls (within $0.1D$ of the sides). This

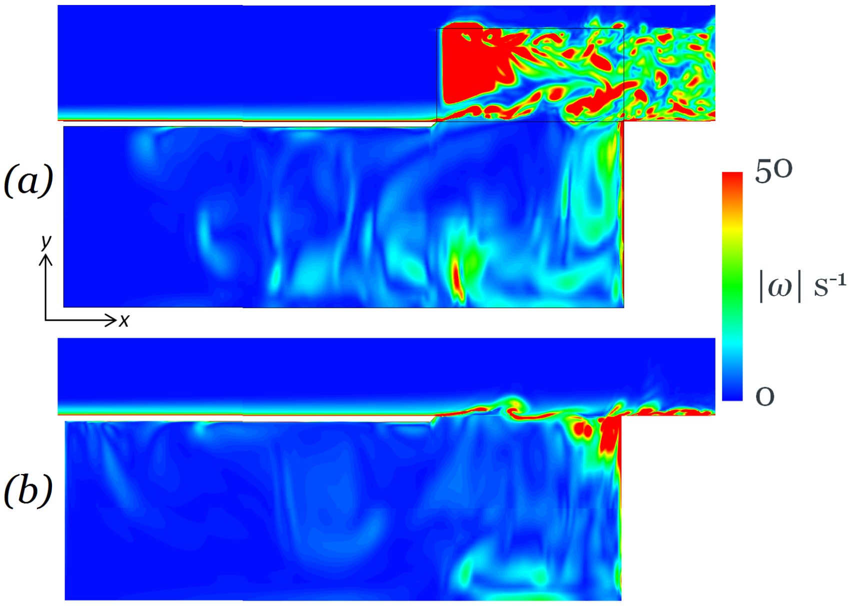

Figure 6.13: Contours of vorticity from plane at $z = 0.47D$: (a) covered cavity with rear doors; (b) baseline (clean) covered cavity

flow then expands above the cavity ($y > 0$) and around the lengthwise door vortices. This upwards flow from the sides of the cavity is what causes the upward deflection of the shear layer near the sides.

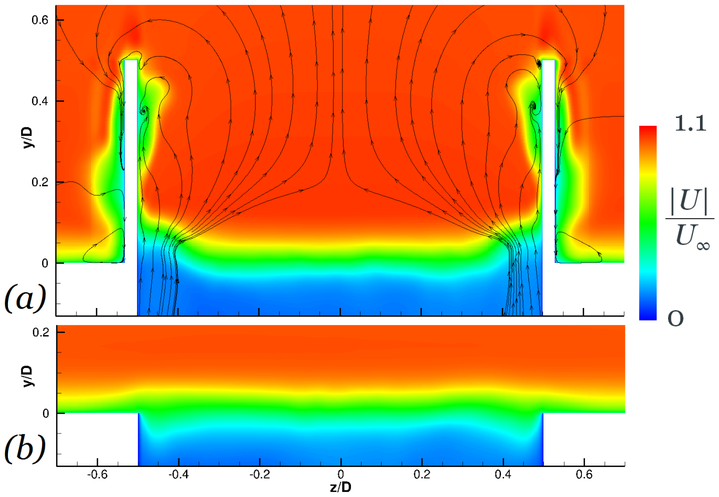

Figure 6.14: Contours of velocity magnitude from plane at $x = x_{LE} + 0.5D$: (a) covered cavity with rear doors; (b) baseline (clean) covered cavity

Despite these differences, the frequency content at the other monitor points in the shear layer are overall quite similar to the clean-cavity configuration. A typical example is shown in in Figure 6.15, at $x_{LE} + 0.75D$ and $z = 0.45D$. The mode 1 tone, which was equally dominant with mode 2 in the clean configuration, is not significant anywhere in the configuration with the rear doors. The mode 2 tone is fairly similar throughout the shear layer. (The experiments of Murray et al [49], found that the open doors completely suppressed all resonance in the shear layer, but that was with $M = 1.5$ and $L/D =$

9. The conclusions from high-aspect-ratio weapons-bay configurations therefore may not be directly translatable to landing-gear bay applications.) Amplitudes at mid-to-higher frequencies ($\approx$ 1kHz - 10kHz) at $z = 0.45D$ are slightly lower with the rear doors, due most likely to the raising of the shear layer away from the $y = 0$ plane where these monitors are located; at $z = 0$, the monitors at $x_{LE}+0.75D$ are very similar between the rear-doors and the clean configuration, except for the removal of mode 1. Moving further downstream, up to $x_{LE} + 0.95D$, the difference in FFT data between the two span locations became quite small (Figure 6.16), similar to the trend in the clean cavity.

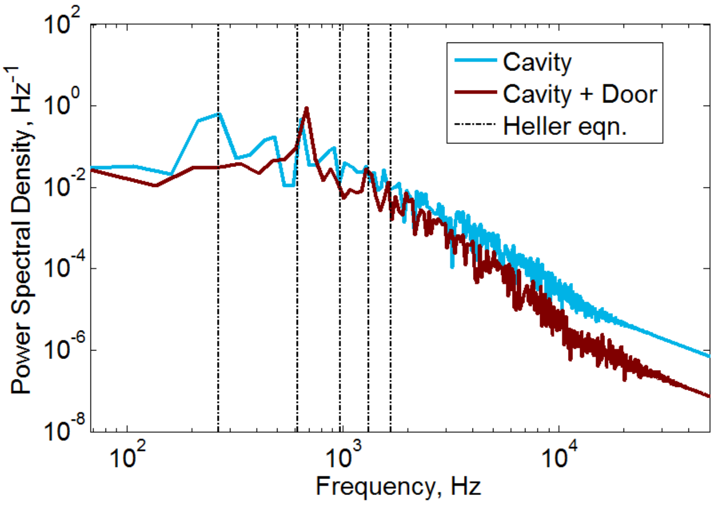

Figure 6.15: PSDs of pressure at monitors at Point 9 ($x_{LE}+0.75D, z = 0, 0.45D$, as shown in Figure 5.5)

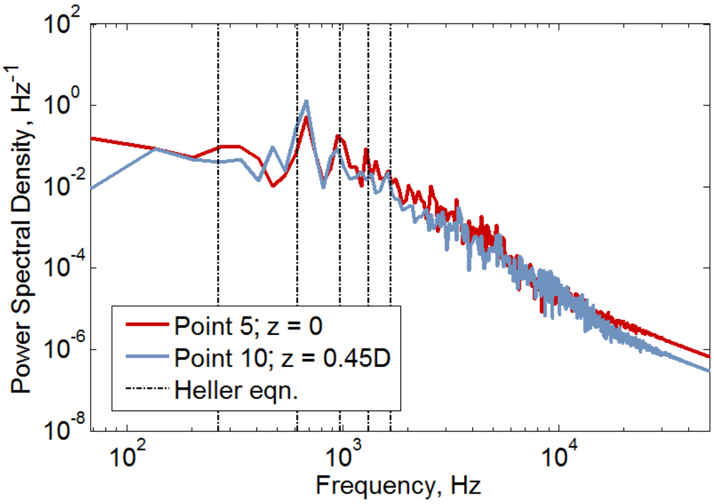

Figure 6.16: PSDs of pressure from covered cavity with rear doors, at Point 5 and 10 ($x_{LE} + 0.95D$, as shown in Figure 5.5)

At the trailing edge of the cavity ($x = x_{TE}$), Figure 6.17 compares contours of mean pressure overlaid with mean streamlines for the cavity with and without the rear doors, on a $Y - Z$ plane aligned with the cavity trailing edge, where $y < 0$ is on the downstream wall of the cavity. Shear layer flow impinging on this wall is directed upward, downward or laterally. Where the flow is vertical (i.e. up to about $z = 0.2D$ with the doors and $0.4D$

without), the dividing streamline between the upward and downward deflection indicates the stagnation point where the flow impinges on the rear wall. This is fairly similar between the two cases away from the side walls. In the clean cavity, approaching the side wall (within about $0.1D$) the flow is driven upwards and laterally, forming a small vortex. With the rear doors, the streamlines outside the cavity deflects outwards towards the doors. This is due to the reattachment of the flow around the downstream edge of the doors in the $X-Z$ plane. This is illustrated in Figure 6.18, which shows the mean pressure and streamlines at the $y = 0.25D$ plane from the positive-z side door. Downstream of the blunt door there is a reattachment of the flow (the cause of the outward w velocity), with counter-rotating separation bubbles, and an associated low-pressure region. The w component outside the cavity at x_{TE} is still quite small relative to the u component.

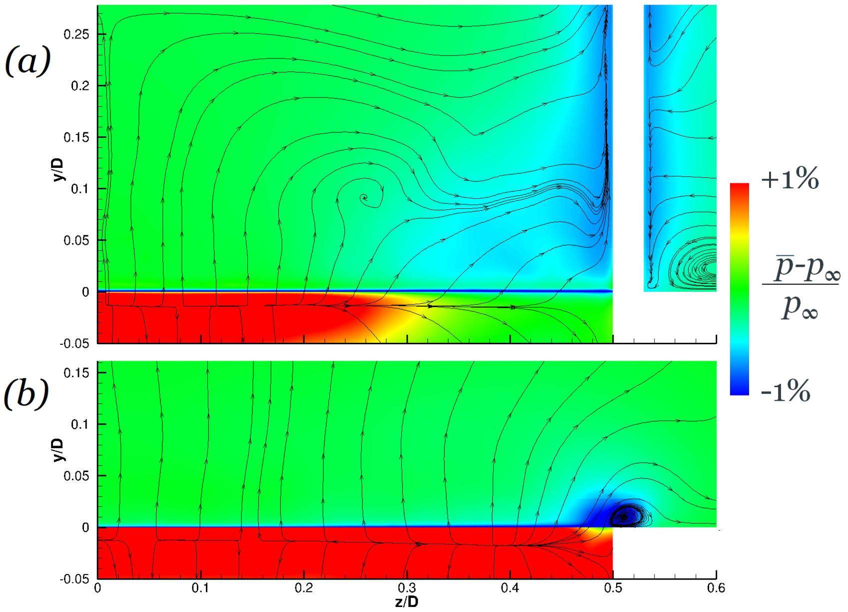

Figure 6.17: Contours of mean pressure, and streamlines, from plane at $x = x_{TE}$: (a) covered cavity with rear doors; (b) baseline (clean) covered cavity

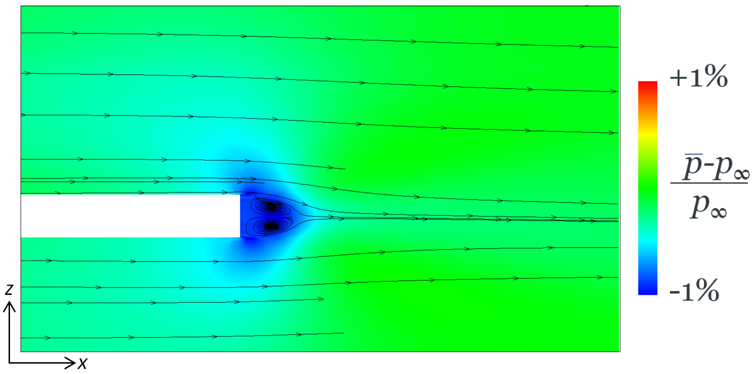

Figure 6.18: Contours of mean pressure, and streamlines, from plane at $y = 0.25D$ from simulation of covered cavity with rear doors

Returning to Figure 6.17, the pressure field on the wall ($y < 0$) is high, due to the impact of the shear layer flow on the solid wall. With the rear doors, this high-pressure region is significantly reduced within $0.2D$ of the side walls. This is due to the raising of the shear layer near the rear doors, as previously discussed; since the shear layer is higher, more of the flow is able to attach smoothly to the flat plate downstream of the cavity, and there is less of a pressure impact on this vertical wall. The thin region of low pressure just above $y = 0$ corresponds to the recirculation bubble downstream the cavity, where the flow impinging on the wall deflects upward and then downstream by the freestream flow. Figure 6.19 compares the mean velocity and in-plane streamlines at the mid-span and near the edge, with and without the rear doors. With the rear doors, the incoming streamlines are slightly higher; the lifting of the flow field near the side walls obviously has some influence even at the mid-span plane. The downstream recirculation bubble is correspondingly slightly smaller. Overall, though, the two flow-fields are fairly similar at $z = 0$. Near the side walls ($z = 0.475D$), however, there is a signficant difference; the rear doors lift the shear layer much higher, and the flow impingement in the $X - Y$ plane is very close to the top surface. It is noted, however, that the downstream recirculation bubble is still present, and is actually slightly larger than at the mid-span. The recirculation bubbles form because the flow impinging on the downstream wall is diverted upwards by the vertical wall, and then downstream by the freestream/shear-layer flow. With the rear doors, near the side wall, the higher shear layer should mean a smoother reattachment to the downstream wall, as shown by the drop-off in pressure. However it also means lower u-velocities in the vicinity of $y \approx 0$, which allows a larger recirculation bubble to develop. In contrast, the simulation without rear doors has a very small downstream recirculation bubble (if any) at $z = 0.475D$. This is presumably because the upwards flow here is also diverted laterally over the side walls (as seen in Figure 6.17(b)), which is not possible with the rear doors.

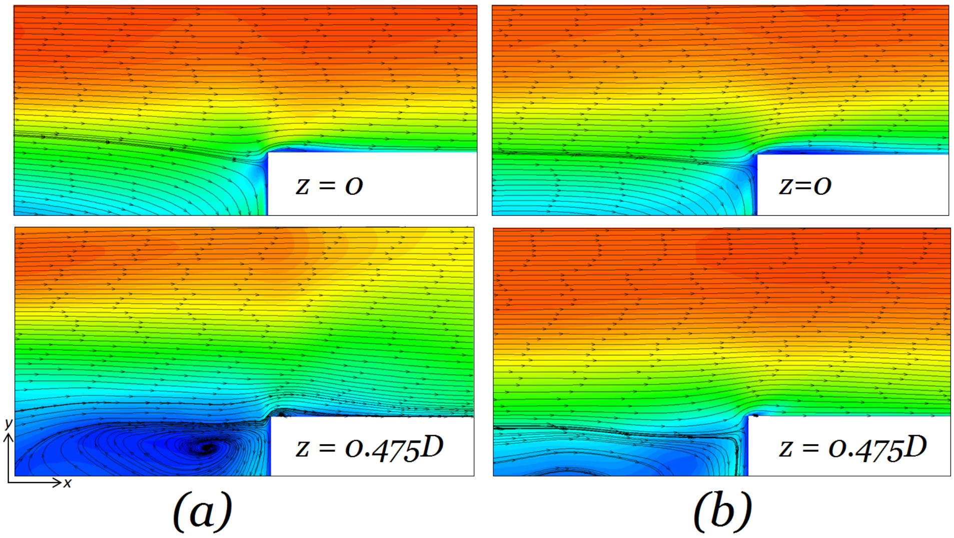

Figure 6.19: Contours of mean velocity, and in-plane streamlines, from planes at $z = 0$ and $z = 0.475D$: (a) covered cavity with rear doors; (b) baseline (clean) covered cavity

Further downstream, the PSDs of pressure at monitors at $0.5D$ downstream of one of the rear doors is shown in Figure 6.20. Pressure monitors from the same locations relative to the other door were observed to display the same trends, as expected from this symmetric flow-field. Just above the shear layer, the spectrum is broadband and no particular tonal peaks are observed. Downstream of the top of the door, however, the mode 2 peak is clearly observed, indicating that the tone from the shear layer is introduced to the wake shed from the top of the door. Figure 6.13 showed the shear layer, deflected upwards at the leading edge, mingling with the vortex shedding from the top of the door near the side of the cavity, so this result is not surprising. These results also show that the bluff separation around the blunt trailing edge of the door, visualized in Figure 6.18, is not associated with any tonal vortex shedding.

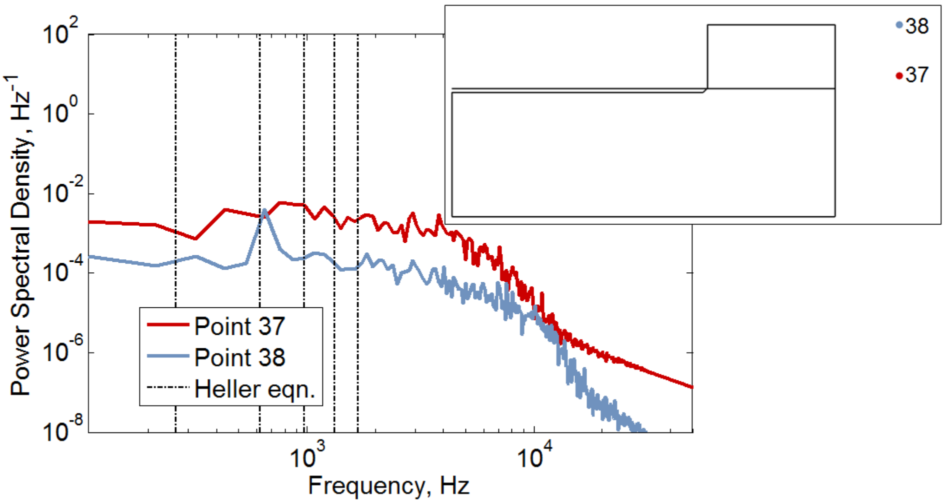

Figure 6.20: PSDs of pressure at monitors at $x = x_{TE} + 0.5D, z = 0.5D$ (downstream of door); inset: location of pressure monitors (also shown in Figure 6.6)

6.6.3 Interaction between the Shear Layer and the Strut

Figure 6.21 compares iso-surfaces of the Q-criterion in and around the shear layer, with and without the strut. The presence of the strut significantly disrupts the coherence of the shear layer vortices. Its influence appears to extend across the entire span of the cavity, and downstream to the trailing edge. Directly upstream of the strut, small-scale structures are visible, propagating upstream to the leading edge of the cavity. Regular coherent large spanwise vortical structures are only observed upstream of the strut and towards the sides of the cavity.

The instantaneous perturbation pressure in the shear layer is compared in Figure 6.22. Although Figure 6.21 showed significant changes in the shear layer vortex structures, the perturbation pressure still shows fairly regular bands of p' across the shear layer, suggesting that coherent vortex structures are still developing with the strut, and therefore so is shear layer resonance. Downstream and alongside the strut there is some instantaneous asymmetry with the pressure bands slanting in one direction, due most likely to the alternating-direction vortex shedding in the wake which is typical of cylinder flow. Upstream of the cylinder, small but regular bands of alternating pressure are observed, growing most defined towards x_{LE}. The wavelength of this pressure wave is estimated at $\lambda \approx 0.12D$.

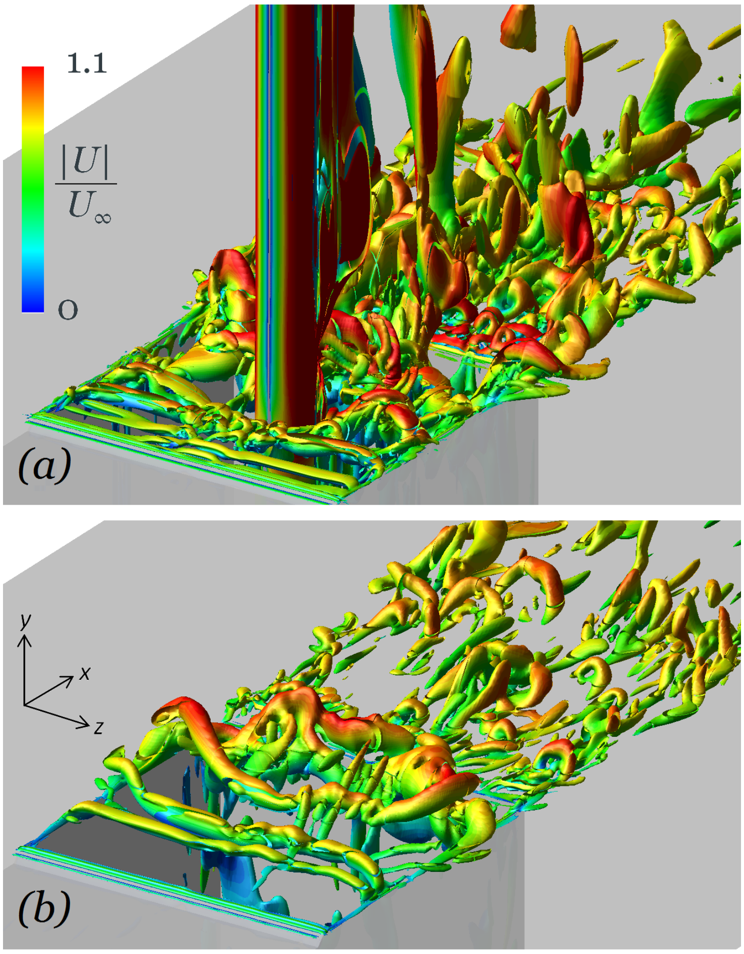

Figure 6.21: Iso-surfaces of the Q-criterion coloured by velocity magnitude; (a) covered cavity with strut; (b) baseline (clean) covered cavity

Pressure monitors in the shear layer at a point $0.05D$ downstream of x_{LE} are compared at $z = 0$ with and without the strut in Figure 6.23. Strong tones are visible at Rossiter mode 1 and 2 in both cases. The introduction of the strut causes strong spectral 'humps', at $f \approx 3.2$kHz and $f \approx 6.4$kHz. The latter tone is most likely a harmonic of the former. Moving outward from the mid-span $z = 0$ to $z = 0.25D$ and $z = 0.45D$, Figure 6.24 shows that tones at Rossiter modes 1 and 2 are fairly constant across the span, consistent with the relatively spanwise-uniform vortex structures observed near the leading edge in Figure 6.21. Away from the centre-span the secondary 6.4kHz tone disappears, and the 3.2kHz tone is weaker but still present. This tone is signficantly weaker even in the mid-span plane moving downstream to $x_{LE} + 0.25D$. All of this indicates that this tone corresponds to the small-scale pressure fluctuations observed upstream of the strut in Figure 6.22(a), as that pattern was also the most clearly defined towards $(x, z) = (x_{LE}, 0)$. Looking at the bands of fluctuation pressure, and the region of influence, it seems very likely that this feature is a result of a smaller shear-layer resonance being set up between the cavity leading edge and the front surface of the cylinder. Separated flow from the shear layer moving downstream will impact on the vertical face of the cylinder, in a similar manner as it would on the downstream cavity wall, exciting acoustic waves which propagate upstream; and a resonance may thus be established across this smaller length.

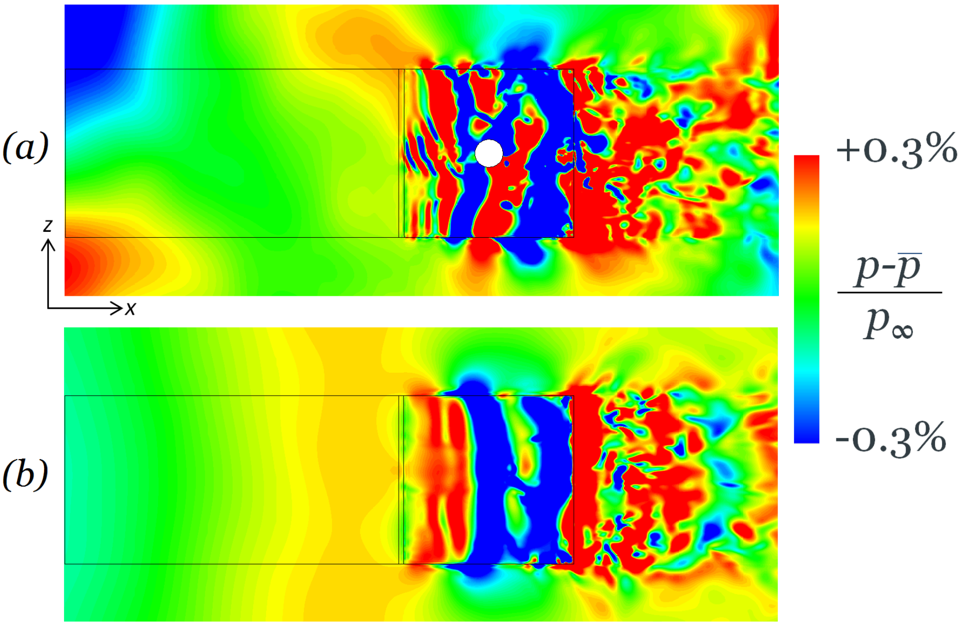

Figure 6.22: Contours of instantaneous perturbation pressure from plane at $y = 0$: (a) covered cavity with strut; (b) baseline (clean) covered cavity

Defining a modified length L_2 as the distance between the leading edge of the cavity and the upstream edge of the cylinder, $L_2 = 0.05$m ($L_{open}/2 - D/2$). Using L_2 as the length scale in the Heller equation (Equation 2.5) yields, for $m = 4$, $f_4 = 3.2$kHz, which agrees with the tonal peaks observed in Figure 6.23 and Figure 6.24. The visual evidence from the p' plot confirms this; for $m = 4$, the corresponding lengthscale of a shear layer mode (based on Equation 2.6) would be $0.3L_2$, which equates to $0.12L_{open}$, in good agreement with the rough estimate based on Figure 6.22(a). Therefore it may be concluded that the presence of the strut through the shear layer does set up a smaller secondary shear layer resonance cycle, with the dominant mode being $m = 4$ based on this smaller lengthscale. Despite being formed upstream of the strut, Figure 6.22 shows that the pressure wave does weakly extend to the side walls of the cavity, and the 3.2kHz tone is present in the pressure monitors towards the sides. The other tone at $\approx$ 6.5kHz could be a direct harmonic of this tone; it also agrees reasonably well with the $m = 8$ tone, which gives 6.6kHz.

Figure 6.24 also shows tones developing at Rossiter mode $m = 3, 4$ and 6, which were not observed in the clean cavity configuration (Figure 6.23). The interaction of the shear layer with the smaller structures from this secondary resonance may be producing higher modes in the shear layer, as was observed to be the effect of the rear doors near the edge. Introducing perturbations at smaller scales and higher frequencies would favour the development of higher modes, which also have smaller scales (in terms of the vortex separation distance, at least) and higher frequencies. Moving down to $x_{LE} + 0.25D$ these higher modes are less pronounced, and they mostly disappear in the downstream half of the shear layer. Unlike with the rear doors, however, the development of the higher modes does not come at the expense of the first mode, which (at this upstream location in the shear layer) is of a similar amplitude throughout the span with and without the strut.

Around the strut, contours and streamlines of mean velocity in the $y = 0$ plane are

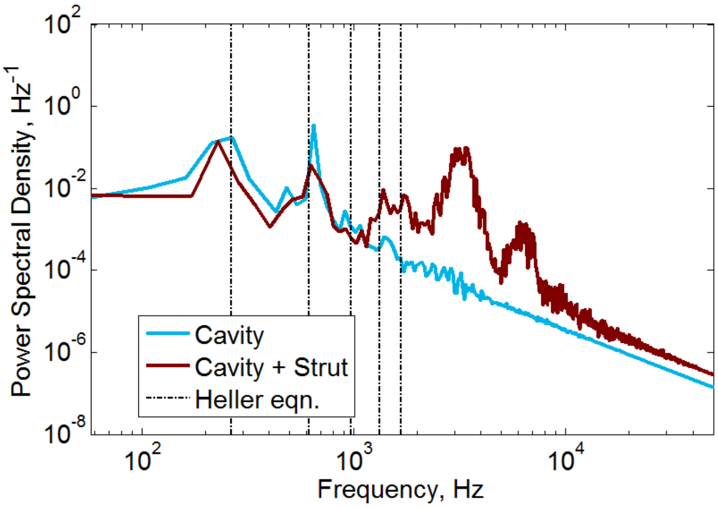

Figure 6.23: PSDs of pressure at monitors at Point 1 (mid-span, $x = x_{LE} + 0.05D$, as shown in Figure 5.5)

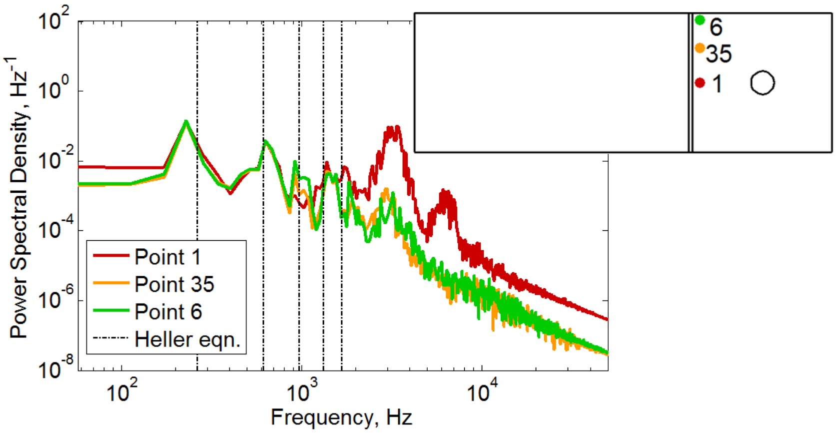

Figure 6.24: PSDs of pressure at monitors at $x_{LE} + 0.05D$, $z = 0, 2.5D, 0.475D$; inset: location of monitors in $y = 0$ plane (also shown in Figure 6.7)

shown in Figure 6.25. The $X - Z$ streamlines show the flow reattaching fairly smoothly downstream of the strut, with only a small downstream recirculation bubble in this region. There is a slight asymmetry in the reattachment streamline. It is possible that this may be addressed with a longer averaging window. Currently, the mean quantities are calculated over a window of $36T^*$ (861,000 timesteps), similar to the window used for the other simulations. The cylinder shedding frequency, measured from a pressure monitor far away from the cavity, is estimated at 1kHz (St $= 0.23$); the averaging window encompasses ≈ 50 cycles of this frequency, which should suffice to average out any asymmetry in the cylinder wake. However, cylinder flows are particularly liable to asymmetry, even in experimental studies [122]. There may be a low-frequency tendency for alternating direction of the cylinder wake, which is not completely smoothed out over this averaging window. Aside from this issue, however, the mean quantities in the wake have largely converged to a symmetric state, as seen in the contours.

The spanwise velocity component (w) becomes very small (relative to u) by $z \approx 0.2D$, which is $0.5D_{strut}$ away from the side of the strut. The size of the high-velocity regions

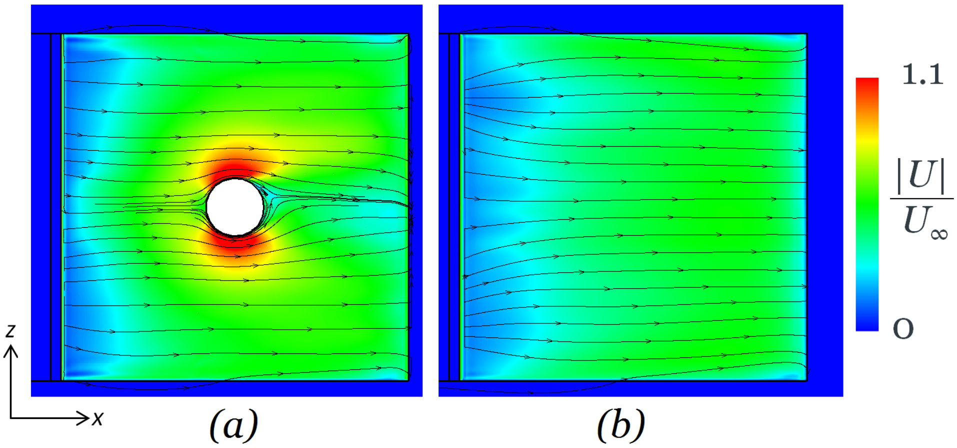

Figure 6.25: Contours of mean velocity magnitude, and in-plane streamlines, from plane at $y = 0$: (a) covered cavity with strut; (b) baseline (clean) covered cavity

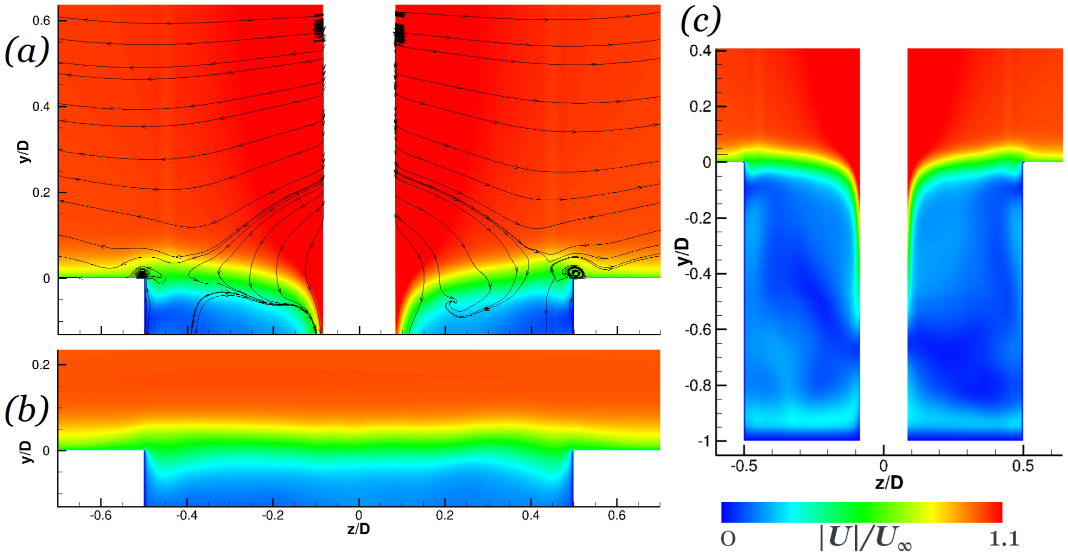

Figure 6.26: Contours of mean velocity magnitude from plane at $x_{LE} + 0.5D$: (a) covered cavity with strut; (b) baseline (clean) covered cavity; (a) covered cavity with strut, wider view

on either side of the strut seem disproportionately large, given the smoothness of the streamlines. Taking a cut-plane in the $Y - Z$ direction through the middle of the strut (i.e. at $x = x_{LE} + 0.5D$), Figure 6.26 shows that the presence of the strut deflects the local shear layer downwards. (The surface of the strut is modelled as a no-slip wall. A thin boundary layer develops between the strut and the surrounding higher-velocity flow; but it is too thin to be distinguished on the scale of Figure 6.26-6.27 and similar plots.) The flow deflecting outward around the strut also tends downward into the cavity, pushing the shear layer down and introducing high-velocity flow from the freestream in towards $y = 0$. This accounts for the high velocity flow seen on either side of the strut in Figure 6.25. This outwards velocity also causes small recirculation regions on the top corners of the side of the cavity. A wider view of the velocity at this plane shows the shear layer flow becoming aligned with the strut surface at around $y = -0.2D$, and persisting down into the cavity up to $y \approx -0.6D$. Taking another slice through the middle of the strut, but this time in the $X-Y$ plane ($z=0$), Figure 6.27 shows that the downward deflection of the shear layer occurs in the lengthwise direction as well. The change is not as pronounced, because the higher u velocity drives the flow forward (as opposed the $Y-Z$ plane, where there is no component of the freestream velocity). Still, compared to the clean covered cavity, the influence of the strut causes a downwards deflection of the shear layer all the way upstream to the leading edge, and downstream to the trailing edge. The shear layer downstream is also significantly thicker, due to the disruption of the flow by the strut, and the lower pressure in the strut wake. Figure 6.28 shows the mean pressure at the $y=0$ plane on a relatively wide scale, showing the strong low-pressure region around the sides and downstream of the strut.

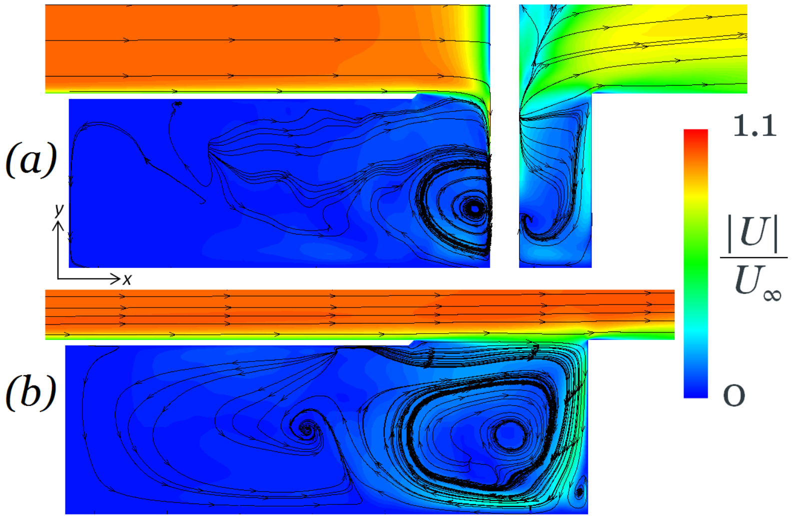

Figure 6.27: Contours of mean velocity magnitude and in-plane streamlines from plane at $z=0$: (a) covered cavity with strut; (b) baseline (clean) covered cavity

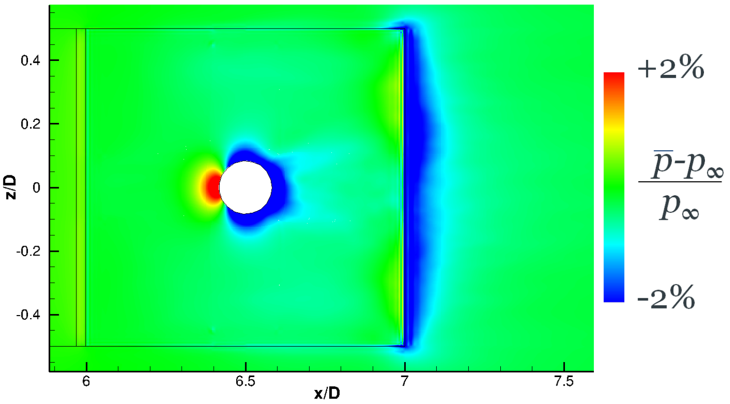

Figure 6.28: Contours of mean pressure from plane at $y=0$, from simulation of covered cavity with strut

In terms of the fluctuating components, the RMS pressure in the shear layer is compared with and without the strut in Figure 6.29. As expected, there is a region of high p_{RMS} around and downstream of the strut, due to the separated flow around the strut and the disruption of the shear layer. In the span direction, this region extends to around

$z \approx \pm 0.3D$ ($1.5D_{strut}$). Further to the side than this, p_{RMS} levels are fairly similar to the clean cavity case. Comparison of pressure monitors at $(x, z) = (x_{LE} + 0.75D, 0)$, i.e. in this wake region, is shown in Figure 6.30. The difference in RMS pressure comes from a higher amplitude of high-frequency oscillations (around 2-11kHz), over a broadband range, not any particular tonal peak. Tones corresponding to shear layer Rossiter modes $m = 1$ and $m = 2$ are still present, although slightly weaker than in the clean configuration. Other pressure monitors downstream of the strut showed generally similar trends: increased high-frequency broadband noise and $m = 1, 2$ Rossiter modes but with smaller peaks. Comparing across the span, the points at $z = 0$ showed the highest amplitudes (as expected, due to the higher RMS pressure levels), but the same relative shapes of the PSD distribution. The difference across the span decreased towards the trailing edge, moving further from the strut.

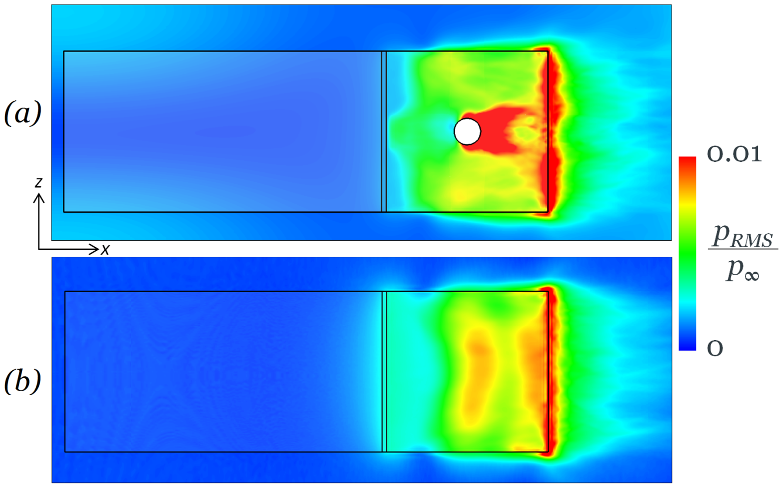

Figure 6.29: Contours of RMS pressure from plane at $y = 0$: (a) covered cavity with strut; (b) baseline (clean) covered cavity

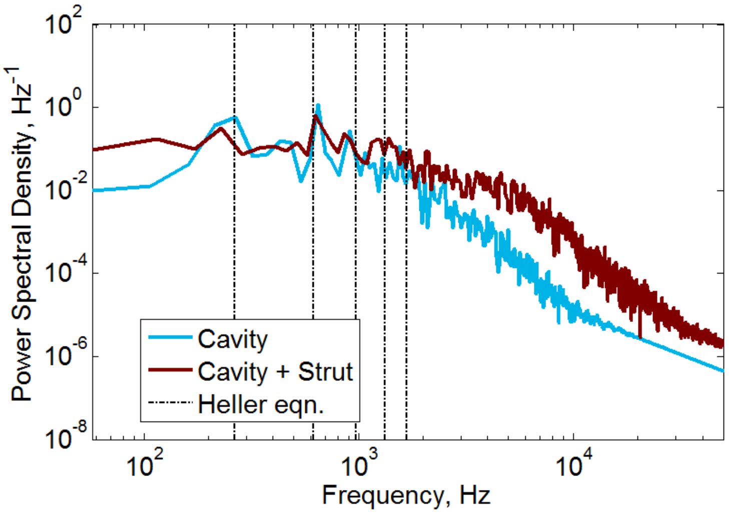

Figure 6.30: PSDs of pressure at monitors at Point 4 ($z = 0, x_{LE} + 0.75D$, as shown in Figure 5.5)

On a plane aligned with the downstream wall of the cavity (i.e. $x = x_{TE}$), contours of mean pressure and streamlines are compared in Figure 6.31. A strong low-velocity region is observed above the cavity and downstream of the strut ($|z| < 0.2D$). However towards the side walls, a fairly similar flow field is observed with and without the strut: flow is diverted up and over the side walls, causing recirculation bubbles of similar sizes.

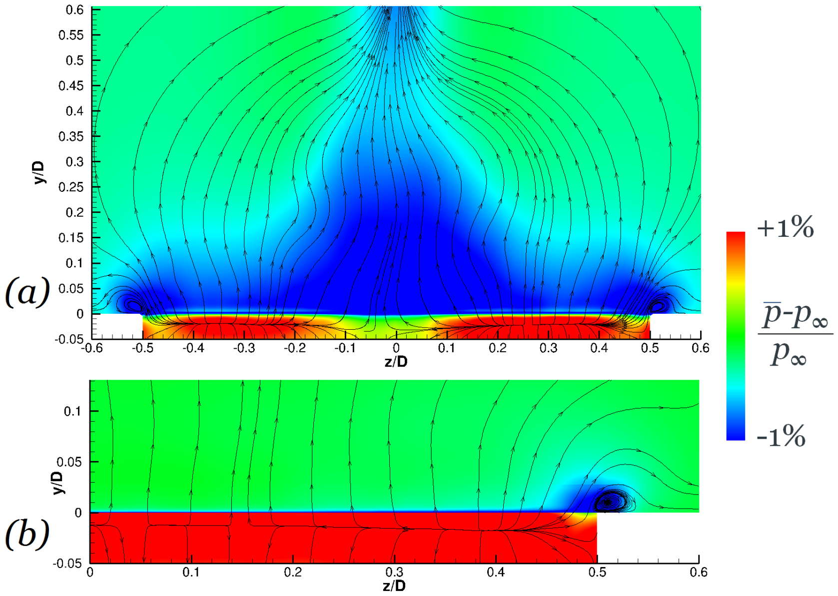

Figure 6.31: Contours of mean pressure, and in-plane mean streamlines, from plane at x_{TE}: (a) covered cavity with strut; (b) baseline (clean) covered cavity

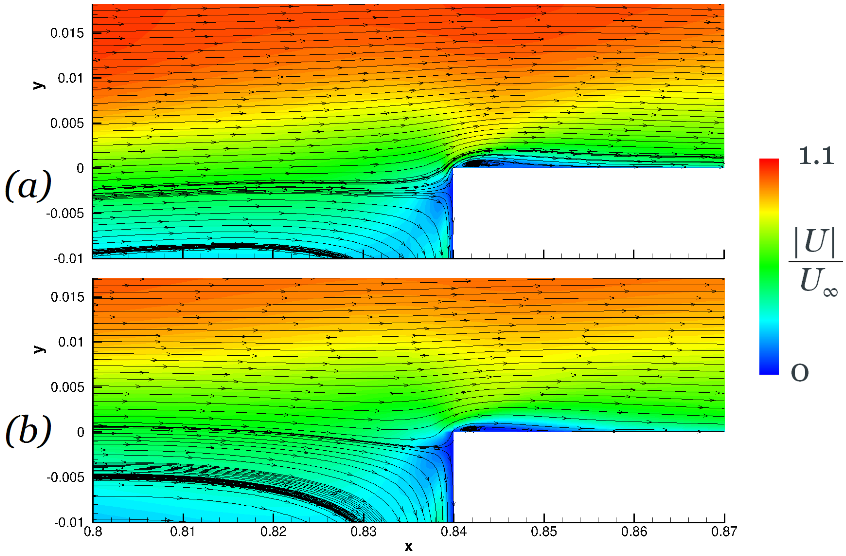

Figure 6.32: Contours of mean velocity magnitude, and in-plane streamlines, from plane at $z = 0.25D$, at the trailing edge of the cavity: (a) covered cavity with strut; (b) baseline (clean) covered cavity

Above the cavity, a large low-pressure region is created downstream of the strut, extending all the way to the side of the cavity. The flow impinging on the downstream wall is diverted upwards and, near the side walls, outwards. Towards the middle the span (but slightly away from $z = 0$, due to the asymmetry in the strut wake discussed earlier), the mean streamlines are directed inwards as well as upwards, towards the low-pressure region in the wake of the strut. The low pressure in the strut wake also causes a significant reduction in the impingement pressure on the top of the downstream wall. Away from this region, the height of the stagnation point (visualized through the dividing streamline between positive and negative vertical flow) is fairly similar between the two cases; slightly lower with the strut, due to the downward deflection of the shear layer. The lower shear layer can also be seen in plots of the mean velocity in the $X - Y$ plane, at $z = 0.25D$ (i.e. halfway between the strut and the side wall), Figure 6.32. The velocity field is otherwise broadly similar, with the flow impinging on the wall and then forming a small recirculation bubble downstream in both cases.

6.7 Comparison of Flow Field Inside the Cavity

Iso-contours of velocity magnitude and streamlines in the $X-Y$ plane are compared across the three cases in Figure 6.33 and Figure 6.34 for $z = 0$ and $z = 0.475D$, respectively. The clean configuration develops a comparatively orderly two-vortex system inside the cavity; one vortex in the open section, and a counter-rotating vortex under the covered section. Near the side ($z = 0.475D$), the covered-section vortex is distorted in shape, but the streamlines still show a circulating flow. With the rear doors, the open-section vortex is fairly similar to the clean configuration in the middle of the span, but the covered-section vortex is less well-defined. Near the side walls, where the door vortices lift the shear layer, the open-section vortex is stretched upwards and downstream. Some of the vortex streamlines are raised out of the cavity, and a secondary core develops towards the downstream edge. The covered-section vortex is distorted by this flow. With the strut, since it extends all the way to the floor of the cavity, the flow-field inside the cavity is even more significantly affected. No coherent covered-section vortex is observed in either plane. In the mid-strut plane (also the mid-span plane, $z = 0$) the open-section vortex is split in two by the strut, with both smaller vortices rotating in the same direction. Near the side wall a single open-section vortex is observed, but of a much smaller size and near the shear layer. Streamlines along the floor of the cavity are able to travel deeper into the covered section, in the absence of a strong open-section vortex to draw the flow back upwards.

Slice planes of the turbulent kinetic energy, at the mid-span plane ($z = 0$), and the mid-x plane in the shear layer ($x = x_{LE}+0.5D$), are compared in Figure 6.35. The introduction of the rear doors, in raising the shear layer, reduces the turbulent kinetic energy downstream of the cavity (as the reattachment is smoother). In the $Y - Z$ plane, the regions of k associated with the separated flow around the doors are visible near the top of the inner sides, and near the base of the outer sides. Inside the cavity, however, the bands of k along the downstream wall and the floor are overall fairly similar with and without the doors. The regions of high k are slightly wider with the clean configuration, likely because the lower shear layer means more of the shear layer unsteadiness is swept into the cavity, but overall the shape and the levels are fairly similar. With the strut, unsurprisingly, much

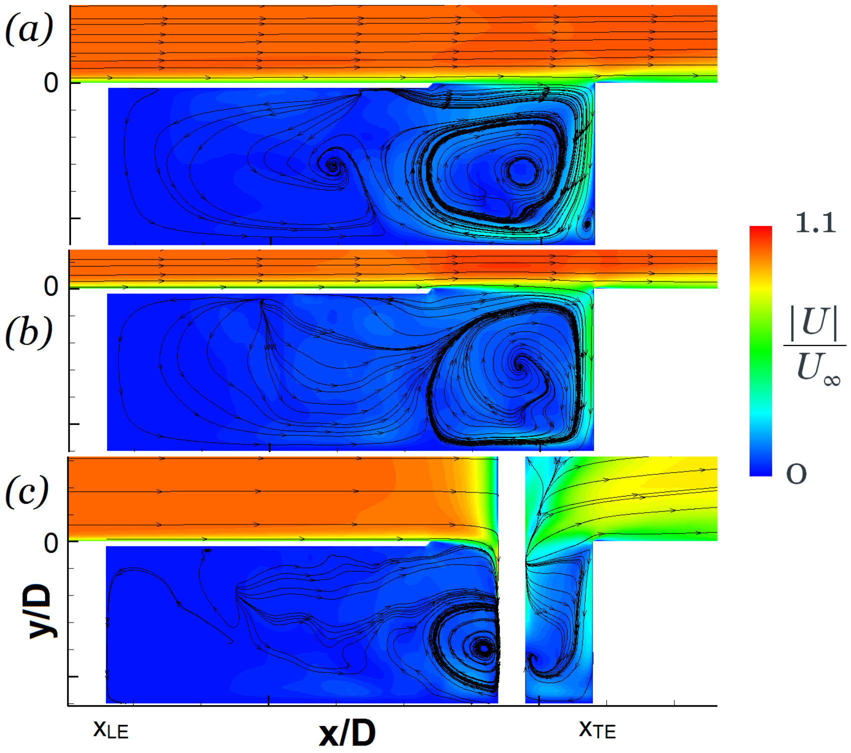

Figure 6.33: Contours of velocity magnitude, and in-plane streamlines, from plane at $z = 0$: (a) baseline (clean) covered cavity; (b) covered cavity with rear doors; (c)covered cavity with strut

higher turbulent kinetic energy develops downstream of the strut in the unsteady wake, causing a big difference at the $z = 0$ plane and in the dowstream half of the shear layer. However, in the upstream half of the shear layer, and even along the floor at $x_{LE} + 0.5D$, the levels of k are comparable to the clean configuration.

The frequency content of the pressure monitors inside the cavity were found to be broadly similar at most locations. In the open section, an example is shown in Figure 6.36 for a point on the downstream wall at $y = -0.75D$ (i.e. three-quarters of the way down) in the mid-span. The case with the strut has higher levels at around 1kHz, due to the wake region downstream of the strut. All three cases have similarly strong mode 2 tones. The strut and the clean configurations have similar mode 1 tones, and the rear-doors and the clean cases have similar secondary mode 3 tones. As observed in the shear layer, the addition of the rear side doors almost completely destroys the mode 1 resonance. The 3.5kHz peak from the interaction of the door shedding with the shear layer ($m = 10$ resonance) is also present, even inside the cavity.

An example of a pressure monitor in the upstream section (halfway down the upstream wall) is shown in Figure 6.37. The overall noisiness in this region is less, so the tones are clearer, but the resonant behaviour is basically the same as at the downstream wall. Comparing all three cases together, it is interesting to note that both the doors and the strut produce additional, smaller peaks at higher modes ($m = 4$ and 6, most visibly), compared to the clean cavity which shows no tones for $m > 3$. The tonal amplitudes are a little higher with the strut, but the same modes appear to be triggered in both geo-

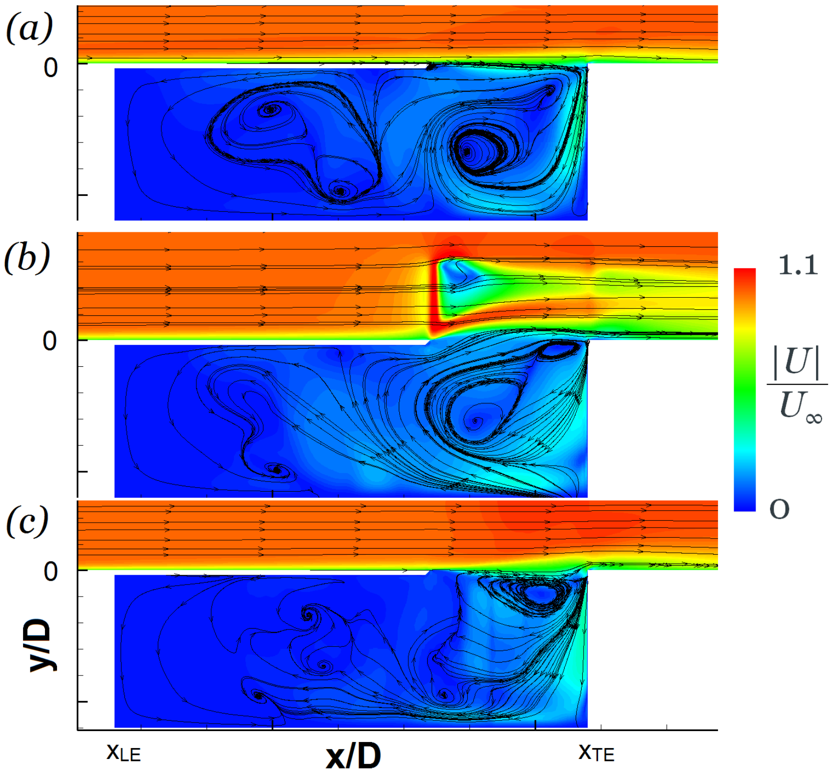

Figure 6.34: Contours of velocity magnitude, and in-plane streamlines, from plane at $z = 0.475D$: (a) baseline (clean) covered cavity; (b) covered cavity with rear doors; (c)covered cavity with strut

metric modifications. Both cases effectively introduces a high-frequency regular pressure perturbation into the upstream part of the shear layer: the doors, through the small-scale vortex shedding; and the strut, through the development of a secondary Rossiter resonance between the shear layer and the upstream strut surface. In spite of these different mechanisms, the frequencies of these additional pressure waves are actually fairly similar ($\approx$ 3.5kHz from the door and $\approx$ 3.2kHz from the strut). It may be concluded, therefore, that the introduction of a pressure wave at this frequency into the shear layer has the effect of producing the extra tones observed in Figure 6.36 and Figure 6.37. Despite the various differences in the shear layer, this is the main effect of the geometry modifications on the frequency response inside the cavity.

The spatial variation of the RMS pressure is shown in Figure 6.38, for planes aligned with the side, floor and downstream walls of the cavity. The highest p_{RMS} on the downstream wall is produced by the clean configuration. The weakest is produced by the case with the rear doors, due to the upward deflection of the shear layer. Overall p_{RMS} levels inside the cavity with the rear doors are also lower. In the span-wise and depth-wise directions (y and z), RMS pressure is generally fairly constant inside the cavity. The main variation is observed in the length direction, with all three cases showing a significant increase in p_{RMS} towards the upstream wall of the cavity. As discussed in Section 5.7.4, this is probably because the flow in this region is the most constrained (by the walls in the three direction), so the build-up of pressure is amplified. The strongest build-up of p_{RMS} is from the clean

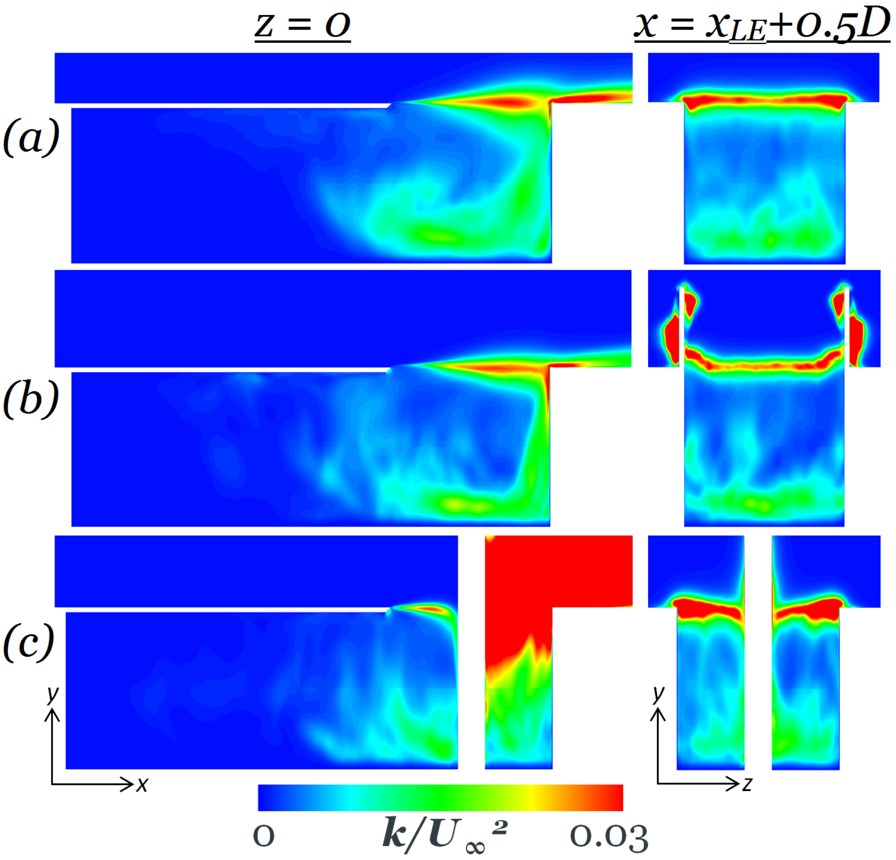

Figure 6.35: Contours of turbulent kinetic energy from planes at $z = 0$ and $x = x_{LE}+0.5D$: (a) baseline (clean) covered cavity; (b) covered cavity with rear doors; (c)covered cavity with strut

configuration, which had the strongest tones (mode 1 and 2) in the shear layer, supporting the idea that the pressure fluctuations inside the cavity are driven by the shear layer. Generally, the p_{RMS} distributions do not show any sign of regularly-spaced vertical bands which would be associated with lengthwise acoustic modes developing inside the cavity. Comparing the frequencies of the N_x modes against the Rossiter modes, the only two that are close are $N_x = 2$ and $m = 3$ (0.95kHz and 0.97kHz respectively). It does not seem likely that this coupling is occuring, as the $m = 3$ mode is weaker than $m = 1, 2$ in most cases, and the p_{RMS} plots do not show the correct shape. Also, instantaneous contours of the perturbation pressure (Figure 6.39) show generally opposite pressure in the upstream and downstream sides of the cavity, the same trend as was observed throughout one f_1 cycle with the clean cavity in Section 5.7.4. If this was an acoustic mode it would be an $N_x = 1$ mode, but that would produce a 470Hz tone, which is not present in the pressure monitors. Therefore, the tones inside the cavity may be attributed to the same mechanism in all three cases, as was shown for the clean cavity in Section 5.7.4: the fluctuations in the shear layer cause an alternating build-up and release of pressure inside the open section; and this induces pressure fluctuations in the covered section, with a phase lag such that the opposite ends of the cavity generally have opposite pressures.

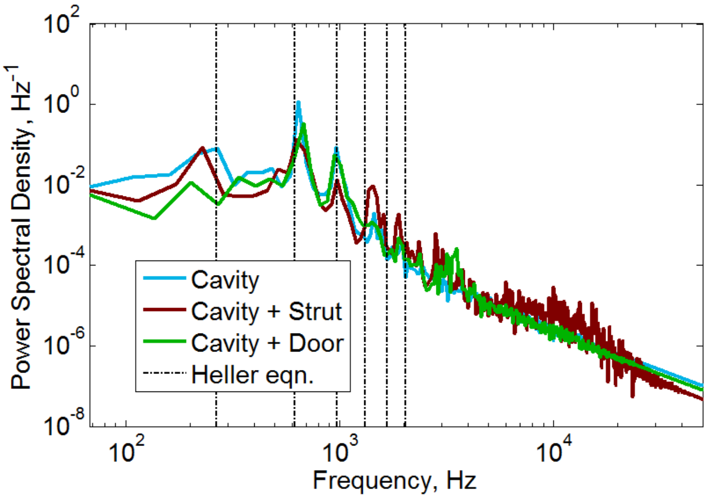

Figure 6.36: PSDs of pressure at monitors at Point 15 ($x = x_{LE}, y = -0.75D$, as shown in Figure 5.5)

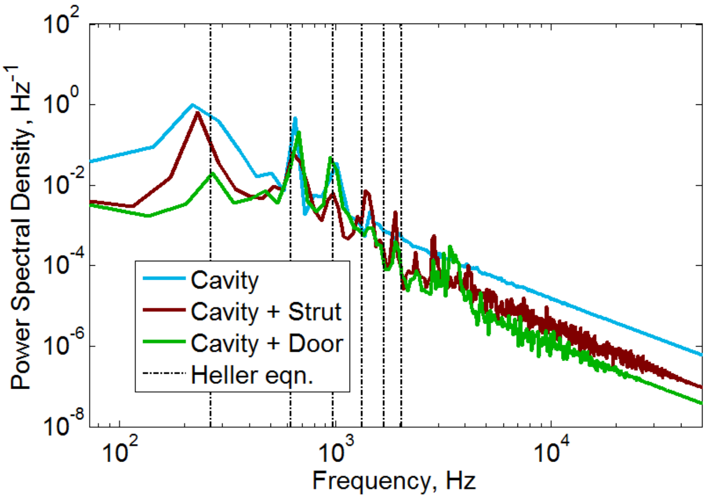

Figure 6.37: PSDs of pressure at monitors at Point 27 ($x = x_{LE} - 2D, y = -0.5D$, as shown in Figure 5.5)

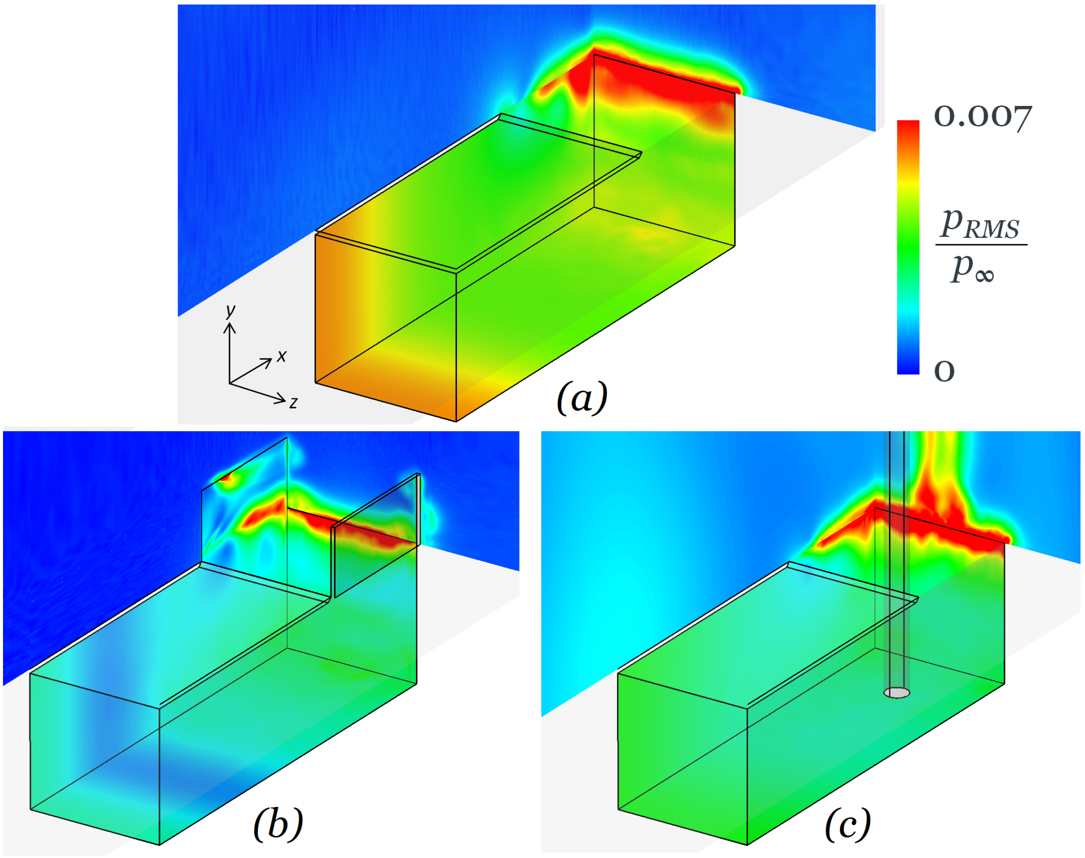

Figure 6.38: Contours of RMS pressure from planes at $(x, y, z) = (x_{TE}, -D, -0.5D)$: (a) baseline (clean) covered cavity; (b) covered cavity with rear doors; (c)covered cavity with strut

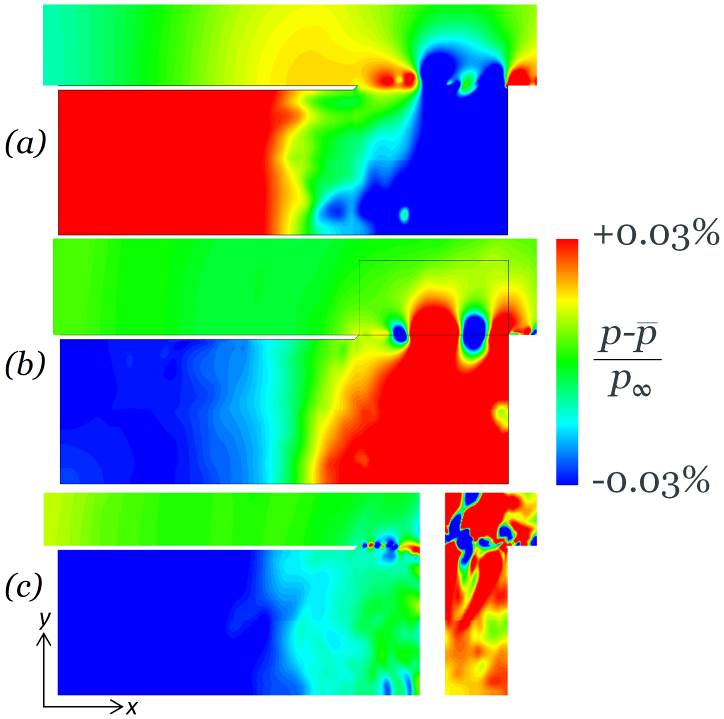

Figure 6.39: Contours of instantaneous perturbation pressure from plane at $z = 0$: (a) baseline (clean) covered cavity; (b) covered cavity with rear doors; (c)covered cavity with strut

6.8 Summary

The effect of introducing rear doors, and of a main central strut, into this covered cavity configuration were explored separately using DDES. The rear doors create small-scale pressure waves from the unsteady separation and vortex shedding around the front of the doors, extending downwards towards the shear layer, and causing a 10^{th}-mode resonance in the shear layer, at $f \approx 3.5$kHz. The mean field from the door vortices were also found to drive the shear layer upwards, especially towards the sides. The strut causes a secondary shear layer resonance between the leading edge of the shear layer and the upstream face of the strut, introducing an additional $f \approx 3.2$kHz frequency into the shear layer. The strut also drives the shear layer downwards. In terms of the resonance, it was found that the same mechanisms cause resonance in all cases: Rossiter modes develop in the shear layer, imposing pressure fluctuations in the open section, which then induce pressure fluctuations in the upstream covered section. A strong mode 2 resonance was observed for all three geometries. A strong mode 1 was also observed from the clean configuration and with the strut, but not with the rear doors. Both the rear doors and the strut were found to produce higher modes, both in the shear layer and inside the cavity, especially visible in the quieter flow inside the cavity. This is attributed to the introduction of small-scale and high-frequency fluctuations into the shear layer from the geometric modifications, which in both cases imposed a perturbation frequency of $f \approx 3$kHz.

Overall, the DDES methodology was successfully applied to more complex geometries. Compared to the clean partially-covered cavity in Chapter 5, a significant effect was observed on the flow, which was then quantified and analyzed. The thesis objective of exploring the unsteady characteristics of the landing gear cavity flow-field, and nearby geometries, has therefore been achieved.

These simulations, and the simulations in Chapters 4 and 5, all used DES analysis. As previously discussed, although this is an efficient method of resolving the separated flow, it simplifies the upstream boundary layer as a steady RANS boundary layer, and therefore is unable to resolve the small-scale turbulence. This is likely to affect the modelling of the cavity flow-field, which is known to be sensitive to the condition of the upstream boundary layer (Section 2.4.5). Therefore the next chapters in this thesis focus on LES, which is able to resolve boundary layer turbulence, to explore how changing this modelling method affects the simulated flow field. Chapter 7 returns to a simple flat-plate boundary layer geometry in order to develop the methodology, and a smaller-scale version of the partially-covered cavity geometry is considered with LES in Chapters 8 and 9.

Chapter 7

LES of Flat Plate Turbulent Boundary Layer

7.1 Overview

As discussed in previous Chapters, the DES approach used thus far has some drawbacks. Most significantly, it is unable to resolve the turbulence in an attached boundary layer flow, and models the flow in those regions as a steady flow field (using a RANS approach). This, in conjunction with the periodic boundary condition in the span, was observed to cause a high degree of spanwise correlation in the cavity shear layer, as was found in Chapter 5; also, the literature review indicated that the cavity flow is sensitive to the details of the upstream boundary layer (Section 2.4.5). The under-prediction of the turbulent kinetic energy at the cavity leading edge when using DES was also discussed in Section 4.3.

Therefore, there is interest in developing and validating an LES approach, with more accurate resolution of the boundary layer. This Chapter details a numerical modelling study to this purpose. A turbulent flat plate with zero pressure gradient is selected as a test case, as this is the geometry upstream of the simplified partially-covered cavity used in Chapters 5 and 6. Also, this test case has been well studied in the literature as a standard benchmark, so there is high-quality experimental and numerical (DNS) data available for validating against. Thus the purpose of this chapter is to develop guidelines for the use of LES to fully and accurately resolve a turbulent flat-plate boundary layer. This addresses the research objective of developing an efficient LES methodology for resolving turbulent boundary layer flow.

The test configuration is a zero-pressure-gradient flat plate at subsonic speeds ($M = 0.25$), using wall-resolved LES, with an artificial trigger for laminar-turbulent transition. The effect of grid, timestep and LES model on the 3D turbulent flat plate LES simulation are investigated using the SotonCAA solver. Results were validated against experimental and DNS measurements from the literature. The guidelines developed based on the numerical parameter study in this Chapter will then be applied to a partially-covered cavity geometry (similar to that of Chapter 5) in Chapters 8 and 9.

7.2 Geometry and Setup

7.2.1 Geometry

The freestream Mach number was set at $M_\infty = 0.25$, the same as the covered-cavity simulations, in the middle of the range of interest for landing gear flows. A plate length L of 0.15m was selected for test purposes which, using standard properties of air, corresponded to a plate Reynolds number $Re_L = 8 \times 10^5$. This is comparable to the developing boundary layer upstream of the nose landing gear on an experimental scale civil aircraft (1/15$^{\mathrm{th}}$-scale), which would be around $Re_L = 1.5 \times 10^6$. Some earlier tests were also performed using $M_\infty = 0.20$ and $L = 0.40$m ($Re_L = 1.8 \times 10^6$). Similar trends were observed for both configurations. In terms of the momentum thickness Reynolds number (Re_θ), an important parameter in characterising boundary layer flow, the simulation scale allows comparison with the experimental and numerical (DNS) data from the literature at $Re_\theta = 1000$, which has been well studied [38, 40]. It was observed from the simulations that $Re_\theta = 1000$ generally occurred at $x \approx 0.5L$ (i.e. about halfway across the plate), equivalent to $150\delta_0$ downstream of the inlet, which gives a local value of $Re_x = 4 \times 10^5$.

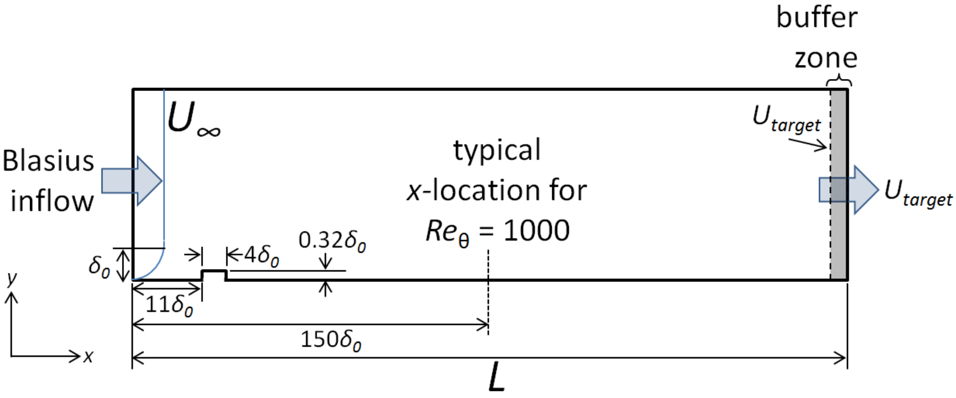

Figure 7.1: Schematic of $X - Y$ geometry for 3D LES simulations, including transition step as described in Section 7.3.

7.2.2 Boundary Conditions and Simulation Settings

The $X - Y$ geometry is shown in Figure 7.1. An inflow velocity profile is imposed at the upstream edge, ranging from 0 at the wall to U_∞ outside the prescribed boundary layer thickness δ_0. A no-slip wall is used across the floor to represent the wall. The boundary layer flow passes over a small step, using the step tripping method to impose bypass transition to turbulence described in Section 2.3.3. At the outflow the buffer-zone method is used, where U_{target} values for the outflow were obtained from mean values at $0.015L$ upstream of the outflow. Plots of the boundary layer growth across the plate (discussed in Section 7.6) demonstrated only a small deviation towards the trailing edge, confirming that the outflow boundary condition does not unduly influence the flow in the domain.

All simulations were performed using SotonCAA, with the same spatial schemes described in Section 3.4 and the 6^{th}-order implicit filter [109], with cutoff wavenumber κ_C ranging between 0.60 and 0.80, generally set at 0.70 unless otherwise specified. The LES methodology is used, modified to implement the SISM subgrid-scale model, which was selected as being the most appropriate for this boundary layer application. The standard Smagorinksy model was also tested.

7.2.3 Baseline Mesh Settings

The mesh topology had uniform spacing in x and in z, growing in y with a geometric growth rate of 2% up to the height of the step and 3% afterwards, as used by Berland et al [46]. For the main $M_\infty = 0.25$ simulations, the cell sizes gave $\Delta x^+ = 58$, $\Delta y^+ = 1$ and $\Delta z^+ = 17$. The earlier $M_\infty = 0.20$ simulations used a baseline mesh with $\Delta x^+ = 66$, $\Delta y^+ = 1$ and $\Delta z^+ = 21$.

The grid spacing was uniform in z, and periodic boundary conditions were applied in the span. The span (in the z direction) length was set at $L_z = 14\delta_0$, resulting in $N_z = 100$ for the baseline simulation. Berland et al [46] used the same spanwise resolution and boundary condition, and their results were found to be in good agreement with the literature, with no detrimental interaction observed between the periodic span boundary and the spanwise flow development. The effect of L_z was also tested using the earlier $M_\infty = 0.20$ configuration. In terms of inner scaling ('plus' units), $L_z^+ = 830$ and 2000 were compared, and very little difference was observed in the resultant mean and RMS velocity profiles. The length for the baseline $M_\infty = 0.25$ simulation equates to $L_z^+ = 1750$, which should therefore be more than enough to allow spanwise structures to properly develop.

7.3 Transition to Turbulence

As discussed in Section 2.3.3, the numerical transition method used in this study will be the small step as advocated by Berland et al [46] and Gloerfelt [42]. A diagram of the method is shown in Figure 7.2, and the same setup is used in the present geometry (Figure 7.1). Instead of the freestream inflow used in Section 4.2, a laminar velocity profile is imposed at the inflow, using the Blasius velocity profile for a given boundary layer thickness δ_0:

$$\frac{u}{U_\infty} = \begin{cases} (y/\delta_0) \times (2 - 2\,(y/\delta_0)^2 + (y/\delta_0)^3), & y < \delta_0 \\ 1, \quad y > \delta_0 \end{cases} \tag{7.1}$$

The value of δ_0 was set at 5×10^{-4}m, in order to give $Re_\theta \approx 300$, in accordance with [46]. The total plate length and domain height are $300\delta_0$ and $60\delta_0$ respectively. A step is imposed slightly dowstream of the inflow, extending through the full span (z) of the domain, beginning at $x/\delta = 11$ with a width of 4δ. The height used by Berland et al [46] was $0.14\delta_0$, but in this study it was found that the transition mechanism was more reliable with a height of $0.32\delta_0$. The initial flow-field is seeded with random perturbations in v, which are then allowed to diffuse out with time; no perturbations are required in the inflow velocity, thus eliminating the spurious noise often caused by inflow perturbations. Since the authors of [46] did not specify a form for the initial pertubations, this study used random y-velocity perturbations, independant at each grid point, taken from a uniform probability distribution function (i.e. all values in the range are equally likely), with a range [-0.30U_∞, 0.30U_∞]. (This probability distribution results in a mean perturbation velocity $v_{pert} = 0$ with a standard deviation of $0.17U_\infty$; therefore very few points approach the extents of the nominal range.)

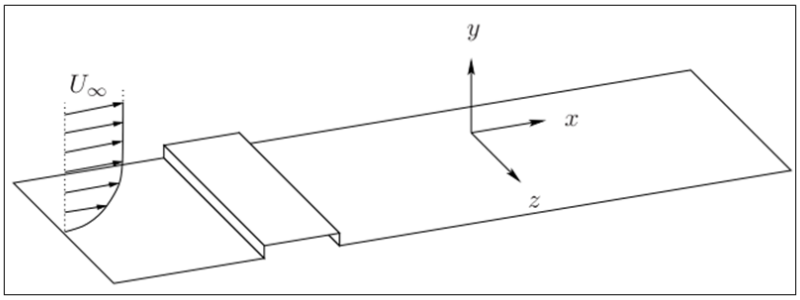

Figure 7.2: Schematic of flow tripping technique using small step; reproduced from Berland et al [46]

Defining a reference time T^* based on the plate length L and U_∞, it was found that within $t/T^* \approx 0.01$, the perturbations had dissipated out of the flow field. Using the inital step height of $0.14\delta_0$, the flow-field had settled into a smooth laminar boundary layer by $t/T^* = 0.30$. Increasing the step height to $0.32\delta_0$, the perturbations had also dissipated by around $t/T^* \approx 0.01$, but now boundary-layer turbulence was observed to develop downstream of the step. By $t/T^* \approx 1$ the entire boundary layer downstream of the step was found to be turbulent. An example of this is shown in Figure 7.3, where the boundary layer vortex structures are illustrated by means of iso-surfaces of the Q-criterion.

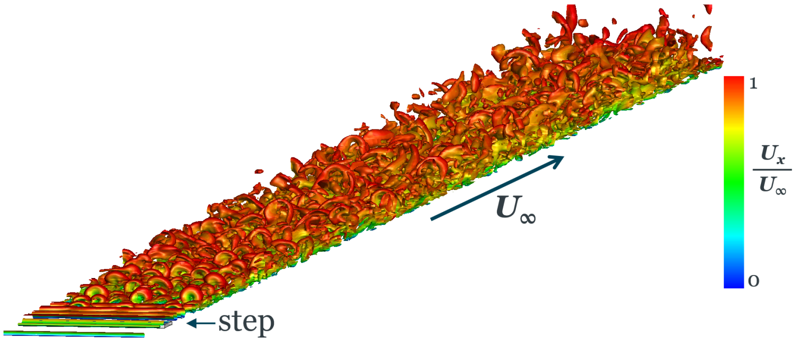

Figure 7.3: Turbulent boundary layer structures developing downstream of tall step ($0.32\delta_0$) with initial-field perturbations, visualized using iso-surface of Q-criterion

As an alternative, simulations were performed using the original step height of $0.14\delta_0$ and small inflow perturbations. These perturbations were also imposed in the v-velocity, but were deterministic (unlike the random perturbations used in the initial field), varying sinusoidally in the span direction with a maximum amplitude of $0.1U_\infty$, and Gaussian scaling in the vertical direction with a peak at $y = 0.3\delta_0$ and standard deviation of $0.50\delta_0$. A sinusoidal variation was also used in time. The frequency was selected following the method of Inoue et al [123], who found that the mixing layers were most strongly tripped using a frequency f based on $f * \theta/(U_1 + U_2) \approx 0.02$; in this case U_1 was taken as U_∞ and $U_2 = 0$.

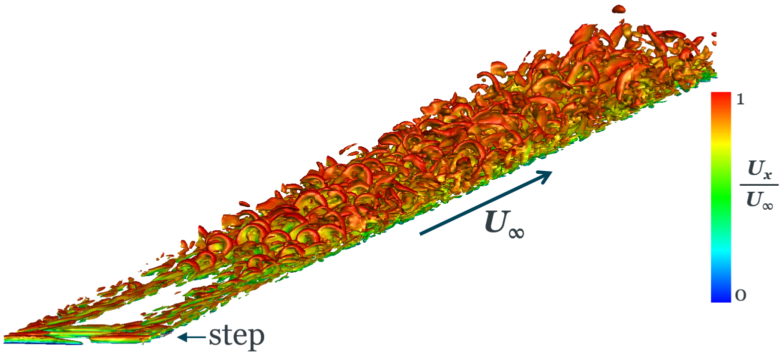

Figure 7.4: Turbulent boundary layer structures developing downstream of shorter step $(0.14\delta_0)$ with inflow perturbations, visualized using iso-surface of Q-criterion

An example of the boundary layer structures is show in Figure 7.4. A turbulent boundary layer is clearly also generated, but the development length is longer than with the taller step and no inflow perturbations. Comparison of the mean and RMS velocity profiles downstream of the step found that at $x/L > 0.50$ the two methods give identical solutions. This confirms that the taller step does not distort the development of the downstream boundary layer. (Additional tests were also performed using OpenFOAM, removing the step and imposing stronger inflow perturbations, and again the velocity and RMS profiles were eventually found to be identical with and without the step geometry.) The method with the taller step was selected for the rest of this study due to the shorter development length, simplicity of implementation, and the avoidance of inflow perturbations which can cause spurious noise.

The characteristic streaky nature of the near-wall vortical structures can be visualized through the skin friction coefficient $C_{f,x}$ at the wall. An example of the developed $C_{f,x}$ field from the taller strep is given in Figure 7.5. Figure 7.5(a) shows structures developing downstream of the step within about $0.1L$ (i.e. $30\delta_0$), and along the length of the plate. The outflow buffer-zone region ($x/L > 1$) is smoothly similar to the rest of the flow, as desired. Figure 7.5(b) shows a closeup in the vicinity of $x/L = 0.50$, scaled in wall units. The length and spanwise spacing of the streaks, $\approx$ 1000 × 120 in wall units, is broadly consistent with the literature on such flows [34].

These simulations were performed using the SISM subgrid-scale model. Some testing was also performed using the standard Smagorinsky model, as a reference. It was found that even with the taller step, the standard Smagorinsky model exhibited re-laminarization of the flow by $t/T^* = 2$, due to the excessive damping of the model in the near-wall region, as described in Section 3.3.2. However, the Smagorinsky model with the coefficient C_S reduced from 0.16 to $C_S = 0.10$ was able to sustain a turbulent boundary layer with the taller step and initial-field perturbations.

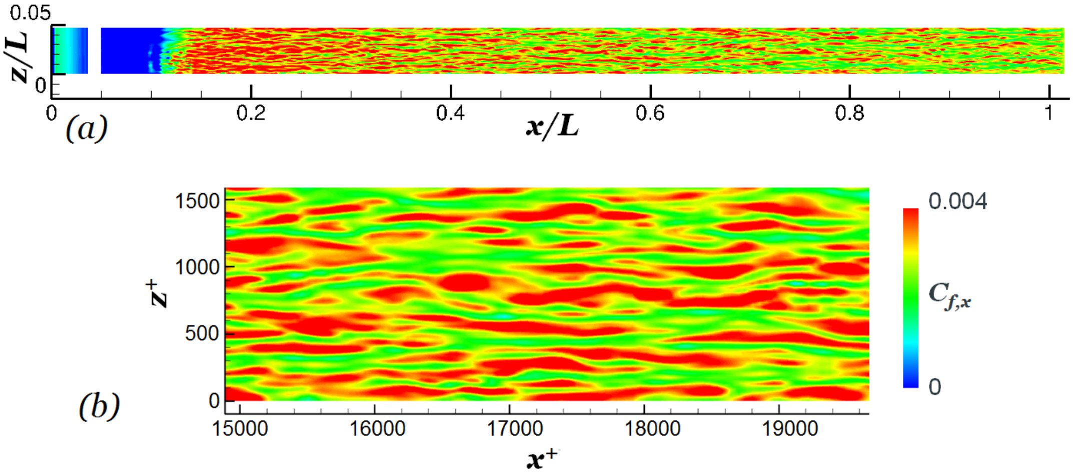

Figure 7.5: Turbulent streaks developing downstream of the taller strep, visualized using contours of skin friction on the wall: (a) over the full length of the plate, plotting scaled by L; (b) close-up near $x/L = 0.50$, plotting in wall units

7.4 Sensitivity to Simulation Parameters and Discretization

7.4.1 Filtering

As mentioned in Section 3.3.2, errors in the numerical scheme and filtering can cause excessive dissipation in the flow field, similar to the effect of the SGS model. To avoid this as much as possible, an implicit filtering scheme is used with ghost points over the block boundaries, which has been shown [109] to produce less damping than explicit filtering schemes. However, the flow field is still sensitive to the filter cutoff wavenumber κ_C, which controls the degree of filtering. The lowest degree of filtering ($\kappa_C \approx 0.90$) was found to cause numerical instabilities in an underdeveloped flow field; however, significantly lowering this value, although improving stability, affects the results. Figure 7.6 illustrates the difference in the mean and RMS velocity profiles with different values of the interior and boundary filter coefficients (κ_C and $\kappa_{C,boundary}$). The best results were obtained with $\kappa_C/\kappa_{C,boundary} = 0.90/0.78$, although this required an initial simulation of $t/T^* = 1.0$ using lower values to stabilize the flow. In all cases, increasing κ_C reduced the over-prediction of u_{RMS} and improved the velocity profile. The highest possible value of κ_C in SotonCAA is 0.95, but testing with a variety of $\kappa_{C,boundary}$ values and initial fields found that it was not possible to go above $\kappa_C = 0.90$ and obtain a stable solution. Therefore, $\kappa_C = 0.90$ is selected as the best compromise between accuracy and stability. However, due to the difficulty in initializing this simulation for stability, for more complex geometries it may be necessary to go to $\kappa_C \approx 0.80$. In this case u_{RMS} will be over-predicted, but this may be a reasonable trade-off for stability, as the behaviour of the flow is not significantly affected.

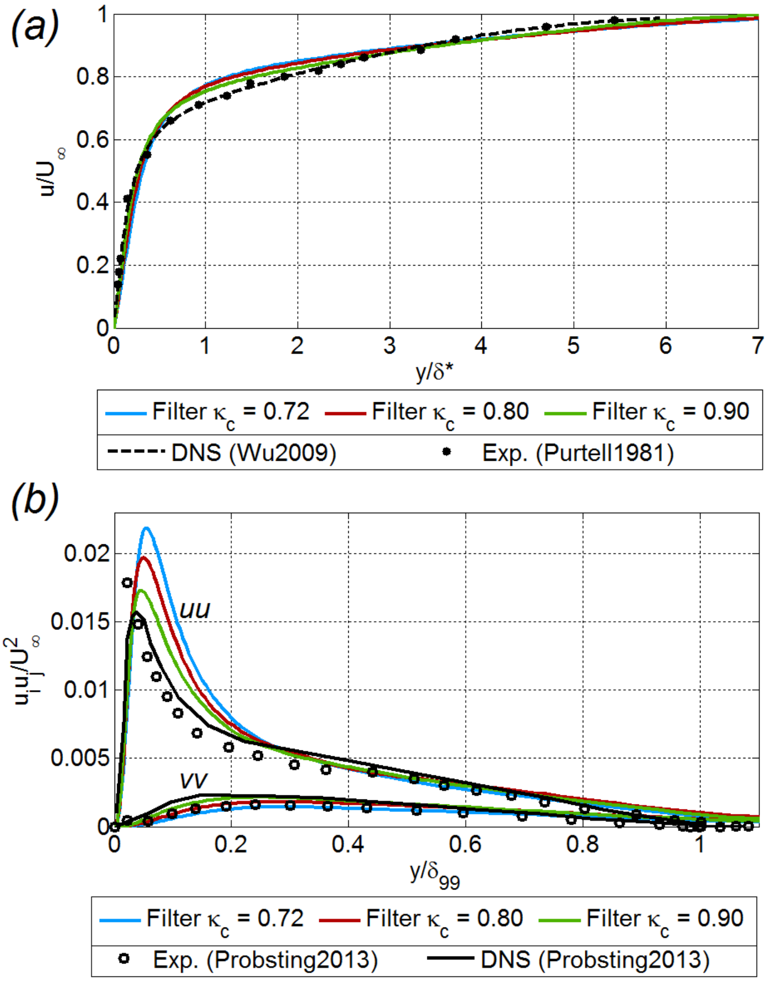

Figure 7.6: Effect of implicit filter cutoff wavenumber κ_C at $Re_\theta = 1000$: (a) mean u-velocity profile; (b) RMS velocity profiles

7.5 SGS Viscosity Model

Viscosity clipping

As discussed in Section 3.3.2, the original implementation of the SISM model involves a clipping of ν_{SGS} if the value goes below zero. However, closer examination of the model showed that this in fact causes a non-zero turbulent viscosity near the wall. Figure 7.7 shows instantaneous plots of the model's turbulent viscosity ratio at $x/L = 0.50$, after the turbulent boundary layer has been fully developed. The span-averaged result is compared with a scatter plot showing the instantaneous variation across the span. It shows that in fact the amplitude of the scatter caused by the turbulence of the flow-field is significant, even in the near-wall (viscous sublayer) region of the simulated flow. With the clipping removed, the average trend has $\nu_t/\nu \approx 0$ near the wall, as desired. This shows that the local mean strain $|\langle\overline{S}\rangle|$ is correctly computed, since the mean trend in ν_t (which is proportional to $|\overline{S}| - |\langle\overline{S}\rangle|$) is close to zero. However, when the negative values in ν_t are omitted, the remaining positive values cause the mean to skew positive. In this case the mean ν_t is primarily a diagnostic tool, as the local ν_t values are what influence the flow field. Still, this suggests there may be some merit in allowing ν_t to go locally negative; although not technically physical, the overall effect could cancel out the effect of locally positive values, to give an overall better estimate of mean (both time-averaged and span-averaged) behaviour in the flow field. To test this, the clipping was removed from the solver and the effect on the simulation was compared, with the same mesh and $\kappa_C = 0.90$. As shown in Figure 7.8, the mean velocity profile is unaffected; however the over-prediction of u_{RMS} is significantly improved, to the point where the peak u_{RMS} value is now an excellent match to the reference DNS data. (The other turbulent quantities are unaffected, but were well predicted with both versions of the model.) The higher average ν_t in the near-wall region, like the lower filter cutoff, may be considered as causing an overly high level of damping of the resolved flow field in the near wall region. The effect on the flow is therefore similar to the effect of lowering the filtering cutoff wavenumber, and it is seen that both cause the same tendency to over-predict u_{RMS} in the results. Therefore, for the remainder of this study, the version of the code with the ν_t clipping omitted will be used.

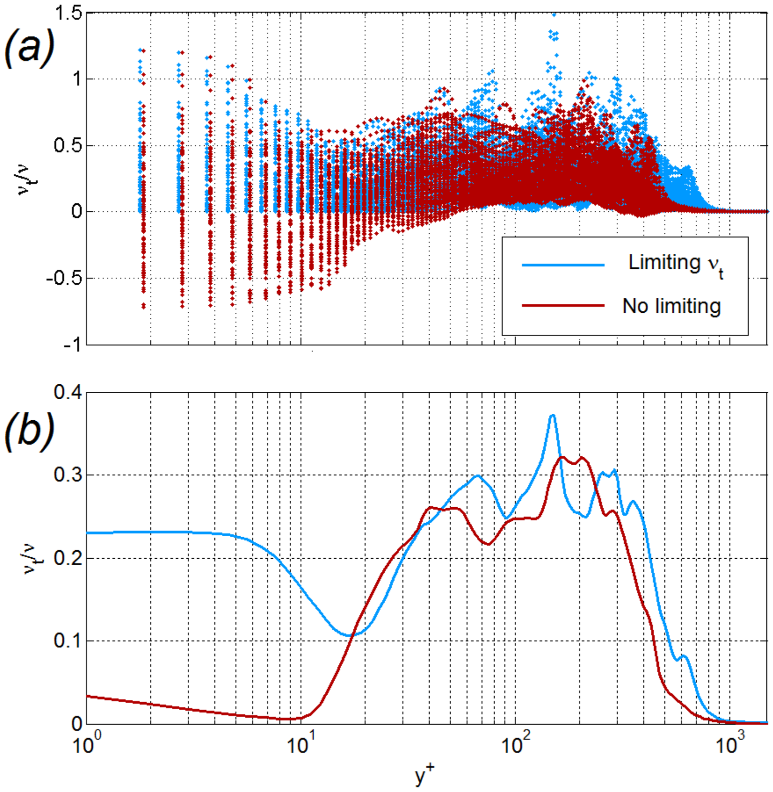

Figure 7.7: Instantaneous computed turbulent viscosity ratio from $x/L = 0.50$; (a) scatter plot showing range of data across z direction; (b) averaged in z direction

Smagorinsky Coefficient

The SISM LES model (Equation 3.10) utilizes the Smagorinsky coefficient C_S, which is generally set to the commonly used value $C_S = 0.16$. However, a number of studies [97, 124, 125] using the standard Smagorinsky model in wall-bounded flow have obtained better results with $C_S = 0.10$. A comparison of the results with these two values is shown in Figure 7.9. The decreased C_S causes a slight improvement in the sharpness of the u_{RMS}

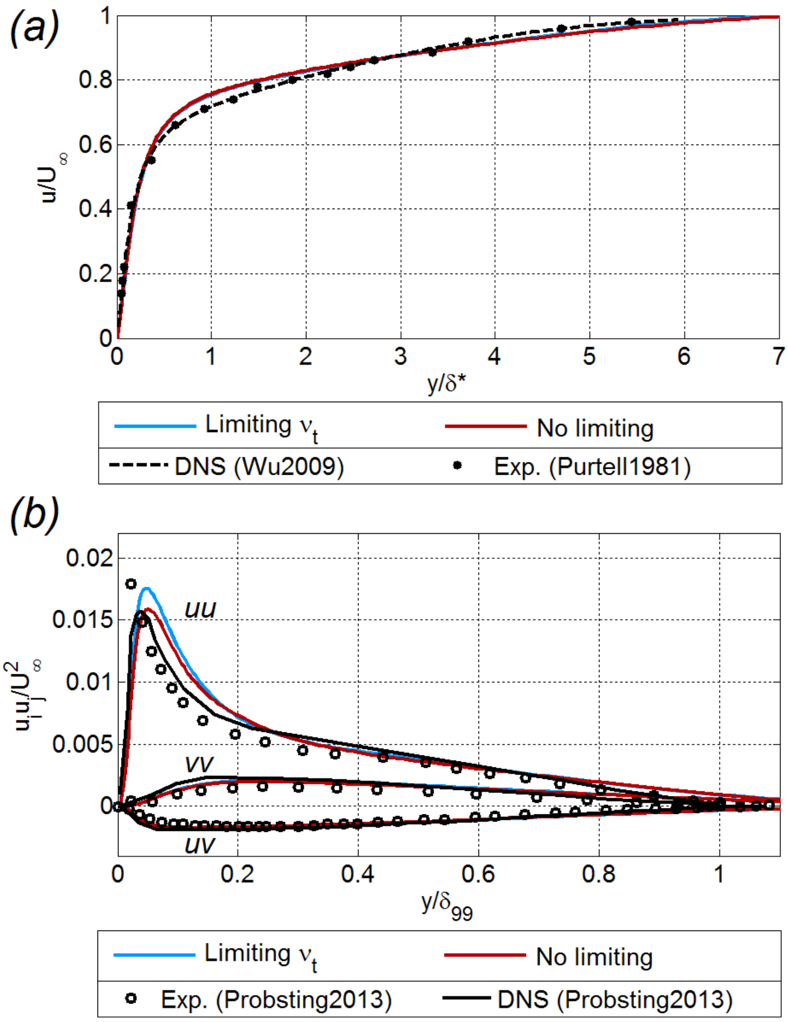

Figure 7.8: Effect of limiting negative values of ν_t to be zero, from averaged data at Re_θ = 1000: (a) mean u-velocity profile; (b) RMS velocity profiles

peak, but the peak u_{RMS} becomes strongly over-predicted. Therefore the standard value of C_S = 0.16 appears to give the best performance. This is consistent with the theory of the model; the authors using C_S = 0.10 with the standard Smagorinsky model were attempting to ameliorate the excessive SGS viscosity in the near-wall region. Since the SISM model does the same job by accounting for the near-wall strain, it was not expected that reducing C_S would be necessary or helpful. Since C_S = 0.16 was recommended on the grounds of giving the best results for turbulence away from the wall region, it is desirable to retain this value. It has also been shown from numerical testing that $C_S \approx 0.18$ produces a subgrid-scale energy dissipation consistent with the Kolmogorov cascade for the energy spectrum [124]. Therefore since the higher value of C_S is more consistent with recommendations from the literature, and it gives a better estimate of the peak u_{RMS} in the present tests, C_S = 0.16 is retained for all further LES simulations.

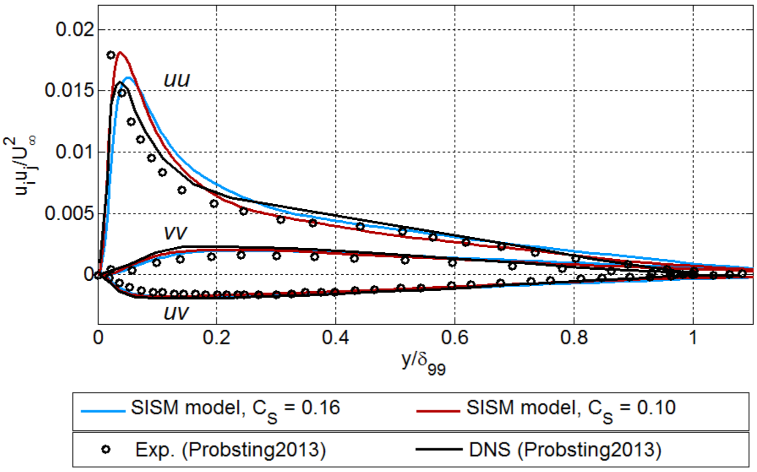

Figure 7.9: Comparison of RMS velocities using SISM model with Smagorinsky coefficient $C_S = 0.16$ and $C_S = 0.10$, at $Re_\theta = 1000$

SISM vs. Standard Smagorinsky

The effect of the SISM modification to the standard Smagorinsky model (with no damping) was further investigated by comparing them directly. As mentioned in Section 7.3, due to the difficulty of the standard Smagorinsky model in sustaining turbulence, the reduced value of $C_S = 0.1$ was used for this comparison. The computational effort (in terms of the wall time per timestep) was found to be similar for both models. Resultant simulation data is shown in Figure 7.10. It is clear that the SISM modification significantly improves the quality of the results, particularly in terms of the height and spread of the u_{RMS} peak. The SGS viscosity profile (instantaneous, but span-averaged) is also illustrated in Figure 7.11. The high near-wall viscosity caused by the standard Smagorinsky model is clearly evident, and the reduction from the SISM model is also shown. It is also shown that in the outer part of the boundary layer, the SISM model recovers ν_{SGS} values similar to the standard Smagorinsky model in this region, as desired. Therefore the SISM modification to the Smagorinsky model appears to be correctly implemented and was found to give a significant improvement in the performance of the model. The values of $\nu_t/\nu \approx 0.1 - 0.2$ in the outer part of the boundary layer is consistent with what has been used with good results for past LES simulations [124, 126].

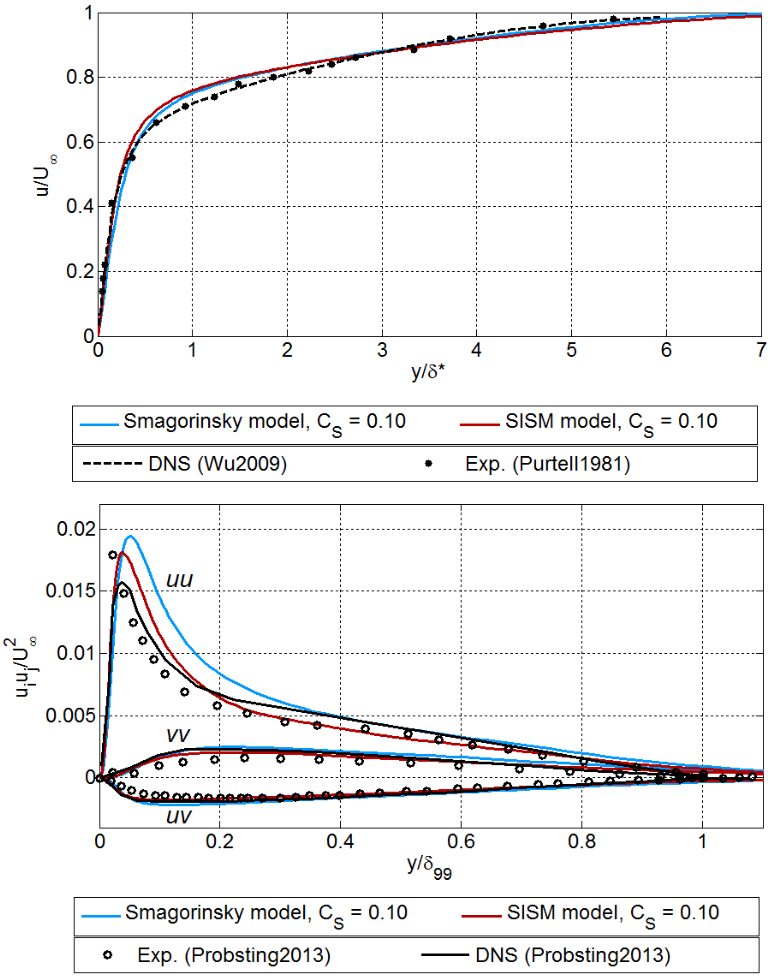

Figure 7.10: Comparison of standard Smagorinsky and SISM LES models at $Re_\theta = 1000$, using $C_S = 0.10$: top: mean u-velocity profile; bottom: RMS velocity profiles

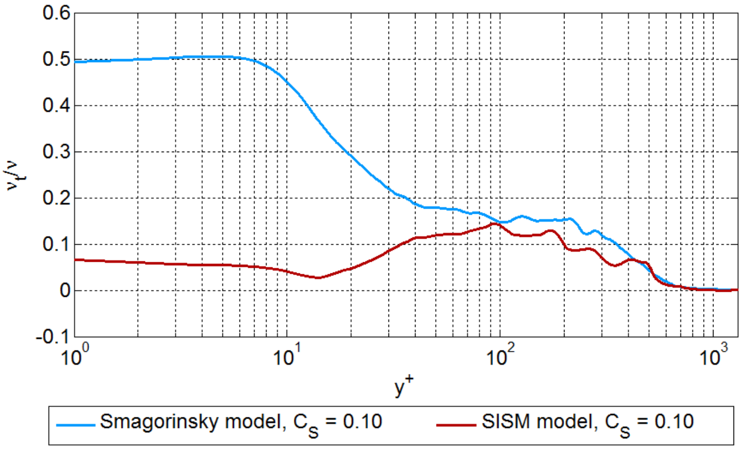

Figure 7.11: SGS velocity profiles, computed using standard Smagorinsky and SISM LES models at $Re_\theta = 1000$.

Lengthscale

So far, the lengthscale Δ used in Equation 3.10 is the cube-root of the cell volume, as has been used with reasonably good results for a variety of LES applications (e.g. [88, 125]). However, the authors of Shur et al [126] found that the cube-root volume gave poorer performance for wall-bounded flows than a proposed alternative, which calculated the lengthscale as a function of both the cell dimensions and the wall distance. They proposed that near the wall, the lengthscale should only be a function of Δx and Δz (to avoid the steep variations caused by the typical growth in Δy); far away from the wall, the maximum cell dimension should be used, which should be similar to the cube-root volume for most LES grids regardless; and in the region between, the lengthscale varies linearly with the wall distance d_w between prescribed limits. This led to the following proposed hybrid lengthscale:

$$\Delta_{Shur} = \min\left\{\max\left(0.15d_w, 0.15\Delta_{max}, \Delta_{wn}\right), \Delta_{max}\right\} \quad \Delta_{max} = \max\left\{\Delta x, \Delta y, \Delta z\right\} \quad (7.2)$$

The cell size in the wall-normal direction Δ_{wn} is equivalent to Δy_1 in this application. A comparison of the resultant RMS velocity profiles is shown in Figure 7.12. There is a small increase in the peak u_{RMS} value, and a slight reduction of the peak width, but overall the two results are very similar. The mean velocity profiles were observed to be nearly identical. It should be noted that the Shur lengthscale requires both the wall-normal distance and the wall-normal direction, which will become more difficult to implement when this geometry is extended to landing-gear bay configurations. Given this increase in complexity, and the small difference in the results, the cube-root lengthscale was selected for the remainder of the simulations, as representing a good balance of accuracy and robustness.

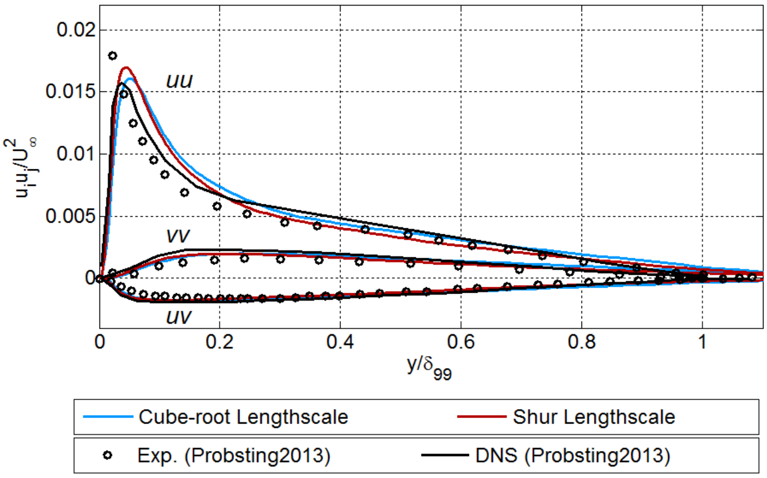

Figure 7.12: Comparison of the RMS velocity profiles $Re_\theta = 1000$, computed using different LES lengthscales.

7.5.1 Temporal resolution

Timestep

The temporal scheme described in Section 3.4 allows the use of CFL numbers greater than 1. For the basic simulations a timestep $\Delta\ t$ of 0.0054s was selected, which corresponds to $T^*/\Delta\ t = 37{,}500$, and a CFL number of 4.0, which was still found to give a stable solution. Time-averaged values were obtained by sampling at every timestep after $t/T^* = 2.0$ (to avoid any start-up transients) for a period of at least $1T^*$. The change in mean and RMS quantities from increasing this averaging window further was found to be within 1% and considered negligible. From early tests with $M_\infty = 0.20$ simulations, the timestep sensitivity was tested using by taking a converged solution computed using CFL = 3.3, halving the timestep, and running for an additional $1.0T^*$. Mean and RMS values computed with the reduced timestep were found to be effectively identical to the original values. For the $M_\infty = 0.25$ simulations, the base timestep with CFL = 4 was compared against a larger timestep with CFL = 5 (i.e. a 20% increase). The mean velocity profiles were also found to be indistinguishable; the RMS quantities (shown Figure 7.13) were found to agree to within 2%. Therefore it can be concluded that the solution is not sensitive to the timestep in this range, and a timestep of CFL ≈ 4 is sufficient to efficiently resolve the temporal characteristics of this flow field.

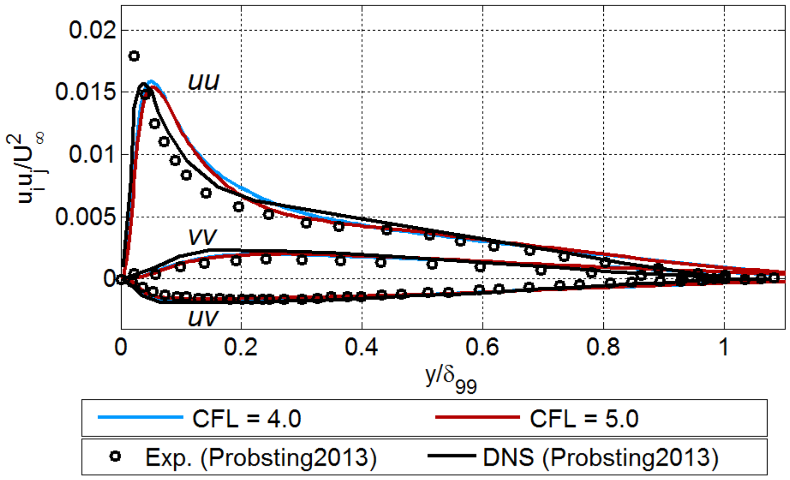

Figure 7.13: Effect of increasing timestep on RMS velocity profiles, computed at $Re_\theta = 1000$

Number of Subiterations in the Implicit Time Scheme

The number of subiterations required to converge a solution is linked to the timestep. The selected timestep of $\Delta t = T^*/37500$ (CFL = 4) may be considered on the larger side for this application, as CFL > 1 is only viable due to the implicit numerical scheme. Previously, simulations were performed using 4 subiterations per timestep, based on general best practice guidelines from other users of this code. A simulation was performed with 6 subiterations per timestep for comparison, and the mean and RMS velocities were found to be indistinguishable between the two cases. Therefore, 4 subiterations with $\Delta t = T^*/37500$

is sufficient resolution of the temporal characteristics of the flow.

7.5.2 Spatial resolution

In order to gain a more complete understanding of the effect of the grid on the LES result, the grid sensitivity in each of the three Cartesian directions was considered separately. Using the older $M_\infty = 0.20$ setup, $\Delta y_1^+ = 1$ and $\Delta y_1^+ = 0.50$ were tested, since the standard procedure for LES is to have $\Delta y_1^+ \leq 1$ [93] . In the finer y-mesh, the number of points across the step height was correspondingly doubled (from 22 to 45), and the density of y-points in the boundary layer was also increased (by keeping the same $N_Y = 68$ above the step, but reducing the spread from $0.125L$ to $0.05L$). The resolution in the other directions was maintained as $\Delta x^+ = 66$ and $\Delta z^+ = 21$ in both meshes. The resultant RMS velocities were was found to be within 5% after the flow had developed. Therefore, $\Delta y_1^+ = 1$ is sufficient resolution for this study.

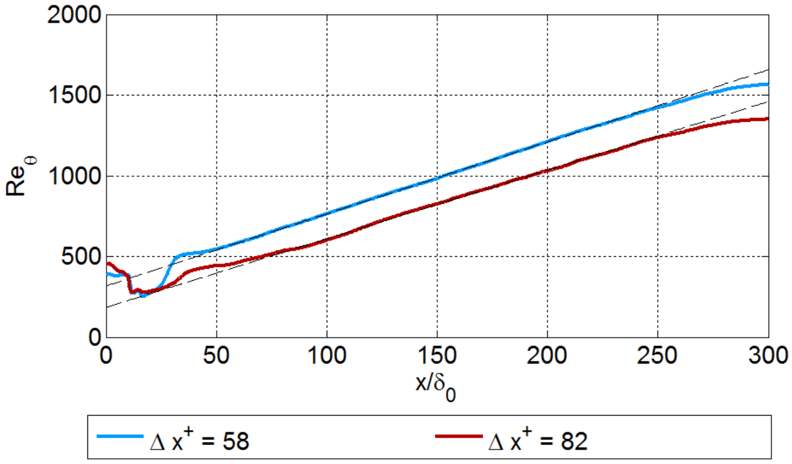

Figure 7.14: Effect of x-resolution on growth of boundary layer momentum thickenss

The streamwise (x) resolution (Δx^+) was tested using both $M_\infty = 0.20$ and $M_\infty = 0.25$. With the $M_\infty = 0.20$ setup, with Δy^+ and Δz^+ unchanged, x cell sizes corresponding to $\Delta x^+ = 66$ and $\Delta x^+ = 40$ were compared (both within the standard range for an LES mesh [93]). The resultant mean and RMS velocity profiles were found to agree to within 2%. For the $M_\infty = 0.25$ setup, $\Delta x^+ = 58$ and 82 were compared, with $\Delta z^+ = 25$. The boundary layer thickness was found to be lower with the coarser mesh, although exhibiting the same growth rate with x (Figure 7.14). For comparison, slices were taken at the x-locations which corresponded to $Re_\theta \approx 1000$ (which occurred slightly further downstream for the coarser mesh). The resultant mean and RMS velocity profiles (Figure 7.15) were found to be virtually identical. Therefore, it is concluded that for $M_\infty = 0.20 - 0.25$, $\Delta x^+ \approx 60 - 80$ gives appropriate resolution of the turbulent boundary layer. $\Delta x^+ = 58$ was retained for the flat plate validation case, but for extending to more complex geometries $\Delta x^+ \approx 80$ may be used to reduce mesh size without compromising solution quality.

The spanwise resolution was tested with the $M_\infty = 0.25$ setup, using $\Delta x^+ = 58$ and comparing $\Delta z^+ = 17$ and 25 (i.e. a 40% increase in mesh size). The boundary layer

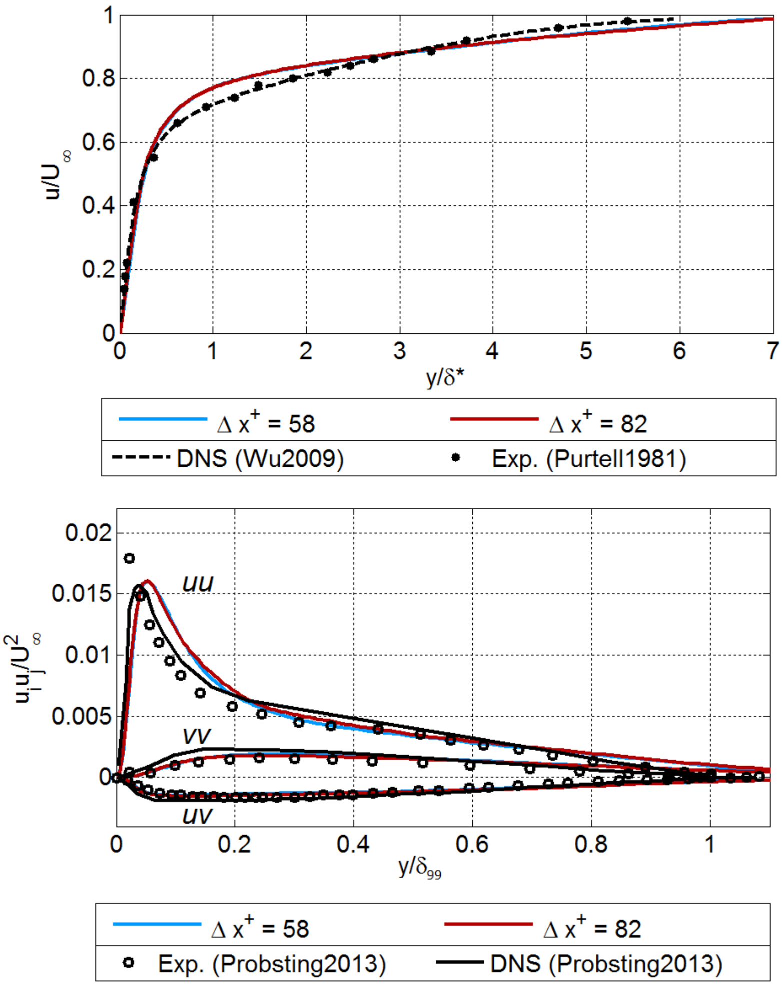

Figure 7.15: Effect of x-resolution on RMS velocity profiles at $Re_\theta = 1000$

thickness (Figure 7.16) was observed to be fairly similar, although the growth rate (slope of Re_θ against x/δ_0) is reduced by 14%. (This is an interesting contrast to the effect of the x-resolution, where the curve was offset downwards but the growth rate was identical.) Taking slices at $Re_\theta \approx 1000$ ($x/L = 0.50$ in both cases), the mean and RMS velocity profiles are compared in Figure 7.17. The finer mesh gives a very slight improvement in the mean velocity profile (of the order of 1%). The peak u_{RMS} is the same in both grids, and the u_{RMS} profiles are within 3% (relative to the peak value) of each other; the v_{RMS} and uv profiles are effectively identical. Therefore, although the spanwise resolution was found to affect the growth of the boundary layer thickness, the flow structures within the boundary layer are suitably resolved with $\Delta z^+ = 17$ and 25. As with the x-resolution, the finer mesh is retained for the flat plate boundary layer validation, but $\Delta z^+ = 25$ may be considered sufficient resolution for more complex geometries where mesh size is a limiting factor.

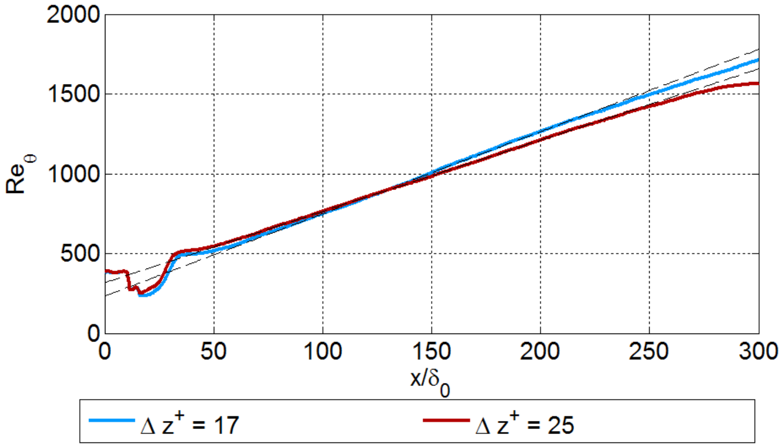

Figure 7.16: Effect of z-resolution on growth of boundary layer momentum thickenss

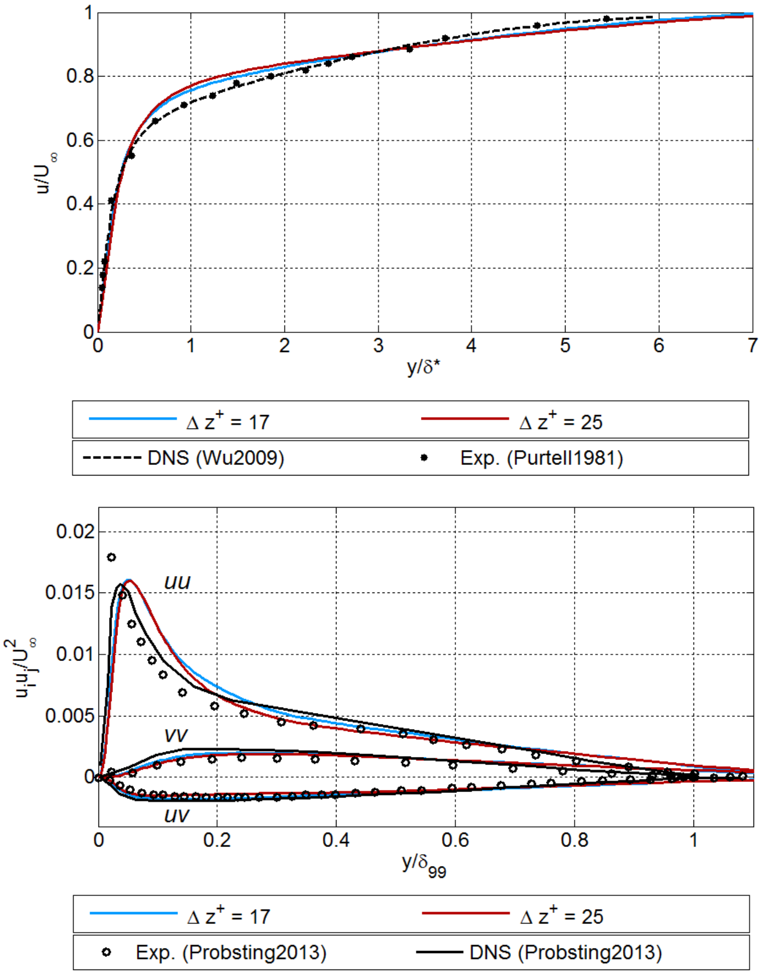

Figure 7.17: Effect of z-resolution at $Re_\theta = 1000$; top: mean u-velocity profile; bottom: RMS velocity profiles

7.6 Validation of Best-Practice Simulation data

This section evaluates the performance of the LES simulation using the filtering and mesh parameters selected based on comparisons in the previous sections. Qualitatively, the development of boundary layer turbulent structures is illustrated in Figure 7.3. It is clear that structures are growing in the downstream direction, as expected. The growth of the turbulent boundary layer may be more accurately quantified by computing the evolution of the momentum thickness θ. From the time-averaged flow field (omitting the start-up transients), eight z-slices were extracted from the flow field and averaged to create a mean $X-Y$ flow field. (Tests with fewer slices indicated that the span-averaging has converged with this many slices, as there is already minimal spanwise variation in the time-averaged flow field.) The computed momentum thickness Reynolds number is plotted in Figure 7.18. It is seen that the results follow a linear trend, as expected [46]. The slope of 5.2 (Re_θ against x/δ_0) is in excellent agreement with previous LES simulations in the literature; Lund et al [127] also obtained a slope of 5.2, and Berland et al [46] computed a similar value of 5.5.

Figure 7.19 shows the development of the shape factor H_{12} as evaluated from the present LES, over the developed region of the boundary layer ($x/L = 0.15$ to 0.99, to avoid the development region near the step, and the outflow). This data is compared against DNS data [29] and the correlation of Monkewitz et al [32], and the agreement is very good. The shape factor is within 4% of the values from the literature across the length of the plate, and the slope of H_{12} against Re_θ is very well captured. Therefore, it may be concluded that the LES simulation is correctly modelling the spatial development of the boundary layer.

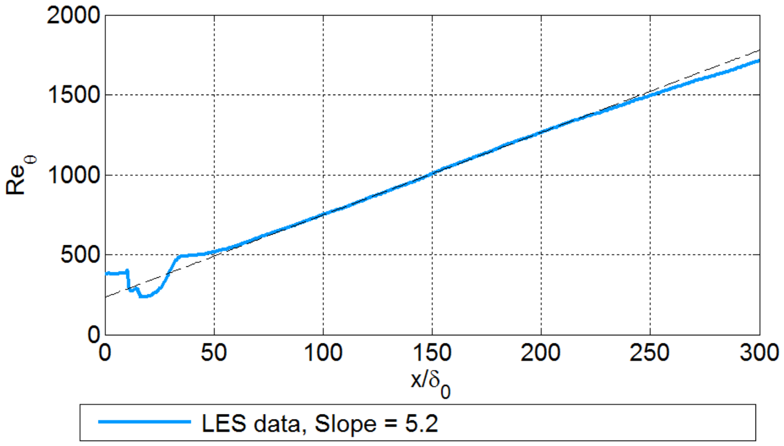

Figure 7.18: Growth of boundary layer momentum thickness, computed from time-averaged and span-averaged LES flow field.

The local velocity and RMS profiles at $Re_\theta = 1000$ ($x/L = 0.50$), in outer scaling (i.e. with δ and U_∞) are shown in Figure 7.20. The mean velocity profile is within 5% of the experiment and literature [38,40,128], and the RMS quantities are very well predicted; the peak u_{RMS} magnitude is within 2% of the experimental and DNS data from Probsting et al [40], and the peak location is also within $0.01\delta_{99}$ of that data. The vv and uv

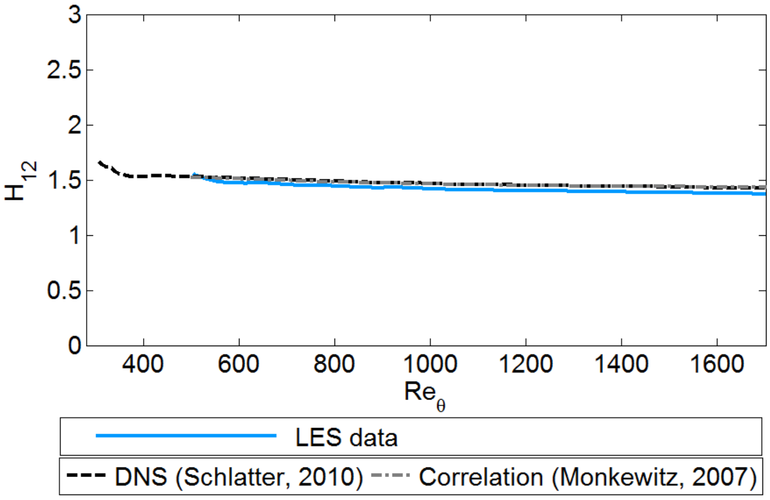

Figure 7.19: Development of boundary layer shape factor H_{12}, computed from time-averaged and span-averaged LES flow field, and compared with data from [29] and [32].

components are likewise very well predicted. Cuts taken further downstream, and as far upstream as $x/L = 0.20$, show that the profile shapes are similar and that the boundary layer is therefore fully developed.

The same simulation data is presented in inner scaling in Figure 7.21. The agreement with the analytical profiles (as described from Section 2.3) and DNS data (from [38]) is not as good; the mean velocity in the log-region is over-predicted, as are all the RMS velocity components, especially u_{RMS}. However it is noted that the general shapes are correct. Since the profiles matched well in outer scaling, it seems unlikely that the discrepancy in Figure 7.21 is due to significant inaccuracies through the boundary layer. It is more likely that the dimensionless wall units used for the inner scaling are inaccurate, as they are calculated directly from the wall shear stress, which is notoriously difficult to predict correctly using LES (e.g. [129]).

This is confirmed by assessing the skin friction coefficient $C_{f,x}$ and the friction velocity u_τ. The distribution of the skin friction coefficient along the plate is presented in Figure 7.22, comparing the present LES results against the Schlichting empirical curve for a turbulent boundary layer (Equation 2.2) and the skin friction profile for a Blasius (laminar) boundary layer [28]. Downstream of the step, the skin friction from the LES (as calculated from the near-wall flow field) increases significantly above that of a laminar boundary layer, due to the transition to turbulence. However, the values are still under-predicted relative to the turbulent profile.

In terms of the friction velocity, the simulation gives $u_\tau = 3.53m/s$; however, Equation 2.2 [28] predicts $u_\tau = 3.99m/s$. Therefore the LES under-predicts u_τ by 11%, which will thus affect the scaling of y^+ and u^+. Repeating the analysis using the Schlicting u_τ (instead of the calculated value), finds the LES data collapsing quite well on the DNS and analytical data (Figure 7.23).

The solution settings described in the previous sections were also assessed for their effect on the under-prediction of wall shear stress, but but none were found to fully recover the desired value. Moving from the standard Smagorinsky to the SISM model caused an

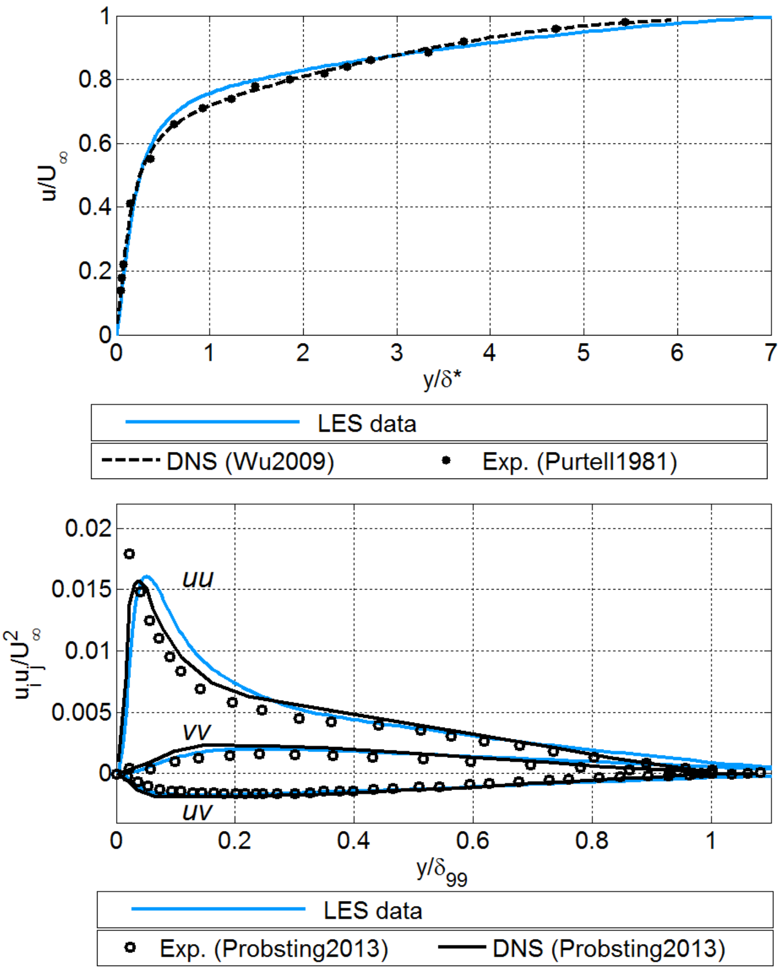

Figure 7.20: Comparison of LES data with experimental and DNS data [38, 40, 128] in outer scaling; top: mean u-velocity profile; bottom: RMS velocity profiles.

increase in u_τ of 9%, further confirming the superior performance of the SISM model to the standard Smagorinsky for this application. Decreasing the z-resolution was observed to slightly decrease (i.e. worsen) u_τ by 3%; similarly decreasing the x-resolution was found to decrease u_τ by 3%. In both cases, as shown in Section 7.5.2, the profiles in outer scaling exhibited very little difference.

It may thus be inferred that it might be possible to correctly estimate the wall shear stress (and therefore the inner-scaling units) by further increasing the grid resolution. However, the other characteristics of the boundary layer are unlikely to change, and are already well predicted. It should also be noted that significantly further reducing the cell sizes will begin to bring the resolution into DNS territory, which is outside of the scope of this study. Additionally, the purpose of this LES study was primarily to provide realistic boundary layer flow for feeding upstream of a landing gear cavity. The forces on the upstream wall (i.e. the shear stress) is of less importance, given that the turbulent structures are well resolved. For these reasons, a decision was made to retain the mesh and numerical parameters described in this chapter as the ‘best practice’ for this application, and to apply these as closely as possible to the more complex cavity flow field.

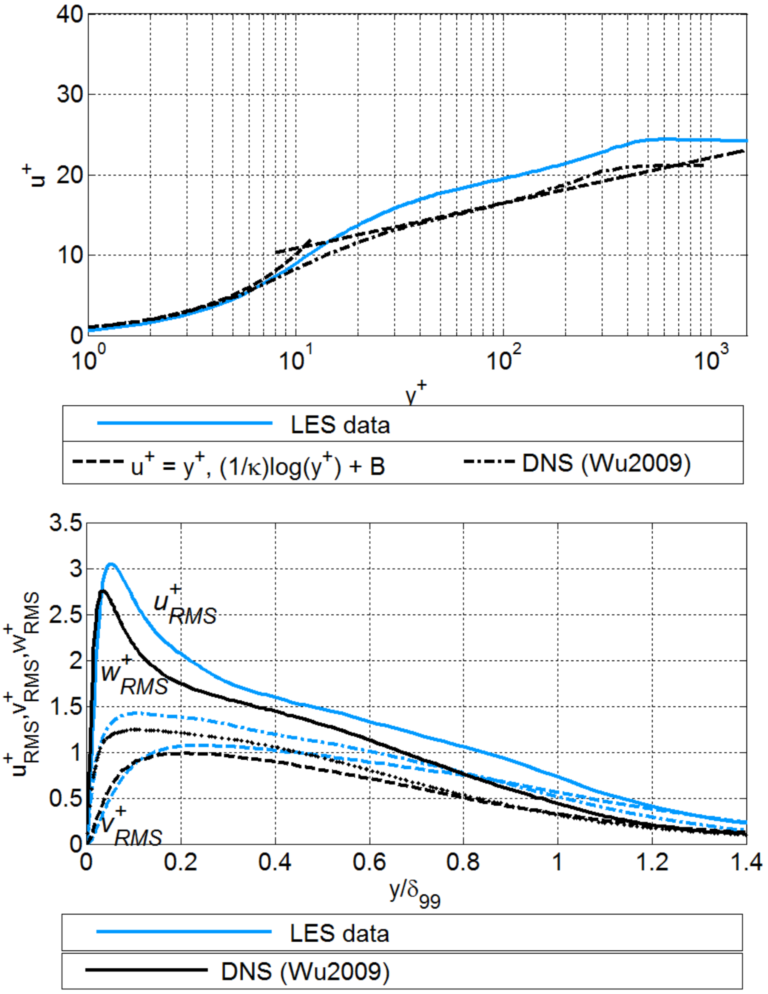

Figure 7.21: Comparison of LES data with DNS data [38] in inner scaling; top: mean u-velocity profile; bottom: RMS velocity profiles.

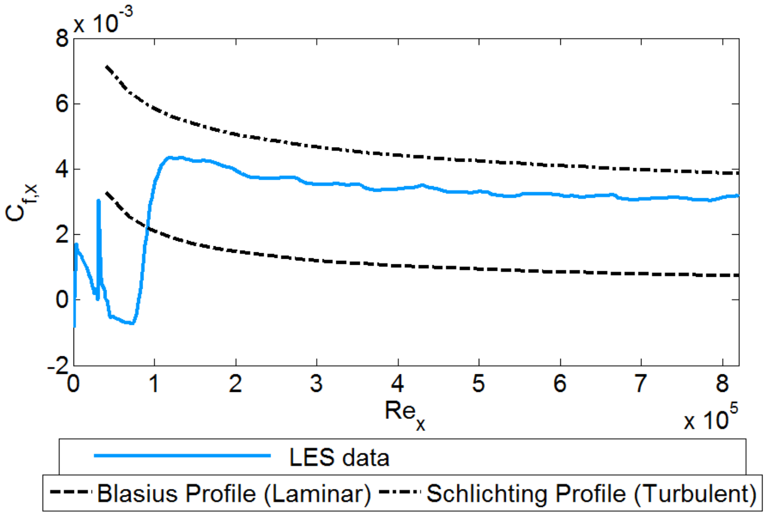

Figure 7.22: Comparison of skin friction coefficient $C_{f,x}$ from present LES data, against empirical profile for a turbulent boundary layer (Equation 2.2) and for a Blasius (laminar) boundary layer [28]

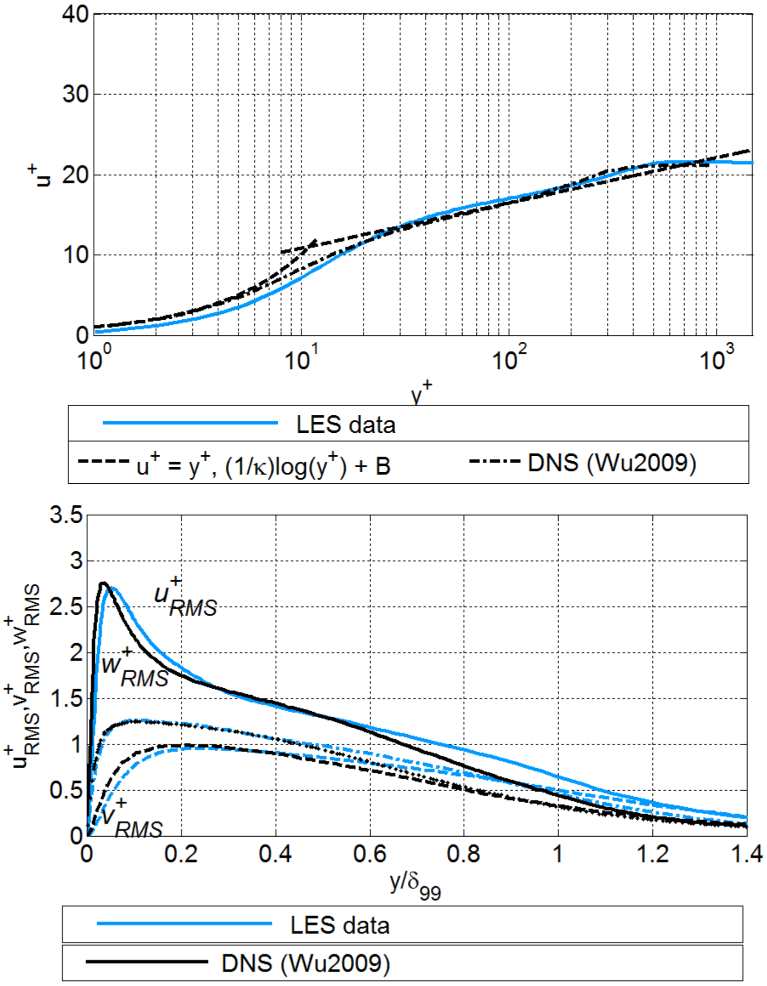

Figure 7.23: Comparison of LES data with DNS data [38] in inner scaling, with u_τ replaced by the value from the Schlichting relation for turbulent flat plates (Equation 2.2, [28]) top: mean u-velocity profile; bottom: RMS velocity profiles.

7.7 Summary

The simulations in this section have found that the in-house SotonCAA code is able to produce a reasonably accurate wall-resolved turbulent boundary layer simulation without inflow perturbations, using the step-tripping method of Berland et al [46]. The Shear-Improved Smagorinsky model of Leveque et al [91] was implemented into the solver, using an ensemble-averaged strain rate computed in both time and the homogenous (span) direction. This was found to give a significant improvement in the performance over the standard Smagorinsky model, without any observable increase in the computational effort. The effect of grid and timestep resolutions were tested, and it was found that overall a grid with $\Delta x^+ \approx 60$, $\Delta y^+ = 1$ and $\Delta z^+ \approx 20$ seemed to produce sufficient resolution of the mean and RMS profiles. Decreasing the timestep below CFL = 4.0 ($\Delta t = T^*/37500$) was also found to make no significant difference.

The growth rate of the boundary layer - in terms of the momentum thickness Reynolds number - was found to be a very good match to previous LES studies in the literature [46]. Cuts through the boundary layer at $Re_\theta = 1000$ were also found to be in very good agreement with experimental and DNS data from the literature, when plotted in outer scaling. However a discrepancy was observed when using inner scaling, which is attributed to the under-estimation of the wall shear stress - and therefore of the friction velocity u_τ - by about 11%. The mesh senstivity study indicates that u_τ may be more sensitive to the resolution than the mean and RMS profiles in outer scaling and that, therefore, it might be possible to mitigate this error by increasing the mesh refinement. However, for the purposes of the present study, improving the prediction of the wall shear stress does not necessarily justify the additional computational cost of a finer mesh. The mean and RMS profiles (in outer scaling) are not expected to change, and increasing the mesh resolution would make extending this application to complex geometries more prohibitive. The upstream wall shear stress is of little interest in this application; the main purpose is to correctly resolve the turbulent boundary layer structures, which appears to be satisfied with the current mesh. It is also considered that a much finer mesh risks verging on becoming a DNS mesh, which is outside of the scope of this work.

Therefore the meshing and simulation parameter guidelines developed in this Chapter, and validated in Figures 7.20 and 7.23, will be applied to extending this geometry to incorporate a partially-covered cavity downstream. The overall characteristics and span effects will be discussed in Chapter 8, and the sensitivity of a baseline simulation to changes in the modelling method and upstream boundary layer conditions will be discussed in Chapter 9. In both Chapters, the grid and simulation settings will be based on the guidelines developed in this Chapter, which have been shown to resolve the unsteady features of the boundary layer with reasonable accuracy. This contrasts with the DES approach from the previous Chapters, where the upstream boundary layer was modelled with RANS.

Chapter 8

LES Study of Partially-Covered Cavity with Side Walls

8.1 Overview

In this chapter, wall-resolved LES is applied to a partially-covered cavity geometry (as described in Chapter 5). The simulations are performed based on the guidelines developed in Section 7.6. The purpose of this chapter is to explore the characteristics of the partially-covered cavity flow when the incoming turbulent boundary layer structures are fully resolved using LES. The guidelines for efficiently resolving a turbulent boundary layer with LES, developed in Chapter 7, will be applied to a scaled-down model of the partially-covered geometry discussed in Chapter 5.

Previous studies (Section 2) have indicated that there is likely to be interaction between the turbulent structures in the boundary layer and the development of resonant modes in the shear layer. This can take the form of changing the amplitudes of the resonant modes, or suppressing them entirely. The interaction between the shear-layer (Rossiter mode) resonance developing in the open section of the cavity, and the covered section upstream, will also be investigated.

This chapter therefore contributes towards the objective regarding the effect of upstream turbulence on the cavity flow. This combination of partially-covered geometry, compressible flow regime and wall-resolved LES has not, to the author's knowledge, been investigated before. Therefore the analysis in this study serves to expand the existing knowledge about cavity flows.

In particular, the focus on this chapter is on the effects of the span width and the side walls. This builds upon the research objective about exploring the sensitivity of the cavity flow to span effects, by extending the analysis to incorporate resolved upstream boundary layer turbulence. The results from this LES analysis may be contrasted against the outcomes from the DES comparison in Chapter 5. This will illustrate the effect, produced by the small-scale structures from the resolved upstream boundary layer in the LES, on the development of vortex structures in the cavity shear layer. To this end, the geometry is built up in three stages. First, a case is considered with a quarter-span width ($L_z/D = 0.25$) and periodic span boundary conditions, in Section 8.2. This may be considered a baseline case for the LES analysis of the partially-covered cavity. Secondly, the spanwise extent is extended to the full span ($L_z/D = 1$) in Section 8.3, to explore the effect of the span length on the flow structures. The analysis in Chapter 5 indicated that, for using a DES methodology, there is a significant difference in the mean flow characteristics and the dominant mode. This section extends this analysis to include LES with a resolved incoming turbulent boundary layer. Finally, no-slip side walls are added to the full-span cavity ($L_z/D = 1$) in Section 8.4, to explore the effect of the side walls when compared to a spanwise-periodic configuration. Again, the DES analysis in Chapter 5 found that this caused a significant difference in the flow behaviour; this section extends that to expore the effects with wall-resolved LES.

8.2 Baseline Simulation: Periodic-Span Boundary Conditions with $L_z/D = 0.25$

8.2.1 Geometry

A sketch of the $X - Y$ plane of the geometry is shown in Figure 8.1. The inflow and upstream boundary layer follow the guidelines proposed in Section 7.3. The freestream Mach number is retained as $M_\infty = 0.25$ ($U_\infty = 85$ m/s). A laminar (Blasius) velocity profile is imposed at the inflow, with $\delta_0 = 5 \times 10^{-4}$m. A small step is introduced downstream to promote transition to turbulence, with height $0.28\delta_0$ and length $4\delta_0$, spanning the full width (z-direction) of the domain. Between the step and the leading edge of the cavity x_{LE}, a distance of 0.057m is allowed for the turbulent boundary layer to develop. This is equivalent to $115\delta_0$ downstream of the step, and a total $129\delta_0$ downstream of the inlet, with a local $Re_{x,LE} = 3.5 \times 10^5$. These values are similar to the reference x location used in Chapter 7 ($150\delta_0$ from the inlet, and $Re_x = 4 \times 10^5$), and the analysis from Chapter 7 indicated that this is more than sufficient for the turbulent boundary layer to develop. (For example, Figure 7.16 shows the boundary layer growth rate settling into the linear trend at around $x = 55\delta_0$.)

In terms of the cavity geometry, the distance 0.057m is also equivalent to $2D$, where the cavity depth $D = 0.0285m$. The cavity has an overall length $L = 3D$, with the open section length $L_{open} = D$, and the thickness of the covered-section plate being $0.03D$ with a 45° slant at the edge, as in Chapter 5. The streamwise coordinate of the leading edge and trailing edge of the open section of the cavity will be denoted x_{LE} and x_{TE} respectively, as indicated in Figure 8.1. In the vertical direction, $y = 0$ is taken as the surface of the flat plate (i.e. the top of the cavity). In the span direction, the width L_z will be varied. The present, baseline case uses $L_z/D = 0.25$ and periodic boundary conditions in the span. A wider geometry with $L_z/D = 1$ and the same periodic-span boundary conditions is considered in Section 8.3, and a fully-3D configuration with no-slip side walls and $L_z/D = 1$ is tested in Section 8.4.

In terms of scale, the dimensional value of D is reduced to 0.0285m for this simulation (vs. 0.12m in Chapter 5). This brings the Reynolds number Re based on L_{open} to 1.6×10^5, and the overall scale to 1/44 from full-scale, instead of 1/10.5. A feasibility study found that this was the only way to complete the simulations within the time and computational hardware constraints of this project. (However, the guidelines derived from this study may be applied in the future to a larger scale model if desired). Since the partially-covered cavity has so far generally exhibited the same aeroacoustic mechanisms as rectangular cavities in the literature (shear layer Rossiter modes and acoustic modes), and since past studies on rectangular cavities have generally found the cavity response to be insensitive to Re (Section 2.4.1), it is therefore expected that this change in scale will not materially affect the cavity flow field. In fact, the experiments of Ahuja et al [30] considered $Re \approx 1 \times 10^5 - 5 \times 10^5$ for $M = 0.25$, which is very similar to the reduction in scale here (from 6.6×10^5 to 1.6×10^5), and those authors found that the tonal response was largely independant of Re. Therefore the work in this section may be considered an extension of the previous work at 1/10.5 scale.

The same buffer zone method as described in Section 7.2 is used at the outflow, with a width of two cells, and the target value constantly evolving to match the mean value slightly upstream. Therefore the outflow condition allows for the change in the downstream boundary layer due to the cavity, and will prevent unphysical reflections or influence on the upstream flow.

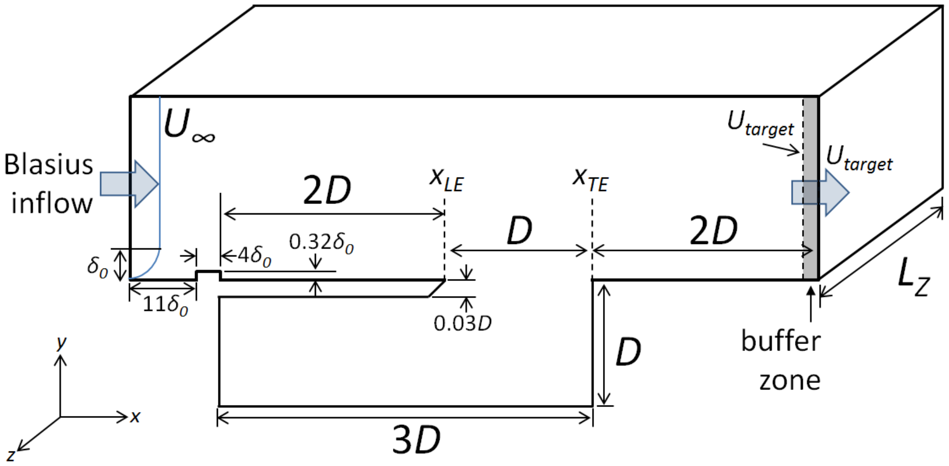

Figure 8.1: Schematic of geometry for baseline LES cavity simulations (not to scale); $2D = 115\delta_0$.

8.2.2 Mesh and Simulation Parameters

In keeping with the LES guidelines developed in Section 7.5.2, selecting the coarsest acceptable sizing to maximize efficiency, the nominal grid spacings in the boundary layer/shear layer regions are $\Delta x^+ \approx 70$, $\Delta y_1^+ \approx 0.9$, and $\Delta z^+ \approx 22$ (based on friction velocity u_τ calculated from the upstream turbulent flat plate section). Across the open section of the cavity there are 108 points in the spanwise (x) direction, with additional clustering at the leading edge ($\Delta x_{LE}/D = 1/570$) and the trailing edge ($\Delta x_{TE}/D = 1/1900$). Across the covered section there are 125 points (allowing for the lower velocities in this region), with clustering towards the upstream wall. Based on the reference $\Delta x^+ \approx 70$ grid size in the vicinity of the shear layer, and the points-per-wavelength requirements of the numerical scheme described in Section 3.4.1, the grid should be able to accurately resolve the streamwise propagation of acoustic wave structures at frequencies up to 250kHz, which is well above the expected region of interest based on Rossiter modes. In the vertical direction, there are 115 nodes across the depth of the cavity, with additional clustering towards the floor of the cavity ($y_{floor}/D = 1/280$). Overall, the wall-normal spacing at cavity walls is maintained at $\Delta^{+}_{wall-normal} < 3$ inside the cavity (less than 1 in most places). Some regions of the $X - Y$ grid are shown in Figure 8.2.

In the spanwise (z) direction, the baseline geometry uses a periodic boundary configuration with a length $L_z/D = 0.25$, which equates to 71 points with a uniform spacing to give $\Delta z^{+} \approx 22$. This is the same spanwise extent and resolution that was found to give adequate resolution of the LES boundary layer turbulence for the flat plate configuration. Later sections will explore the effect of L_Z, and the effect of the spanwise-periodic configuration.

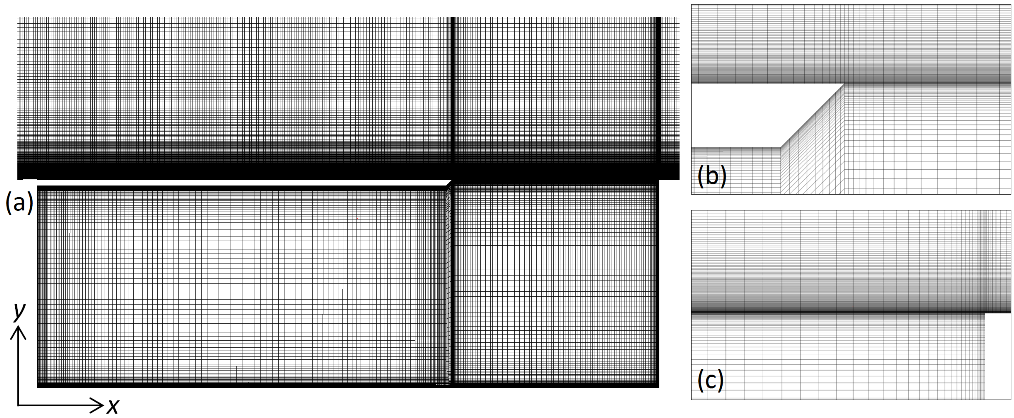

Figure 8.2: $X - Y$ mesh from baseline LES cavity simulations: (a) cavity region; (b) close-up near leading edge lip; (c) close-up near trailing edge.

The baseline simulation was carried out using the same boundary conditions and solver settings as in the flat plate boundary layer LES study. The SISM model was used, with $C_S = 0.16$, and the averaged strain rate was computed both through time-averaging and averaging in the z-direction, as described in Section 3.3.2. The timestep was set for a CFL number of 4 (in dimensional units, $\Delta t = 4.7 \times 10^{-8}$s). Defining a dimensionless time T^* based on U_∞ and L_{open}, this equates to $T^*/\Delta t = 7125$. The 6^{th}-order implicit filter was used; however, early tests showed that it is necessary to reduce the filtering cutoff to $\kappa_C = 0.80$, as simulations with $\kappa_C = 0.90$ were found to be unstable in combination with the cavity geometry. As discussed in Section 7.4.1, this will cause a small over-prediction of the u_{RMS} component, but the general shape and behaviour of the turbulent boundary layer is expected to remain reasonably well predicted.

The solution was initialized by peforming a 2D unsteady RANS simulation until the flow field had settled, then extruding the solution field uniformly in z. Perturbations in v were superimposed in the boundary layer region, drawn from a uniform probability distribution as described in Section 7.3.

The mean flow-field was computed by sampling at every time step, with the region of start-up transients removed. (The cutoff time for start-up transients was determined from the time history of the pressure monitors and varied slightly between the different simulations, generally in the vicinity of $40T^*$; total run times were around $120T^*$). Pressure monitors were also recorded at every timestep. In the mid-z plane of the cavity, the points are as shown in Figure 8.3, with an additional row of monitors in the shear layer near the z extent of the domain (Figure 8.3(b)). The pressure measurements were recorded at every timestep (with the start-up transients removed), and normalized with the freestream dynamic pressure. The pressure time series was then divided into overlapping windows, fast-Fourier transforms were performed, and the resultant power spectral densities were averaged to smooth the results, as in Chapter 5. Depending on the run duration and the noisiness of the data, between 5 and 7 windows were used in this analysis.

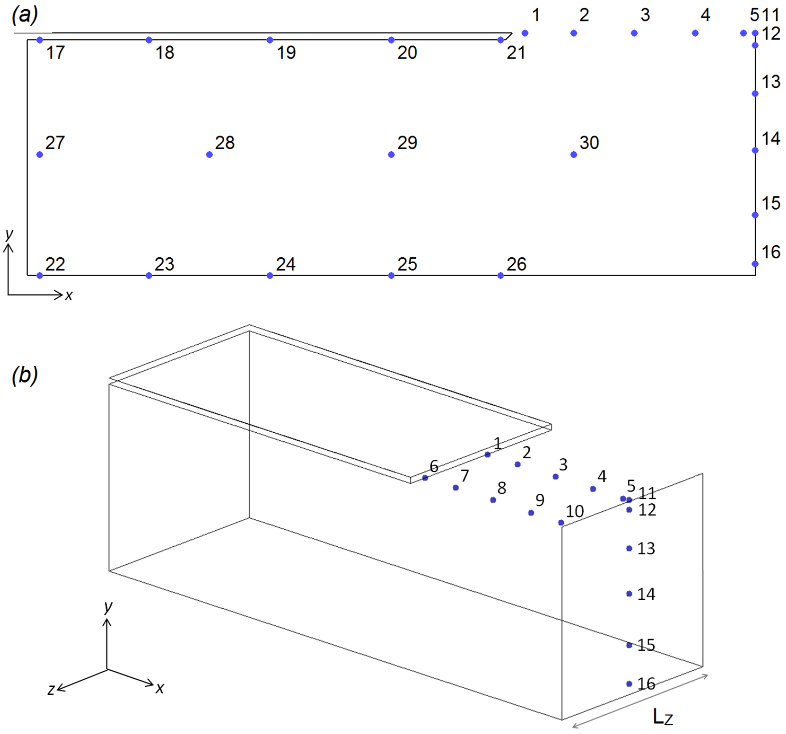

Figure 8.3: Monitor points in covered-cavity geometry; (a) in mid-z plane; (b) in the open section

8.2.3 Results - Shear Layer

A snapshot of instantaneous vortex structures from the developed flow field is shown in Figure 8.4. Small turbulent structures develop from the step and propagate downstream, indicating that the step transition method is working correctly. Analysis of the mean field confirms that the boundary layer profiles have settled to turbulent behaviour by about $30\delta_0$ downstream of the step, which is still $1.4D$ upstream of x_{LE}. The growth in momentum thickness θ is linear, as expected, and the shape factor H_{12} has settled to within 2% of the DNS and correlation data from the literature [29, 32], indicating a fully-developed turbulent boundary layer upstream of the cavity.

Downstream of the cavity, the boundary layer structures are visibly larger, indicating a thickening of the boundary layer after the cavity reattachment. The area of most interest is the shear layer: across the shear layer, the structures appear to be very similar to the upstream boundary layer region. No qualitative change at the separation point (x_{LE}) is discernable in this plot. DES simulations of the partially-covered cavity in previous chapters showed organized intermitted flow structures across the shear layer, whose size and spacing corresponded to the Rossiter modes. Neither the 3D view nor the side view of the Q-criterion in Figure 8.4 show those structures in this LES simulation. Although both the DES and the present turbulence-tripped LES are modelling a turbulent boundary layer upstream, as the LES has more resolution of the boundary layer flow structures, the shear layer structures produced by the LES simulation are expected to be closer to the true physical behaviour.

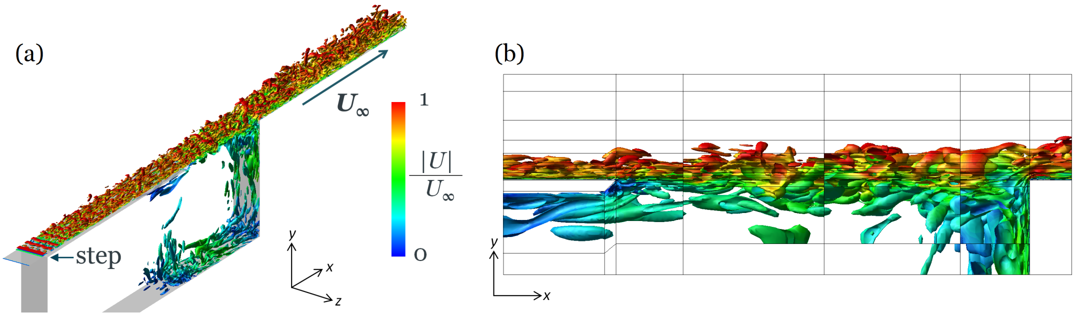

Figure 8.4: Iso-surface of instantaneous Q-criterion from baseline LES cavity simulation; (a) 3D view; (b) close-up $X-Y$ view

The time-averaged turbulent kinetic energy (k) is shown in Figure 8.5. The turbulence in the upstream boundary layer, developing after the step, is visible. Across the shear layer, there is a region of very high k immediately after x_{LE}. Mean streamlines in this region (see Figure 8.6(a)) show a small recirculation region at the edge of the lip. It appears that the recirculation bubble, interacting with the separation of the shear layer, is the cause of this high kinetic energy at the lip. Moving downstream, Figure 8.5 shows this high k peak diminishing away from x_{LE}, so that by about $0.2L_{open}$ downstream the turbulent kinetic energy is almost constant across the height of the shear layer. The thickness of the turbulent shear layer (in terms of the band of k) widens steadily - approximately linearly - across the open section of the cavity.

At the trailing edge wall, some of the kinetic energy band is swept downwards into the open-section vortex (consistent with the Q-structures shown in Figure 8.4). At the top of the downstream wall, and immediately downstream of the cavity, there are two small regions of high k. Mean streamlines (Figure 8.6(b)) indicate that the shear layer impacts the wall slightly below the top edge, causing the high k at the top of the wall; and the flow forms a small recirculation bubble on reattachment to the downstream wall, which corresponds to the high-k region just downstream of the cavity in Figure 8.5. The band of turbulent kinetic energy in the boundary layer downstream of the cavity is widened as a result, which is consistent with the larger structures observed in this area in Figure 8.4.

The characteristics of the shear layer may be further investigated by considering the pressure monitors. Figure 8.7 shows the FFT results for monitors placed across the shear layer in the centre-span plane. (7 windows were used for this simulation, leading to a frequency resolution of 127Hz.) Near x_{LE} there is a broad spectral hump at around 20kHz. This is

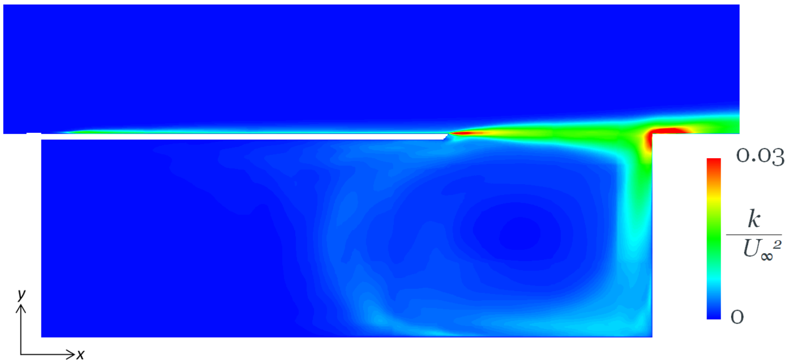

Figure 8.5: Contours of mean turbulent kinetic energy (k) at the mid-$z$plane, from the baseline LES cavity simulation

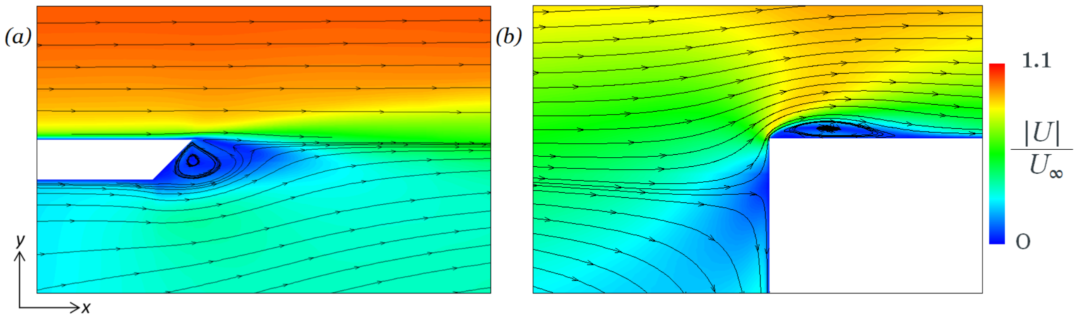

Figure 8.6: Contours of mean velocity, and streamlines from the baseline LES cavity simulation; (a) near x_{LE}; (b) near x_{TE}

likely to be associated with the small recirculation region in the near vicinity of the lip shown in Figure 8.6(a), and its influence on the nearby regions of the shear layer, as this hump has mostly vanished by Point 2 ($0.25D$ downstream of x_{LE}). The other points in the shear layer show a fairly flat FFT, with no resonant modes visible. Consistent with the Q-criterion plot (Figure 8.4), there is no evidence of strong coherent structures developing in the shear layer.

8.2.4 Inside the Cavity

The mean velocity at a representative z plane is shown in Figure 8.8. The two-vortex structure seen in the other covered cavity simulations is clearly visible. The Q-criterion plot (Figure 8.4) showed that at the trailing edge of the cavity (x_{TE}), structures are swept down along the wall and floor of the cavity, carried by the open-section vortex (which is shown in the mean streamlines). The covered section showed no vorticity at that level of Q, suggesting that the shear-layer vortical structures are less likely to be transmitted to the covered-section vortex.

The mean pressure field (Figure 8.9) shows a region of low pressure at the centre of the stronger open-section vortex, and a buildup of high pressure in the covered section. The pressure monitor at the centre of the open-section vortex showed a steady but small downwards trend with time (roughly 0.2% over $30T^*$). This was later attributed to a numerical limitation of the span boundary condition, as discussed in Section 8.3. However

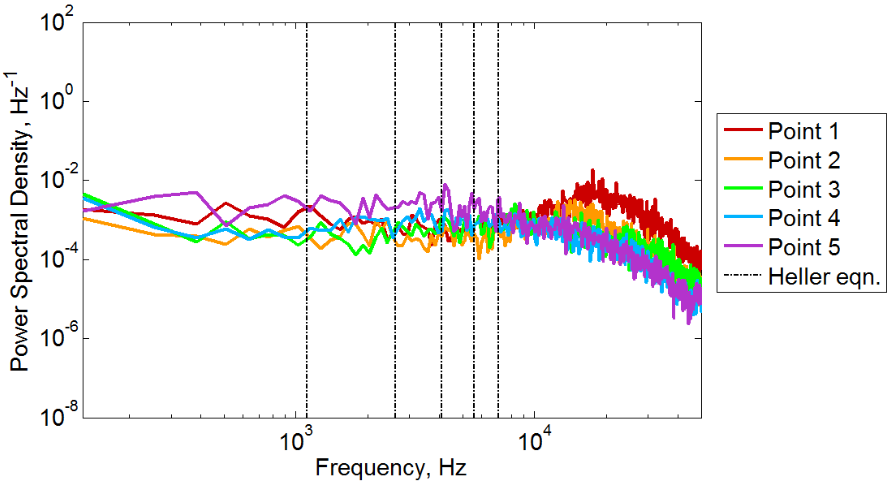

Figure 8.7: PSDs of pressure at monitors along the shear layer in the baseline LES cavity simulation; point locations are as shown in Figure 8.3

the fluctuation behaviour (and therefore the frequency content breakdown in the FFT data) does not change, and pressure monitors in other locations are not significantly affected.

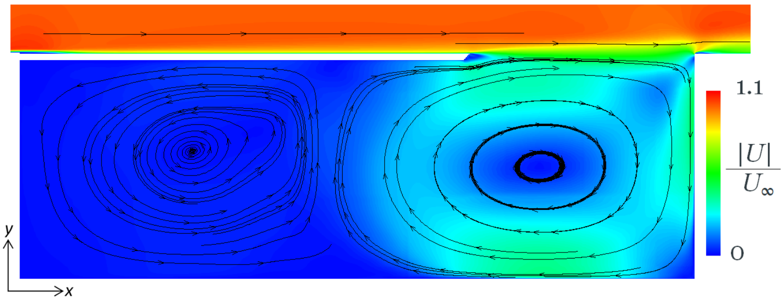

Figure 8.8: Contours of mean velocity, and streamlines, at the mid-$z$plane, from the baseline LES cavity simulation

FFT data from points at the upstream and downstream walls of the cavity are compared in Figure 8.10. Unlike in the shear layer, there are sharp resonant peaks clearly visible at 4kHz, 6kHz, and 8kHz. Similar behaviour was observed at the other points inside the cavity. Figure 8.11 compares the pressure monitors at the top and bottom of the downstream wall. It is evident that the monitor in the shear layer has higher levels at all frequencies, which may be masking any influence of the resonance inside the cavity on the shear layer. At the bottom of the downstream wall, the same peaks are visible as in Figure 8.10, with additional peaks at 10, 12, 14 and 16kHz.

The strongest tone at 4kHz is a good match for the third Rossiter mode; however the presence of the other tones (6kHz, 8kHz 10kHz etc) strongly suggests harmonics of some fundamental behaviour at 2kHz, which does not correspond to any of the Rossiter mode frequencies. Figure 8.12 shows instantaneous snapshots of the perturbation pressure (instantaneous pressure with a mean pressure $\overline{p}$ subtracted) at seven equally-spaced times, spanning a total time equivalent to 1 cycle of a 2kHz frequency. (The mean pressure $\overline{p}$ used here is calculated over the length of the cycle, to avoid effects from the downward

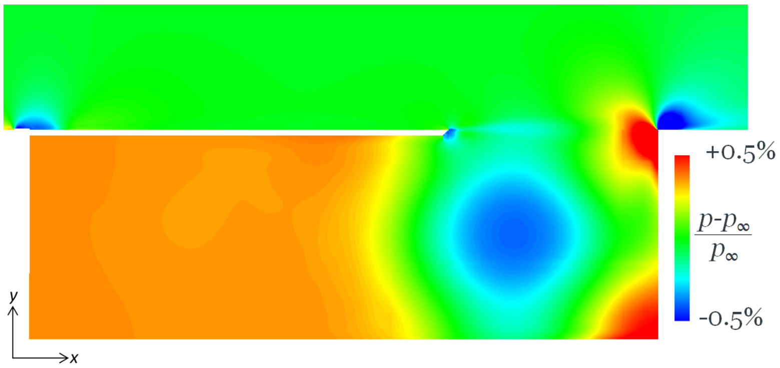

Figure 8.9: Contours of mean pressure at the mid-$z$plane, from the baseline LES cavity simulation

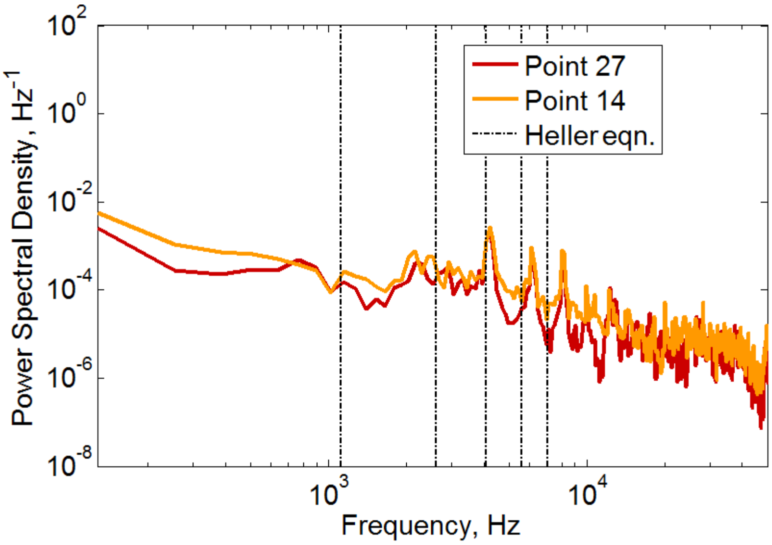

Figure 8.10: PSDs of pressure at monitors along the mid-depth of the cavity at the upstream wall (Point 27) and the downstream wall (Point 14), from the baseline LES cavity simulation; point locations are as shown in Figure 8.3

drift in p.) Across the shear layer, there are patterns of alternating high and low pressure in the shear layer, caused by the small unsteady vortex structures. The plots show evidence of pressure waves propagating upstream from the cavity trailing edge, indicative of the acoustic feedback which is often associated with Rossiter-mode shear layer resonance. Inside the cavity, where the tonal peaks are most pronounced, there are alternating regions of high and low pressure. The pattern is disrupted by small-scale unsteadiness but, broadly speaking, the pressure fluctuations appear to be largely similar through the depth of the cavity but alternating in the x-direction, i.e. the length. This suggests that the driving mechanism of these tones is a length-wise acoustic mode inside the cavity.

This is consistent with the trends in the literature discussed in Section 2.4.4. The top two-thirds of the cavity are covered, so the current geometry is comparable to the experiments of Shaw et al [63] on a rectangular cavity with a small opening. Both have $L_{open}/L = 0.33$, similar values for L/D (3 vs. 3.1 in [63]), and the open section is at the downstream end; the main difference is that here the opening spans the whole width, and in [63] it was limited to $W_{open}/L_z = 0.2$. In the experiments, the measured tones were found to give good

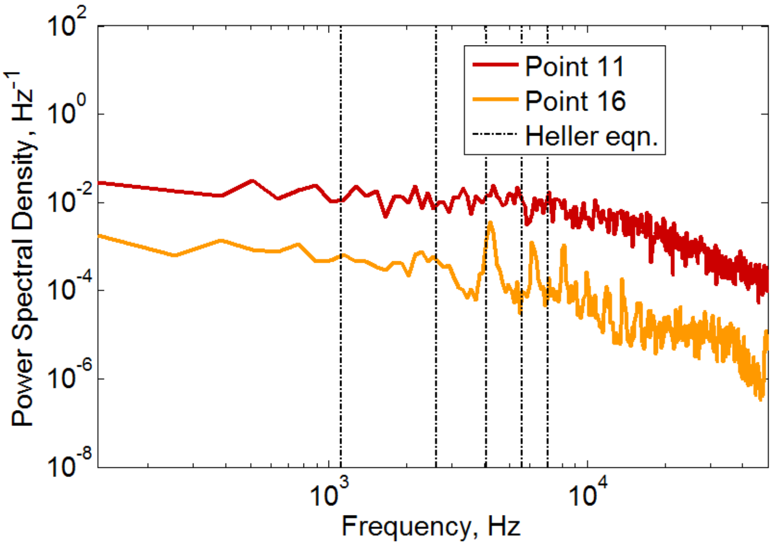

Figure 8.11: PSDs of pressure at monitors along the downstream wall of the cavity, from the baseline LES cavity simulation; point locations are as shown in Figure 8.3

agreement with Equation 2.8 for acoustic modes inside the cavity. Evaluating Equation 2.8 for the current configuration and assuming lengthwise modes ($N_y = N_z = 0, N_x = 1, 2, 3...$) yields a fundamental frequency of 2kHz (with harmonics at 4kHz, 6kHz etc.), which is in excellent agreement with the frequencies observed in Figure 8.10-8.11.

The strongest peak is at 4kHz, which suggests that the second lengthwise mode is dominant (this is also visualized in some of the snapshots in Figure 8.12, especially t_3 and t_7, where the positive and negative pressure bands from the circular pressure wave at the trailing edge, can be seen to line up with positive and negative fluctuation pressures in the shear layer). Shaw et al [63] also observed a $N_x = 2$ dominance for their covered cavity, at the closest Mach number where resonance was observed ($M = 0.60$). In that experiment, the $N_x = 2$ frequency was not near any of the Rossiter mode frequencies.

It has been observed from past studies that the small vortex structures in a turbulent boundary layer produce a 'jittering' effect on the cavity shear layer [18], which attenuates resonant shear layer oscillations by interrupting the coherence of the structures (e.g. [31,56, 77]; see Section 2.4.5). Considering the criteria of Ahuja et al [30] for turbulent boundary layer cavity resonance in a rectangular cavity, those authors found that $\delta/L < 0.066$ is required to develop tones; their experimental data at $\delta/L = 0.066$ showed no feedback tones at all. In this case, the relevant geometry lengthscale should be the length across the shear layer, L_{open}. Evaluating the boundary layer thickness just upstream of the cavity gives $\delta/L_{open} = 0.064$; technically less than 0.066, but very close. Therefore based on that criteria, it is possible that the thick turbulent boundary layer is suppressing the development of Rossiter modes in this case. Visually, no resonant-mode vorticity structures could be distinguished in the Q-criterion plots in Figure 8.4. The pressure monitors in the shear layer also show a fairly broadband spectra (Figure 8.7), due to the influence of the small-scale vortical flow structures propagating from the turbulent boundary layer upstream, which would support this theory.

In this case, however, there is evidence to suggest that at least some Rossiter-mode res-

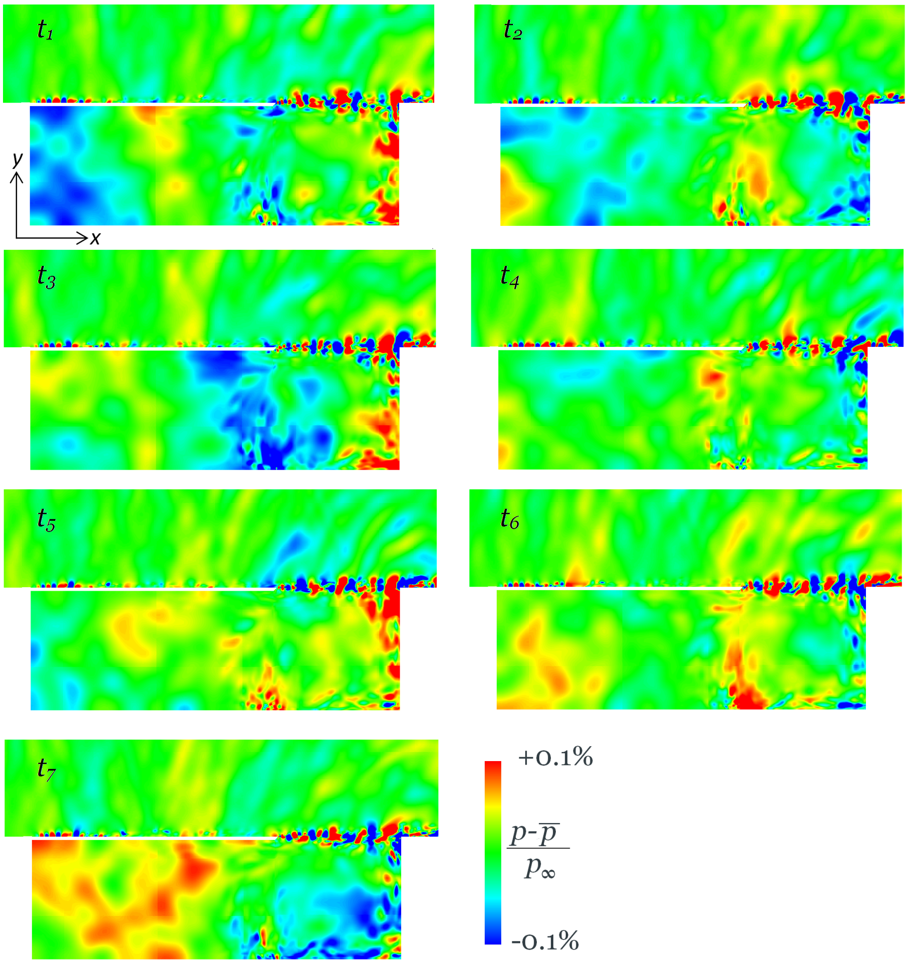

Figure 8.12: Snapshots of instantaneous perturbation pressure in the mid-span over a total time equivalent to 1 cycle at $f = $ 2kHz, from the baseline LES cavity simulation

onance is developing in the shear layer. The perturbation pressure plots in Figure 8.12 show acoustic waves propagating upstream outside the cavity, suggestive of Rossiter-mode feedback. It is also noted that according to Equation 2.5, the 3^{rd} Rossiter feedback tone is also at 4kHz, which is the frequency of the dominant tone. Several studies [51, 63, 65] have shown that the strongest oscillations occur when the acoustic modes couple with the shear layer modes, at the intersection of the frequencies from the two mechanisms. Overall, it seems that although the upstream boundary layer turbulence does interference with the coherence of the shear layer vorticity structures (based on the vorticity plots and the spectra in the shear layer), there is some development of shear layer resonance, which has a coupling and amplifying effect on the $N_x = 2$ acoustic mode.

8.3 Full-Span Case with Periodic-Span Boundary Conditions

8.3.1 Overview

The effect of L_z was tested by comparing the baseline simulation ($L_z/D = 0.25$) against a simulation with $L_z/D = 1$, with all other grid and simulation settings the same. The mesh size therefore quadruples, from 8.9M cells in the $L_z/D = 0.25$ case to 35.6M cells in the $L_z/D = 1$ case. Previous DES analysis on the effect of spanwise length with periodic-span boundary conditions (Section 5.6) showed that going from $L_z/D = 0.25$ to $L_z/D = 1$ completely changed the behaviour in the shear layer. In those simulations, the open-section vortex became distorted, deflecting the shear layer upwards from the leading edge, and changing the trailing-edge impingement location. Most significantly, the flow field no longer developed the same length-wise acoustic mode inside the cavity, and the dominant mode in the shear layer changed from mode 3 (which coupled with acoustic mode $N_y = 2$) to mode 4. No systematic trend in behaviour was observed with increasing L_z. Some of the behaviour of that simulation was attributed to a tendency observed in the literature [120] for periodic-span configurations to exaggerate the spanwise coherence of separated shear layer flows, beyond what is expected from a physical flow field. In the case of the present LES study, although periodic span boundary conditions are still used, the resolved turbulent boundary layer upstream is generating small-scale vortex structures which should be decorrelated in the span (based on the analysis on the flat plate, and from other flat plate studies [46]). These small structures feed into the shear layer, and should therefore interrupt any non-physical coherence developing in the span. The iso-contours of Q from the baseline LES simulation (Figure 8.4) do suggest that this is ocurring. Therefore in the present LES analysis, it is expected that there will be much less difference in behaviour between the $L_z/D = 0.25$ and $L_z/D = 1$ cases.

In the shear layer and upstream boundary layer regions (where the flow is dominated by small turbulent structures), the degree of spanwise coherence was quantified using the correlation coefficient. This was defined as $R(\Delta z)$ across a separation distance of Δz, based on the form used for temporal autocorrelation [130]. For example, for the u velocity, the correlation is calculated according to:

$$R(\Delta z) = \frac{\dfrac{1}{N_z - 1} \sum\limits_z (u_z - \overline{u})(u_{z+\Delta z} - \overline{u})}{\dfrac{\sum (u - \overline{u})^2}{N_z - 1}} \tag{8.1}$$

The numerator of the above is an estimate of the sample covariance, and the denominator represents the estimated variance. In terms of sampling, data is extracted from the instantaneous flow field at time t, at a given x and y, and $R(\Delta z)(t)$ is evaluated for each separation Δz. The mean value $\overline{u}$ is taken from the mean flow field, which is calculated by sampling every timestep over the last $\approx 30T^*$, and therefore those values are well converged. This procedure is repeated for a number of different time instances (50 for $L_z/D = 0.25$, and 30 for $L_z/D = 1$), and then averaged over time to smooth out the local noise in the final $R(\Delta z)$. The correlations for v, w and p are calculated in the same manner.

8.3.2 Upstream Boundary Layer

The spanwise correlations at $0.90D$ upstream of x_{LE}, where the turbulent boundary layer is fully developed, are presented for $L_z/D = 0.25$ and $L_z/D = 1$ in Figure 8.13, at $y^+ = 8$. In both cases and for all variables, $R(\Delta z)$ has dropped to an amplitude of less than 0.05 by $\Delta z^+ = 600$. (The total span width for $L_z/D = 0.25$ corresponds to $L_z^+ = 1600$). The same behaviour was observed at $y^+ = 20$ and $y^+ = 100$. This confirms that the turbulent structures are effectively uncorrelated across the half-span even with the shorter L_z, which confirms that the width is sufficient for the boundary layer vortex structures to properly develop without interference from the periodic span condition.

The minima for u and v relate to the width of the streaks. Schlatter et al [29] found minima at $\Delta z^+ \approx 25$ for v and ≈ 60 for u; however those authors used a grid with spacing $\Delta z^+ = 11$, which is verging on DNS resolution [93], and so they were able to resolve that level of detail in the correlation distribution. In these simulations $\Delta z^+ = 22$, and the minima are correspondingly broadened due to the limits of the grid resolution. The peak for v is at $\Delta z^+ \approx 60 - 80$, and for u is $\Delta z^+ \approx 80 - 120$, which is broadly consistent with the expected trend of the minimum for u being roughly twice that for v [29]. The correlation profiles are also very similar between the two simulations. The correlation for p was observed to be the most prone to sampling noise, and the difference in $R(\Delta z)$ for p - which is within 0.1 - is most likely attributable to sampling noise, as other x-locations did not show the same trend. In terms of the mean flow, the two simulations exhibited similar mean and RMS boundary layer velocity profiles upstream of the cavity, and the shape factor H_{12} was also identical.

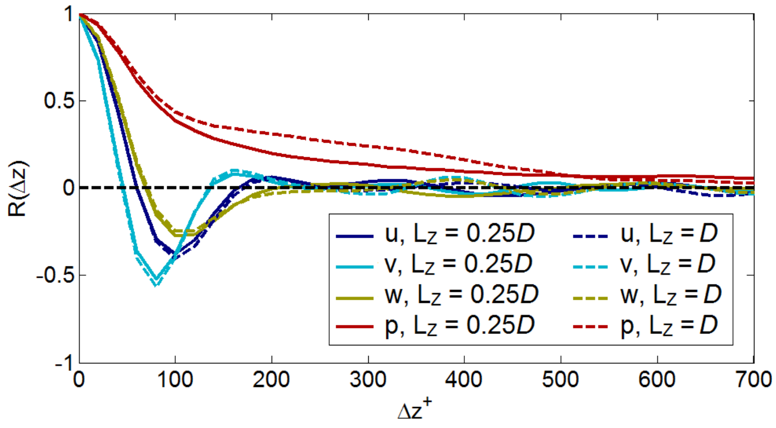

Figure 8.13: Spanwise correlation from LES simulations at $x_{LE} - 0.90D$ and $y^+ = 8$, comparing baseline simulation ($L_z/D = 0.25$) with $L_z/D = 0.25$

8.3.3 Shear Layer

Instantaneous iso-surfaces of the Q-criterion are compared between the two simulations in Figure 8.14, with a close-up in the vicinity of x_{TE} in Figure 8.15. The same type of

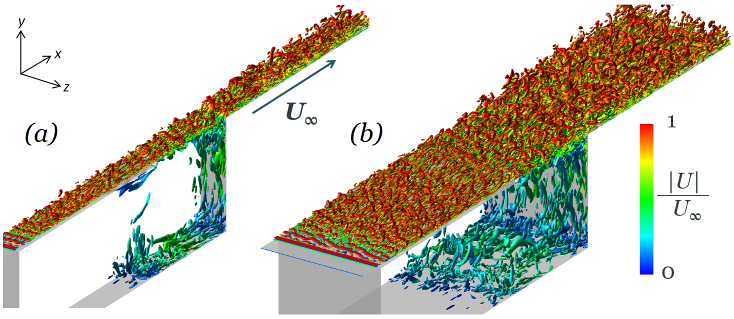

Figure 8.14: Iso-surfaces of Q-criterion coloured by velocity magnitude; (a) from $L_z/D = 0.25$ simulation; (b) from $L_z/D = 1$ simulation

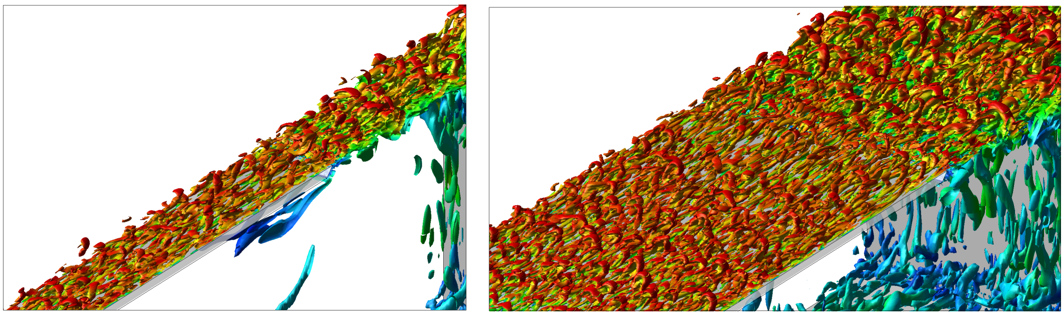

Figure 8.15: Close-up of Q-criterion plots from Figure 8.14; (a) from $L_z/D = 0.25$ simulation; (b) from $L_z/D = 1$ simulation

structures are observed in both simulations; hairpin vortices in the upstream boundary layer, growing and widening in the shear layer. In both simulations there is visual evidence of coherent shear layer Rossiter-mode structures. The spanwise correlation at $0.3D$ downstream of x_{LE} is shown in Figure 8.16. The minima associated with the streaks is no longer present in the data, due to the change of the flow from wall-bounded turbulence to shear layer structures, but the correlation coefficient still drops to within 0.1 over $\Delta_z^+ \approx 600$, showing that the spanwise length even with the quarter-span is enough to accomodate these structures. It would therefore be expected that the flow field in the shear layer would be same between the two simulations.

This is confirmed by the frequency content of the pressure monitors, which was found to be insensitive to L_z. An example is shown in Figure 8.17, which is in the middle of the open section (i.e. $x_{LE} + 0.5D$). No tones are present, and there is a generally high level of pressure fluctuations due to the incoming boundary layer turbulence. Similar agreement was at all points in the shear layer. The RMS pressure distribution in the shear layer (Figure 8.18), and the mean pressure at the point of shear layer impingement on the downstream wall (Figure 8.19) were also very similar between the two span lengths. The pressure is slightly higher from the narrower span, but the locations of the maximum pressure (i.e. the stagnation points) are very similar.

However, there is a small difference in the shear layer in terms of the turbulent kinetic energy. Figure 8.20 shows that the wider geometry has a slightly higher peak values of k across the shear layer. Examination of the flow in the vicinity of the cavity leading edge (Figure 8.21) shows that with the $L_z/D = 0.25$, there is more interaction between

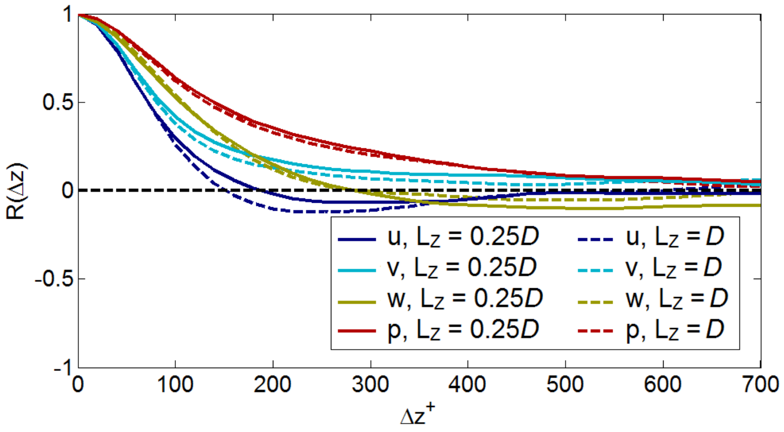

Figure 8.16: Spanwise correlation from LES simulations at $x_{LE} + 0.30D$ and $y^+ = 8$, comparing baseline simulation ($L_z/D = 0.25$) with $L_z/D = 1$

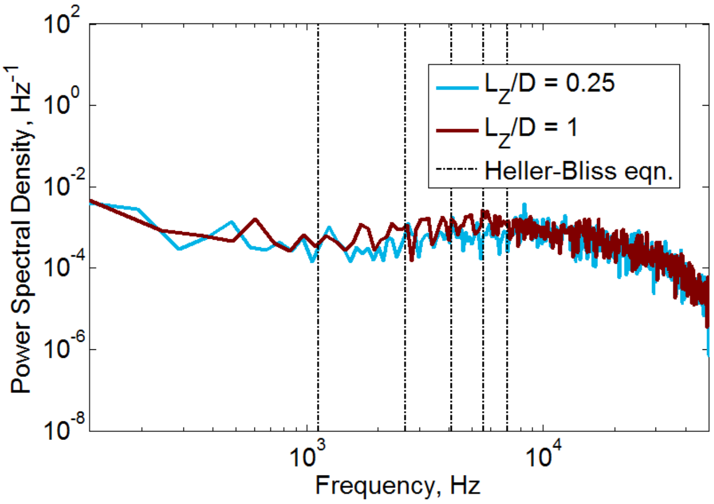

Figure 8.17: PSDs of pressure at monitor Point 3 (at the mid-length of the shear layer), comparing $L_z/D = 0.25$ with $L_z/D = 1$

the shear layer kinetic energy and the lip vortex, with a band of k being drawn along the underside of the lip vortex. This suggests that with the narrower span, the lip vortex is slightly stronger. The interaction causes small changes the development of k in the upstream shear layer, causing a slightly higher peak of k in the immediate vicinity, but lower levels further downstream. The same trends were observed plotting u_{RMS}, v_{RMS} and w_{RMS} separately. In the downstream half of the shear layer, the higher k for the full-span simulation may also be induced by the higher level of k in the open section inside the cavity.

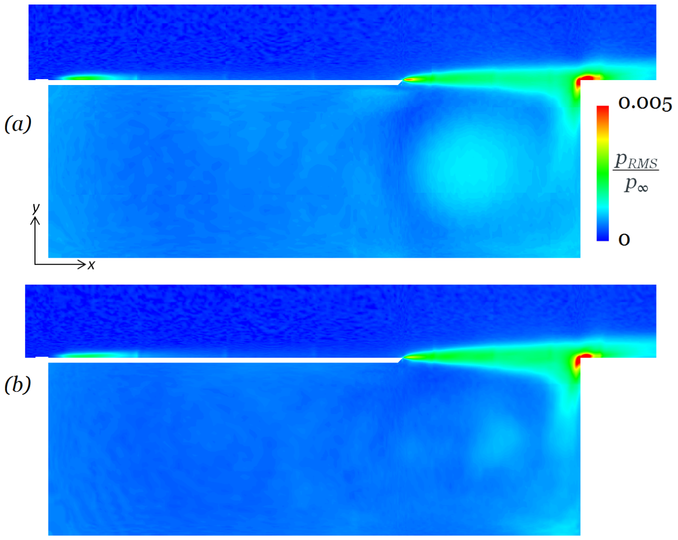

Figure 8.18: Contours of RMS pressure from mean field; (a) from baseline LES simulation, $L_z/D = 0.25$; (b) with $L_z/D = 1$

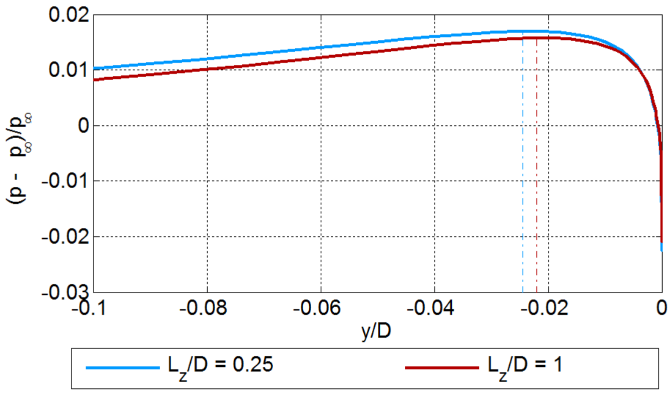

Figure 8.19: Comparison of mean pressure on downstream wall of cavity with $L_z/D = 0.25$ and $L_z/D = 1$

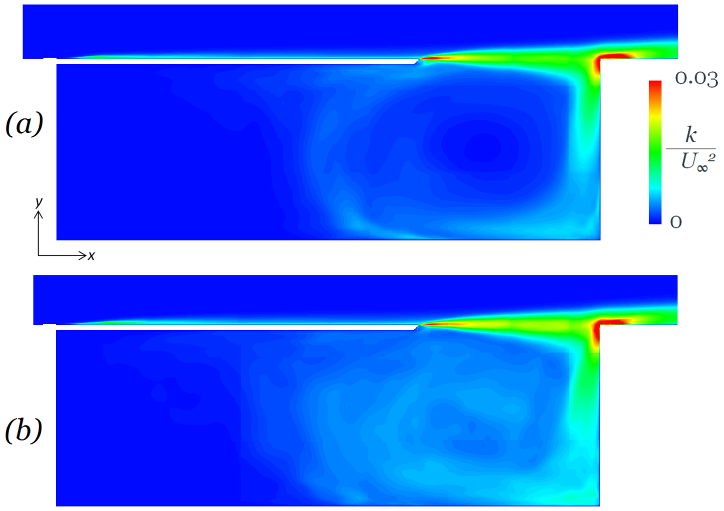

Figure 8.20: Comparison of turbulent kinetic energy contours: (a) from baseline LES simulation, $L_z/D = 0.25$; (b) with $L_z/D = 1$

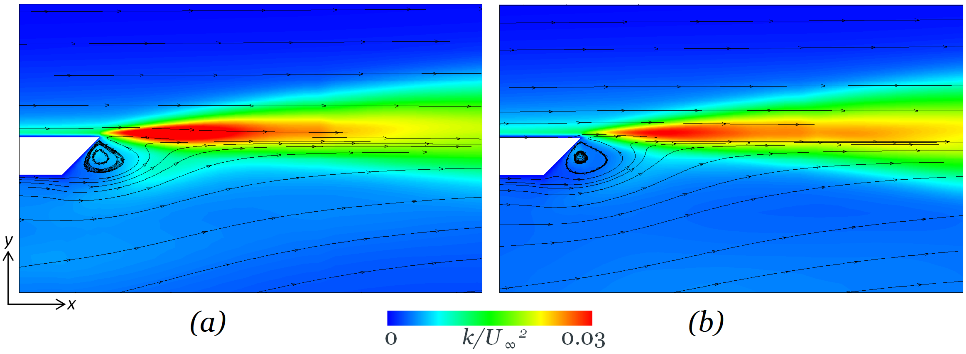

Figure 8.21: Comparison of turbulent kinetic energy contours, close-up around x_{LE}: (a) from baseline LES simulation, $L_z/D = 0.25$; (b) with $L_z/D = 1$

8.3.4 Inside the Cavity

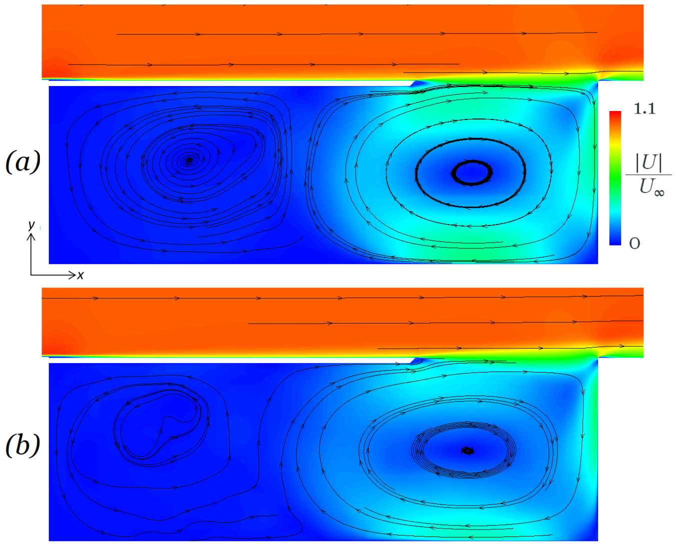

Figure 8.22: Comparison of velocity magnitude contours and streamlines: (a) from baseline LES simulation, $L_z/D = 0.25$; (b) with $L_z/D = 1$

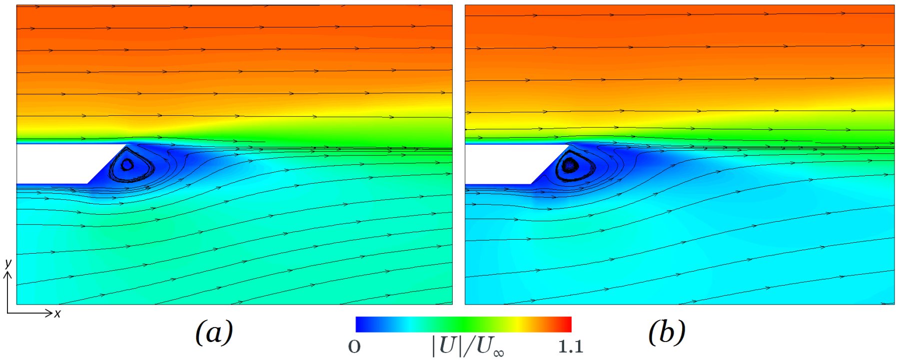

Figure 8.23: Comparison of velocity magnitude contours and streamlines, close-up around x_{LE}: (a) from baseline LES simulation, $L_z/D = 0.25$; (b) with $L_z/D = 1$

As shown in Figure 8.20, the wider-span geometry has more turbulent kinetic energy inside the cavity, particularly in the centre of the open-section vortex. All three components (u_{RMS}, v_{RMS} and w_{RMS}) showed this difference in behaviour. Contours of velocity magnitude inside the cavity (Figure 8.22) illustrate that the $L_z/D = 0.25$ simulation shows higher velocities in the open section, particularly along the floor and back upwards. Since the shear layer impinges slightly below the top of the downstream wall, the flow is swept down the wall and then around the open-section vortex. The higher velocity magnitudes in those regions indicate a stronger vortex. Close-ups of the velocity near the shear layer leading edge (Figure 8.23) show the higher velocity under the cavity lip from the $L_z/D = 0.25$ simulation. It is likely that the small vortex under the cavity lip is at least partly induced by this flow from inside the cavity; the stronger open-section vortex with $L_z/D = 0.25$ is therefore responsible for the stronger lip vortex. The open-section vortex is also slightly more concentrated in the x-direction in the $L_z/D = 0.25$ simulation, as the streamlines do not extent as far into the covered section.

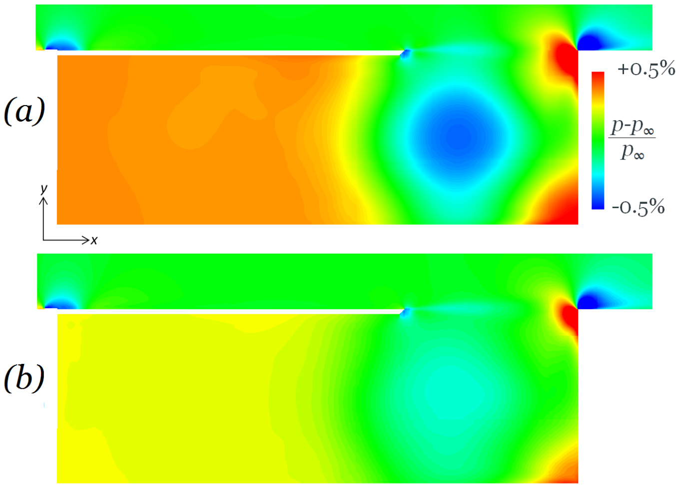

Figure 8.24: Comparison of mean pressure: (a) from baseline LES simulation, $L_z/D = 0.25$; (b) with $L_z/D = 1$

Contours of mean pressure are shown in Figure 8.24 on a finer scale, and there is a clear difference. The quarter-span ($L_z/D = 0.25$) simulation shows a lower pressure in the centre of the open section, indicating a stronger and more coherent open-section vortex, as seen in the mean velocity plots. (The low-pressure region associated with the small lip vortex is also stronger, for the same reason.) Instantaneous pressure plots at the mid-depth of the cavity showed that, for both simulations, the vortex core pressure does not vary in the span direction. In the covered section, where the pressure is positive (above p_∞), the full-span simulation ($L_z/D = 1$) has a lower pressure. In other words, the full-span simulation has pressure levels closer to ambient throughout the cavity. The higher covered-section pressure for the $L_z/D = 0.25$ simulation may be the reason why the open-section vortex does not extend as far into this region.

It seems likely that the pressure build-up in the covered section is induced by the pressure and the flow-field in the open section vortex. Therefore, the differences between the two simulations are essentially attributable to the exaggerated strength and coherence of the open-section vortex for the narrower span. The coherence may be illustrated by comparing instantanous contours of velocity. Figure 8.25 compares w velocity at the mid-depth of the cavity between the two simulations. Both simulations show smaller-scale perturbations towards the outer edges of the open-section vortex, but the full-span simulation shows larger-scale perturbations being induced all the way through the core of the vortex. The difference in the extent of the perturbations upstream into the covered section is partly due to the full-span simulation having a longer vortex in this direction, and partly due to fluctuations extending into the covered-section vortex. The same trends were observed from plots of u velocity in the mid-depth, and plots of w and v velocities along the vertical centreline of the open-section vortex (see Figure 8.26 for w). For the quarter-span simulation, the centre of the region is smooth and essentially 2D and steady, with no perturbations to the vortex streamlines. It therefore appears that using $L_z/D = 0.25$ limits the development of spanwise variations in the vortex core.

The wider-span simulation, therefore, in allowing space for these perturbations to develop, reduces the coherence of the open-section vortex. This leads to the lower pressure in the core of the vortex, less pressure build-up in the covered section, and a weaker lip vortex affecting the shear layer. The upstream boundary layer, and the shear layer structures, were all observed to be uncorrelated across the quarter-span. However, the open-section vortex scales with D, and is several times larger than the structures in the boundary layer and shear layer, so it is not inconsistent to conclude that the flow in this region may need a larger width to allow fluctuations to develop in the span. Increased coherence and overly strong vortices were also observed as a result of interference from the periodic span boundary in the larger-scale DES simulations (and the review of Bres et al [120] for separated shear flows).

In comparing the two simulations, it is likely that the wider-span simulation gives the better result, since the fluctuations in the open-section vortex are better resolved. In addition, the pressure monitor at Point 30 (i.e. in the vicinity of the open-section vortex), which was observed to exhibit a small but steady downwards drift with the baseline simulation, maintained a perfectly steady mean level with the wider simulation. (It is noted that the small drift was also observed in other simulations with different geometries and modelling techniques, which are discussed in the next chapter, so this issue is not dependant on the geometry or the tubulence modelling method.) That effect is most likely explained by interference from the periodic boundary which creates a small, steady reinforcement of the open-section vortex.

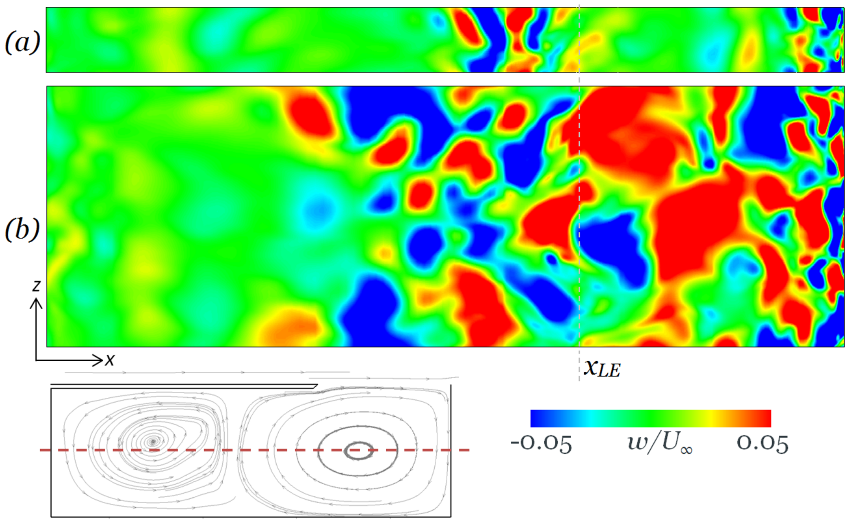

Figure 8.25: Contours of instantaneous w velocity at mid-depth of cavity ($y = -0.5D$): (a) from baseline LES simulation, $L_z/D = 0.25$; (b) with $L_z/D = 1$. Schematic shows location of plane against streamlines from the baseline simulation

Comparison of the RMS pressure from Figure 8.18 showed slightly higher levels inside the cavity for the quarter-span simulation. The higher p_{RMS} levels in the core of the open-section vortex for the quarter-span can be attributed to the downward drift in p due to the span boundary, as they are not observed in the full-span simulation. (RMS pressure is calculated by finding the average value of p^2 and subtracting $\overline{p}^2$, where $\overline{p}$ is calculated from

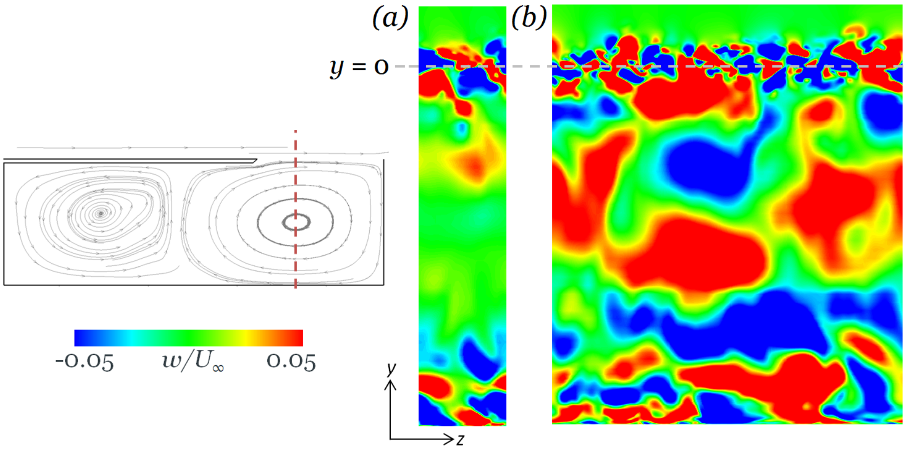

Figure 8.26: Contours of instantaneous w velocity at $x_{LE} + 0.4D$: (a) from baseline LES simulation, $L_z/D = 0.25$; (b) with $L_z/D = 1$. Schematic shows location of plane against streamlines from the baseline simulation

a long averaging window; therefore if $\overline{p}$ is slightly drifting with simulation time, p_{RMS} will be inflated.) In the shear layer and in the covered section, the two simulations give fairly similar results.

However in spite of the issues with the open-section vortex, the resonant behaviour inside the cavity is still very similar. Pressure monitors at Point 30 are compared in Figure 8.27. This point is located near the centre of the open-section vortex, and is therefore the most affected by these issues, yet the same resonant peaks are observed with the quarter-span simulation and with the full-span simulation. The amplitudes are slightly higher due to the higher RMS pressure in the cavity, but the frequencies are identical, and the relative amplitudes of the tones are similar. This was also observed at the upstream top corner of the cavity (Figure 8.28), and indeed at all the monitor points inside the cavity. Therefore the same resonance mechanism seems to be developing in both cases. An instance of the fluctuation pressure, showed in Figure 8.29, confirms the presence of lengthwise pressure variations throughout the cavity, consistent with a lengthwise acoustic mode developing in the cavity. Evidence of pressure waves propagating upstream from the trailing edge is also observed, suggestive of the acoustic feedback from a Rossiter mode, similar to the $L_z/D = 0.25$ case. The FFTs of the pressure monitors in the shear layer were also noted to be very similar, so the overall tonal content of the simulation does not change with L_z. This is very different from the observation in the larger-scale DES, where the flow field and tonal content were found to be completely different between $L_z/D = 0.25$ and $L_z/D = 1$.

8.3.5 Conclusion

Overall, for periodic-span (quasi-2D) configurations using wall-resolved LES, span widths of $L_z/D = 0.25$ and 1 were compared. It was found that the quasi-2D characteristics of the flow field are overall consistent across the two span lengths. This includes the trailing edge impact pressure and the mean velocity field; the acoustic tones were also very similar, with identical frequencies. These features, being common across both span widths, can

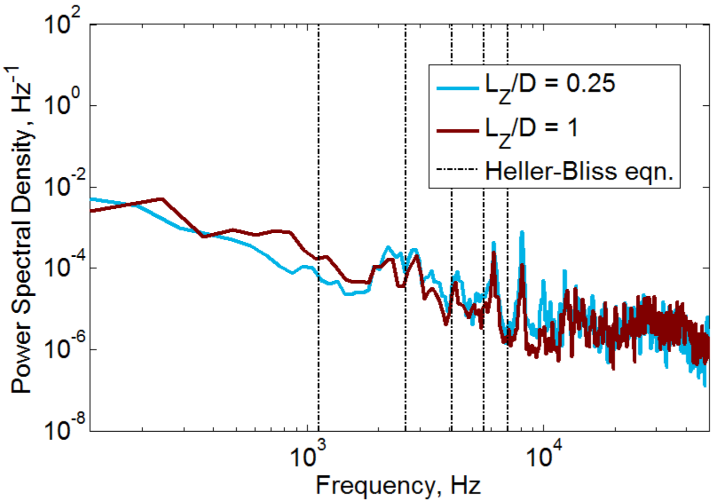

Figure 8.27: PSDs of pressure at monitor Point 30 (in the open-section vortex), comparing $L_z/D = 0.25$ with $L_z/D = 1$, Point location is as shown in Figure 8.3.

be taken as being representative of the 2D characteristics of the cavity flow field. This consistency is an improvement on the behaviour shown in the DES in Chapter 5, where increasing L_z/D from 0.25 to 1 caused a drastic change in flow behaviour, making it unclear which case is representative of the 2D characteristics of the cavity. In the present LES, the shear layer structures are decorrelated across the span for both widths; this is also a significant improvement in behaviour compared to the DES, where both simulations had shear layer structures which were still correlated in the span. The difference between the two modelling methods is due largely to the influence of the resolved small-scale structures in the upstream boundary layer. In the LES these structures are resolved, and therefore feed into the shear layer, and interfere with the spanwise coherence; but in the DES these structures are RANS-averaged, so the upstream boundary layer is steady and spanwise-uniform.

Some differences were observed between the simulations, which indicates that the quarter-span width, in conjunction with the periodic span boundary condition, does affect the development of spanwise fluctuations in the centre of the open-section vortex, causing the vortex to be more coherent, and strong, than in the $L_z/D = 1$ case. This in turn affects the mean and RMS pressure amplitudes inside the cavity.

Comparing the two cases, the $L_z/D = 1$ case was found to exhibit no drift in the mean pressure, and allowed perturbations in the vortex to penetrate all the way through the vortex core. Therefore it is concluded that the $L_z/D = 1$ simulation gives a better result, and where the differences are observed between the two configurations (mainly in the mean pressure), the results from the $L_z/D = 1$ simulation are more reliable. However, since the other characteristics were found to be consistent, the $L_z/D = 0.25$ setup with LES does have some value as a first approximation for the quasi-2D characteristics of the cavity flow, and is able to accurately simulate the resonance characteristics and mean velocity field, at a fraction of the computational cost.

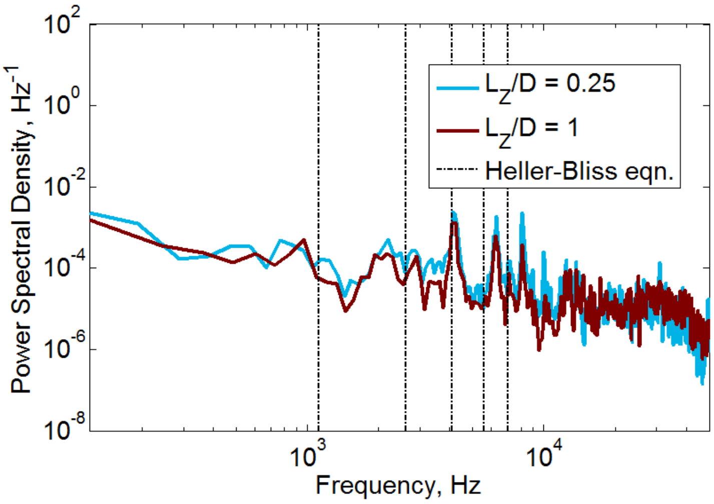

Figure 8.28: PSDs of pressure at monitor Point 17 (near the top upstream corner of the covered section), comparing $L_z/D = 0.25$ with $L_z/D = 1$, Point location is as shown in Figure 8.3.

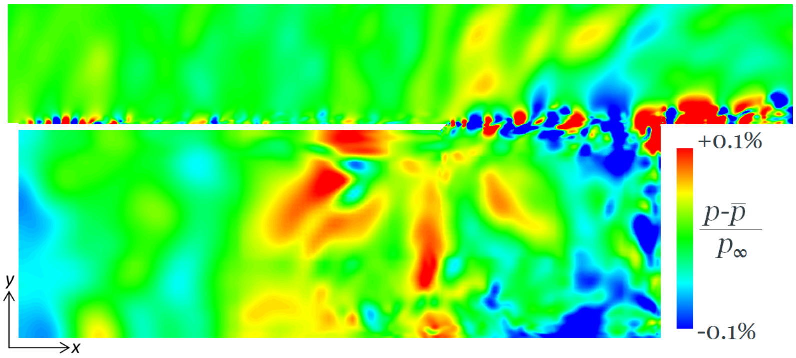

Figure 8.29: Instantaneous contours of perturbation pressure from $L_z/D = 1$ simulation

8.4 Full-Span Case with Side Walls

8.4.1 Geometry and Mesh

In this section, the effect of solid side walls (i.e. in the z direction) on the LES cavity flow will be considered. In the $X - Y$ plane, the geometry follows the same schematic as the baseline, shown in Figure 8.1. The only difference is that the height of the domain is reduced from D to $0.7D$ for computational efficiency, as the previous results all showed that the vertical extent of the flow disturbances from the cavity (and even the downstream boundary layer) are well within $0.2D$. In the Y-Z plane, a schematic of the spanwise geometry is shown in Figure 8.30. The total width of the cavity is $W = D$, the same dimensions as considered in Section 8.3, and previously in Chapter 5. The spanwise-periodic simulation with $L_z/D = 1$ from Section 8.3 is used a baseline in this section, to identify the specific effect of the side walls. A no-slip condition is used on the side walls, the same as on all the other walls. On either side of the cavity, the flat plate is extended by $0.5D$, to allow the cavity flow to spill over the sides and to prevent the z boundary conditions from intefering with the cavity flow. At the z-extents of the domain, a buffer zone is used (the same formulation as at the downstream x outflow). The purpose of this is to minimize any reflections back into the domain, in case any flow structures from the cavity reach this boundary; however, simulation tests confirmed that the flow in this region has settled back into a quasi-2D state, as desired. The z axis is defined with $z = 0$ in the centre of the cavity, and therefore $z = \pm 0.5D$ at the walls.

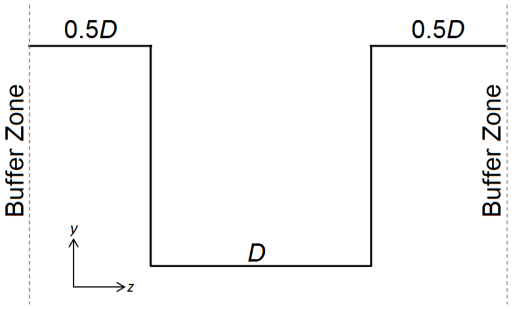

Figure 8.30: Schematic of span-wise geometry for simulation with side walls

The mesh in the z direction uses the same Δz throughout most of the cavity ($\Delta z^+ \approx 22$), with additional resolution near the side walls, reducing Δz by 80% at the wall. The flow inside the cavity is at a lower velocity than the outer boundary-layer flow upon which the inner scaling is based, so this equates to a local $\Delta z_{wall} \lesssim 3$. Outside the cavity, previous DES analysis of the cavity with side-walls indicated that the 'spill' of the cavity shear layer structures over the side walls occupied a narrow area of $\approx 0.05D$. Therefore, the baseline z-resolution was maintained for $0.1D$ on either side of the cavity, after which the mesh was allowed to grow in z. This also allows any perturbations to be damped by the grid before reaching the outer boundary, further reducing the likelihood of span-boundary interference. A total of 87 points were used in the plate wall on each side, bringing the total grid size up to 53M points. Images of the mesh in the z-direction, taken from slices at $x = x_{LE} + 0.5D$, are shown in Figure 8.31.

The numerical methods and solver parameters are mostly identical to those used in the previous sections. The only difference was in the calculation of the averaged strain rate for the SISM SGS model, as ensemble-averaging in the span is no longer appropriate, since the geometry now varies in the span direction. Therefore the algorithm was modified to remove the ensemble-averaging, and the averaged strain rate was calculated solely with time-averaging.

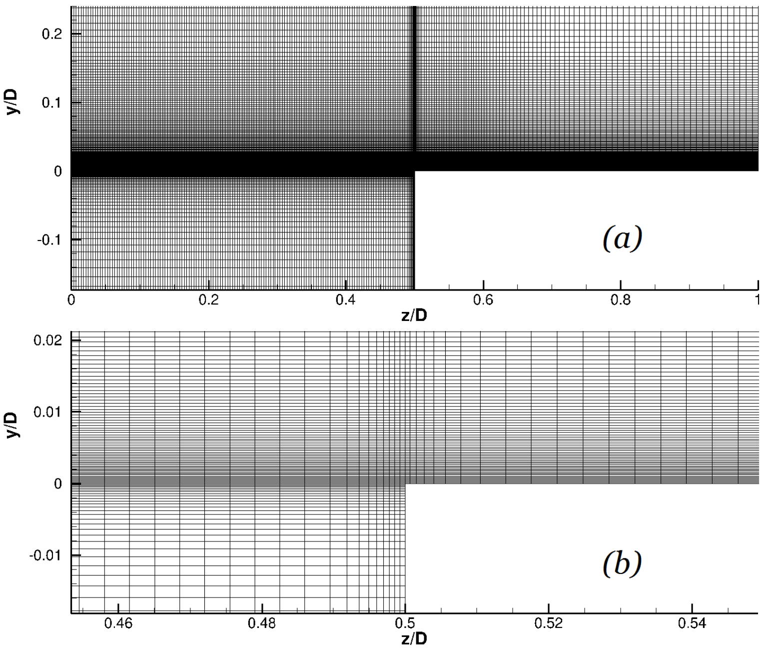

Figure 8.31: Example of $Y - Z$ mesh from simulation with no-slip side walls, from $x = x_{LE} + 0.5D$: (a) across half-width of domain; (b) close-up of finer-resolution cells where the shear layer meets the side walls

8.4.2 Shear Layer

The vortex structures in the boundary layer and shear layer are visualized through isosurfaces of the Q-criterion in Figure 8.32 and Figure 8.33. The diminished structures towards the spanwise extents of the domain are due to the coarsening of the mesh, but in the near vicinity of the cavity the structures are still well-resolved. Compared with the spanwise-periodic simulation, the structures across the shear layer are visually very similar, with both simulations showing hairpin-type vortices on a relatively small scale, with no clear indication of the kind of regular vortex structures that would be associated with shear-layer resonant modes. The growth of the shear layer, in terms of the spreading of the vortex structures in the y-direction moving downstream across the open section, is also very similar between the two simulations. Visually, there is no qualitative change in the shear layer behaviour from the addition of side walls.

The turbulent kinetic energy is compared between the two simulations in Figure 8.34, from the $z = 0$ plane. The simulation with side walls has a slightly higher k in the shear layer and inside the cavity. The w_{RMS} component would be expected to increase inside the cavity due to the interaction with the walls, but examination of the RMS velocity components indicates that, in fact, all three components increase with the side wall simulation. Furthermore, this increase was observed across nearly the whole span, not just in the vicinity of the walls. The higher levels of k in the shear layer may therefore be induced by the higher k inside the cavity. The RMS pressure was also found to show a similar small increase in the shear layer.

The variation of the shear layer in the span direction for the simulation with side walls is shown in Figure 8.35, which plots the vorticity and mean turbulent kinetic energy at a

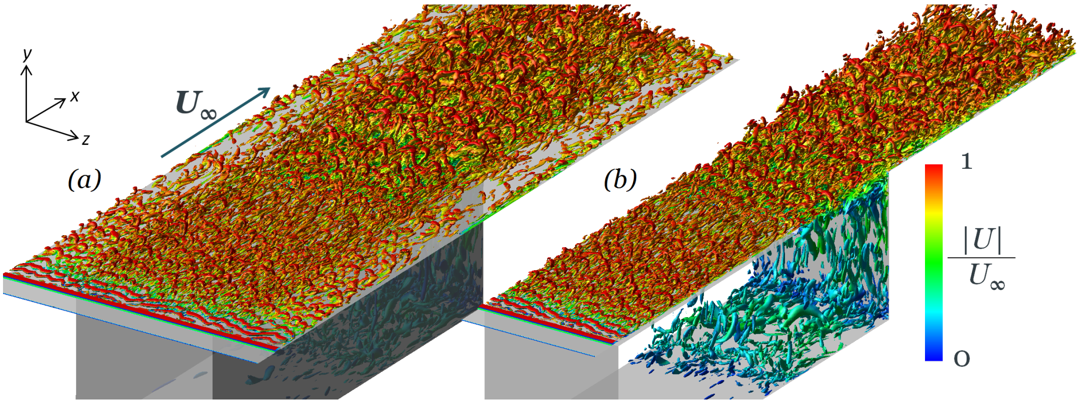

Figure 8.32: Iso-contours of instantaneous Q-criterion, coloured by velocity magnitude, 3D view: (a) cavity with side walls; (b) cavity without side walls (periodic in the span)

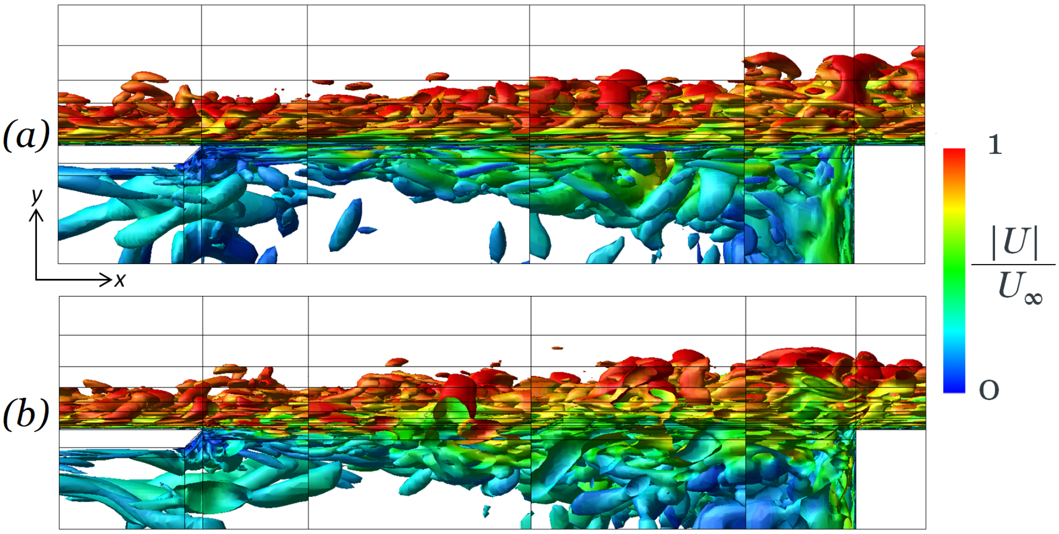

Figure 8.33: Iso-contours of instantaneous Q-criterion, coloured by velocity magnitude, $X - Y$ side view: (a) cavity with side walls; (b) cavity without side walls (periodic in the span)

plane halfway across the open section ($x = x_{LE} + 0.5D$). Small vorticity structures develop in the z direction. Away from the wall, the values of k in the shear layer are largely constant along the span. The small variations in peak k have a random appearance and therefore are probably attributable to turbulent noise; an even longer averaging window (the current results use an average over $72T^*$) would most likely smooth this out entirely. Within about $0.05D$ from the walls, the peak k in the centre of the band decreases, due perhaps to the effect of viscosity from the no-slip side wall boundary condition. The kinetic energy band also slopes slightly downward at the side walls. (The RMS pressure band at this plane was found to exhibit the same trend.) The instantaneous vorticity plot indicates that the vortex structures in this region partially spill over the side walls, and are partially deflected downwards into the cavity. Comparison of the mean streamwise velocity contours at this location in Figure 8.36 shows that the side walls cause a slight downwards deflection of the shear layer in the near vicinity. On the outside of the cavity, Figure 8.35(b) shows that

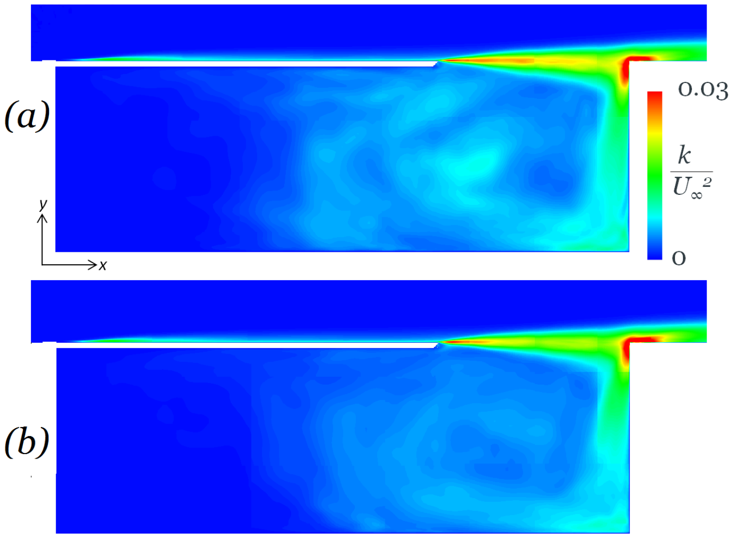

Figure 8.34: Contours of turbulent kinetic energy from plane at $z = 0$: (a) cavity with side walls; (b) cavity without side walls (periodic in the span)

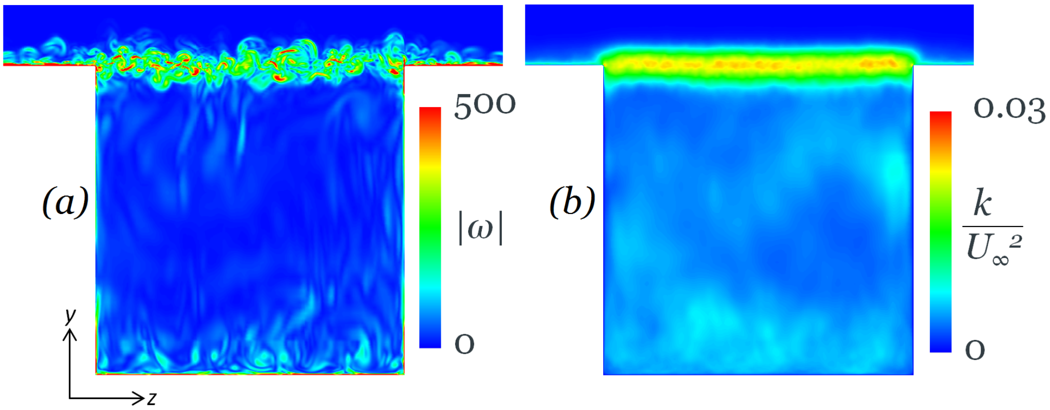

Figure 8.35: Slice plane at $x = x_{LE} + 0.5D$ (i.e. halfway across open section), from LES of cavity with side walls: (a) contours of instantaneous vorticity magnitude, calculated from normalized velocity; (b) contours of mean turbulent kinetic energy

the high k from the shear layer extends over the edge by $\approx 0.05D$, which is well within the region of high z-resolution in the mesh.

Moving downstream, the spreading of the shear layer across the open section is visualized in Figure 8.37 through an $X - Z$ plane of k at $y = 0.03D$. The variation of the high-k region downstream of the cavity has a random appearance and therefore is probably also attributable to random turbulent fluctuations. The spill over the side-walls, even at the downstream edge, occupies a region of about $0.05D$ and is therefore suitably resolved by the grid topology.

At the downstream wall of the cavity (at the x_{TE} plane), the mean pressure field is compared between the two simulations in Figure 8.38, overlaid with mean streamlines in the $Y - Z$ direction. (Both mean flow-fields were observed to be symmetric in the span, so only half the span is plotted for convenience). On the wall itself, the high-pressure regions are very similar between the two cases. The simulation with side walls shows a

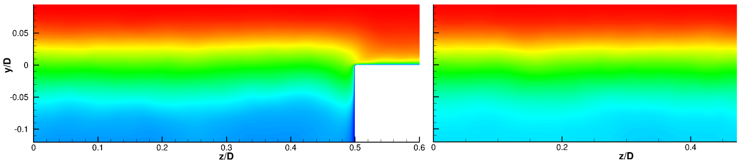

(a)

(b)

Figure 8.36: Contours of mean u velocity from plane at $x_{LE} + 0.5D$: (a) cavity with side walls; (b) cavity without side walls (periodic in the span)

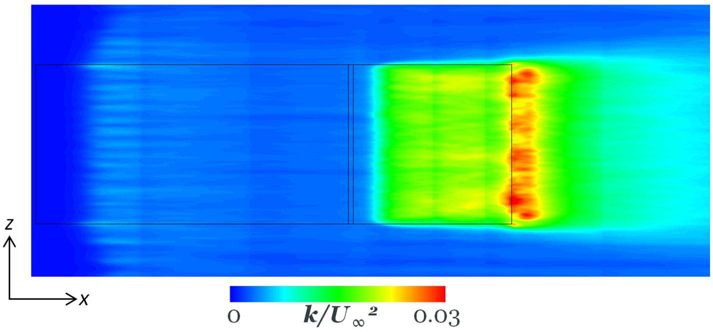

Figure 8.37: Contours of from turbulent kinetic energy from plane at $y = 0.03D$, from simulation of cavity with side walls

slight narrowing of the high-pressure band at about $0.1D$ from the edge, but overall there is not much variation in the span, and the span-averaged mean pressure on the wall was observed to agree to within 2% comparing the two simulations. The vertical stagnation point (visualized through the horizontal streamline) is at almost exactly the same location in both cases, $y = -0.02D$. Above the stagnation point, the simulation with side-walls shows a tendency for the streamlines to be directed laterally as well as upwards, as the high-pressure flow impacting the wall can ‘escape’ over the sides of the cavity as well as downstream. This w component grows stronger towards the side walls, culminating in a small recirculation bubble to the side of the cavity, as evidenced both by the circular streamlines and the low-pressure region. Even at the mid-span in the simulation with side walls, the streamlines have a slight outward component, compared with the spanwise-periodic simulation where the $v - w$ streamlines in this plane are strictly vertical.

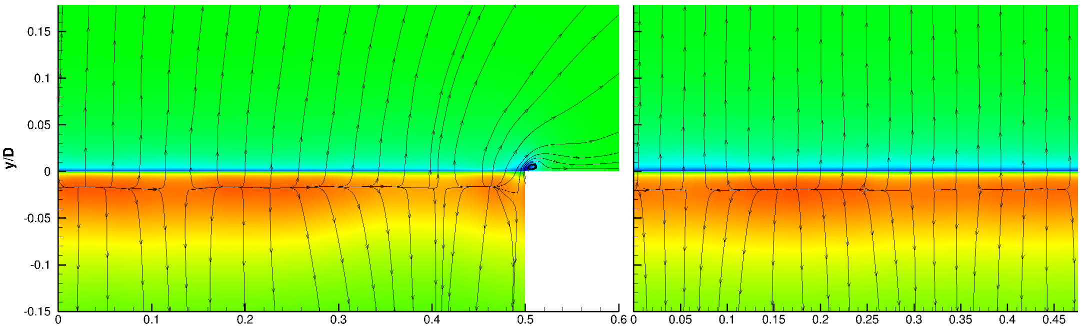

(a)

(b)

Figure 8.38: Contours of mean pressure, and streamlines, from plane at x_{TE}: (a) cavity with side walls; (b) cavity without side walls (periodic in the span)

The thin band of low pressure at $y > 0$ corresponds to the recirculation bubble downstream of the cavity. This pressure is slightly weaker in the simulation with side walls, mostly due to the diversion of the flow over the sides, weakening the development of this downstream vortex. The difference in the recirculation bubble pressure between the two simulations is nearly constant across the span, so the influence of the side walls, in this respect, is felt throughout the span. Comparison of the positive vertical velocity at x_{TE} is shown in Figure 8.39; the introduction of the side walls causes a small reduction in v across the whole span, compared to the periodic-span simulation. This velocity is the flow driven upwards by the impingement on the wall, which then forms the recirculation bubble as it travels downstream; a decrease in v ought therefore to reduce the height and strength of the bubble, thereby accounting for the weaker suction pressure at the vortex core. The mean velocity in the $X - Y$ plane at the mid-span is shown in Figure 8.40, and confirms that downstream recirculation bubble is very slightly shorter with the side walls.

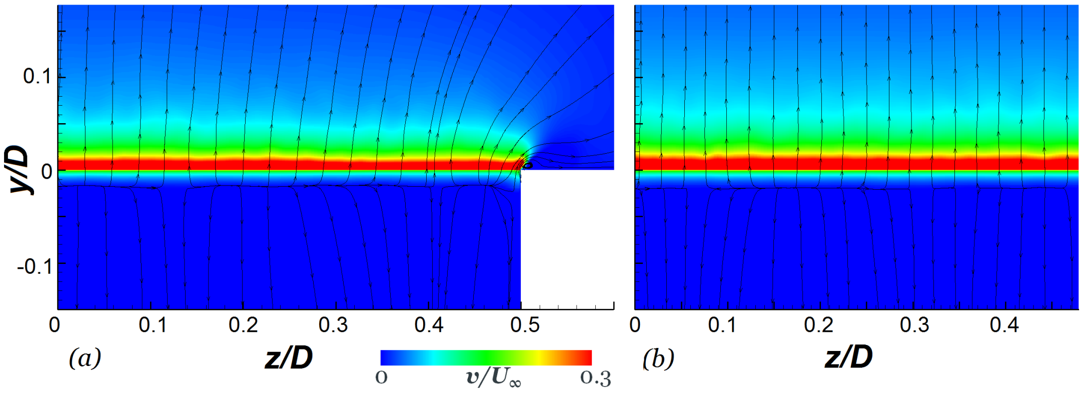

Figure 8.39: Contours of mean y-velocity, and streamlines, from plane at x_{TE}: (a) cavity with side walls; (b) cavity without side walls (periodic in the span)

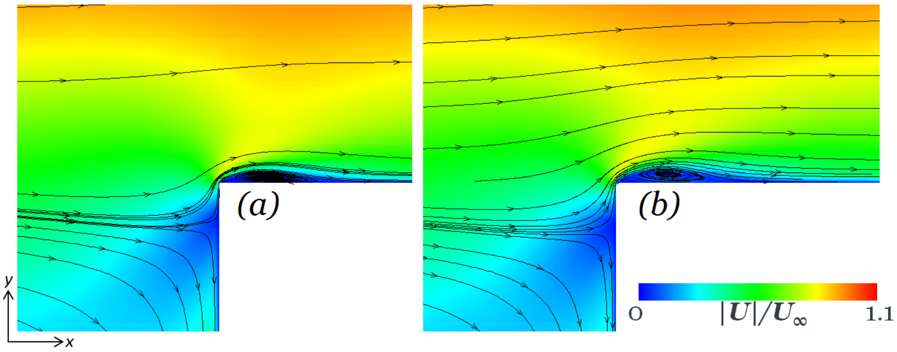

Figure 8.40: Contours of mean velocity magnitude, and streamlines, from plane at $z = 0$: (a) cavity with side walls; (b) cavity without side walls (periodic in the span)

In terms of the unsteady characteristics of the shear layer, Figure 8.41(a-b) shows that the RMS pressure on the back wall is fairly similar between the two simulations. The additional small regions over the side walls correspond to the lateral recirculation bubble seen in Figure 8.38(a); since the shear layer is turbulent, the flow being driven upwards and outwards in this region is also unsteady. Within the span of the cavity there is not much variation, aside from some small fluctuations which are mostly likely attributable to random turbulent motions, which would reduce with longer averaging. The two cases are compared more quantitatively in Figure 8.41(c), which is a line plot showing the spanwise variation of RMS pressure exactly at the trailing edge ($x = x_{TE}, y = 0$). The similarity observed in the contour plots is confirmed by the line plot in this region.

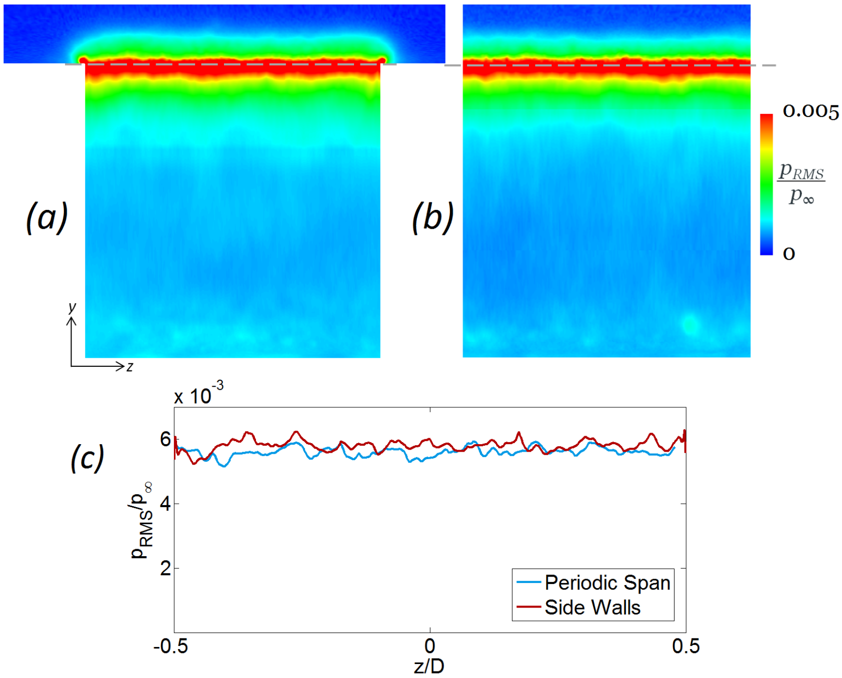

Figure 8.41: RMS pressure at the cavity downstream wall ($x = x_{TE}$): (a) $Y-Z$ plane contours, from the cavity with side walls; (b) $Y-Z$ plane contours, from the cavity without side walls (periodic in the span); (c) line plot at $y = 0$ (i.e. in line with the cavity leading edge and trailing edge). Location of line for plot (c) is indicated by gray dashed lines in (a) and (b).

In Section 8.2 and Section 8.3, the PSD data (from the FFT analysis of the pressure monitors) was presented using 5 overlapping averaging windows. Tests with up to 10 averaging windows were performed, but no systematic change was observed in the frequency spectra - especially in the shear layer, where the spectra remained largely broadband - so $n = 5$ windows was retained as a trade-off between smoothness and frequency resolution. However, for the simulation with side walls, averaging with more windows was found to distinguish small peaks at some Rossiter mode frequencies at some points in the shear layer. The high number of windows required to distinguish the tone from the noise for this simulation necessitates a trade-off with the frequency resolution, as the total time signal (about $72T^*$) needs to be divided into smaller segments. The PSD figures in this section use the same $n = 9$ windows for both the simulation with side walls and the reference periodic-span configuration, so the results may be directly comparable.

Figure 8.42 compares FFT data from three monitors at $x = x_{LE} + 0.05D$: from the periodic-span simulation, at $z = 0$ (Point 1); and from the simulation with side walls, at $z = 0$ and $z = 0.49D$ (Point 6, i.e. $0.01D$ from the side wall). With the side walls, a small peak is observed at 2.7kHz, which is within the frequency resolution of the second Rossiter mode frequency, $f_2 = 2.6$kHz. Similar Rossiter-mode peaks were also observed at a few other points in the shear layer, most significantly at the mid-length of the open section ($x = x_{LE} + 0.5D$). The same comparison (between the two cases, and between the two span locations) is presented at $x_{LE} + 0.5D$ in Figure 8.43. Small but distinct peaks are observed at f_2, f_3 and, from the $z = 0.49D$ point, at f_1.

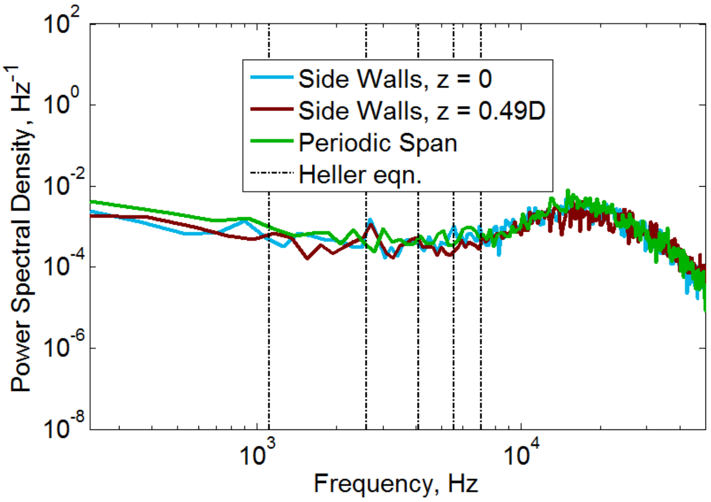

Figure 8.42: PSDs of pressure at monitors at $x = x_{LE} + 0.05D$, $z = 0$ and $z =$ 0.49D (Points 1 and 6, as shown in Figure 8.3)

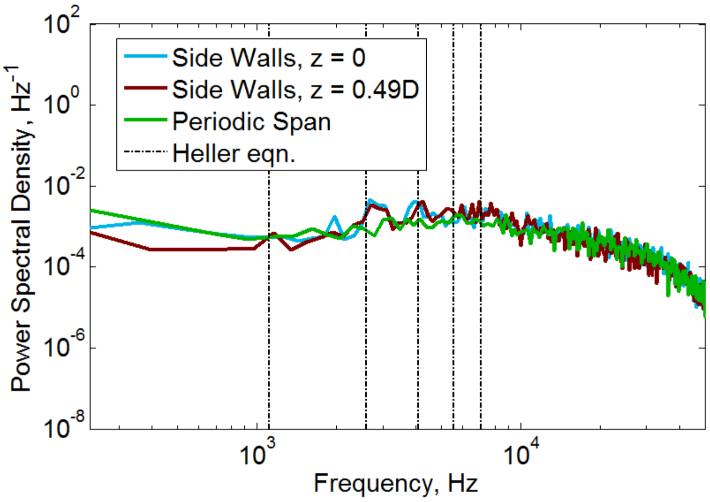

Figure 8.43: PSDs of pressure at monitors at $x = x_{LE} + 0.5D$, $z = 0$ and $z =$ 0.49D (Points 3 and 8, as shown in Figure 8.3)

The amplitudes of these tones are not large, relative to the broadband levels at the surrounding frequencies, and at first glance these tones may not appear to be significant. However it should be noted that, especially for f_2, these tones appear at both monitor points from the simulation with side walls, but not in the simulation with a periodic span. (The FFT of Point 6 and 8 from the periodic-span simulation also did not show these tones; they are not shown in this comparison as that simulation exhibited uniform behaviour across the span, as expected.) This suggests that the difference, although small, may be systematic, and therefore indicative of a slightly different behaviour from the simulation with side walls.

Across the span of the simulation with side walls, the frequency content between $z = 0$ and $z = 0.49D$ was found to be largely the same. Figures 8.42 and 8.42 illustrate this for $x = x_{LE} + 0.05D$ and $x = x_{LE} + 0.5D$, and the same trend was observed at all other stations in the shear layer. The RMS pressure at $x = x_{LE} + 0.5D$ (Figure 8.44) shows a fairly uniform distribution across the width of the cavity, until the shear layer spills over the edge; broadly consistent with the trend shown at the downstream wall in Figure 8.41. The instantaneous perturbation pressure, plotted at a plane slightly above the cavity surface ($y = 0.05D$) in Figure 8.45, exhibits no distinguishable systematic variation of the pressure structures near the side walls of the cavity. The alternating positive and negative pressure regions also do not correspond to any particular wavelength. (However it is not necessarily to be expected that the pressure structures from resonant modes would be clearly visible in this type of plot, as the tonal peaks were barely distinguishable even in the averaged FFT data.)

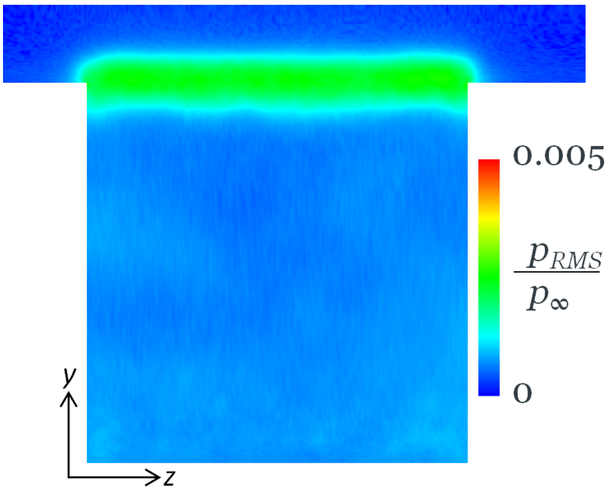

Figure 8.44: Contours of RMS pressure from plane at $x = x_{LE} + 0.5D$ for cavity with side walls

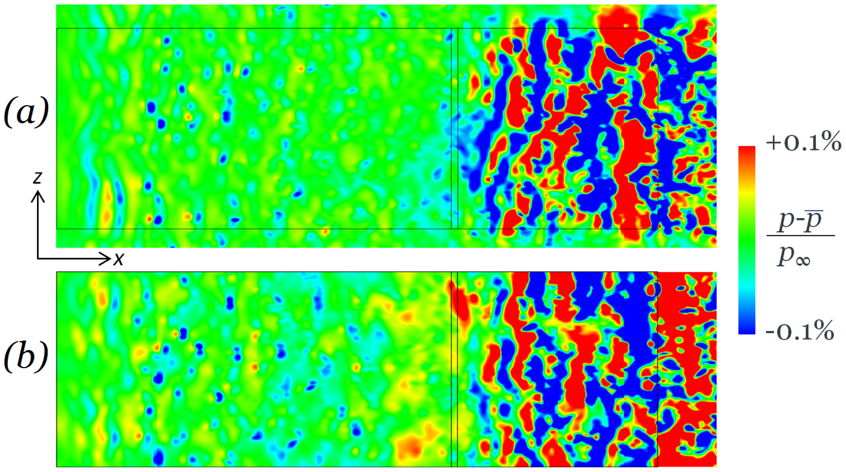

Figure 8.45: Contours of instantaneous perturbation pressure from plane at $y = 0.05D$: (a) cavity with side walls; (b) cavity without side walls (periodic in the span)

8.4.3 Inside the Cavity

Inside the cavity, the mean velocity at the mid-span is compared in Figure 8.46. The simulation with side walls has a less defined vortex in the covered section. Unlike the periodic-span condition, which allows the mean flow field to settle into a quasi-2D state, the side walls inside the cavity reflect pertubations in the w-velocity component. This causes a more chaotic/unsteady flow-field (affecting u and v as well), as evidenced by the higher turbulent kinetic energy inside the cavity seen in Figure 8.34. The turbulence inside the cavity particularly affects the covered-section vortex, which is weaker and has lower mean velocities.

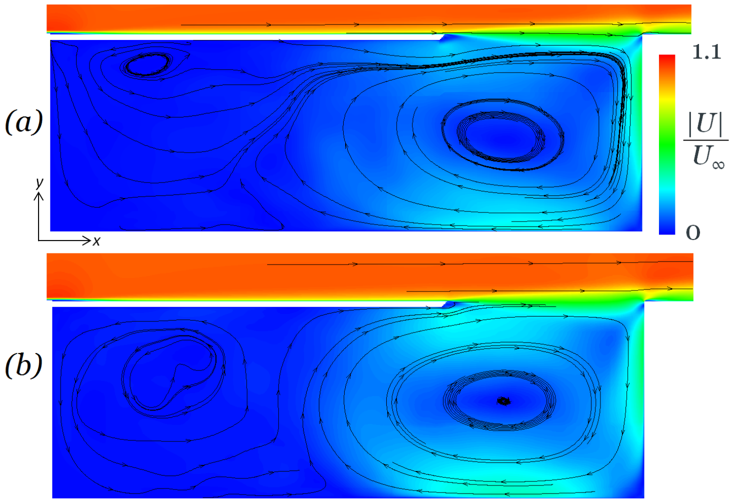

Figure 8.46: Contours of mean velocity from plane at mid-span ($z = 0$): (a) cavity with side walls; (b) cavity without side walls (periodic in the span)

The open-section vortex, which has a more regular and quasi-2D mean flow, still exhibits differences between the two simulations. Figure 8.46 shows that the velocity magnitudes around the vortex are lower with the side walls, indicating a weaker vortex. The strength an coherence of the vortex is reflected by the suction pressure at its core. The mean pressure at the mid-span plane is compared in Figure 8.47, and the simulation with side walls does indeed have a weaker low-pressure region in the centre of the open-section vortex. The pressure buildup on the bottom corner of the downstream wall is also lower with the side-wall configuration. This was observed to be the case throughout the span, albeit with a slight increase near the side walls. The high pressure in this region results from the impact of the flow directed downwards along the downstream wall, which forms part of the open-section vortex; therefore the difference in pressure in this region is another manifestation of the weaker vortex.

In the covered section of the cavity, the pressure is much closer to ambient in the simulation with side walls. It might be expected that the solid side walls would cause more of a build-up of pressure in this region of constrained flow. However, from the spanwise-periodic setup it was observed that the high mean pressure developing in the covered section is induced by the open-section vortex; from Section 8.3, comparing the $L_z/D = 0.25$ and $L_z/D = 1$ simulations, the narrower span had a stronger open-section vortex and a correspondingly higher buildup of pressure in the covered section. In the present simulations, the side walls further reduce the strength of the open-section vortex, and the covered-section pressure is thereby also weaker.

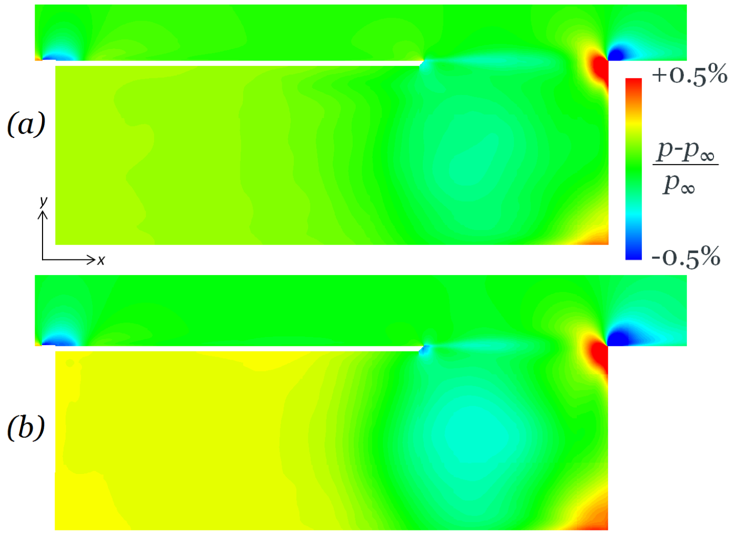

Figure 8.47: Contours of mean pressure from plane at mid-span: (a) cavity with side walls; (b) cavity without side walls (periodic in the span)

The interference of the side walls with the open-section vortex core can be seen more clearly by plotting the mean pressure on a finer scale. Figure 8.48 shows slice planes through the centre of the open-section vortex (at $y = -0.5D$ and $x = x_{LE} + 0.3D$). Both show that the low-pressure region associated with the vortex core is significantly reduced in the vicinity of the side walls (particularly within around $0.1D$ from the walls). The no-slip side wall condition and the associated boundary layer prevent the vortical flow field from extending all the way to the edges. The low-pressure region takes an almost circular form in the $Y - Z$ plane, and an oval shape in the $X - Z$ plane, suggesting that the influence of the side walls is felt almost all the way through the cavity span. (The mean pressure distribution at the vortex core from the periodic-span setup was effectively uniform in the span direction.) Therefore, the influence of the sidewalls can be directly linked to the weakening of the open-section vortex and the associated effect on the mean pressure field. Additionally, the slightly higher level turbulent kinetic energy inside the cavity may also be disrupting the coherence of this vortex.

The frequency content halfway down the downstream wall of the cavity (i.e. at $x = x_{TE}, y = -0.5D$) is compared between the two simulations in Figure 8.49. The 4kHz peak noted in other simulations, and attributed to the $N_x = 2$ acoustic mode, is visible and similar across the two simulations. The $N_x = 3$ mode (6kHz) is significantly weakened by the presence of the side walls. The most striking difference, however, is that the introduction of the side walls produces another peak of almost equal magnitude to the $N_x = 2$ mode, at a frequency corresponding to Rossiter mode $m = 2$. As discussed, a weak tone at this frequency was observed at a few points in the shear layer, but of an amplitude barely distinguishable from the surrounding frequencies. Inside the cavity, however, away from the high broadband levels in the shear layer (caused by the resolved boundary layer

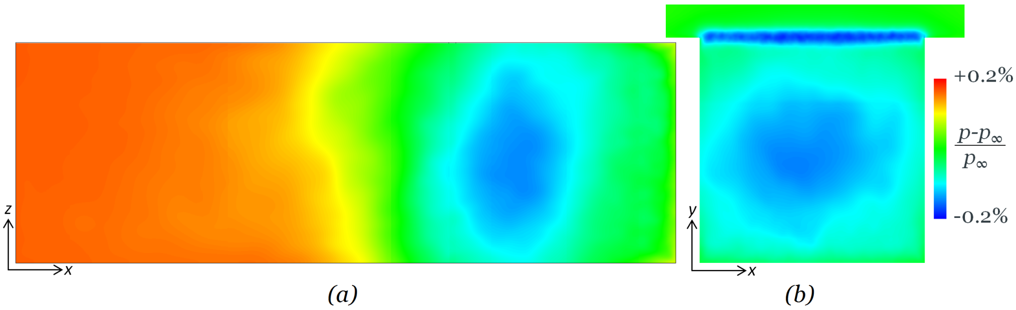

Figure 8.48: Contours of mean pressure from simulation of cavity with side walls; (a) at mid-depth ($y = -0.5D$ (b) at $x_{LE} + 0.3D$, near the centre of the open-section vortex

structures from the upstream flow), this mode now appears quite significant. Moving downwards along the x_{TE} wall, Figure 8.50 shows that further into the cavity the two tones become more pronounced. Therefore, the shear layer $m = 2$ resonance - although barely distinguishable in the shear layer itself - does appear to be present in this simulation. It has a strong influence on the flow inside the cavity, which appears to lock onto this frequency.

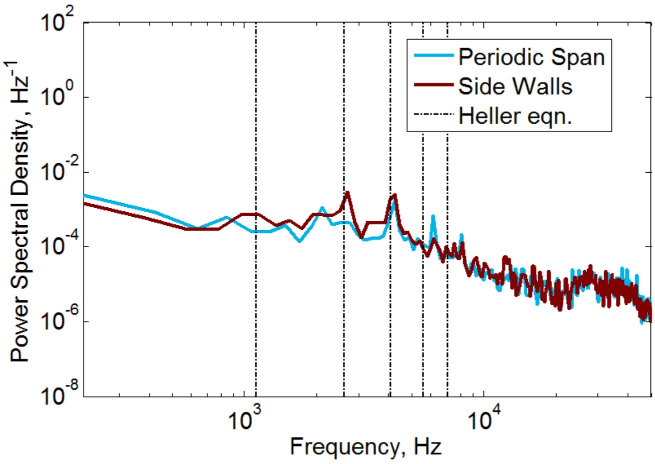

Figure 8.49: PSDs of pressure at monitor Point 14, at x_{TE} and mid-depth (as shown in Figure 8.3)

A small tone was also observed in the shear layer at $m = 3$, which coincides in frequency with $N_x = 2$ ($f = 4.1$kHz vs 4kHz) and may be reinforcing that mechanism. Figure 8.49 suggests that the 4kHz peak is slightly higher from the simulation with side walls than in the periodic-span simulation. The RMS pressure at the mid-span plane is compared in Figure 8.51 and shows that inside the cavity, the vertical bands of high p_{RMS} corresponding to the $N_x = 2$ mode are slightly higher with the side walls, which is consistent with the idea that this mode is reinforced by the corresponding stronger $m = 3$ tone in the shear layer.

Pressure monitors at Point 30, in the open section, are compared in Figure 8.52, along with an inset comparing this location with the mean streamlines from the simulation with side walls (at the same mid-span plane). This point is amost exactly at the centre of the open-section vortex. With the side walls, the f_2 frequency is strong; stronger even than

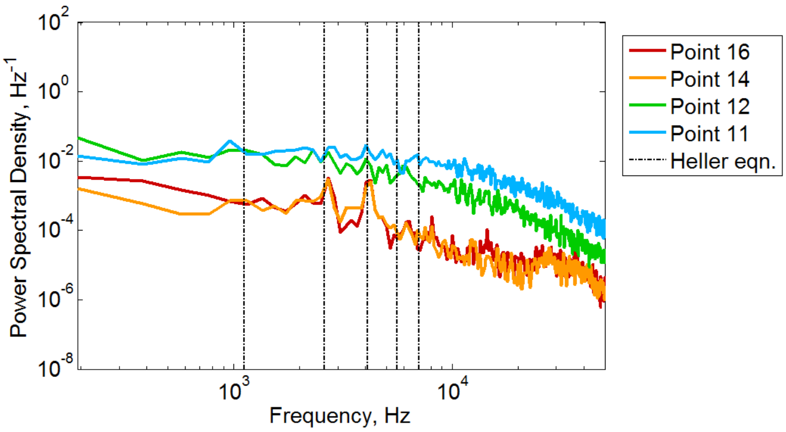

Figure 8.50: PSDs of pressure at monitors from the simulation with side walls, at various points on the downstream wall ($x = x_{TE}$; points are as shown in Figure 8.3)

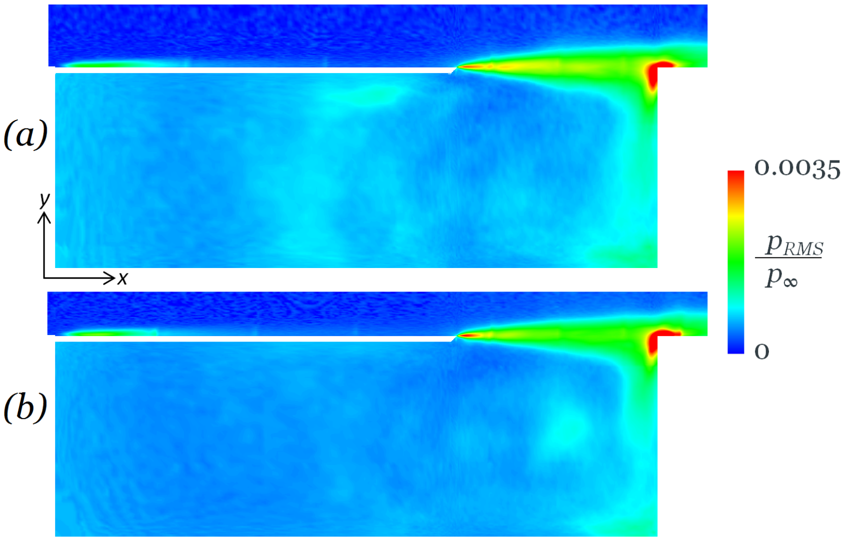

Figure 8.51: Contours of RMS pressure from plane at mid-span: (a) cavity with side walls; (b) cavity without side walls (periodic in the span)

the $N_x = 2$ mode, making the second Rossiter mode the dominant tone in this location. Peaks at $N_x = 3, 4, 5$ are still present with the side walls.

Around the x_{LE} lip, the pressure monitor at the underside of the edge is compared with the pressure monitor downstream in Figure 8.53. The two points are not far from each other, but the Point 21 monitor is located in the open-section vortex, and at the underside of the cavity cover, away from the turbulent shear layer. Point 1 is located in the vertical middle of the shear layer, $0.05D$ downstream of x_{LE}. The comparison of the pressure monitors shows that the small peak near f_2 in the shear layer, which is barely visible above the noise at surrounding frequencies, directly corresponds to a more significant peak at the same frequency inside the cavity. This follows the trend observed along the downstream wall in Figure 8.50; the turbulent boundary layer/shear layer contains fluctuations with high PSD levels almost evenly across all frequencies, but shear-layer resonant modes are still developing, and the flow inside the cavity locks onto those resonant mode frequencies.

Moving further upstream, under the covered section, pressure monitors at $x_{LE} - D$ were

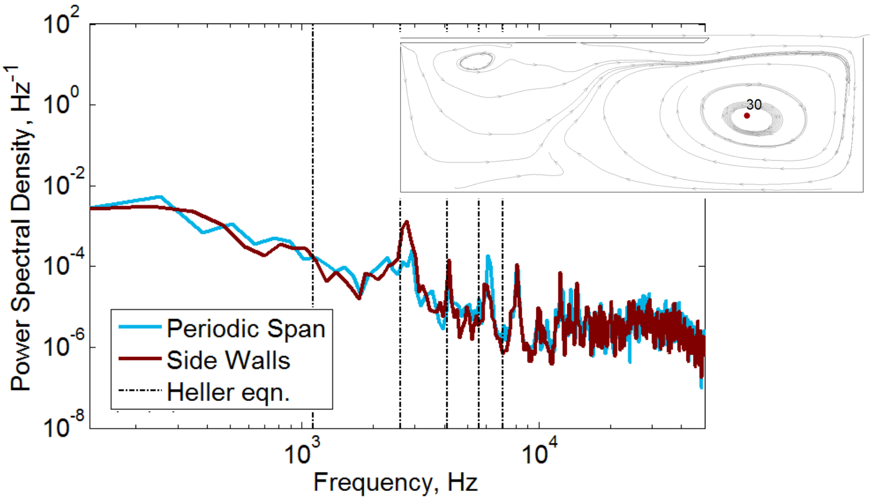

Figure 8.52: PSDs of pressure at monitor Point 30 (as shown in Figure 8.3); inset: location of Point 30 relative to mean streamlines from side-walls simulation

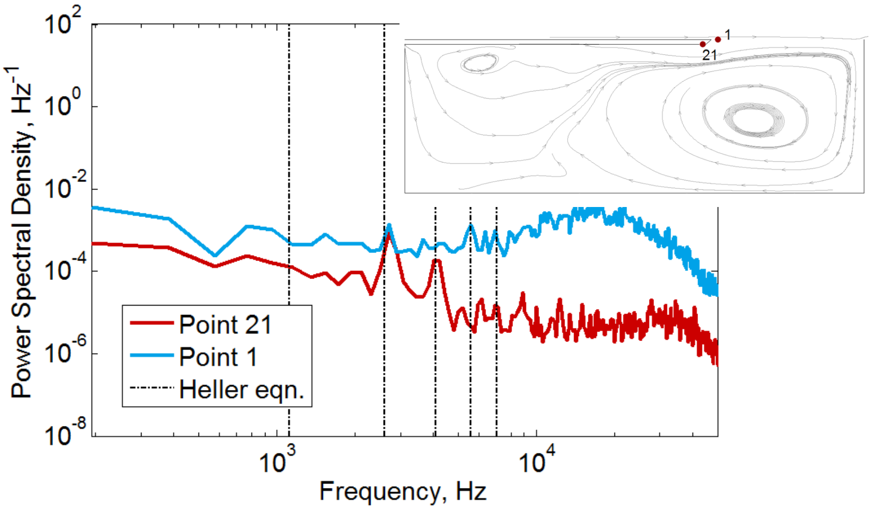

Figure 8.53: PSDs of pressure at monitor Points 21 and 1 (as shown in Figure 8.3) from simulation with side walls; inset: location of Point 30 relative to mean streamlines from side-walls simulation

found to have significantly weaker $m = 2$ tones than in the surrounding regions, both at the top and the bottom of the cavity (Figure 8.54). Comparison of the monitor locations with the mean streamlines (Figure 8.54, inset) shows that these points may be considered as being between near the border between the two vortex structures. Further upstream (into the covered section) from here, the f_2 tone becomes stronger again. The interaction between the two vortices appears, therefore, to have a detrimental effect on the f_2 resonance inside the cavity. However, this does not affect the $m = 3/N_x = 2$ frequency. Another mode is also visible at 1kHz, which is within the frequency resolution of the $m = 1$ shear layer mode, $f_1 = 1.1$kHz. (Reducing the number of windows from $n = 9$ to 5, to increase the frequency resolution, was observed to bring this tone to 1.05kHz.) It is concluded that this tone corresponds to a resonating of the $m = 1$ frequency. Some points in the shear layer were also observed to show small peaks at f_1 (see, for example, Figure 8.42).

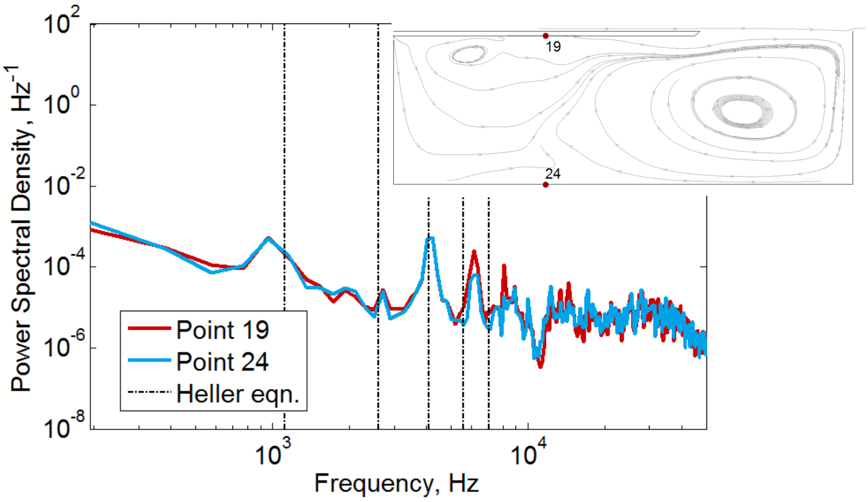

Figure 8.54: PSDs of pressure at monitors at $x = x_{LE} - 0.5D$, from simulation with side walls; inset: locations of monitor points relative to mean streamlines

Moving upstream to the wall of the covered section, the tone at f_1 was observed to grow stronger in the covered section. Figure 8.55 compares the pressure monitor at the at the mid-depth of the cavity on the back wall, with and without side walls. The side walls cause a weakening of the $N_x = 1$ and $N_x = 3$ modes. Strong tones are introduced corresponding to the first two Rossiter modes, with the tones at $m = 1$, $m = 2$ and $m = 3/N_x = 2$ being of similar amplitudes in the simulation with side walls. At the upstream wall of the cavity, Figure 8.56 shows that there is no difference in the strength of the three dominant tones between the top, mid-depth and bottom of the cavity. The frequency content is therefore largely constant through the depth at this location.

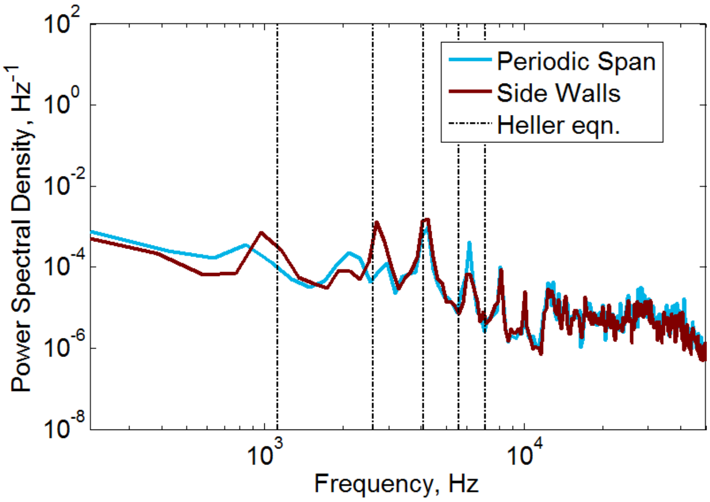

Figure 8.55: PSDs of pressure at monitor Point 27 (on upstream wall of cavity, at mid-depth, as shown in Figure 8.3)

The presence of the f_1 and f_2 tones inside the cavity, and especially in the covered section, suggests a similar resonance mechanism as was observed in the DDES analysis of cavities with side walls in Section 5.7. Resonant shear-layer modes impose pressure fluctuations on the open section, which are then transmitted upstream to the covered section with

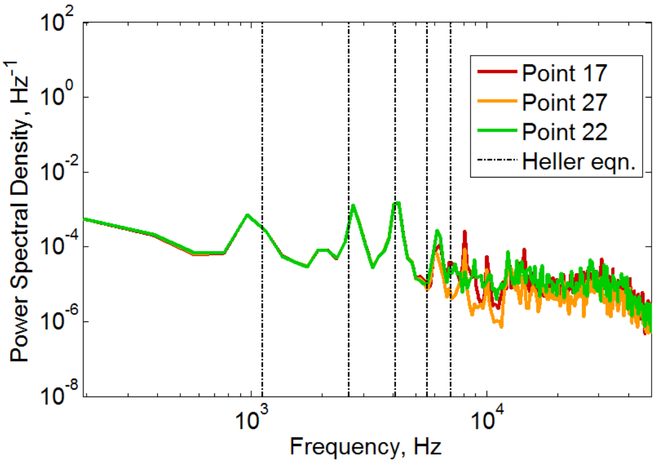

Figure 8.56: PSDs of pressure at monitors from simulation with side walls along the upstream wall of the cavity (top, mid-depth and bottom; locations are as shown in Figure 8.3)

a phase lag, causing an alternating build-up and release of pressure inside the partially-covered cavity, where the flow is constrained by the side walls. The pressure fluctuations from this pattern were observed from the DDES to be mostly uniform across the depth and span. In this case, however, lengthwise acoustic modes appear to be developing as well, as seen by the tones at higher harmonics of 2kHz. Plots of the instantaneous perturbation pressure from the simulation with side walls are shown in Figure 8.57 at the mid-depth and mid-span planes. Some smaller-scale unsteadiness is present inside the cavity, but overall it is confirmed that the pressure variations occur mainly in the lengthwise (x) direction, particularly in the upstream (covered) section of the cavity.

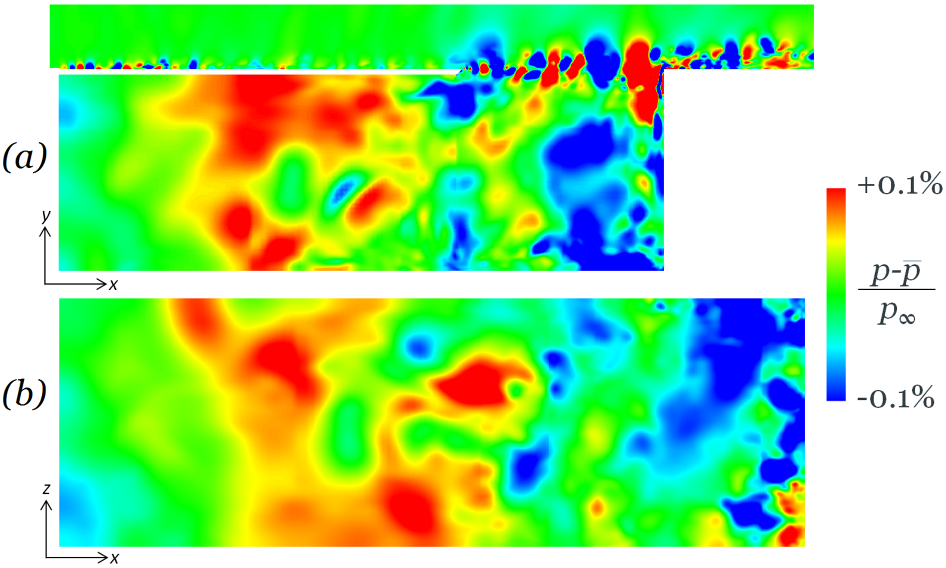

Figure 8.57: Contours of instantaneous perturbation velocity from simulation with side walls: (a) plane at mid-span $z = 0$; (b) plane at mid-depth ($y = -0.5D$)

It is not clear exactly why the presence of the side walls enables the shear layer to develop more low-mode shear layer resonance than the periodic-span simulation. One possible explanation is that the influence of the walls affects the local thickness of the shear layer.

The mean velocity contours at the mid-x plane (Figure 8.36) showed a downward deflection of the shear layer near the side walls. This might be effectively making the shear layer thinner in this region, and thinner shear layers (from thinner upstream boundary layers, at least) are more prone to resonance [30].

Compared with the DES analysis of the same geometry (with the side wall) at a larger scale and with a thicker boundary layer in Section 5.7, the same $m = 1$ and $m = 2$ tones were observed to dominate in the upstream covered section, and throughout the cavity, with the $m = 1$ tone growing stronger towards the upstream wall. The instantaneous pressure field from the DES simulation also showed the main pressure variation in the lengthwise direction, with very little in the span and depth directions. The similarity of these resonance characteristics suggests that the presence of these features may be determined by the geometry, and therefore be relatively insensitive to scale and the condition of the boundary layer.

The main differences between the present simulation and the DES from Section 5.7 are: in the DES the structures were more coherent, due presumably to the lack of unsteady boundary layer flow feeding into the shear layer; the strength of the reverberation inside the cavity caused a significant increase in p_{RMS} towards the upstream (covered-section) wall, which is not observed in the LES; and no acoustic tones were observed inside the cavity, as are observed here. The differences in the setup are the scale, the boundary layer thickness and the addition of resolved boundary layer turbulent structures. Scale effects have been shown to be fairly small, although a scale comparison was not performed with the LES cavity. It seems likely that the 'jittering' of the resonant shear structures is the main cause of the differences, as the would account for a weakening of the shear-layer induced pressure variations, and therefore allow the acoustic modes to develop; this would also explain the weaker p_{RMS} inside the cavity. However the mean boundary layer thickness may be a factor as well. It would be of interest, in future studies, to compare these effects separately.

It should be noted that the upstream boundary layer thickness has not changed from the baseline, and according to the experiments of Ahuja et al [30], the present $\delta/L_{open} = 0.064$ is expected to suppress most shear layer resonance. However even the periodic-span cases showed some suggestion of shear layer resonance, and shear layer resonance is definitely occuring in this case. Those authors measured tones using a microphone outside the cavity, whereas here the analysis is based on direct pressure measurements in the cavity and shear layer. However, an additional monitor placed above the open section of the cavity (at $x = x_{LE} + 0.25D, y = 0.2D$) showed that the PSD exhibited a small but distinct peak at f_2, confirming that the shear layer tone is perceptible outside the cavity (as expected), so the difference in conclusions is not due to the measurement location.

There are several other differences between the present simulation and the experiments of Ahuja et al [30], to which the difference in the development of shear layer resonance may be attributed. Most notably, there is the additional covered section in the present study. Also, the Mach number is slightly lower in the present work (currently 0.25, vs 0.40 in [30]); the L_{open}/D ratio over the open section is also lower (1 vs 3.75); and the W/L_{open} ratio is different (1 vs 2.1). The width is the least likely to have an effect, as those authors found the cavity flow to be effectively 2D at those dimensions, and the present work finds the unsteady pressure characteristics to be uniform across the span as well. The covered section is the biggest difference between the two cases, and the most likely cause of the difference in resonant behaviour, although more investigation would be required to determine whether the different dimensions of the open section are a factor.

8.4.4 Conclusion

The addition of no-slip side walls caused the development of small low-frequency shear-layer resonant modes. The fluctuations in the shear layer imposed pressure fluctuations on the cavity flow, which locked on to those frequencies. Modes 1 and 2 were found to be dominant. The fluctuation pressure inside the cavity showed relatively little variation in the depth and span directions, and the low-mode tones were found to increase in strength towards the upstream (covered-section) part of the cavity. All of this is consistent with observations from the DES analysis of the partially-covered cavity with side walls in Chapter 5. This suggests that these characteristics are not as sensitive to the modelling method or the upstream boundary layer; it appears to be a physical response to the presence of side walls in this partially-covered cavity configuration. These physical characteristics of the flow field are of interest from a research perspective, as they can inform future design efforts to minimize the aeroacoustic response of the landing gear bay by altering the span geometry. The significant effect caused by the side walls on the flow field, with both modelling methods, also highlights the importance of resolving the no-slip side walls in order to accurately model the features of the cavity flow. The change in shear layer dominant modes, and the amplification of the pressure fluctuations inside the cavity, are both important to capture from a practical perspective, as they will affect the loads applied on other components and transmitted through the aircraft.

8.5 Summary

Simulations were successfully performed using LES on a wall-resolved turbulent boundary layer upstream of a partially-covered cavity. Using a baseline quarter-span spanwise-periodic configuration, the turbulent boundary layer structures were found to interfere with the development of resonant structures in the shear layer. Still, a weak shear-layer resonance does appear to develop, coupling with a lengthwise acoustic-mode resonance inside the cavity which occurs at a similar frequency. Increasing the width of the periodic-span domain allowed more spanwise fluctuations to develop in the open-section vortex. The quarter-span width has an overly coherent open-section vortex, which affects the mean pressure field inside the cavity. All other characteristics of the flow field, however, were found to be consistent between the two span widths. In this respect this LES analysis is more robust than the DES discussed in Section 5.6. Adding side walls to the wide cavity allowed small resonant modes ($m = 1$ and 2) to develop in the shear layer. These tones were strong enough to impose pressure fluctuations on the cavity flow, which locked on to those frequencies in a similar manner as observed from the previous DES analysis. However, lengthwise acoustic modes were still observed to co-exist inside the cavity.

The simulations detailed in this chapter are identical in their $X-Y$ geometries, modelling methods and upstream boundary conditions, in order to isolate the effect of the span boundary. This is consistent with the research objective about exploring the sensitivity of the cavity flow to span effects, which has now been dealt with both from a DES perspective and using LES with resolved upstream boundary layer turbulence. The effect of the modelling method and upstream boundary layer will be explored (another of the original research objectives) in the next Chapter, by comparing the effect of changing these parameters. For the sake of computational efficiency, the spanwise-periodic configuration will be used, with $L_z/D = 0.25$. As discussed previously in this Chapter, this will cause a slight overprediction in the relative pressure amplitudes, but the velocity field and resonance characteristics will still be representative of the quasi-2D characteristics of the cavity flow.

Chapter 9

LES Study of Variations on the Baseline Partially-Covered Cavity Simulation

9.1 Overview

The purpose of this chapter is to explore the sensitivity of the LES partially-covered cavity simulations from Chapter 8 to changes in the modelling technique, upstream boundary layer, and some changes in the geometry. This serves to address the research objective about exploring the effect of the upstream turbulence and boundary layer characteristics on this partially-covered cavity configuration. The same LES methodology developed from the guidelines in Chapter 7, and implemented in Chapter 8, will be applied. The same baseline geometry is used, as shown in Figure 8.1, with the same $M_\infty = 0.25$, $D = 0.0285$m, and $\delta_0 = 5 \times 10^{-4}$m.

As discussed at the end of Chapter 8, the quasi-2D (spanwise-periodic) simulation with $L_z/D = 0.25$ will be used as a baseline. The time constraints of the study would not allow a parameter study for the simulation with side walls, although that would certainly be of interest and could be explored in future work. In terms of the span width, as discussed in Section 8.3, aside from the strength and coherence of the open-section vortex core, the two spanwise extents gave fundamentally the same behaviour and spectral responses. Therefore even with $L_z/D = 0.25$ the results should be representative of the 2-D characteristics of the cavity, with the best efficiency in terms of computational expense. Unless otherwise specified, all numerical and modelling settings in this Chapter are identical to that of Chapter 8.

The parameters explored may be broadly classified as being either of numerical or physical interest. From a computational modelling perspective, it is of interest to understand how differences in the modelling technique affect the simulation results. This will inform future work in this area about the necessity of resolving the boundary layer turbulence, and the modelling method. To explore this, the following two cases were compared to the baseline:

- A completely laminar upstream boundary layer, where the upstream tripping step is omitted, and the boundary layer remains laminar up to the cavity leading edge (Section 9.2). This investigates the necessity of tripping the flow, and how the resolved turbulence affects the cavity flow field when all other parameters and modelling methods are the same. This comparison is also of some interest from a physical perspective, comparing an incoming lamianar boundary layer condition against the turbulent boundary layer.

- For a turbulent boundary layer, comparison of the effect of the turbulence modelling method, by contrasting the baseline LES against a DDES simulation (Section 9.3). In this case the geometry is the same, so the comparison is directly between LES and DDES.

Some variations in the baseline geometry were also tested. This part of the study is of more interest from practical perspective, to inform future design efforts by identifying how sensitive (or not) the flow field is to these changes. The following modifications were applied:

- A comparison of the partially-covered cavity simulation with a square cavity using the same modelling methods and gridding parameters (Section 9.4). The purpose of this is to isolate the effect of the upstream covered section, by comparing it against a geometry where this section is effectively removed.
- An investigation of the sensitivity of the flow to the geometry at the lip (the leading edge of the open section) of the partially-covered cavity (Section 9.5). The interdependance of this with the modelling method (LES vs. DDES) is also tested, so this section is combination of physical and numerical parameters.
- An investigation of the sensitivity of the cavity flow to the boundary layer thickness, by reducing the upstream development length (Section 9.6).

9.2 Boundary Layer Condition: Laminar vs Turbulent

9.2.1 Upstream Boundary Layer

The geometry used in this section is the same as the baseline geometry (Figure 8.1), but with the step removed. In the absence of the step, the upstream boundary layer remains laminar until it reaches the cavity.

The mean boundary layer thickness is compared between the two simulations in Figure 9.1. The growth in the turbulent boundary layer downstream of the step is clearly visible; the laminar boundary layer grows at a slower steady rate. The edge of Figure 9.1 is at x_{LE} ($x = 0.0645$m), so the slight drop-off in both boundary layer thicknesses is due to the influence of the cavity propagating upstream. No vortex structures (in terms of the Q-criterion) were observed developing in the upstream boundary layer in the laminar case, so there is no suggestion of natural transition. Since a Blasius boundary layer is imposed at the inlet, it is reasonable to expect that for the laminar case, in the absence of tripping or transition, a well-developed laminar flow would remain throughout the upstream boundary layer. This is confirmed by the shape factor H_{12}, which maintains a fairly constant value of $H_{12} = 2.66$; this within 3% of the value observed from experimental analysis of a laminar boundary layer [33]. Therefore the upstream laminar boundary layer appears to be correctly modelled.

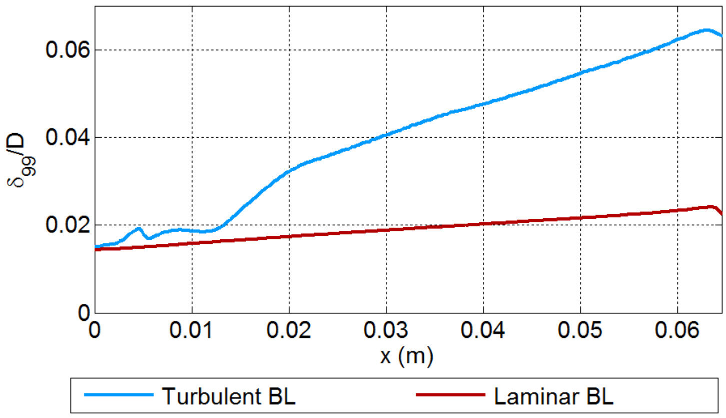

Figure 9.1: Growth of time-averaged boundary layer thickness upstream of the cavity, comparing laminar and turbulent LES simulations.

An idea of whether shear layer resonance is expected can be obtained from the upstream boundary layer thickness and the guidelines from past studies on resonance described in Section 2.4.5. The momentum thickness θ evaluated just upstream of x_{LE} equates to $\theta/L_{open} = 0.0033$. According to one set of parameter ranges [75], resonance occurs for $0.0065 < \theta/L < 0.0125$, therefore this simulation would not resonate according to those guidelines. From the guidelines of Sarohia [76], resonance would require $(L/\delta)(Re_\delta)^{0.5} > 290$ (for $D/\delta > 2$) and $\theta/L > 0.01$. The current simulations satisfies the former condition ($(L/\delta)(Re_\delta)^{0.5} = 2550$ and $D/\delta = 45$), but fails the latter. Experiments have found [57] that when the former condition is satisfied but the latter is not, the laminar-upstream cavity does not exhibit shear layer resonance. Therefore based on these parameters, the simulation with the laminar boundary layer upstream is expected to be non-resonating in the shear layer. It is noted though the those experiments were performed at $M < 0.05$, so the behaviour here with $M = 0.3$ might be different.

9.2.2 Shear Layer

Iso-surfaces of the Q-criterion are compared between the turbulent and laminar upstream boundary layers in Figure 9.2. The lack of vortical structures in the upstream boundary layer in Figure 9.2(b) confirms that the flow stays laminar in this region. At the cavity, however, the shear layer vortex structures begin to show spanwise variation very soon after x_{LE}, and then the vortices break down into smaller structures, indicating a transition to turbulence beginning from early in the shear layer. According to the literature [76], transition to turbulence in the shear layer is expected for $\theta/L < 0.01$, where θ denotes the momentum thickness). The value here is well below that ($\theta/L_{open} = 0.0033$), so the propensity for transition is observed here is consistent. Shear layer transition has been associated with a loss of resonance for very low Mach numbers [76]. The side-view of

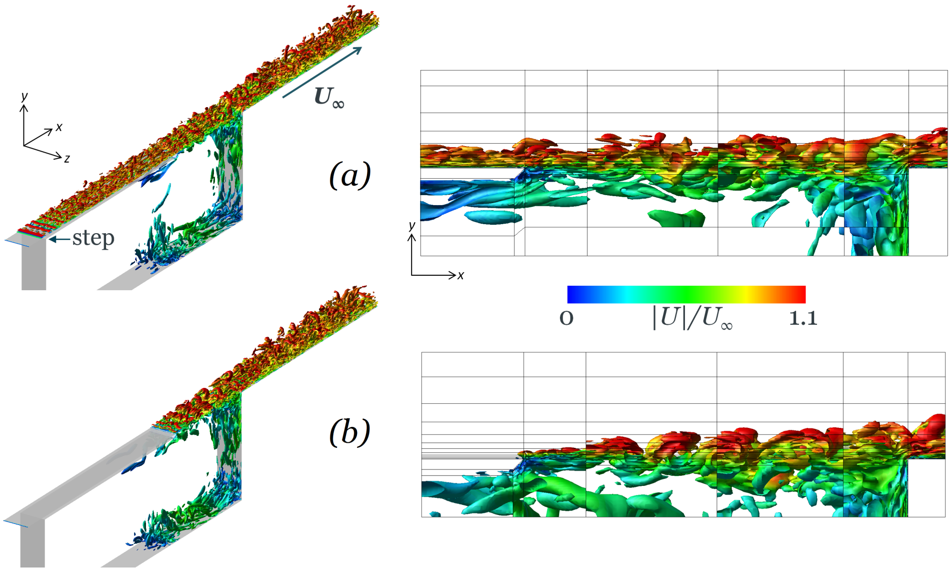

Figure 9.2: Iso-surfaces of the Q-criterion coloured by velocity magnitude, 3D view and side view; (a) turbulent boundary layer (baseline simulation); (b) laminar boundary layer

the Q-criterion in Figure 9.2 appears to show some regular vortex shedding across the shear layer in the upstream-laminar case. The structures are not perfectly distinct, and they grown more difficult to distinguish in the downstream half of the shear layer. The downstream half of the shear layer is visually similar betwen the two cases, dominated by small-scale turbulent structures.

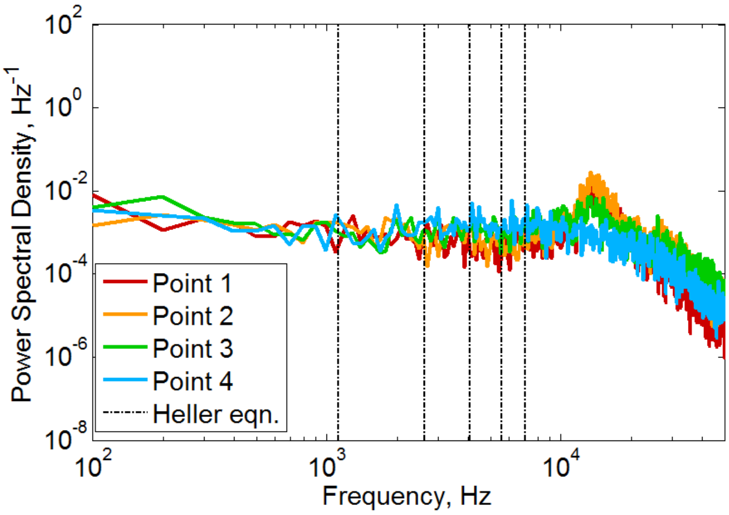

Figure 9.3: PSDs of pressure at monitors in the upstream half of the shear layer from the laminar LES simulation. Point locations are as shown in Figure 8.3.

Power spectral densities of pressure in the upstream half of the shear layer are compared in Figure 9.3. There are no sharp tonal peaks corresponding to the first few Rossiter modes. The hump at high frequencies diminishes moving downstream. In the turbulent simulation this was attributed to the influence of the lip vortex on the shear layer. However, comparing the pressure monitors between the two simulations in the vicinity of the lip vortex (Figure 9.4), the peak from the upstream-laminar case is more defined (i.e. narrower).

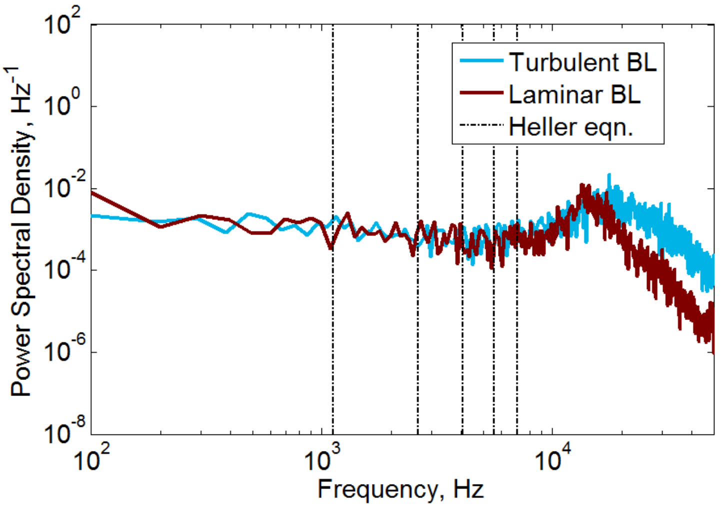

Figure 9.4: PSDs of pressure at monitor Point 1, $x_{LE} + 0.05D$, comparing turbulent and laminar upstream boundary layers

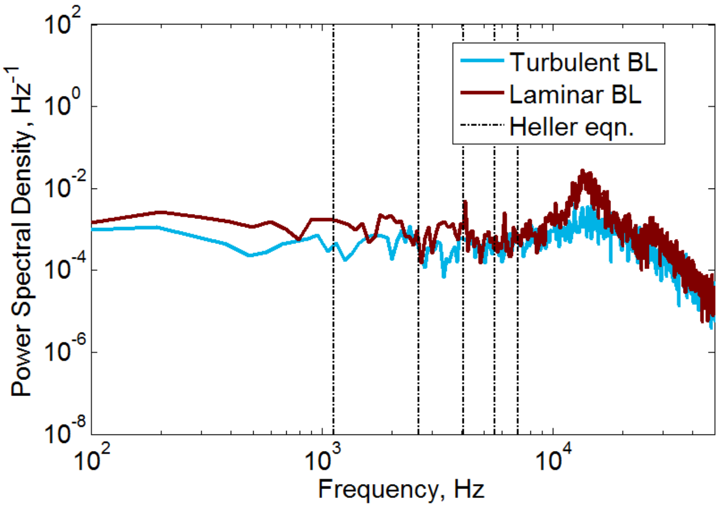

Figure 9.5: PSDs of pressure at monitor Point 2, $x_{LE} + 0.25D$, comparing turbulent and laminar upstream boundary layers

The frequencies are also slightly different; the peak from the upstream-laminar case is at $f \approx$ 13-14kHz, compared to $f \approx$ 18kHz for the turbulent boundary layer. Further downstream, at $x_{LE}+0.25D$, this high-frequency peak is significantly stronger with the laminar boundary layer (Figure 9.5), whereas in the upstream-turbulent simulation this feature is almost diminished by this point. Comparison of the lip vortex (Figure 9.6) does not show a significant difference in the size and extent of this feature between the two simulations; not enough to explain the difference in the frequency content at $x_{LE} + 0.25D$.

The pressure monitor at Point 2 also shows small peaks at 4kHz and 6kHz, and Point 5 also showed a small peak at 4kHz. The peaks at 4kHz indicate Rossiter mode 3 resonance, and the additional peak at 6kHz is suggestive of the longitudinal acoustic modes developing inside the cavity which will be explored in the next subsection.

Therefore, this high-frequency peak from the laminar-upstream case is probably linked to the vortex structures observed in the upstream shear layer in Figure 9.2(b), and may

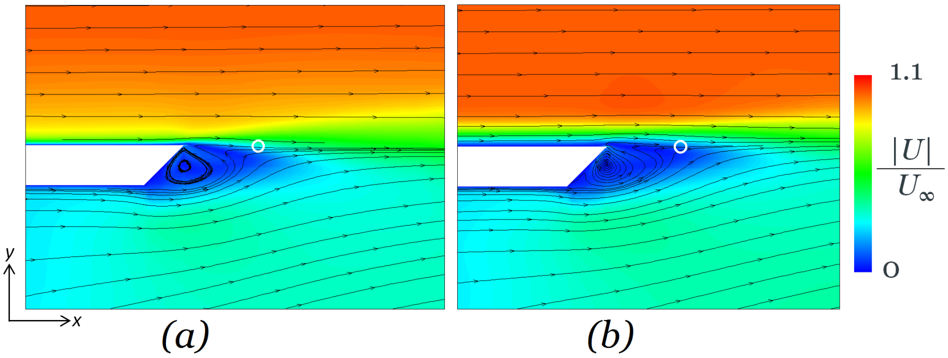

Figure 9.6: Contours of mean velocity and streamlines in the vicinity of x_{LE}; (a) from baseline (turbulent) simulation; (b) from laminar-upstream boundary layer simulation. White circles represent the location of Point 1 ($x_{LE} + 0.05D$).

therefore be an indication of shear layer resonance. The spacing of the structures equates to $\lambda/L_{open} \approx 0.13$, as estimated from the Q-criterion plots. For a Rossiter mode, this corresponds to mode $m = 9$, according to rearrangement of the Heller equation [62] (Equation 2.6). The associated frequency is f_9 = 13kHz, in good agreement with the high-frequency hump in Figure 9.5, where the peak $f \approx$ 13kHz. In the downstream half of the shear layer, the vortex structures are less defined (Figure 9.2), and the tonal peaks at this frequency were shown to become correspondingly weaker. Rossiter mode resonance does require reinforcing acoustic feedback from the cavity trailing edge, which means that the shear layer at the trailing edge must still contain some of that resonant tone. This is more easily visualized in terms of the pressure field; Figure 9.7 shows an example of the instantaneous perturbation pressure, at the mid-z plane. Circular pressure waves emanating from the trailing edge are visible (a classic feature of resonating Rossiter flows [14]). At this instance the wavelength corresponds to the pressure oscillations in the shear layer, still with $\lambda/L_{open} \approx 0.13$. Overall, therefore, it appears that the upstream-laminar case does produce resonance in the shear layer, at a higher mode (and with more easily distinguished vortex structures) than with the upstream-turbulent case.

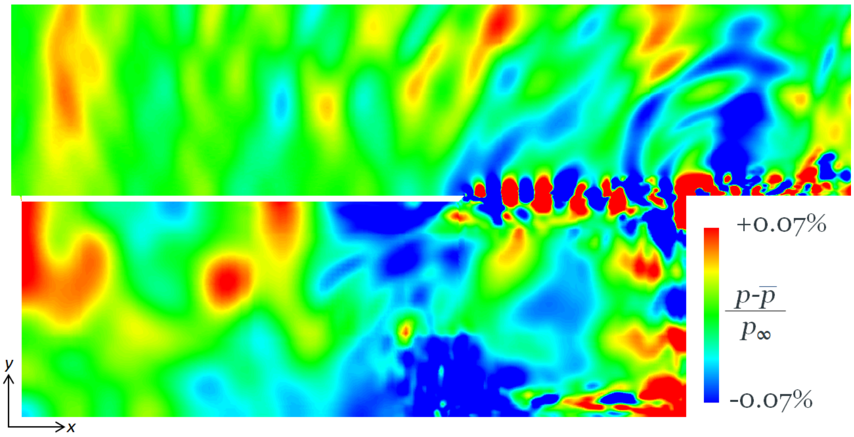

Figure 9.7: Instantaneous contours of perturbation pressure from LES simulation with laminar upstream boundary layer

The time-averaged turbulent kinetic energy, compared in Figure 9.8, showed higher levels of k from the laminar boundary layer, particularly in the upstream half, likely due to the coherent resonant vortex structures. Near x_{TE} the levels become more similar. The thickness of the shear layer, in terms of the band of high k, grows quickly from x_{LE} for about $0.2D$, but after this the shear layer thickness appears fairly similar between the two cases. The mean velocity field at the trailing edge was also found to be quite similar (Figure 9.9); the impingement of the shear layer just below the top of the wall, and the small recirculation bubble downstream of the cavity, are nearly identical. The span-averaged and time-averaged mean pressure on the top downstream corner of the cavity (Figure 9.10) are also similar. The upstream-laminar case produces slightly higher pressure levels overall; but the shape, and the location of the maximum pressure (i.e. the stagnation point of the shear layer streamlines), are identical. The shear layer in the upstream-laminar case underwent transition (from laminar to turbulent), so both simulations are turbulent in the downstream part of the shear layer, which is why the two cases have converged to similar flow-fields in this region. The same behaviour was observed by Grace et al [57] from an experimental comparison of laminar and turbulent upstream boundary layers in a cavity flow.

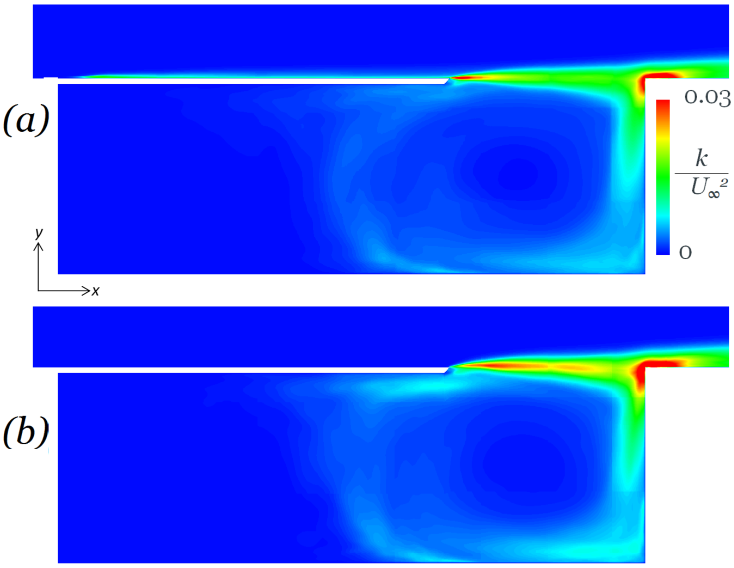

Figure 9.8: Contours of turbulent kinetic energy; (a) baseline (turbulent) simulation; (b) laminar-upstream boundary layer simulation

9.2.3 Inside the Cavity

Inside the cavity, the two simulations gave generally similar flow fields. The turbulent kinetic energy, plotted in Figure 9.8, showed slightly higher levels of k being swept around the open-section vortex, due to the higher levels in the shear layer which, in turn, have been attributed to the coherent vortex shedding in the upstream half of the shear layer. Otherwise, the shape and general trends of the kinetic energy distribution are quite similar. The mean velocity field does not show much sensitivity to the upstream boundary layer condition (Figure 9.11). The turbulent viscosity is at similar levels for both simulations as well. An example of the instantaneous turbulent viscosity ratio is shown in Figure 9.12.

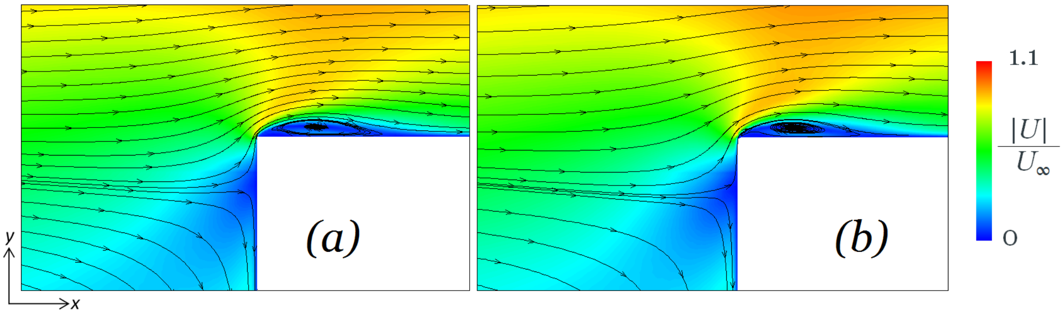

Figure 9.9: Contours of mean velocity and streamlines in the vicinity of x_{TE}; (a) from baseline (turbulent) simulation; (b) from laminar-upstream boundary layer simulation

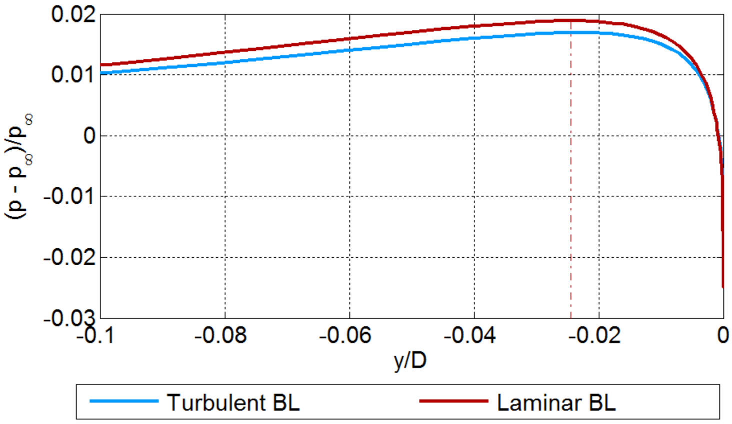

Figure 9.10: Comparison of mean pressure on the top of the downstream cavity wall, with laminar and turbulent boundary layers upstream

Aside from the upstream boundary layer and the very beginning of the shear layer, where the flow is steady and laminar, the SISM model gives generally similar values for both configurations.

The mean pressure field is compared in Figure 9.13. The laminar-upstream simulation exhibited the same slight downwards trend of open-section core pressure with simulation time, which makes the computed mean pressure slightly different due to differences in the averaging windows, as the laminar-upstream simulation took longer for the start-up transients to diminish. However, from comparing the individual pressure time histories, and the general trends from the mean pressure field, the mean pressure levels were generally found to be the same in both simulations.

The frequency content of the pressure monitors inside the cavity gave very similar results at all locations. An example is shown in Figure 9.14, for the pressure monitor on the cavity floor near x_{TE}. Interestingly, even the monitors under the upstream shear layer did not show the ≈ 13kHz peak associated with the upstream shear layer vortices. Instead, the flow was dominated by peaks at 4kHz, 6kHz, 8kHz etc., just as in the baseline simulation, indicative of lengthwise acoustic modes inside the cavity, with the laminar simulation having slightly higher tonal amplitudes. The same peaks were observed in the upstream (covered section) part of the cavity as well.

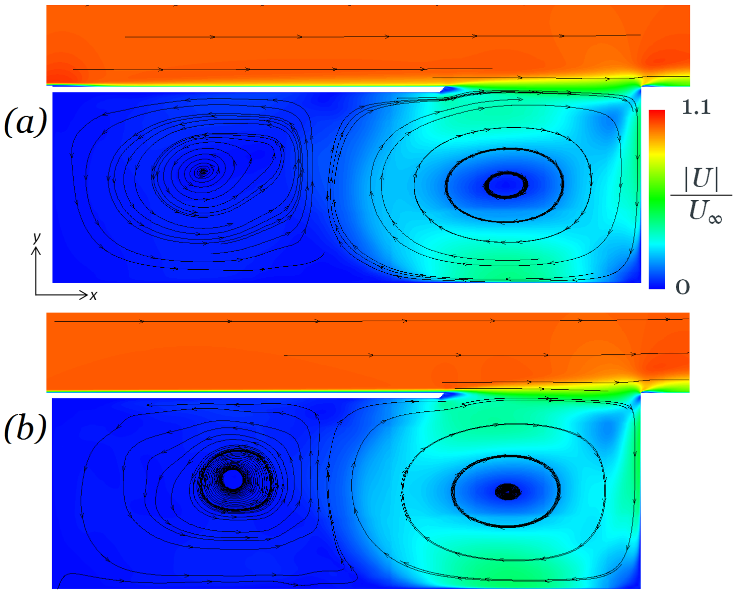

Figure 9.11: Contours of mean pressure field; (a) from baseline (turbulent) simulation; (b) from laminar-upstream boundary layer simulation

The RMS pressure field, compared in Figure 9.15, shows the same trends in both cases, and similar levels. The laminar-upstream boundary layer has a slightly higher p_{RMS} value in the upstream shear layer, due to the vortex shedding as discussed. The levels are also a little higher inside the cavity, as seen in the individual FFT data (Figure 9.14). Aside from the centre of the open-section vortex, the cavity flow shows alternating vertical bands of p_{RMS}, with two low-p_{RMS} bands, indicative of the two nodes of the standing wave associated with second-mode lengthwise resonance ($N_x = 2$). This is consistent with the pressure monitors which all showed peak frequencies at 4kHz. These bands are slightly more distinguishable (on the same scale) than in the turbulent-upstream boundary layer, illustrating that this wave is slightly stronger in the laminar-upstream simulation.
A likely explanation for this is that Rossiter-mode resonance developing in the shear layer (as indicated by the upstream-propagating acoustic feedback waves in Figure 9.7) has a mode 3 component, which is supported by some of the pressure PSD data in the shear layer (e.g. Figure 9.5). This tone is stronger in the shear layer than in the upstream-turbulent case (as the 4kHz tone was not clearly in any of the shear layer PSDs in that case), due most likely to the smoother development of coherent vortex structures in the shear layer, in the absence of interference from upstream-turbulent boundary layer vortical structures. This $m = 2$ tone amplifies the $N_x = 2$ acoustic mode, as in the baseline case, and the stronger shear layer mode therefore leads to a stronger acoustic mode as well, as seen in the higher tonal peaks inside the cavity for the upstream-laminar case. Overall, therefore, this shear layer flow can be broadly classified as resonating, which differs from the predictions from the literature. Those predictions, however, were generally based on $M_\infty < 0.05$ flows, so the acoustic feedback component of shear layer resonance is expected to behave differently in the current case. The covered section may also play a role, as it causes a stronger development of the acoustic mode inside this cavity, at a frequency which amplifies the $m = 3$ shear layer mode.

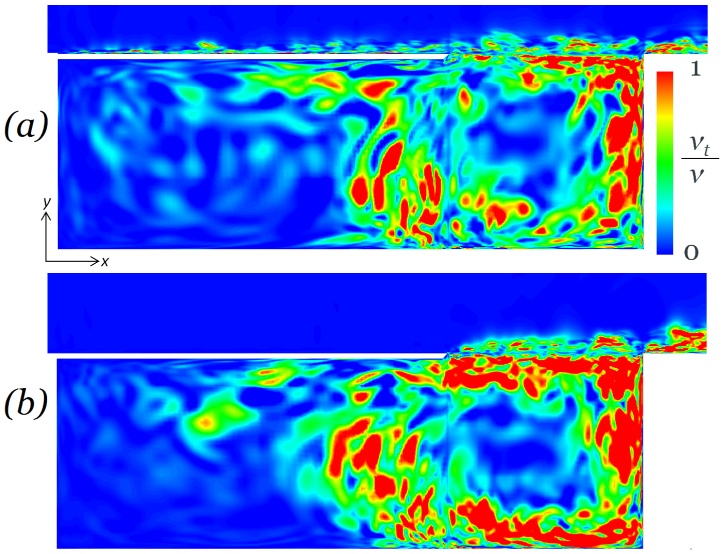

Figure 9.12: Contours of instantaneous turbulent viscosity ratio; (a) from baseline (turbulent) simulation; (b) from laminar-upstream boundary layer simulation

9.2.4 Conclusion

Switching from a turbulent upstream boundary layer to a laminar boundary layer was observed to increase the strength of the shear layer resonance. A high-mode ($m = 9$) tone was observed, especially pronounced in the upstream half of the shear layer (where the flow is less turbulent) and a weak tone at $m = 3$ was also measured in the shear layer. The increased strength of shear layer resonance is most likely due to the absence of the 'jittering'/weakening effect from resolved upstream turbulent boundary layer structures, consistent with trends from the literature [18]. This differs from the prediction based on the literature that this cavity should be non-resonating, although in this case the Mach number is significantly higher ($M = 0.25$, vs $M < 0.1$ from the literature) and this higher Mach number range has generally been found to be be more likely to promote shear layer aeroacoustic resonance [14]. The shear layer begins to undergo transition to turbulence soon after the cavity leading edge, so the two simulations give similar flow fields towards the trailing edge, indicating that the mean flow in the impingement region is not very sensitive to upstream boundary-layer condition. Inside the cavity, the same lengthwise-acoustic-mode tones were observed in both cases. The laminar-upstream case produced slightly stronger tones, due to stronger reinforcement of the $N_x = 2$ tone by the stronger $m = 3$ shear layer tone.

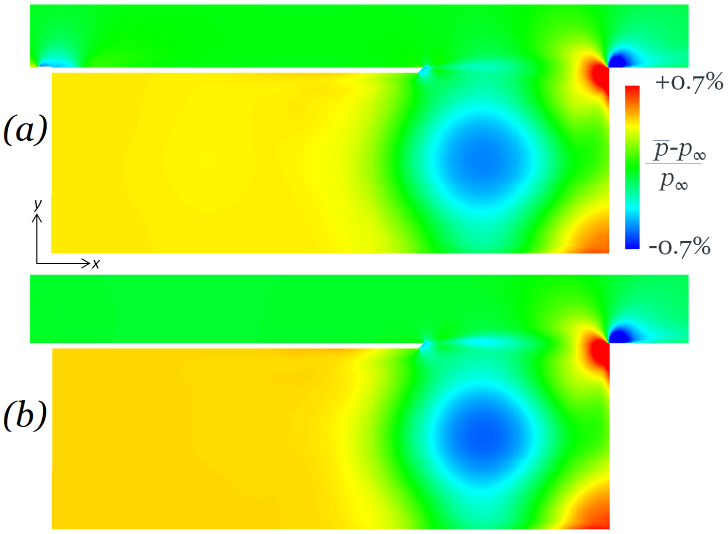

Figure 9.13: Contours of mean pressure field; (a) from baseline (turbulent) simulation; (b) from laminar-upstream boundary layer simulation

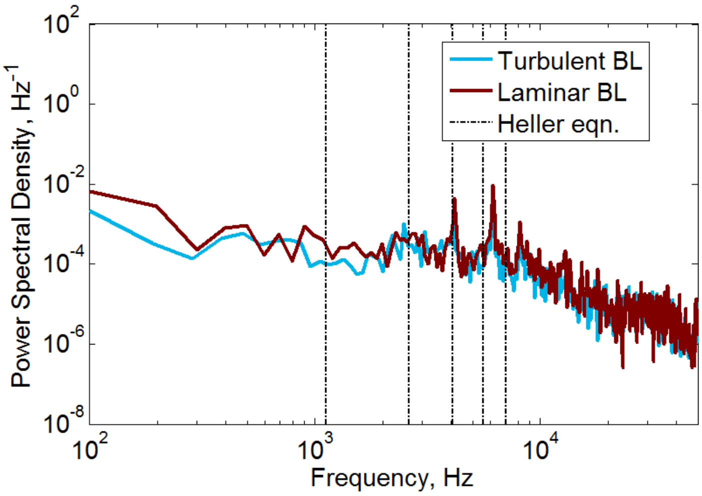

Figure 9.14: PSDs of pressure at monitor Point 26, on cavity floor near x_{LE} (see Figure 8.3, comparing turbulent and laminar upstream boundary layers

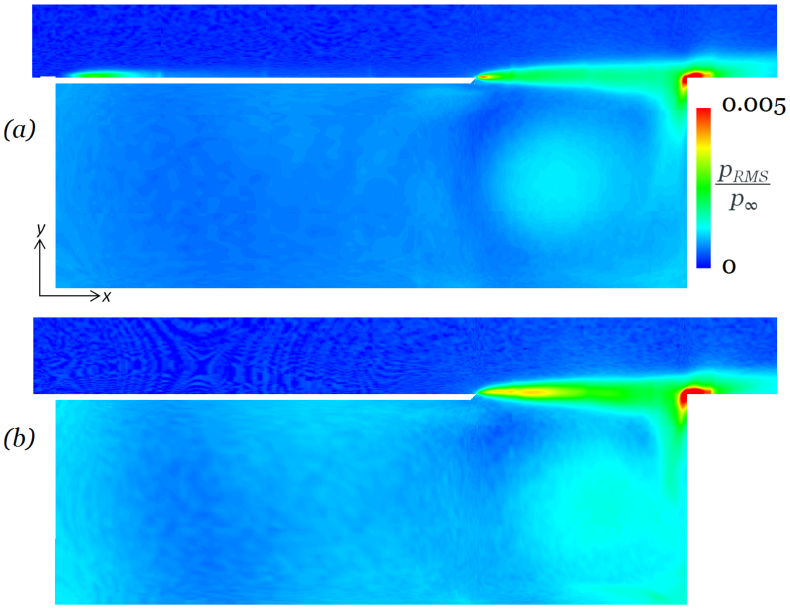

Figure 9.15: Contours of RMS pressure field; (a) from baseline (turbulent) simulation; (b) from laminar-upstream boundary layer simulation

9.3 Turbulence Modelling Method

9.3.1 DES Methodology

For comparison, a DES simulation was also performed on the same geometry as the baseline case. The same DDES methodology was used as in previous chapters. The grid, timestep, and filtering settings were all identical to the LES simulation.

The same initial field (from the developed 2D solution) was used as in the LES simulation. However, plotting the DDES variable f_d ((Figure 9.16(a)) showed that the initial developed solution retained a region of $f_d = 0$ in the open section of the cavity. The turbulent viscosity in the centre of this region was correspondingly very high (up to $\nu_t/\nu = 800$) since the RANS lengthscale d is based on distance to the wall. Analysis of the flow field indicated that the issue was the initial 2D RANS simulation, which gives a high ν_t in this region for the same reason. The DDES variable r_d is proportional to $\nu_t + \nu$ (Equation 3.13). It is supposed to be 1 in a logarithmic boundary layer and drop to 0 towards the edge of the boundary layer, but it is possible that the high value of ν_t in the centre of the open section causes r_d to approach 1 in this region; this causes $f_d \to 0$, and thus the RANS region perpetuates forwards through time. However this theory does not explain why all previous simulations were able to regain $f_d = 1$ in the same region from similar initial fields. This illustrates the necessity of carefully checking the DDES treatment.

To fix this, the flow-field from a developed DDES simulation (taken at $T/T^* = 78$) was modified so that inside the cavity, values of $\nu_t/\nu > 20$ were limited to $\nu_t/\nu = 1$. This was then used as a new initial field for the final simulation. The plot of f_d (Figure 9.16(b)) confirmed that the correct DES behaviour was retained throughout the cavity, and was maintained throughout the rest of the simulation time. This modified simulation is used for all the results presented in this section.

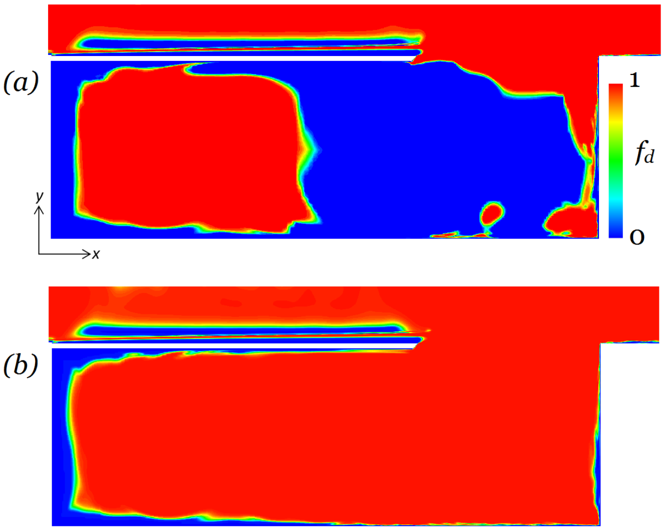

Figure 9.16: Instantaneous DDES variable f_d; (a) initial simulation, developed from initial 2D RANS field; (b) final simulation, developed from initial-field with ν_t limited

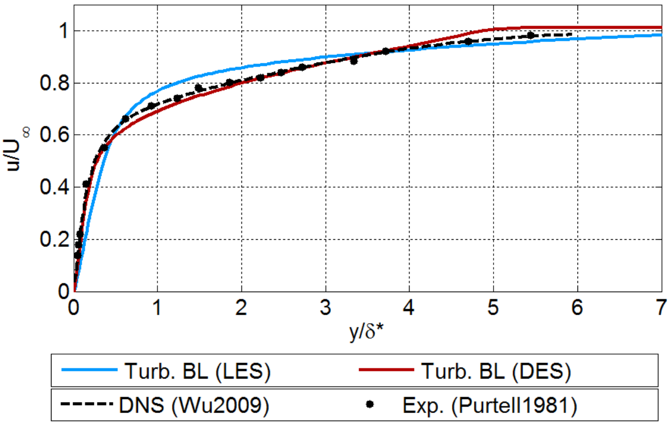

Figure 9.17: Normalized boundary layer velocity profile at $0.7D$ upstream of x_{TE}, comparing LES and DES

9.3.2 Upstream Boundary Layer

Since the DES uses RANS in the attached boundary layer, the steady upstream boundary layer properties are expected to be well predicted. Taking a slice $0.7D$ upstream of x_{LE} (Figure 9.17), the boundary layer profile from DES gives better agreement to the literature than the LES. It should be noted that although the experimental data is measured at $Re_\theta = 1000$, the DES at this location has $Re_\theta \approx 900$ but the LES has $Re_\theta \approx 700$; the discrepancy between the experiment and the LES is partly due to this. The LES does however give a smoother shape through the width of the boundary layer.

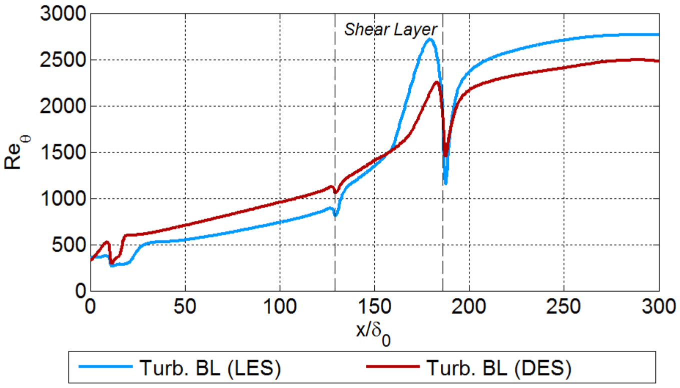

Figure 9.18: Growth of boundary layer momentum thickness, comparing LES and DES

The growth of the boundary layer in terms of momentum thickness θ is compared in Figure 9.18. The DES produces a higher momentum thickness, due partly to the fact that the boundary layer begins to develops turbulent mean quantities from the beginning of the plate (as seen in the sharp increase in θ within the first $10\delta_0$), whereas the LES simulation only begins to transition downstream of the step. (Downstream of the cavity, however, the DES predicts a significantly lower θ than the LES.) By the time the boundary layer reaches x_{LE}, the value of θ from the DES is 26% higher than in the LES. The displacement thickness δ^* showed the same trend, with the DES producing a value 27% higher than the LES. The shape factor H_{12} is therefore slightly higher with the DES, but throughout the developed turbulent boundary layer it is still within 5% of the $Re_\theta - H_{12}$ distribution from the literature [29,32]. The LES is within 2%, and so performs slightly better in this respect.

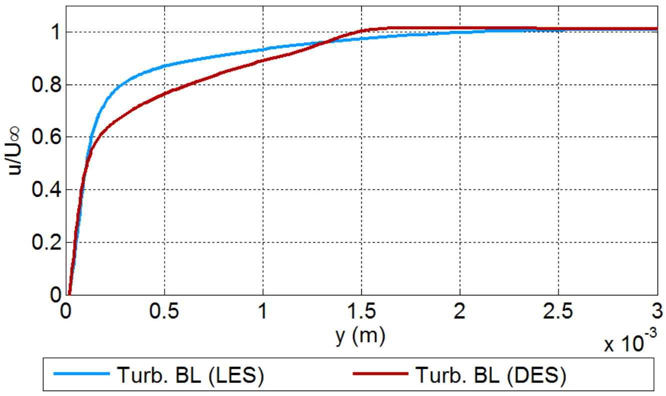

Figure 9.19: Boundary layer velocity profile in dimensional y units at x_{TE}, comparing LES and DES

At x_{LE}, the velocity profiles in dimensional y units are shown in Figure 9.19. Due to the difference in the velocity profiles, the LES has a higher 99% boundary layer thickness, even though the DES gives a larger θ and δ^* (the same trend is seen in Figure 9.17). Comparing the two cases, δ/L_{open} is 0.049 for the DES, compared to 0.063 from the LES. In terms of the unsteady quantities, the LES is of course able to resolve the boundary layer fluctuations, whereas the RANS boundary layer in the DES is not, so the LES produces much higher k at x_{LE} (Figure 9.20). A small amount of unsteadiness is observed in the DES simulation due to the influence of the shear layer and the lip vortex in the immediate vicinity. As little as $0.05D$ upstream, however, the turbulent kinetic energy in the DES boundary layer was observed to be effectively zero, as expected.

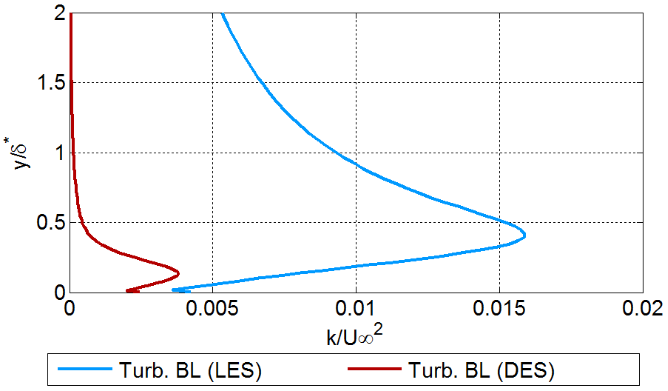

Figure 9.20: Boundary layer turbulent kinetic energy k at x_{LE}, comparing LES and DES

9.3.3 Shear Layer

Figure 9.21 compares the instantaneous iso-surfaces of the Q-criterion between the baseline LES simulation and the final DES. The side view shows that, unlike the LES simulation, the DES shear layer develops regular structures in the shear layer. The spacing between the structures equates to $\lambda/L_{open} \approx 0.4$; from Equation 2.6, for a shear layer resonant

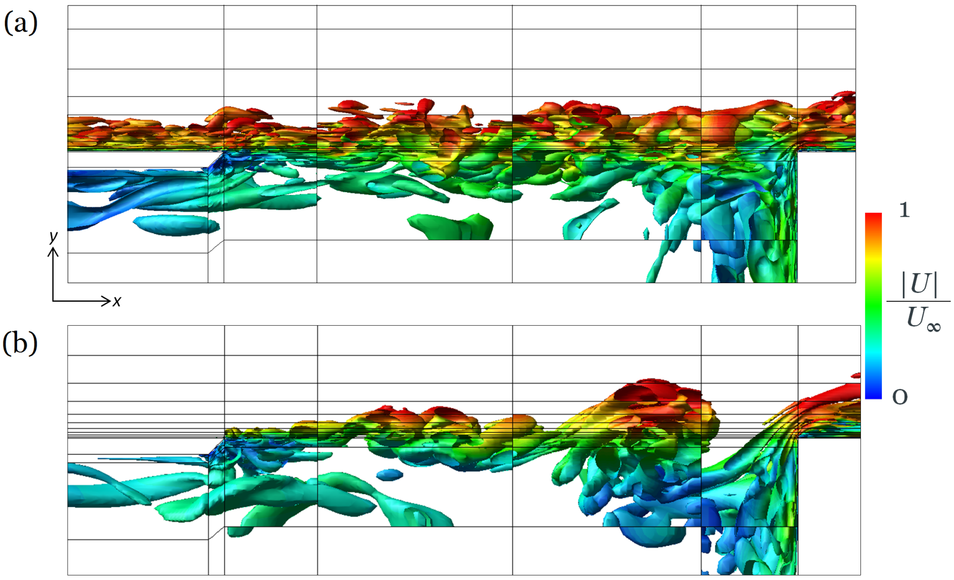

Figure 9.21: Iso-surfaces of the Q-criterion, coloured by velocity magnitude; (a) from baseline LES simulation; (b) from DES simulation

mode, this corresponds to a mode 3 resonance. The turbulent kinetic energy is shown in Figure 9.22.

One possible explanation for the stronger development of resonance in the DES is the thinner upstream boundary layer. The DES gives $\delta/L_{open} = 0.049$, which falls more significantly below the cutoff recommended by Ahuja et al [30], for resonance with a turbulent boundary layer. Another possible explanation is that the stronger resonance is due to the absence of the resolved turbulent boundary layer structures upstream of the cavity. The previous quarter-span DDES of the partially-covered cavity in Section 5.6 had a thicker boundary layer, equal to $\delta/L_{open} = 0.095$, significantly thicker than in the LES. Therefore it may be deduced that the weaker development of resonant shear layer structures in the LES is not due solely to the boundary layer thickness. Therefore, the effect is most likely caused by the influence of the vortical structures from the upstream boundary layer, interfering with the coherence of the shear layer resonance structures (the 'jittering' effect as discussed in Section 2.4.5, e.g [18]). The comparison between the present DES and the results from Section 5.6 is discussed further in Appendix A.

Comparing to the turbulent kinetic energy k (Figure 9.22), the DES shows lower values and a thinner band in in the upstream part of the shear layer, since is it is beginning from a steady (RANS) flow-field at x_{LE}. The mean velocity field near x_{LE} showed a recirculation region under the cover lip which was very similar between the LES and the DES. However, the band of k (and, correspondingly, the region of the unsteady shear layer) grows much wider with x than it did in the LES simulation, due most likely to the growth of the coherent vortex structures. This is particularly prominant in the downstream half of the cavity. (Figure 9.18 also illustrates this; the momentum thickness is calculated from $y = 0$ and above, so the values in the shear layer region may be considered roughly indicative of the half-thickness of the shear layer).

At the downstream end, the region of k near x_{TE} appears similar between the two cases.

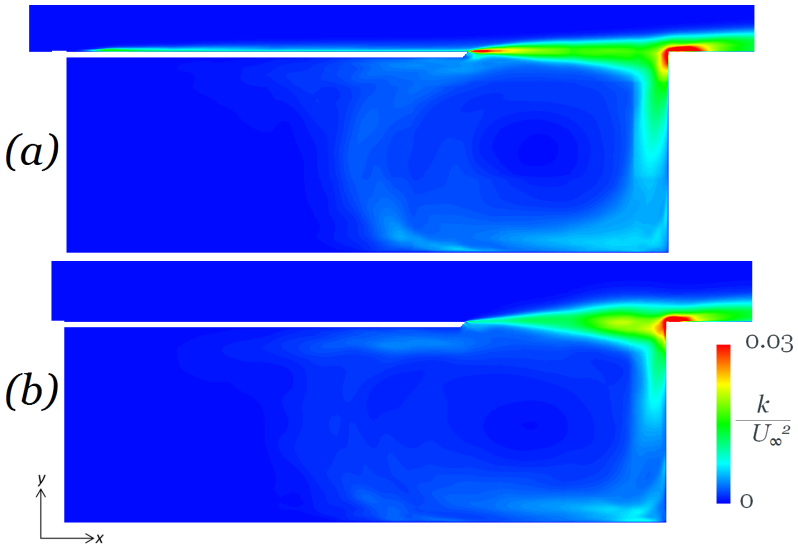

Figure 9.22: Contours of mean turbulent kinetic energy in $X-Y$ plane; (a) from baseline LES simulation; (b) from DES simulation

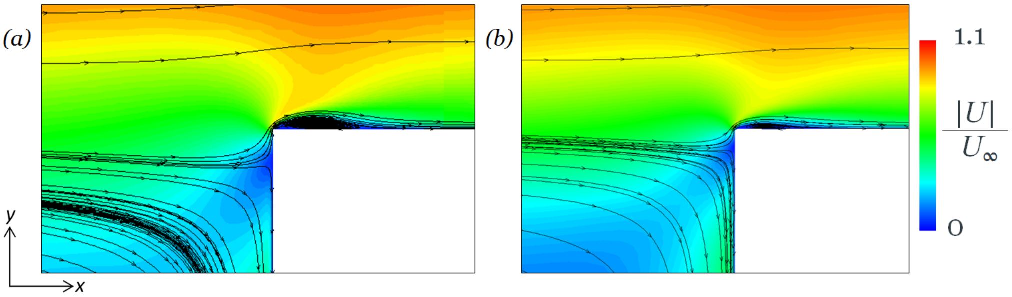

Figure 9.23: Contours of mean velocity, and streamlines, at cavity TE; (a) from baseline LES simulation; (b) from DES simulation

However, a side-by-side comparison of the mean velocity field in this region (Figure 9.23) shows that the DES shear layer streamlines are higher than in the LES, causing a higher point of impingement on the downstream wall and therefore a smaller recirculation bubble downstream of the cavity. This also explains the thinner boundary layer downstream of the cavity in the DES (Figure 9.18); the recirculation bubble causes a thickening of the boundary layer, and this is less pronounced in the DES simulation.

The frequency content of in the shear layer is illustrated in Figure 9.24, which shows the FFT at Point 1 (near x_{LE}) at Point 11 (at x_{TE}). A similar high-frequency spectral hump is observed at Point 1, likely associated with the lip vortex. The DES simulation produces significant tonal peaks, in contrast to the baseline LES simulation. The strongest peak is at 4kHz, which corresponds to the 3^{rd} Rossiter mode, in agreement with the vorticity structures observed in Figure 9.21. A smaller peak is present at 2.7kHz, which is within the frequency resolution of the 2^{nd} Rossiter mode. Tonal peaks are also observed at 2, 6, and 8kHz at various points along the shear layer, which suggests the presence of the same lengthwise acoustic modes, but strong enough in this case to show an influence in the shear layer.

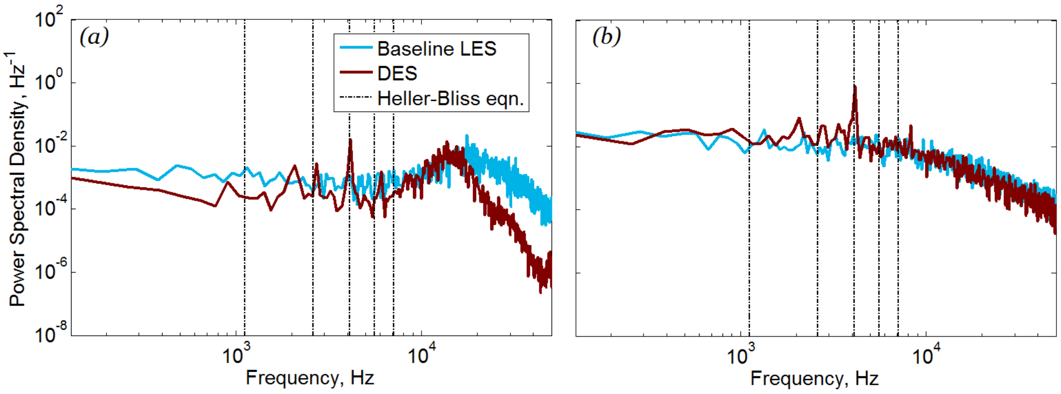

Figure 9.24: PSDs of pressure at monitors along the shear layer in the baseline LES cavity simulation; (a) at Point 1, near x_{LE}; (b) at Point 11, at x_{TE}. Point locations are as shown in Figure 8.3.

9.3.4 Inside the Cavity

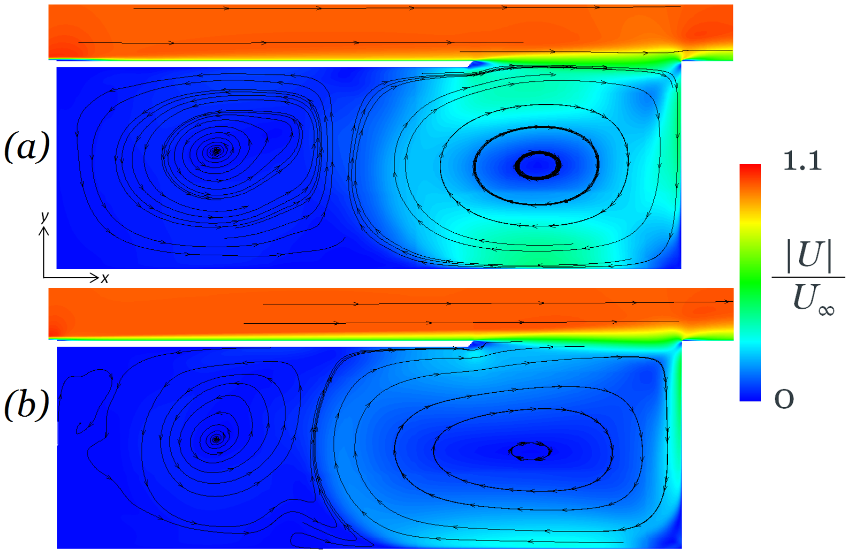

Figure 9.25: Contours of mean velocity; (a) from baseline LES simulation; (b) from DES simulation

Figure 9.25 compares the time-averaged mean velocity profile from the DES against the baseline LES. The same two-vortex structure is observed inside the cavity. The covered-section vortex is slightly smaller with the DES, and the mean velocity magnitudes in the open section are lower; the higher point of impingement on the downstream wall means that less of the higher-velocity shear layer flow is being directed into the cavity. The mean pressure fields also show a significant difference (Figure 9.26). On the upper edge of the downstream wall, the DES has a smaller high-pressure region, due to the higher shear layer impingement (and therefore smoother reattachment). The most significant difference between the two methods is inside the cavity, particularly in the upstream region where the DES gives a significantly lower mean pressure. The values are close to ambient throughout the cavity, aside from a low-pressure region at the centre of the open-section vortex. The pressure monitor at this point (Point 30) showed the same small downward drift with

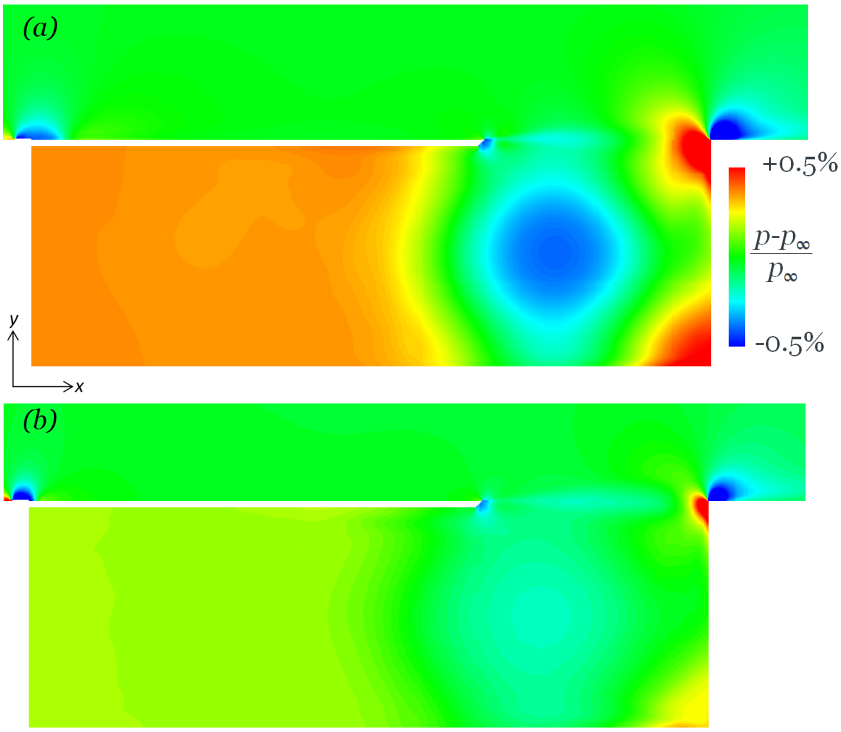

Figure 9.26: Contours of mean pressure; (a) from baseline LES simulation; (b) from DES simulation

solution time as was observed with the LES. (The initial simulation which used RANS in this region did not show this behaviour, suggesting that it is due to the combination of LES methodology in this region with the spanwise-periodic boundary limit.) The pressure monitors at other locations were stable with time.

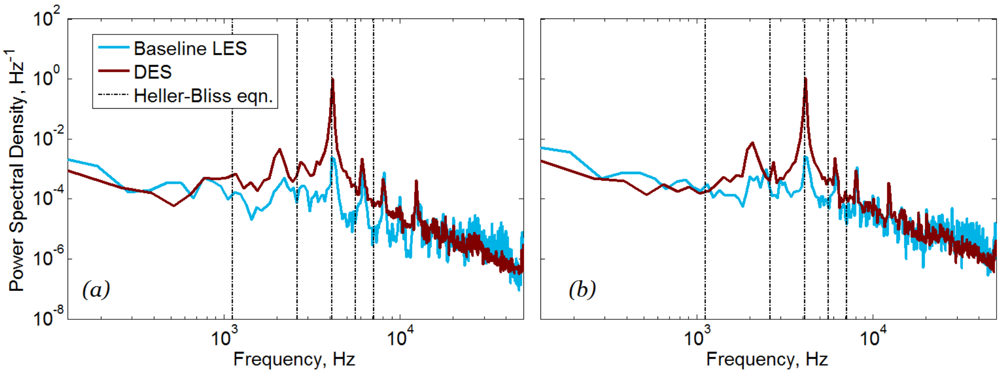

Figure 9.27: PSDs of pressure at monitors in the mid-depth of the cavity (a) at Point 27, near the upstream wall; (b) at Point 14, on the downstream wall. Point locations are as shown in Figure 8.3.

Comparisons of the pressure monitors at the mid-depth of the cavity are shown Figure 9.27, for the points nearest the upstream and downstream cavity walls. (Comparisons at other locations inside the cavity showed the same behaviour.) The 4kHz tone is also dominant with the DES, but much stronger in amplitude than with the LES. The DES also shows a significant peak at 2kHz, as well as the harmonics at 6, 8, and 12kHz. The 2kHz tone, and the other harmonics, clearly do not correspond to any Rossiter modes. As with the LES,

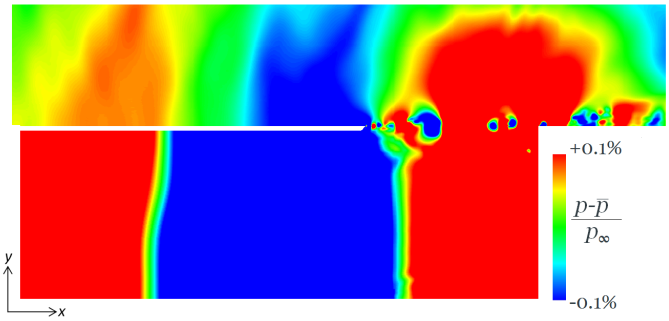

Figure 9.28: Snapshot of instantaneous perturbation pressure from DES simulation

the tonal peaks and harmonics suggest that the resonance is dominated by lengthwise acoustic modes. A small peak at the second Rossiter mode (near 2.7kHz) also perceptible in the open section, supporting the indication of a weak $m = 2$ resonance in the shear layer.

As with the LES, instantaneous perturbation pressures were captured across a cycle of the 4kHz frequency. One instance of this is shown in Figure 9.28. Plotted on the same scale as used in Figure 8.12, the DES simulation saturates over most of the flow field, in correspondance with the higher amplitudes observed in the pressure monitors. Still, the pattern of alternating high and low pressure across the length is clearly visible, and the shape - alternating high, to low, to high, as in a full cosine wave - agrees very well with the expected shape for an $N_x = 2$ acoustic mode, which corresponds to a 4kHz resonance, which was shown in all the FFT data to be strongly dominant.

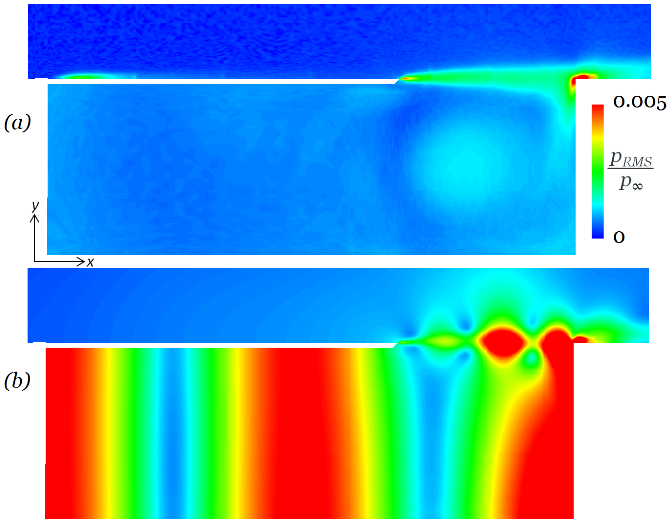

Figure 9.29: Contours of RMS pressure from mean field; (a) from baseline LES simulation; (b) from DES simulation

Therefore, the same modes are present regardless of the turbulence modelling method; but the amplitudes are much higher with the DES than with the LES. This is further confirmed by a comparison plot of P_{RMS} between the two methods (Figure 9.29). The DES shows clear vertical bands of high p_{RMS} inside the cavity, corresponding to the antinodes of the acoustic mode wave. In contrast, the LES simulation (on the same scale) shows much lower levels of p_{RMS}. Some fluctuations are present in the open-section vortex, and there is a slight increase at the inner upstream wall which could be associated with the acoustic modes, but it is much smaller and less clearly defined than in the DES. (The shear layer region in both cases show the same trends observed in the Q-criterion plot from Figure 9.21; slow, steady growth for the LES, and more rapid growth due to coherent resonant-mode structures in the DES.)

It is likely that the increased acoustic-mode strength in the DES is due to the strong shear layer resonance at $m = 3$, since the literature indicates that the shear layer modes locking on to the acoustic modes causes stronger tonal peaks (Section 2.4.5). This supports the idea that the resonance developing in the LES shear layer is much weaker, since the 4kHz tone inside the cavity - although dominant - is still much lower than in the DES. As discussed in the shear layer section, this is attributed to the 'jittering' effect of the upstream boundary layer vortex structures in the LES.

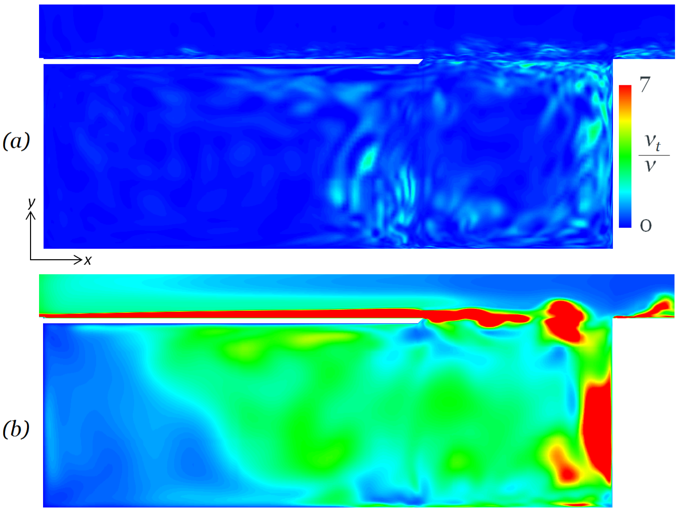

Figure 9.30: Contours of instantaneous turbulent viscosity ratio; (a) from baseline LES simulation; (b) from DES simulation

Although the DES is operating in LES mode in the cavity, the two methods still calculate the turbulent viscosity differently; DDES through the transport equation, and LES using the SISM model. The grid lengthscales are the same for both, but the resultant values are likely to be quite different. A comparison from an instantaneous flow-field is shown in Figure 9.30. The LES clearly has much lower values; $\nu_t/\nu \approx 0.2$ in the boundary layer (as discussed in Section 7.5), and generally $\nu_t/\nu \approx 1 - 2$ in the turbulent structures inside the cavity. The DES shows much higher turbulent viscosity in the upstream boundary layer - which is expected, since the treatment is RANS in this region - and similarly high levels in the region of the coherent vortex structures. Inside the cavity, $\nu_t/\nu \approx 3 - 7$. Of the two methods, therefore, even though the LES shows weaker fluctuations, the DES has a higher degree of turbulent viscosity.

9.3.5 Conclusion

Comparing the two turbulence modelling methods, the DES develops much stronger shear layer resonance at $m = 3$. This is attributed to the absence of the resolved upstream turbulent boundary layer structures, which disrupt the development of the shear layer resonance vortical structures, as described in the literature (e.g. [18]). In both cases, the tones inside the cavity are dominated by the lengthwise acoustic modes; however the amplitudes are much higher with the DES, most likely due to stronger reinforcement from the $m = 3$ shear layer mode which is at a similar frequency to the $N_x = 2$ mode. The strong acoustic modes inside the cavity affect the mean pressure field, as the acoustic standing wave drives the instantaneous pressure perturbations so that the overall mean pressure values are closer to ambient. In the shear layer, the DES simulation produces a higher point of impingement on the downstream wall and therefore a smaller recirculation bubble downstream. Overall, the DES analysis gives an indication of the resonant mechanism and dominant modes, which can be useful as a first approximation. However, the significant differences observed both in the tonal amplitudes and the mean fields illustrate the importance of modelling the upstream turbulent structures, for accurately quantifying the noise and unsteady loads in this cavity flow. Since LES is able to do this and DES is not, LES is recommended for this application and analysis of similar flows.

9.4 Covered-Cavity Geometry vs. Square

In order to examine the effect of the upstream covered section on the unsteady flow development, this section details a simulation that was performed on a modified geometry where the upstream section is closed, and only the square open section is exposed to the flow. The purpose of this is to isolate the effect of the partially-covered section of the cavity in the baseline geometry, as this is section is omitted here. In practice, this comparison may inform future design efforts for similar partially-covered cavity applications, by exploring how sensitive the flow is to the covered-section geometry. The geometry schematic is illustrated in Figure 9.31. All other geometry parameters, including the tripping step and the upstream boundary layer development, are kept the same. The same LES methodology as described in the baseline section is applied to the square geometry.

9.4.1 Shear Layer

Figure 9.32 compares iso-surfaces of the Q-criterion from the square cavity (Figure 9.32(a)) against the baseline partially-covered cavity. The turbulent boundary layer structures upstream are the same, as expected. Across the shear layer, both simulations show vortex structures of different sizes, with no distinguishable clear pattern. The square cavity has slightly larger structures and a generally thicker shear layer. This is likely due to the fact that turbulent structures inside the square cavity are directed upwards along the upstream wall, and therefore interact with the shear layer at x_{LE}. The partially-covered cavity also has structures convecting along the open-section vortex and back up along to the shear layer, but to a smaller degree.

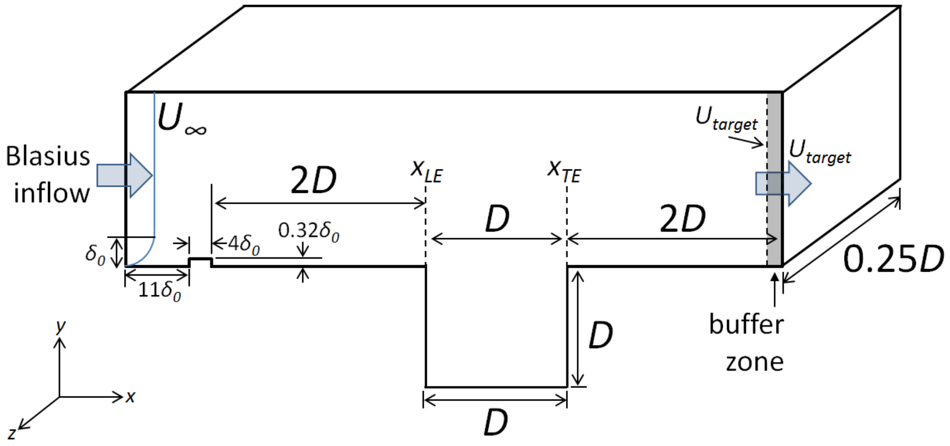

Figure 9.31: Schematic of geometry (not to scale) for square LES cavity simulations.

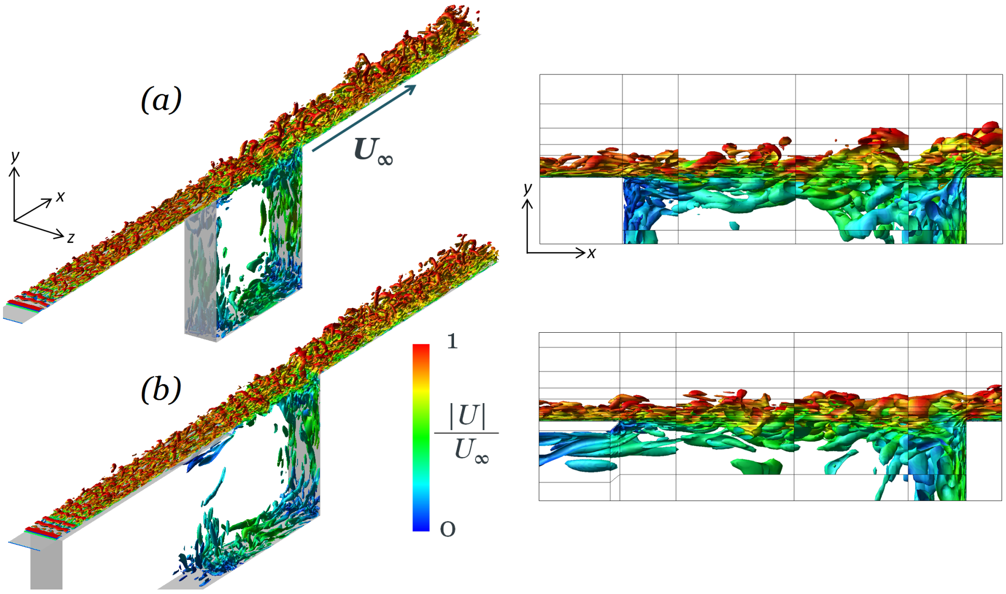

Figure 9.32: Iso-surfaces of the Q-criterion from LES simulations: (a) square cavity; (b) baseline partially-covered cavity

Close-ups of the mean flow at the cavity leading edge are compared in Figure 9.33. Both simulations show small vortices at x_{LE}; in the top upstream corner of the cavity for the square cavity, and in the slant of the cavity lip from the partially-covered cavity. The vortex structure from the slanted cavity lip sits higher, slightly pushing up the streamlines at x_{LE}, and appears to cause an immediate thickening in the shear layer. The square-cavity vortex is lower, so there is less interference with the shear layer, and a more level separation. The growth of the shear layer in the immediate vicinity of x_{TE} is therefore more steady, but the shear layer thickens at a similar rate moving downstream. The frequency content of the pressure monitor at Point 1 (which is just downstream of the small vortices, as indicated in Figure 9.33) is shown in Figure 9.34. The square cavity exhibits a small peak at around 6-6.3kHz. Since this does not correspond to a shear layer Rossiter mode, it is likely that this tone comes from an acoustic mode, as will be discussed in the next subsection. At higher frequencies, a similar spectral hump (peaking at around

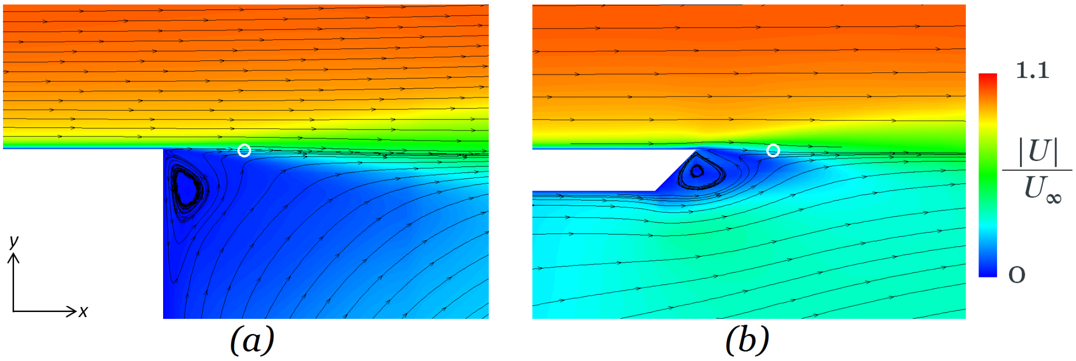

Figure 9.33: Close-up of mean velocity field at x_{LE} from LES simulations: (a) square cavity; (b) baseline partially-covered cavity. White circles indicate the location of pressure monitor at Point 1.

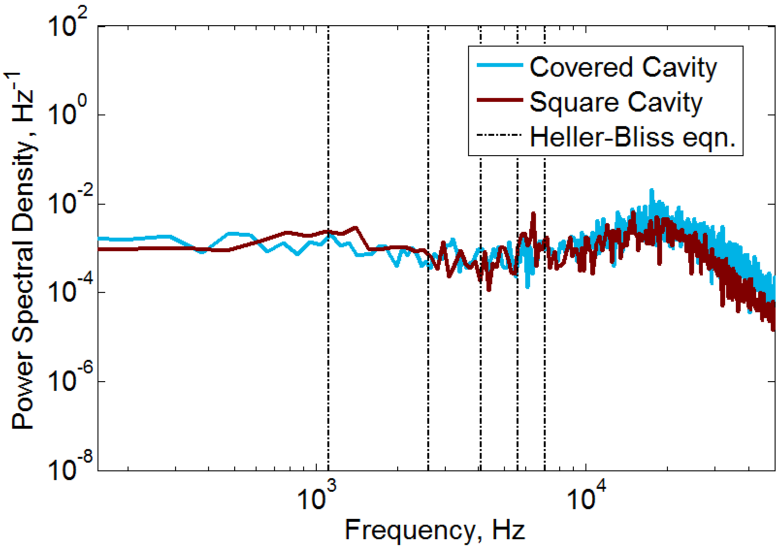

Figure 9.34: PSDs of pressure at monitor Point 1 (location indicated in Figure 8.3 and Figure 9.33, comparing square and covered-cavity geometries.

20kHz) is observed in both cases. This was earlier attributed to the leading-edge separation bubble in the partially-covered cavity simulation, due to its presence only near Point 1. The square cavity showed the same diminishment of this peak at Point 2 and downwards, which supports the idea that it is a feature of the dynamics in this region. Even though the geometry is different, both simulations have the same upstream turbulent boundary layer and a similar-sized recirculation bubble in this region. The recirculation bubble is slightly further away from Point 1 in the square-cavity geometry, which is explains why the amplitudes are slightly lower.

By the cavity trailing edge (Figure 9.35), the square cavity appears to have a slightly thicker boundary layer. Both shear layers impinge on the downstream wall slightly below the top edge. The square cavity impingement location is a little higher, causing a slightly smaller recirculation bubble downstream. The mean pressure on the downstream wall is compared numerically in Figure 9.36, which confirms that the square cavity has a higher impingement location (point of maximum pressure), although the difference is quite small. The shear layer may also be visualized through the turbulent kinetic energy k, which

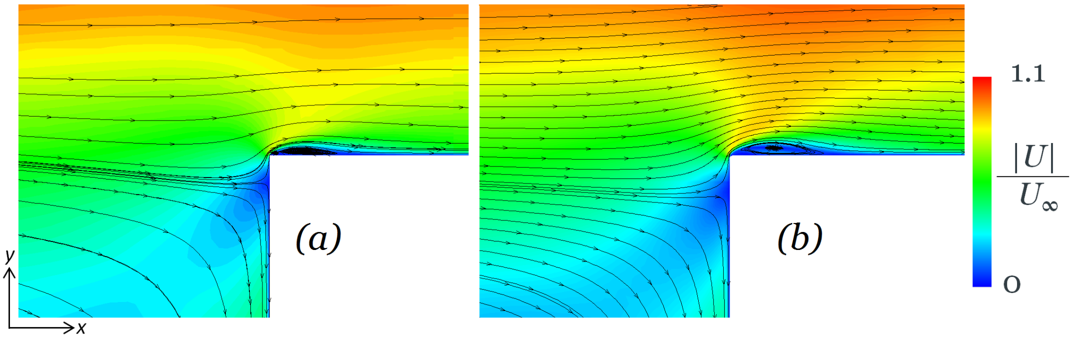

Figure 9.35: Close-up of mean velocity field at x_{TE} from LES simulations: (a) square cavity; (b) baseline partially-covered cavity

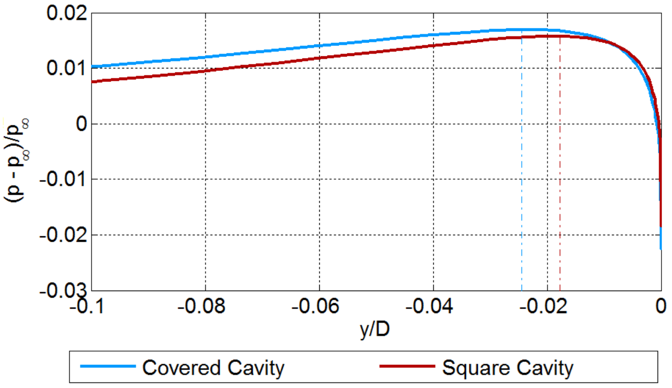

Figure 9.36: Mean pressure at the top downstream wall of the cavity ($y = 0$ represents the top edge), comparing the square and the partially-covered cavities

is compared between the two geometries in Figure 9.37. The square cavity has a more energetic shear layer. The cavity vortex appears to bring a band of k into the shear layer at around $0.1D$ downstream of x_{LE} (downstream of the corner vortex in Figure 9.33(a)), which appears to slightly push the shear layer upwards. It is likely that the higher levels of peak kinetic energy across the shear layer are due to this interaction. The high-k regions at the trailing edge (associated with the impingement and recirculation bubble) are of a similar size and shape.

Pressure monitors in the shear layer, halfway along the open section and at the downstream wall, are compared in Figure 9.38. At Point 3, the peak at $f \approx 6.3$kHz noted at Point 1 is also visible; in fact this peak was observed at all of Points 1-5. At exactly x_{TE} (Figure 9.38(b)) the peak is not visible, however it is noted that the levels are overall higher than at Point 3, and it is likely that the peak is being drowned out, so to speak, by the high broadband levels due to the impingement of the unsteady flow on the wall. Other than the 6.4kHz peak, the frequency content in the shear layer is quite similar between the two geometries.

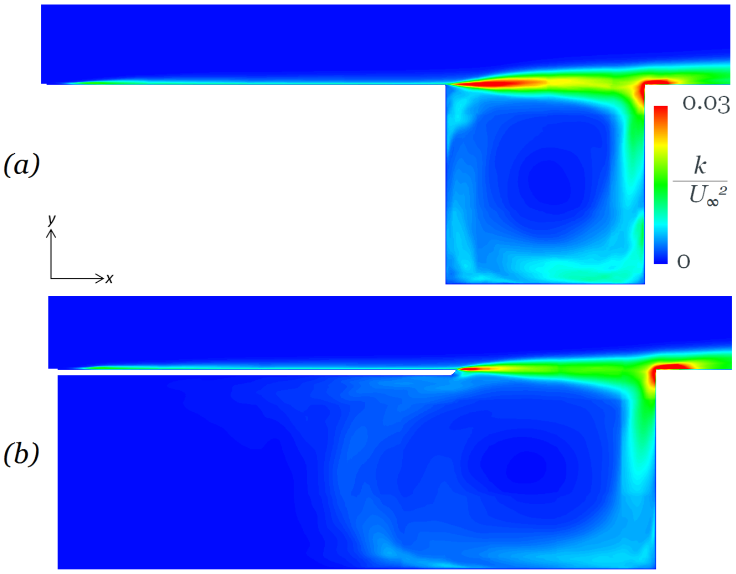

Figure 9.37: Comparison of turbulent kinetic energy k between LES simulations: (a) square cavity; (b) baseline partially-covered cavity

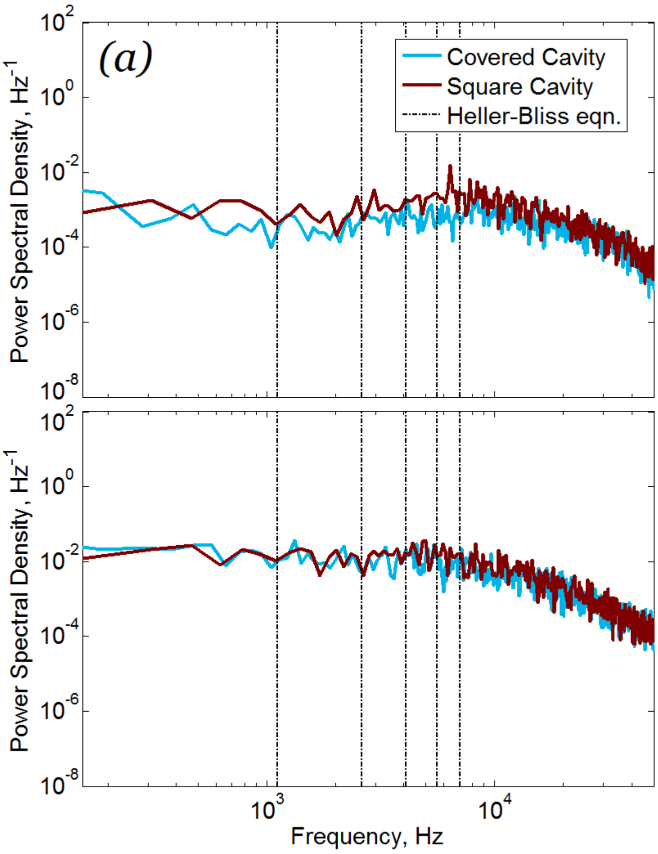

Figure 9.38: PSDs of pressure at monitors in the shear layer from LES simulations: (a) at Point 3 (centre-length of the open section) (b) at Point 11 (at x_{TE}). Point locations are as shown in Figure 8.3.

9.4.2 Inside the Cavity

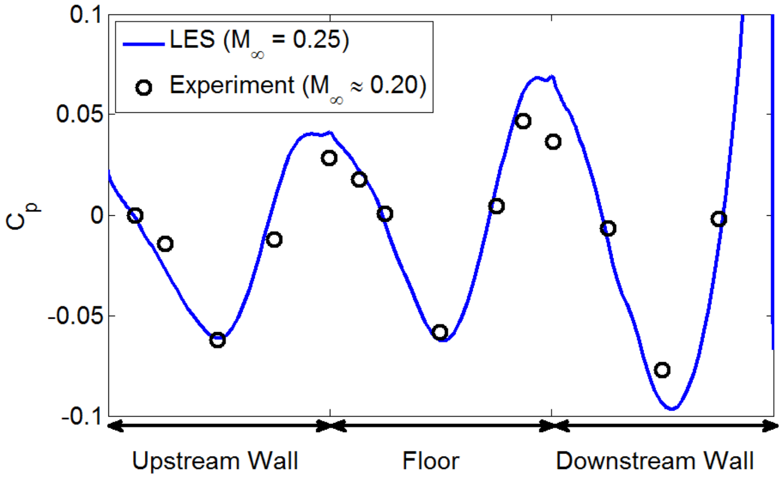

Figure 9.39: Comparison of pressure coefficient C_p along the walls of the square cavity; present LES analysis, compared with experimental results from [52]

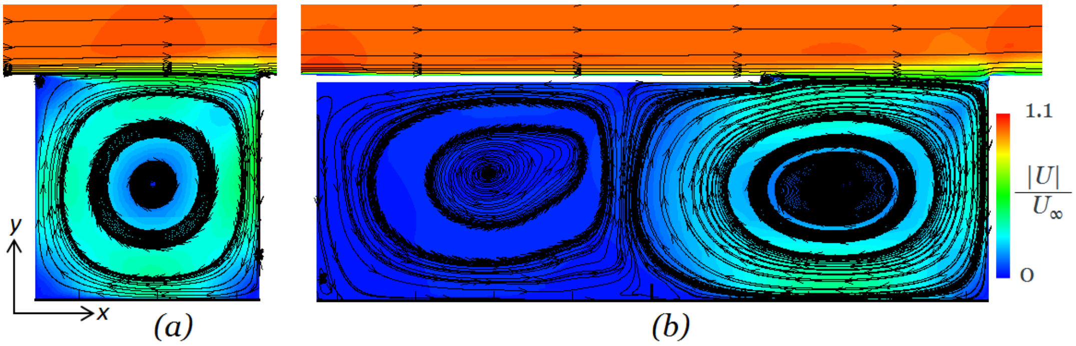

Figure 9.40: Comparison of mean velocity contours and streamlines between LES simulations: (a) square cavity; (b) baseline partially-covered cavity

The mean pressure distribution along the walls is compared with the experimental measurements of Roshko [52] in Figure 9.39. Overall the agreement is good. The positive-pressure peaks are slightly higher in the present simulation (although it is hard to conclude this for certain, given the wider spacing of the experimental measurements). This may be due to the fact that the simulation is performed at a slightly higher freestream velocity (85 m/s compared to 64 m/s in [52], which equates to $M_\infty = 0.20$ if the tunnel was operating at atmospheric temperature and pressure conditions). It may also be caused by the tendency of the quarter-span span-periodic setup to over-predict the vortex strength, as discussed in Section 8.3. However the locations of peaks and troughs are well predicted, as are the amplitudes of the troughs, and the overall shape. This gives confidence that the LES analysis is capable of correctly predicting the flow field inside the cavity. The mean velocity field is shown in Figure 9.40(a). As expected, the square cavity contains a single large vortex, which is also consistent with observations from previous experimental and numerical studies [17, 52, 53].

Comparing the square cavity with the partially-covered cavity (Figure 9.40(a-b)), the presence of the upstream wall at x_{LE} necessarily constrains the cavity vortex compared to

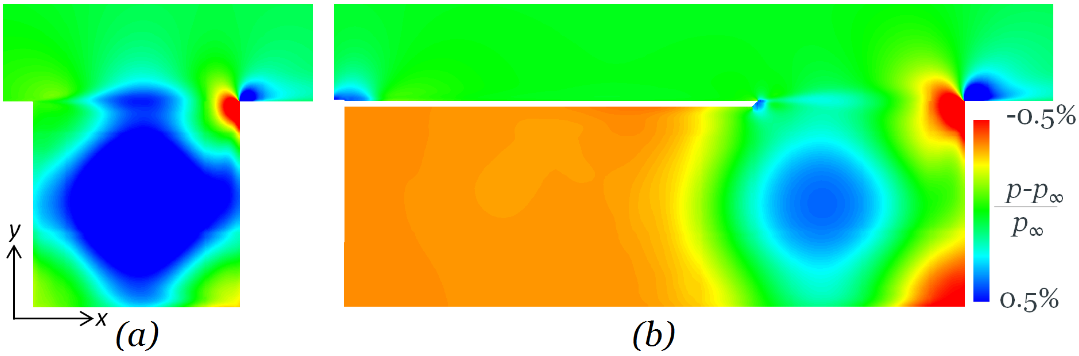

Figure 9.41: Comparison of mean pressure between LES simulations: (a) square cavity; (b) baseline partially-covered cavity

in the partially-covered geometry, where the open-section vortex extends almost $0.5D$ into the covered section. The velocity levels are higher in the square geometry, especially the upwards velocity on the upstream side of the cavity vortex, indicating a stronger vortex than in the partially-covered geometry. This is confirmed by the mean pressure plot in Figure 9.41, where the low-pressure region associated with the vortex core is larger and stronger. The roller-bearing vortex in the bottom downstream corner is however quite similar between the two simulations, as shown in the local mean flow field (Figure 9.42).

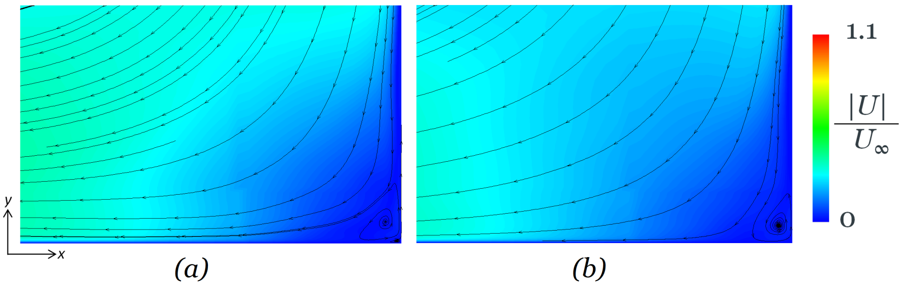

Figure 9.42: Comparison of mean velocity contours and streamlines between LES simulations at the bottom downstream corner of the cavity: (a) square cavity; (b) baseline partially-covered cavity

Along the downstream wall, the high-pressure regions associated with the impingment of the shear layer on the wall, and the flow along the wall onto the floor, are both weaker from the square geometry. There are a few factors which are likely to contribute to this. First, the square cavity has a stronger negative pressure associated with the vortex, and that will have some influence on the flow in the bottom downstream corner. Also, as observed in the shear layer in Figure 9.36, the stagnation point of the square-cavity shear layer is higher, so slightly less of the shear layer flow impinges on the wall and is then swept downstream, causing a lower pressure buildup at those locations. However the similarity of the mean velocity fields at the bottom downstream corner suggests that this does not have a major effect on the flow. The other difference is in the turbulent kinetic energy (Figure 9.37), which is higher for the square geometry both in the shear layer and in the bottom downstream corner of the cavity. This high degree of unsteadiness may be reducing the coherence of the flow in these regions, thereby weakening the impact pressure.

The frequency content inside the cavity showed similar behaviour at all points. Figure 9.43 presents a typical comparison, on the downstream wall at the mid-depth (Point 14). The covered-cavity geometry's peaks at 4, 6 and 8kHz have vanished, as expected, since those were attributed to length modes along the longer length. The square cavity has a single significant tone, peaking at 6.4kHz, but spanning a bandwidth of 5.5-6.7kHz. The amplitude is much higher than that any of the tones in the covered-cavity simulation, which explains why its influence was observed even in the turbulent shear layer. This frequency does not correspond closely to any Rossiter modes (the nearest are $f_3 = 5.6$kHz and $f_4 = 7.1$kHz).

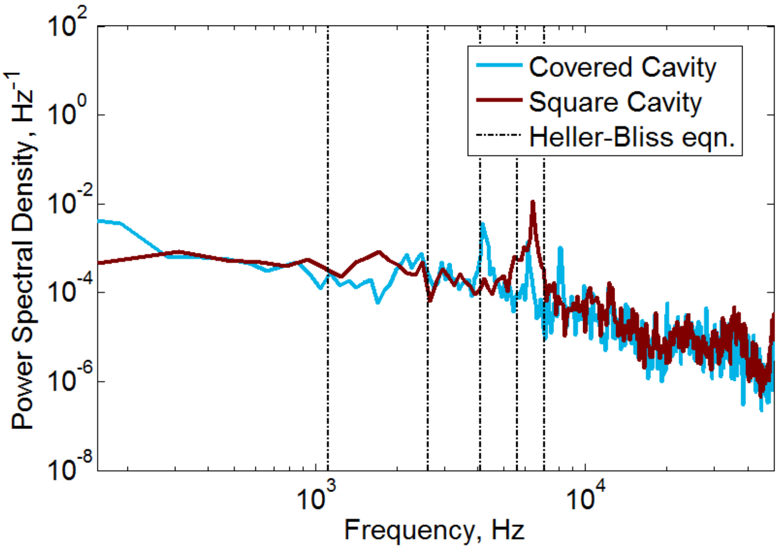

Figure 9.43: PSDs of pressure at monitor Point 14, on the downstream wall at the mid-depth of the cavity, comparing square and covered-cavity geometries

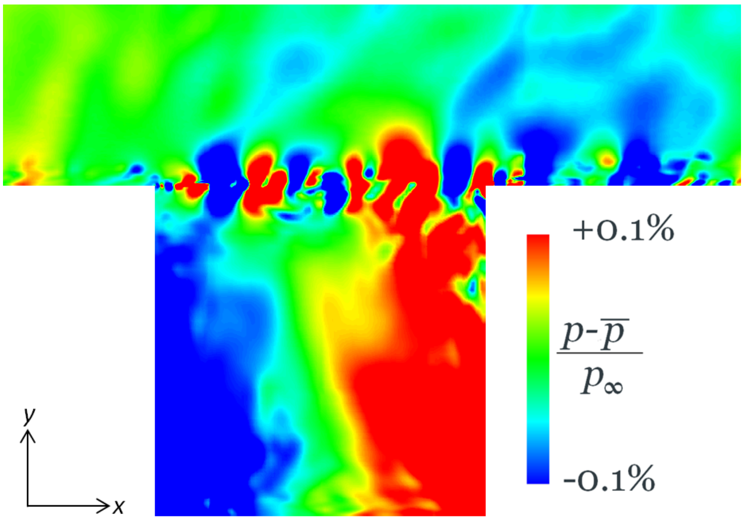

Figure 9.44: Contours of instantaneous perturbation pressure from square cavity LES simulation

An example of the instantaneous perturbation pressure is shown in Figure 9.44, where the mean pressure is calculated over 1 cycle at 6.4kHz to avoid the slight downward drift inside the cavity. There is an indication of some acoustic waves from the trailing edge outside the cavity, although not as regular as in the partially-covered-cavity simulation in Figure 8.12. The pressure field inside the square cavity indicates the presence of a lengthwise acoustic mode with one node, and other snapshots across the cycle exhibited the same behaviour. Evaluating Equation 2.8 for this geometry (i.e. $L = D$) and $N_x = 1$ gives $f = 6.0$kHz, which is close to the centre of the range of the resonant tone in Figure 9.43. This result is interesting, as it suggests that in spite of the shorter L/D ratio ($L_{total}/D = 1$ with the square cavity, versus 3 with the partially-covered cavity), and the absence of a covered section, the dominant tonal response from the square cavity follows the same mechanism as the dominant tonal response from the partially-covered cavity. The upstream boundary layer is the same in both of these simulations, with $\delta/L_{open} = 0.064$, near the criteria proposed by [30] for suppressing shear layer resonance.

9.4.3 Conclusion

In the absence of the upstream covered section, it appears that the tonal response inside the cavity is still dominated by the lengthwise acoustic mode. However, since the total length of the cavity is decreased, the frequency of the acoustic tones are changed. With the partially-covered cavity, the covered section changed the dimensions of the cavity, allowing coupling between an acoustic mode ($N_x = 2$) and a shear layer resonant mode ($m = 3$), which produced similar frequencies. In the square cavity case, none of the shear layer modes are particularly close to the acoustic modes, and the same coupling does not occur. The tonal response is therefore dominated by the first lengthwise acoustic mode inside the cavity, and no higher modes are observed. In terms of the flow field, the upstream wall of the square cavity restricts the size of the vortex, which is significantly shorter than the open-section vortex is the partially-covered case. The restricted square-cavity vortex has a lower core pressure, and also brings more turbulent kinetic energy into the upstream half of the shear layer. However in the downstream half of the shear layer, and particularly at the trailing edge impingement, the flow fields are still very similar.

9.5 Leading Edge Geometry

9.5.1 Overview

The partially-covered-cavity geometry generally used in this study has a slanted leading edge (i.e. the lip of the covered section of the cavity), which was adopted on the grounds that it would save the necessity of resolving the fine scale of a bluff-body separation around a blunt edge. In this section, the sensitivity of the cavity flow to this geometry choice will be tested by comparing the baseline geometry against a squared-off edge. The other aspects of the geometry - cavity dimensions, upstream length, etc. - remain unchanged.
A comparison of the two meshes, in the vicinity of x_{LE}, is shown in Figure 9.45. The blunt-edged mesh has more cells in the y-direction in the open section of the cavity; the mesh topology is dictated by the 1:1 blocking requirement for implementation in SotonCAA. The change in topology does alter the resolution in the y-direction, but this is not expected to have a significant effect on the resolution of the shear layer, given that the upstream

boundary layer already has $y_1^+ = 1$ in both cases. The x and z resolutions are unchanged.

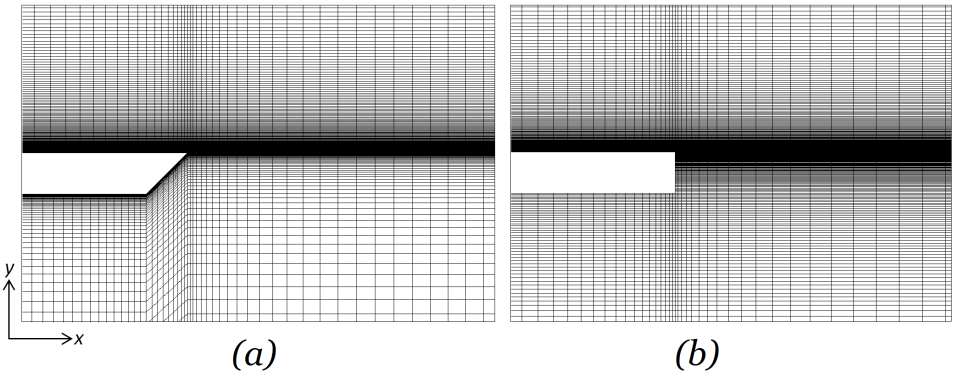

Figure 9.45: Close-up of mesh at x_{LE}; (a) baseline (sharp-edged) geometry; (b) blunt-edged geometry

The simulations are performed in the same manner as the baseline simulations. The flow field is initialized from 2D RANS, extruded in 3D with pertubations added in the initial boundary layer field, and then iterated forward using the SISM LES model. A simulation was also performed using DES (the same DDES model) to compare to the sharp-edged DES simulation. Pressure monitors are placed at the same locations as in Figure 8.3, sampling at every timestep. The time-averaged quantities are determined by averaging every timestep, starting from a cutoff time after the start-up transient flow field (which is judged for each simulation from the pressure monitors). Overall, the simulation times required for the start-up transients, and for the overall simulation to converge, were observed to be fairly similar between both geometries.

9.5.2 LES simulation

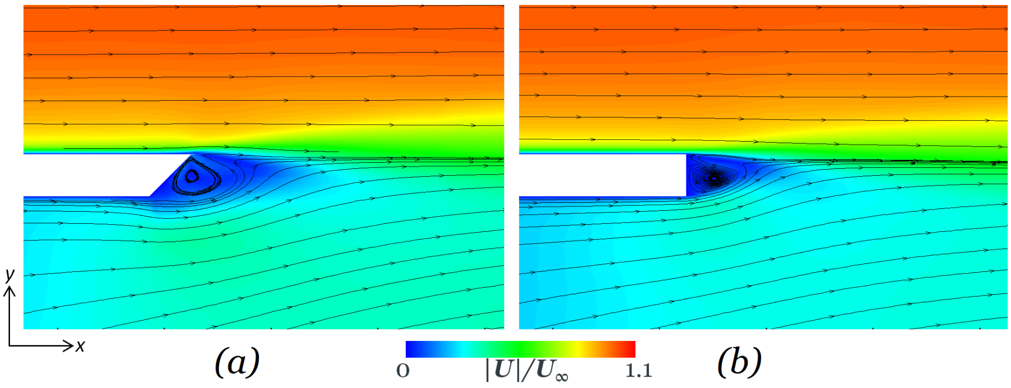

Figure 9.46: Contours of mean velocity from LES simulations; (a) from baseline (sharp-edged) geometry; (b) from blunt-edged geometry

A comparison of the computed mean velocity fields from the two geometries, in the near vicinity of x_{LE}, is shown in Figure 9.46. The incoming boundary layers are the same in both cases, as expected. Both lip geometries cause a small recirculation vortex in the vicinity of the lip, but the blunt-edged simulation produces a smaller vortex, with

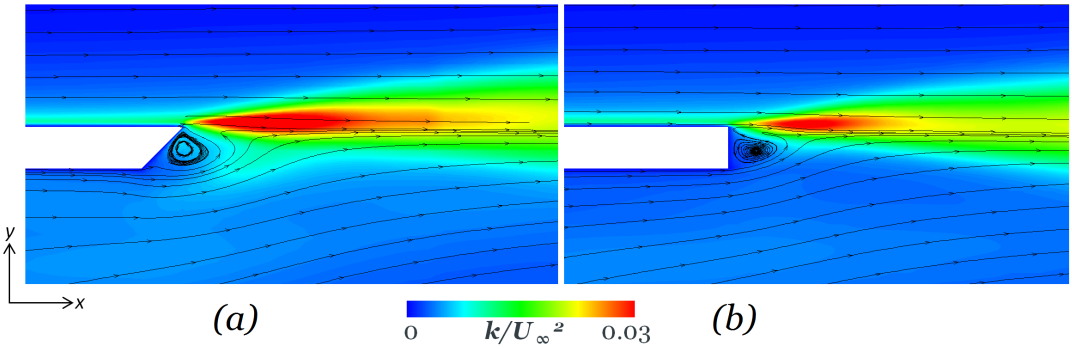

Figure 9.47: Contours of turbulent kinetic energy from LES simulations; (a) from baseline (sharp-edged) geometry; (b) from blunt-edged geometry

a lower centre. Streamlines along the upstream wall ($y = 0$, the top side of the lip) separate smoothly from the blunt geometry, deflecting slightly downwards after the lip vortex. In the sharp-edged geometry, the lip vortex extends the whole height of the lip, and the streamlines separating at x_{LE} are deflected slightly upwards by this small vortex. Therefore the blunt edge produces a slightly more steady flow in this region, which is reflected in the turbulent kinetic energy (Figure 9.47), where the blunt-edged geometry has a lower k in the near vicinity of the separation point, and the sharp-edged geometry produces a slightly higher k at x_{LE} due to the larger lip vortex influencing the upstream flow. This larger lip vortex also appears to draw in some of the kinetic energy band from the shear layer into the underside of the vortex, which was not observed with the blunt leading edge.

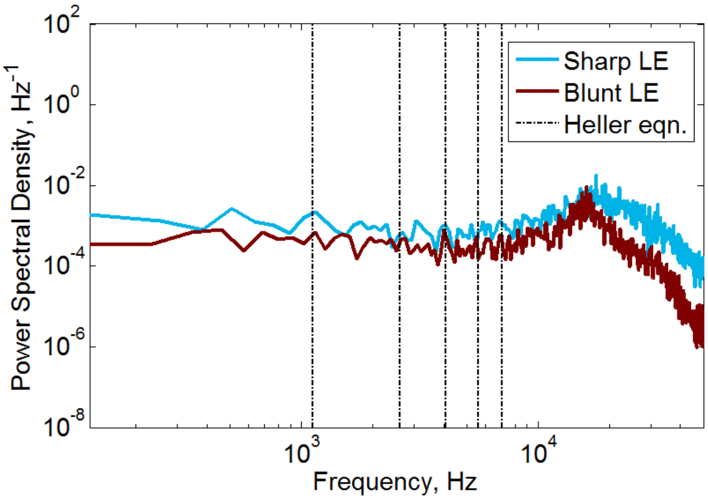

Figure 9.48: PSDs of pressure at monitor Point 1 (just downstream of x_{LE}, as shown in Figure 8.3), from LES simulations

The FFT of the pressure monitors at Point 1 (Figure 9.48) are slightly different, due to the differences in the lip vortex bubbles to which the high-frequency hump is attributed. The blunt-edged geometry has a slightly lower peak frequency in this region and overall lower tonal amplitudes, due to the smaller vortex and smoother flow-field. By Point 2, which is $0.25D$ downstream of x_{LE}, the difference in the tonal content is almost negligible

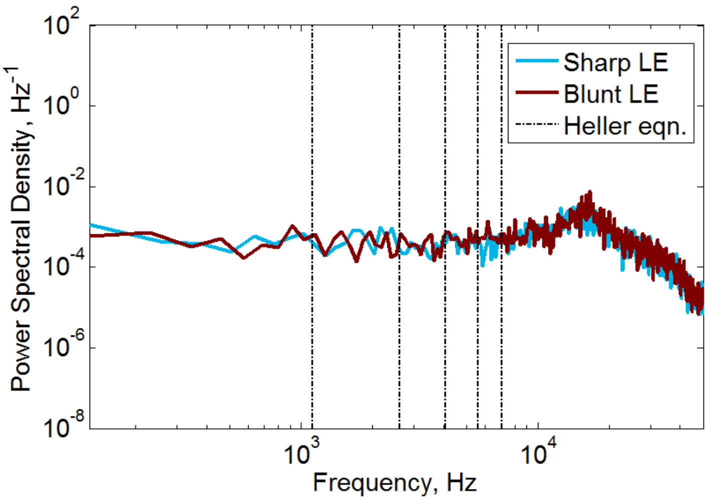

Figure 9.49: PSDs of pressure at monitor Point 2 ($0.25D$ downstream of x_{LE}, as shown in Figure 8.3), from LES simulations

(Figure 9.49). At Point 3 ($x_{LE} + 0.5D$) and further downstream in the shear layer, the pressure monitors gave identical results.

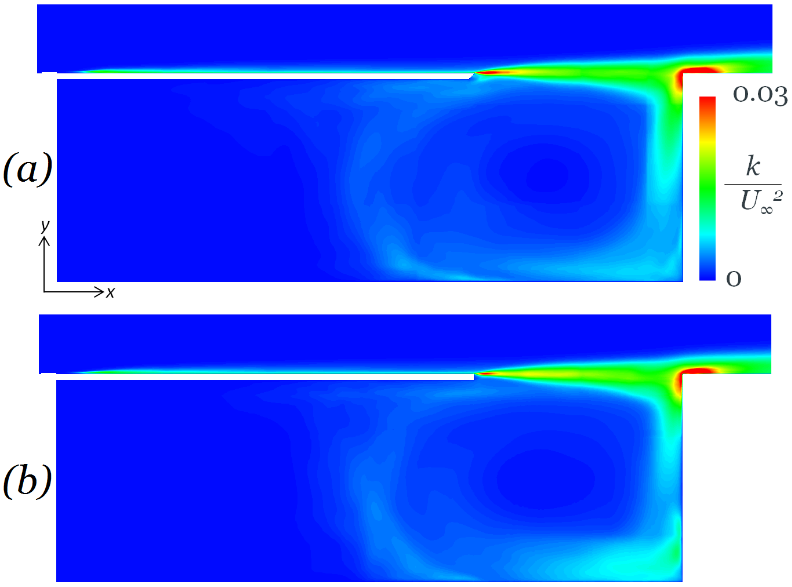

Figure 9.50: Contours of turbulent kinetic energy from LES simulations; (a) from baseline (sharp-edged) geometry; (b) from blunt-edged geometry

The turbulent kinetic energy in the rest of the shear layer is compared in Figure 9.50. The lip geometry affects the distribution of k in the upstream half of the geometry, with the sharp-edged geometry having a larger high-k region at the beginning of the shear layer, while the blunt-edged geometry has a slightly higher peak k throughout the upstream half of the shear layer. In the downstream half of the shear layer, the two simulations have fairly well converged on the same turbulent kinetic energy distribution. The streamlines impinging on the downstream wall, the small recirculation region downstream of the cavity, and the pressure along the downstream wall, were all observed to be identical. The mean velocity fields inside the cavity are quite similar, both in terms of the velocity magnitudes and in the sizes of the two vortices (Figure 9.51). FFTs of pressure monitors at all points inside the cavity showed the same behaviour. An example is shown in Figure 9.52 from the upper corner of the covered-section wall. The overall influence of the lip geometry on the shear layer flow, therefore, appears to be fairly minor, and limited to the near vicinity of the lip vortex.

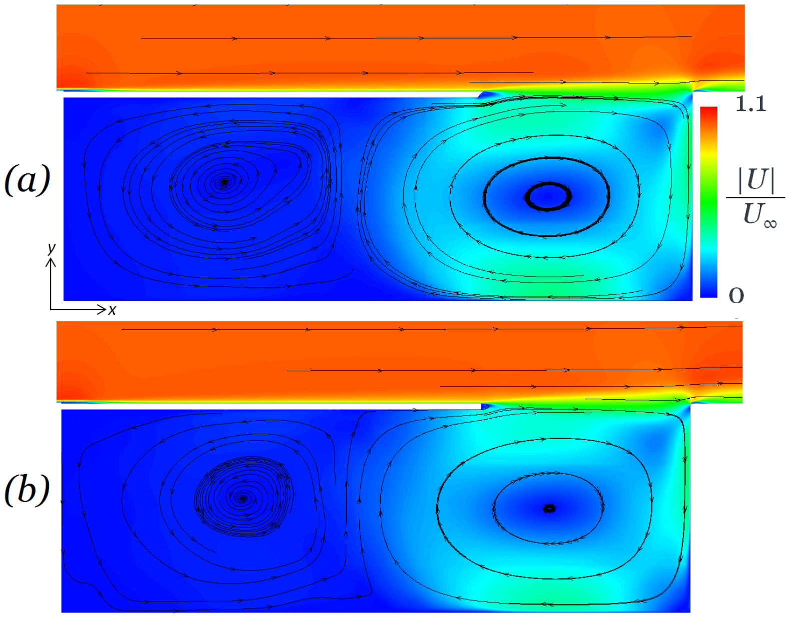

Figure 9.51: Contours of mean velocity from LES simulations; (a) from baseline (sharp-edged) geometry; (b) from blunt-edged geometry

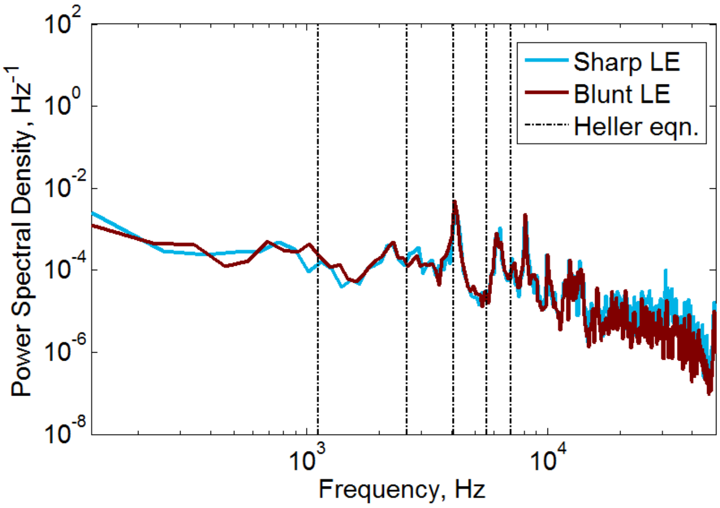

Figure 9.52: PSDs of pressure at monitor Point 17 (upper back wall of cavity, as shown in Figure 8.3), from LES simulations

9.5.3 DES Simulation

For completeness, the same comparison of the lip geometry was performed using the DDES analysis. Since the DES upstream boundary layer is smooth (RANS), it may be more susceptible to small changes in the flow field in the vicinity of the separation point. The mean

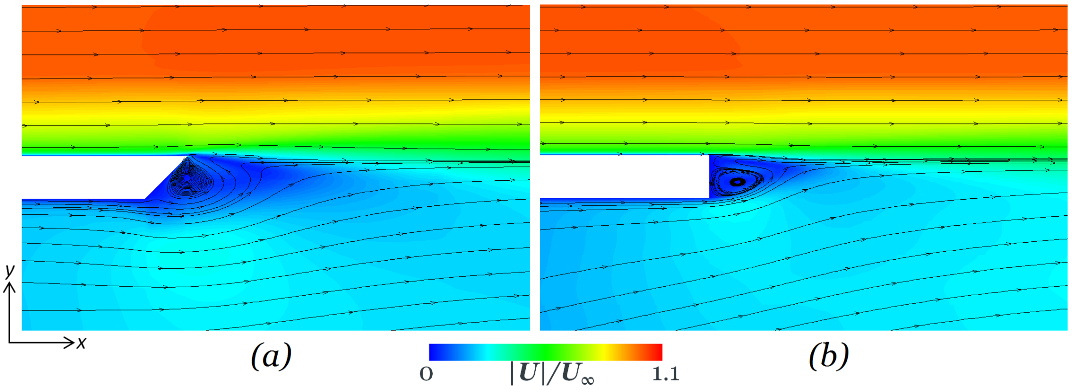

Figure 9.53: Contours of mean velocity and streamlines near the cavity leading edge, from DES simulations: (a) from baseline (sharp-edged) geometry; (b) from blunt-edged geometry

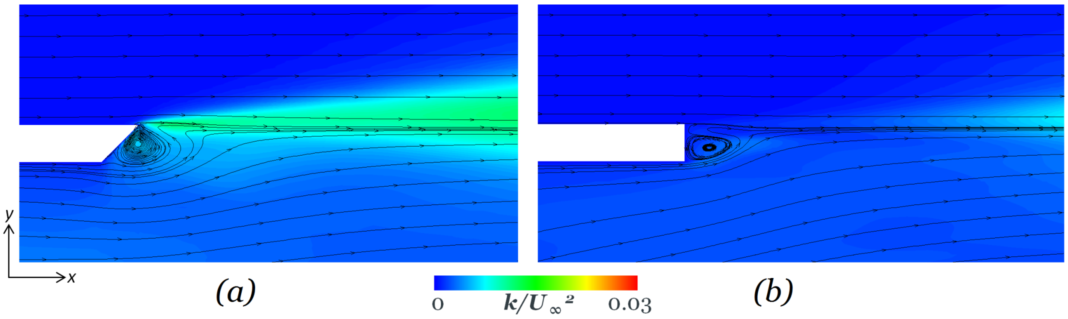

Figure 9.54: Contours of turbulent kinetic energy near the cavity leading edge, from DES simulations: (a) from baseline (sharp-edged) geometry; (b) from blunt-edged geometry

velocity fields in the near vicinity of the lip are compared in Figure 9.53. The characteristics are quite similar to what was observed from the LES: the blunt edge produces a smaller lip vortex, which sits slightly below the separation edge, so that the mean streamlines separate smoothly and then deflect downwards. The sharp edge produces a larger bubble which pushes the flow slightly upwards. As expected, this causes a difference in the turbulent kinetic energy distribution, which was also observed in the LES. The difference with the DES, however, is much more pronounced. From the LES, both shear layers showed high k developing immediately after x_{LE}, within the vicinity of the small bubble. In the DES, however, this only occurs with the sharp-edged geometry (Figure 9.54); the blunt-edged geometry does not develop levels of k visible on this scale until almost $0.25D$ downstream of x_{LE}.

The most obvious explanation for this would be if the DDES model was not functioning properly, and allowing the flow to separate as RANS. However, plots of the DDES variable f_d (Figure 9.55) show that the transition from RANS to LES behaviour occurs in the same region for both geometries. (In fact, the blunt geometry was able to reach this behaviour from the unmodified RANS initial condition, without requiring any clipping of ν_t. This shows that the DDES behaviour can be sensitive to small changes in the geometry and in the initial field.) Overall levels of k are lower in this region than they were in the LES simulations, but that is to be expected since the DES does not have any kinetic energy

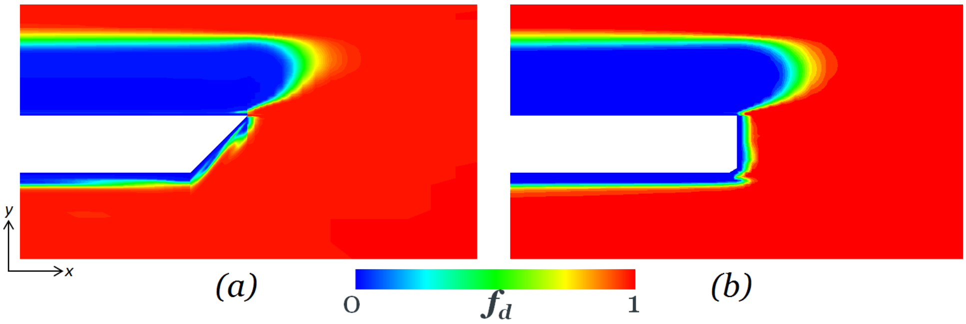

Figure 9.55: Contours of the DDES variable f_d near the cavity leading edge, from DES simulations: (a) from baseline (sharp-edged) geometry; (b) from blunt-edged geometry

incoming from the upstream (RANS) boundary layer.

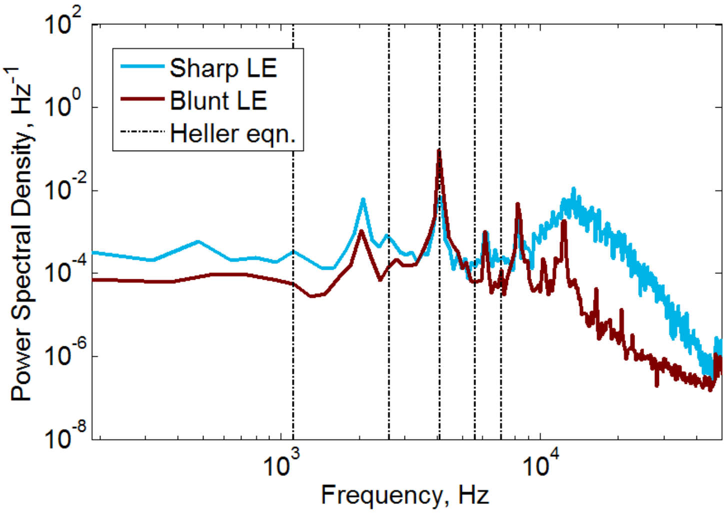

Figure 9.56: PSDs of pressure at monitor Point 1, near x_{LE} (as shown in Figure 8.3), from DES simulations

Pressure monitors at Point 1 and Point 2 (Figure 9.56 and Figure 9.57 respectively) show a significant difference between the two geometries, presumably attributable to the influence of the separation bubble. The turbulent kinetic energy plot shows that for the blunt-edged geometry there is no unsteady interaction between the lip vortex and the shear layer, and the pressure monitors reflect this in the absence of the high-frequency spectral hump. Interestingly, the mean velocity fields around the blunt lip are very similar between the DES and the LES, but the unsteady characteristics are completely different. The sharp-edged geometry gives better agreement between the LES and DES in this region. The larger lip vortex appears to force a degree of unsteadiness at the beginning of the shear layer, which does not strongly affect the flow field computed with turbulent LES (most likely because there is already unsteady flow coming in, from the upstream resolved boundary layer structures), but which does cause a significant difference in the DES simulations (where the upstream boundary layer is modelled with RANS).

Further downstream, the turbulent kinetic energy is plotted in Figure 9.58. The reduction in k near the lip, shown in Figure 9.54, persists over about a quarter of the open section. The band of higher kinetic energy expands in height more quickly than in the blunt-edged

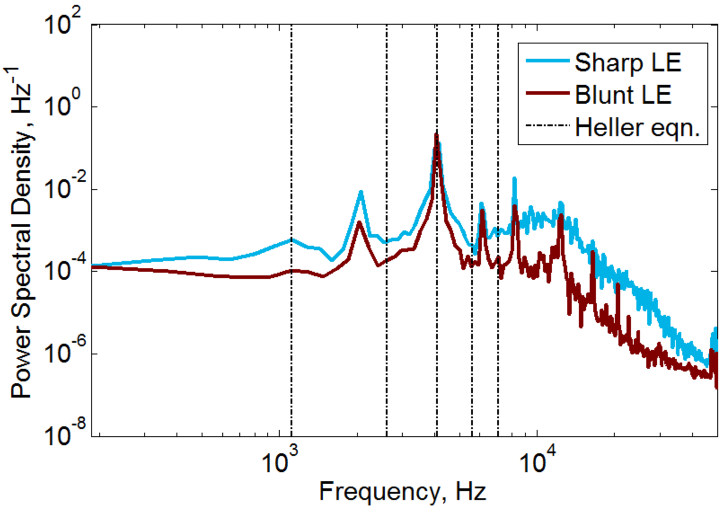

Figure 9.57: PSDs of pressure at monitor Point 2, $0.25D$ downstream of x_{LE} (as shown in Figure 8.3), from DES simulations

geometry. Instantaneous iso-surfaces of the Q-criterion (Figure 9.59) indicate that the shear layer from the blunt-edged geometry, after its smoother initial separation, larger and more coherent vortex structures. The rapid growth of these vortices corresponds to the expansion of the turbulent kinetic energy band in the shear layer. The spacing of the structures ($\lambda/L \approx 0.4$) indicates the dominance of the 3^{rd} Rossiter mode in both cases.

Towards x_{TE} in the shear layer, the sharp-edged geometry shows higher levels of turbulent kinetic energy in the vertical centre of the shear layer. This produces higher levels of k just upstream of the shear layer impingement, and a larger region of k downstream of the cavity. However, the mean features of the trailing-edge impingement and downstream separation bubbles were observed to be very similar, as shown in Figure 9.60 for the velocity, and the mean pressure distributions on the downstream wall were found to be nearly identical. Therefore the difference in turbulent kinetic energy at the trailing edge is solely due to the difference in the upstream shear layer, caused by the unsteadiness introduced into the shear layer by the lip bubble.

Pressure monitors in the shear layer at x_{TE} (Figure 9.61), show that the frequency breakdown is quite similar between the two simulations. The sharp-edged geometry produces slightly higher levels at all frequencies (including the tonal peaks), due to the greater unsteadiness in the shear layer, but the relative spectral content does not appear to be affected by this feature.

Comparison of the mean velocity inside the cavity (Figure 9.62) shows that the blunt-edged geometry has a slightly stronger open-section vortex, in terms of the velocity magnitudes around the vortex. A possible explanation for this is that the smoother shear layer in the upstream part induces a more coherent $+x$-direction flow at the top of the vortex. The higher velocities around the vortex cause a stronger pressure impact on the downstream corner and a stronger low-pressure core at the centre of the vortex, as seen in Figure 9.63. The spectral content inside the cavity, however, is generally unaffected by the lip geometry. An example is shown in Figure 9.64, for pressure monitors near the upper corner of the upstream wall. The same tonal peaks are generally observed, with the sharp-edged

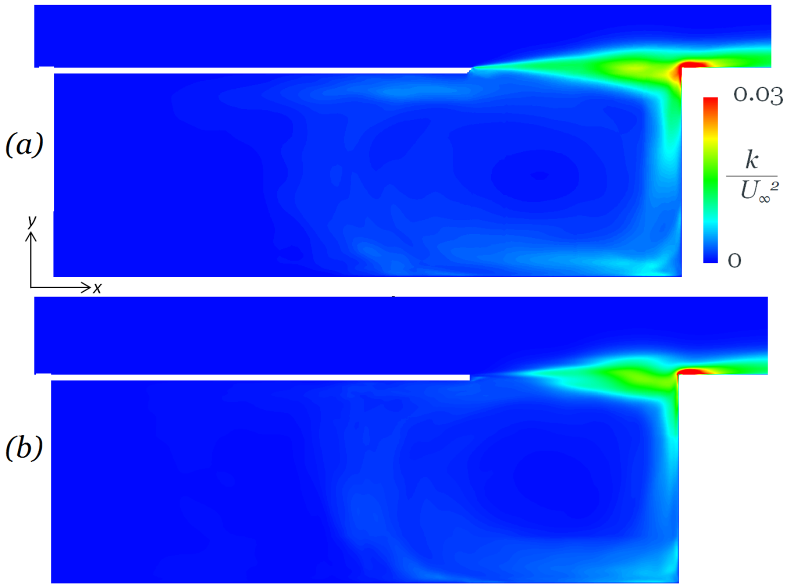

Figure 9.58: Contours of turbulent kinetic energy from DES simulations; (a) from baseline (sharp-edged) geometry; (b) from blunt-edged geometry

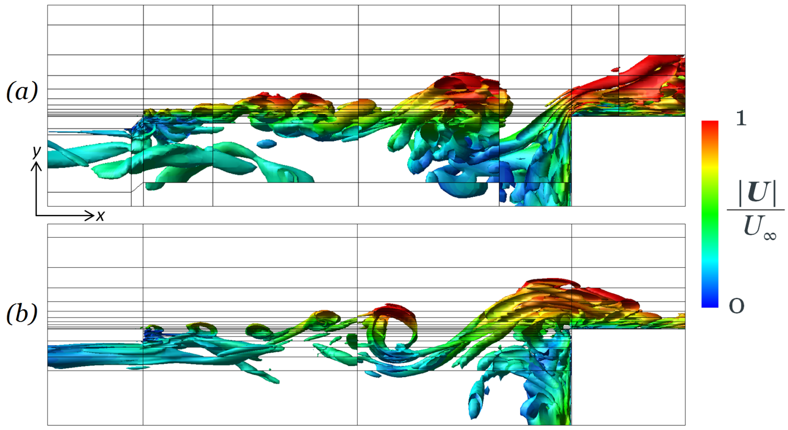

Figure 9.59: Iso-surfaces of the Q-criterion, coloured by velocity magnitude, from DES simulations; (a) from baseline (sharp-edged) geometry; (b) from blunt-edged geometry

geometry producing higher amplitudes. The difference is particularly pronounced at 2kHz and 8kHz ($N_x = 1$ and 4), but the 4kHz mode ($N_x = 2$) remains the dominant tone. RMS pressure contours (Figure 9.65) confirm the presence of the $N_x = 2$ mode inside the cavity. (In the shear layer, the higher p_{RMS} levels in the shear layer correspond to the larger coherent structures as seen in Figure 9.59.)

9.5.4 Conclusion

In conclusion, the difference between the blunt and the sharp edge with the DES was found to be much more significant than with the LES. The differences in the small lip vortex structures causes the blunt geometry to have a largely smooth separation from the leading edge, whereas the shear layer interacts with the lip vortex from the sharp edge. This affects the shear layer further downstream, with the blunt-edged geometry

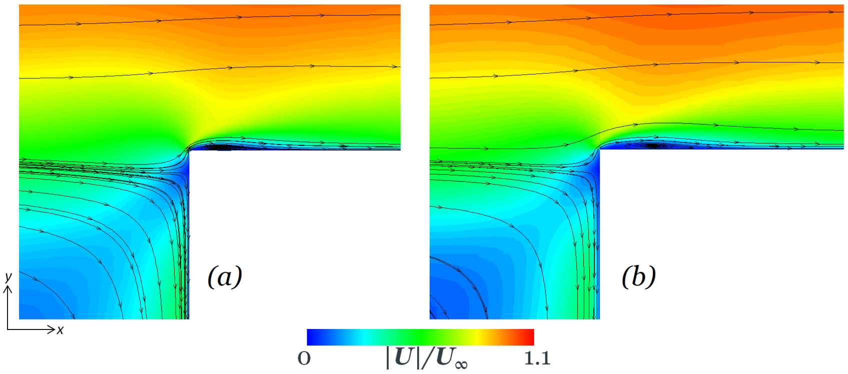

Figure 9.60: Contours of mean velocity, and streamlines, at the cavity trailing edge; (a) from baseline (sharp-edged) geometry; (b) from blunt-edged geometry

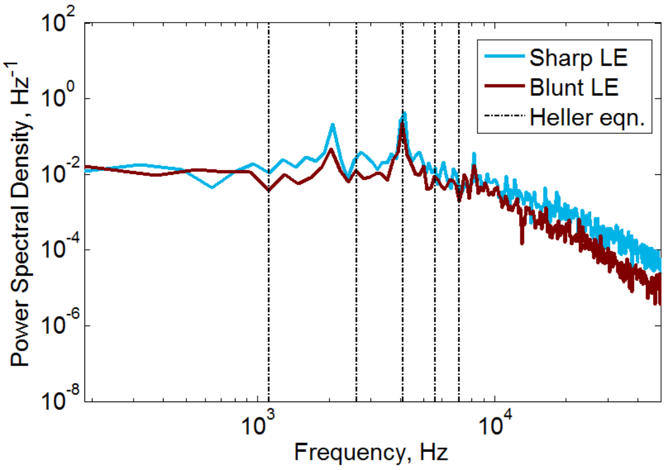

Figure 9.61: PSDs of pressure at monitor Point 11 (in the shear layer at x_{TE}, as shown in Figure 8.3), from LES simulations

producing slightly larger and more coherent vortices, whereas the sharp-edged geometry has higher levels of turbulent kinetic energy due to the unsteadiness from the lip vortex. The larger lip vortex from the sharp-edged geometry produced better agreement between LES and the DES in the upstream shear layer. The impingement of the shear layer on the downstream wall was found to be very similar in terms of the mean quantities. In both cases, the dominant resonant behaviour was observed to be the $N_x = 2$ acoustic mode coupling with the $m = 3$ shear layer mode, causing a very strong tone at $f \approx 4$kHz.

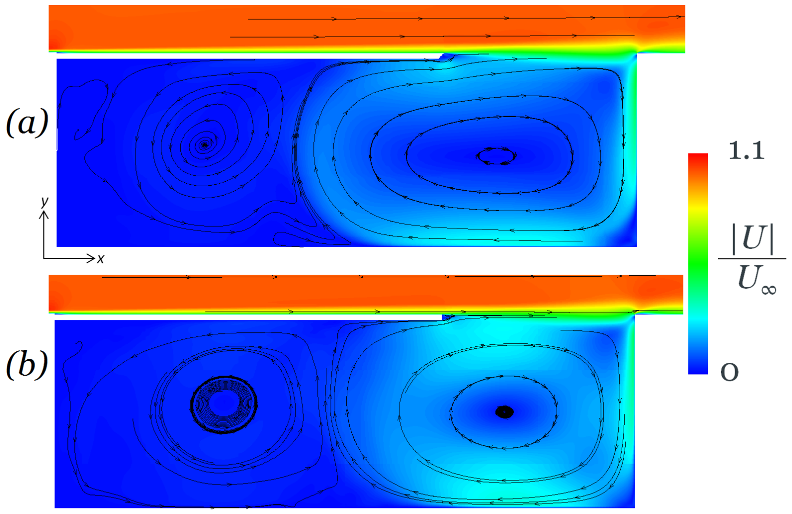

Figure 9.62: Contours mean velocity of from DES simulations; (a) from baseline (sharp-edged) geometry; (b) from blunt-edged geometry

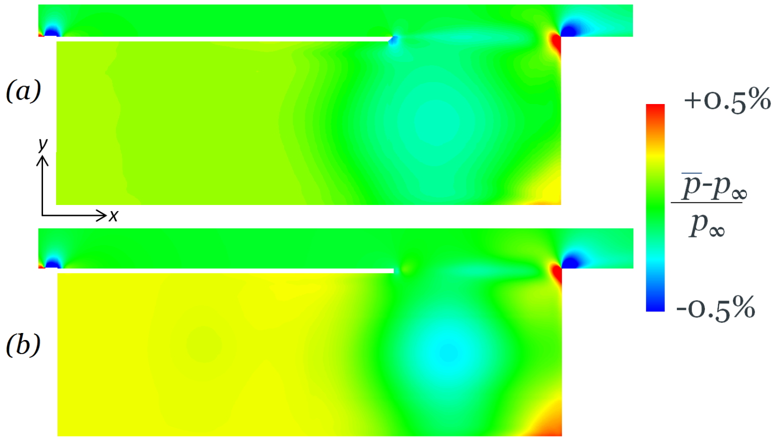

Figure 9.63: Contours of mean pressure from DES simulations; (a) from baseline (sharp-edged) geometry; (b) from blunt-edged geometry

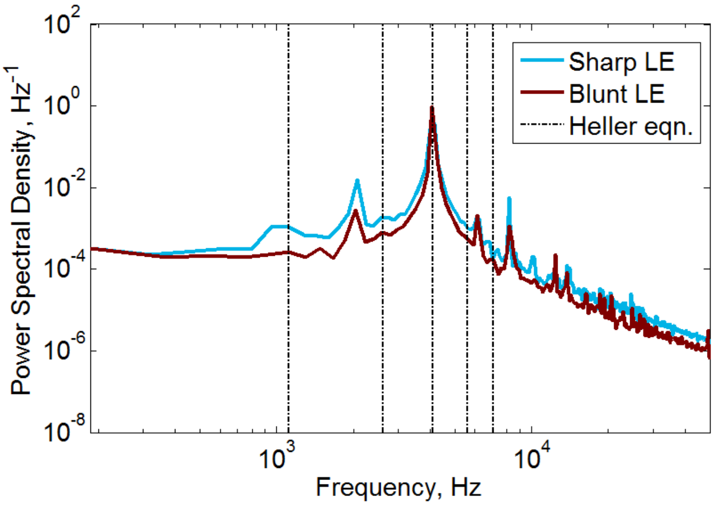

Figure 9.64: PSDs of pressure at monitor Point 17 (upper upstream corner of cavity, as shown in Figure 8.3), from DES simulations

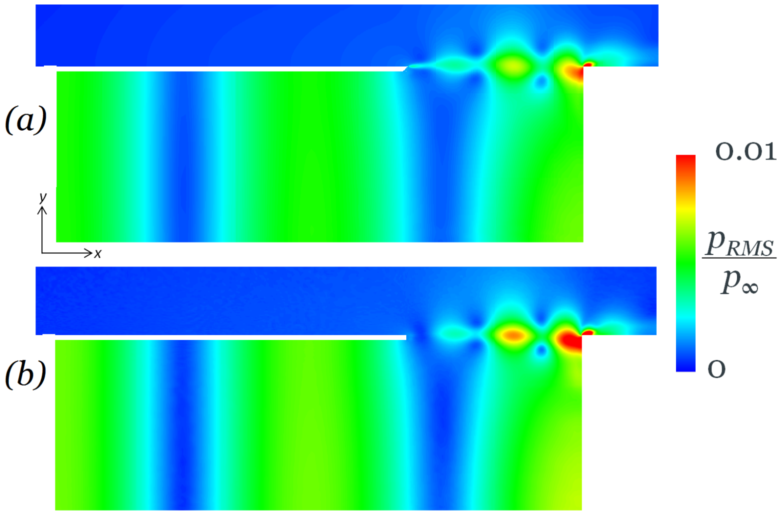

Figure 9.65: Contours of RMS pressure from DES simulations; (a) from baseline (sharp-edged) geometry; (b) from blunt-edged geometry

9.6 Boundary Layer Thickness

9.6.1 Overview

In this section, the effect of the upstream boundary layer thickness is tested. Since the literature has indicated that shear layer resonance is suppressed with $\delta/L_{open} \gtrsim 0.066$ [30], it seems likely that further increasing the boundary layer thickness will not cause a significant difference to the resonance characteristics of the cavity, since the baseline simulation has $\delta/L_{open} = 0.064$ and fairly weak shear layer resonance. Therefore, the comparisons will be performed against thinner boundary layers, generated by reducing the upstream development length.

Two geometries are considered here; one where the upstream boundary layer development length is shortened by $0.5D$ (compared to the baseline), and one where it is shortened by $0.8D$. In both cases there is still sufficient length between the step and the cavity to allow the boundary layer to fully transition to turbulence. It was found from additional tests that decreasing the upstream length further interfered with the development of a realistic turbulent boundary layer upstream, so it was not possible to reduce the development length (and therefore boundary layer thickness) beyond this.

The geometric setup takes the same form as the baseline case, as shown earlier in Figure 8.1. Upstream of the turbulent transition, the same inflow laminar profile, laminar development length and and tripping step are used. Between the step and the cavity, the distance is shortened to limit the growth of the boundary layer. The cavity itself (included the covered section length) is unchanged, as is the downstream length and outflow conditions. A schematic of the shortened geometry is shown in Figure 9.66 for the $0.8D$-shorter geometry, where distance from the step to x_{LE} is reduced from $2D$ to $1.2D$.

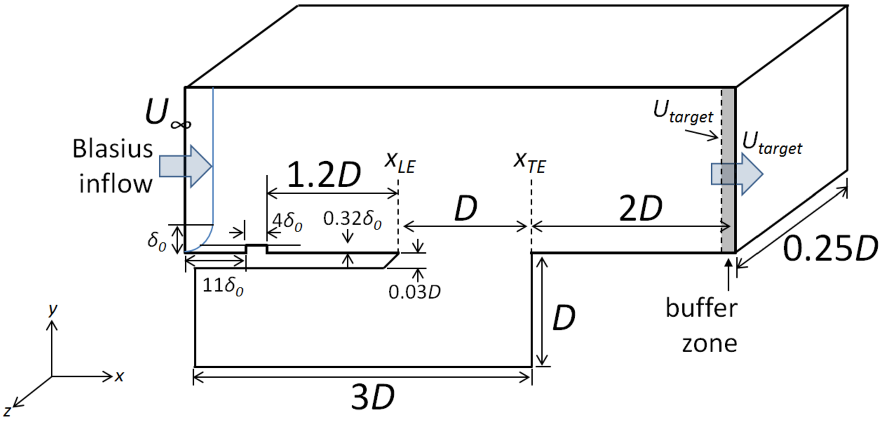

Figure 9.66: Schematic of shortened geometry (not to scale) for reducing boundary layer thickness relative to the baseline case, where the boundary layer development length is reduced by $0.8D$

9.6.2 Upstream Boundary Layer

For the two modified geometries under consideration (shortened by $0.5D$ and $0.8D$), the step tripping was observed to produce a settled turbulent boundary layer within about

$0.5D$ downstream of the step, with the shape factor H_{12} collapsing to within 2% of past DNS and correlation results [29,32]. The growth of the boundary layer thickness relative to the open-section length is shown in Figure 9.67. The three cases equate to $\delta/L_{open} = 0.064$, 0.058, 0.053 respectively. In terms of momentum thickness at x_{LE}, the three cases gave $Re_\theta = 891$, 770 and 713 respectively.

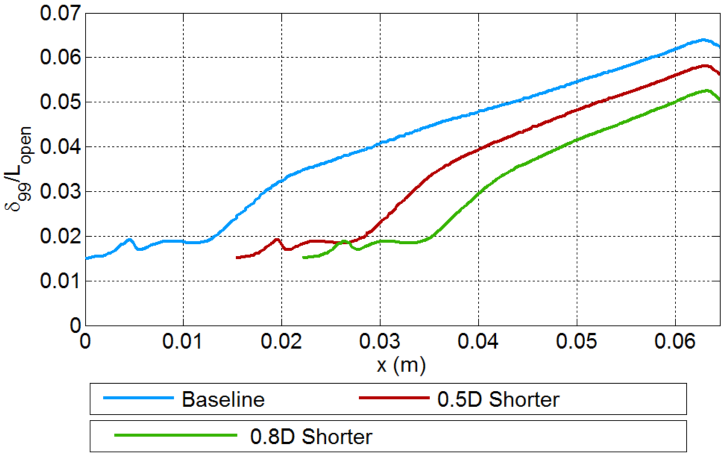

Figure 9.67: Growth of boundary layer thickness upstream of the cavity with different upstream development lengths

It should be noted that in the study of Ahuja et al [30], after the thickest boundary layer of $\delta/L_{open} = 0.066$ where no tones were present, the next thinnest boundary layer tested was $\delta/L_{open} = 0.045$, for which only the second Rossiter mode was present. Therefore, the range of δ/L_{open} in this study is relatively narrow, and may not be able to encapsulate the point at which the boundary layer is thin enough for strong resonance to develop under these conditions. (It is for this reason that the even shorter geometry was tested, which was unable to produce boundary layer turbulence.) On the other hand, for landing-gear applications the upstream boundary layer would develop over the underside of the nose and then the covered section of the cavity, so a significantly shorter development length may be of limited practical application regardless.

The mean velocity profiles and distribution of turbulent kinetic energy through the boundary layer at $0.05D$ upstream of x_{LE} are compared in Figure 9.68. This location is upstream of the influence of the cavity and the lip vortex, so only the developed boundary layers are compared. (The y-ordinate is normalized by D instead of δ in order to plot all three simulations on the same scale.) The mean velocity profiles are all fairly similar, with the slight differences in boundary layer thickness (corresponding to Figure 9.67). The turbulent kinetic energy k increases systematically with the boundary layer thickness, and the peak value varies overall by 7% across the three cases.

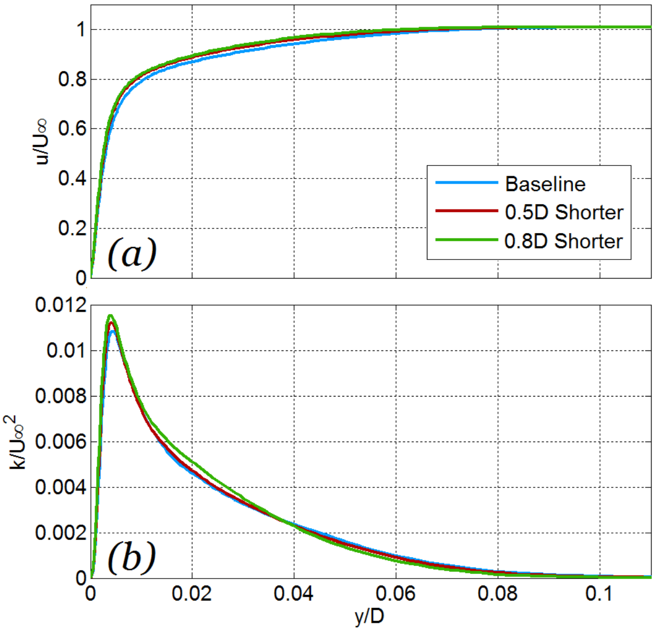

Figure 9.68: Boundary layer profiles taken at $0.05D$ upstream of x_{LE}; (a) mean u-velocity; (b) turbulent kinetic energy distribution

9.6.3 Shear Layer

At the lip of the open section (x_{LE}), contours of turbulent kinetic energy with mean streamlines are compared for the three cases in Figure 9.69. In all three cases the size and extent of the lip vortex appears to be the same. The region of high k just downstream of x_{TE}, which has been attributed to the interaction between the shear layer and the lip vortex, is also fairly similar between the three cases. The values are very slightly higher for the thinner boundary layers, in keeping with the trend observed in the upstream boundary layer, but the overall shape and extent of the high k regions are very similar. The FFT of the pressure monitor at Point 1, in the region of the lip vortex, is compared in Figure 9.70. All three simulations give very similar results; the same hump at higher frequencies, and no discernable tonal peaks. Therefore the flow in this region is not sensitive to these changes in the boundary layer thickness.

In fact, the pressure monitors at all points in the shear layer were found to show very similar spectral content across the three simulations. None of the pressure monitors showed tonal peaks at any frequency, which suggests that in all cases, the spectral content within the shear layer is dominated by the broadband nature of the small-scale vortical structures. Comparison of the instantaneous structures in the shear layer (Figure 9.71) also shows the same behaviour in all three cases.

The growth of the unsteady structures in the shear layer is visualized through the turbulent kinetic energy in Figure 9.72. The separation at x_{TE}, in conjuction with the lip vortex, causes a significant increase in k as shown in Figure 9.69. Further downstream, in spite of the differences in the upstream boundary layer thickness, the shear layer grows across the open mouth of the cavity in a similar manner across the three cases. This suggests that the growth of the shear layer structures is more influenced by the flow field at the point

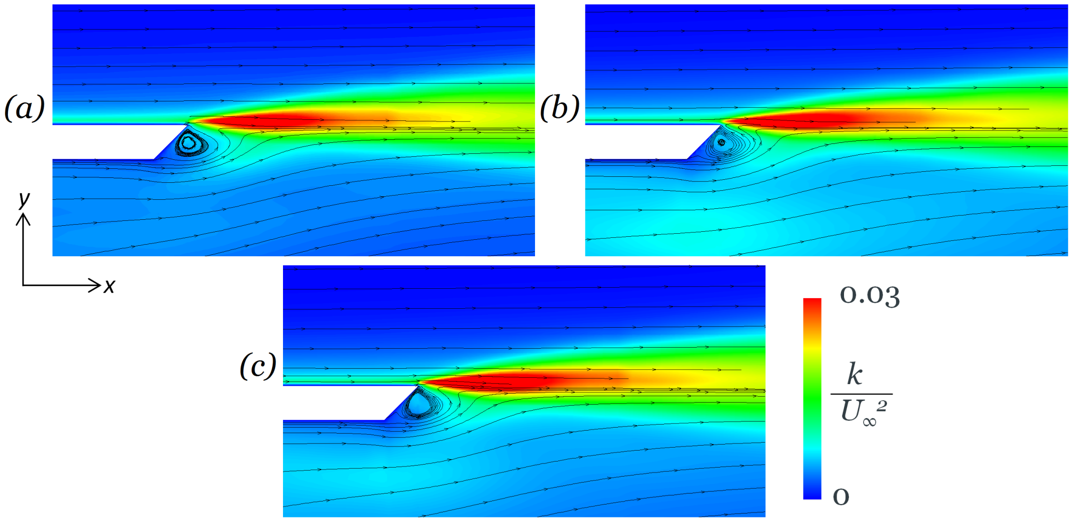

Figure 9.69: Contours of turbulent kinetic energy in the vicinity of x_{LE}; (a) δ/L_{open} = 0.064; (b) $\delta/L_{open} = 0.058$; (c) $\delta/L_{open} = 0.053$

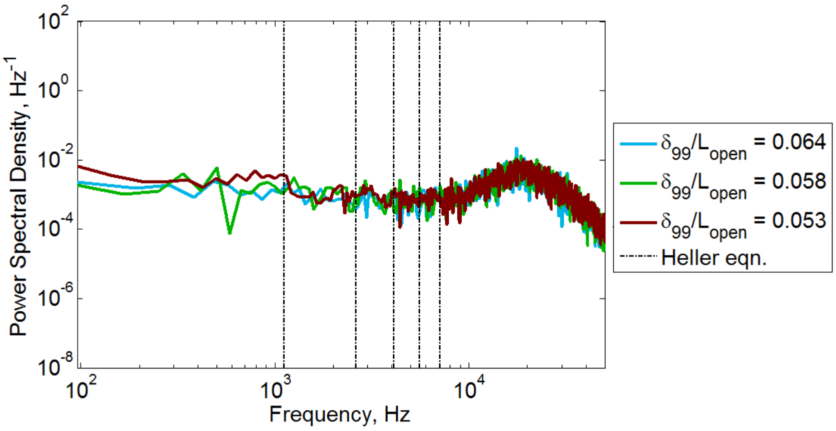

Figure 9.70: PSDs of pressure at monitor Point 1(near x_{LE}, as shown in Figure 8.3)

of separation than by the upstream boundary layer thickness; the thickness of the shear layer, therefore, is not very sensitive to changes in the upstream boundary layer thickness. At the downstream edge of the cavity, the impingement of the shear layer on the trailing edge is identical in all cases, as shown by the mean pressure profile at the top edge of the downstream wall in Figure 9.73. Instantaneous perturbation pressure plots in all three cases also showed the same tendency for acoustic waves to be emitted from this region and propagate upstream. The mean velocity in this region is so similar that the growth of the boundary layer downstream of the cavity is virtually identical for all three simulations, as shown in Figure 9.74. Therefore overall, the differences in the upstream boundary layer thickness do not appear to have a significant effect on the development of the shear layer.

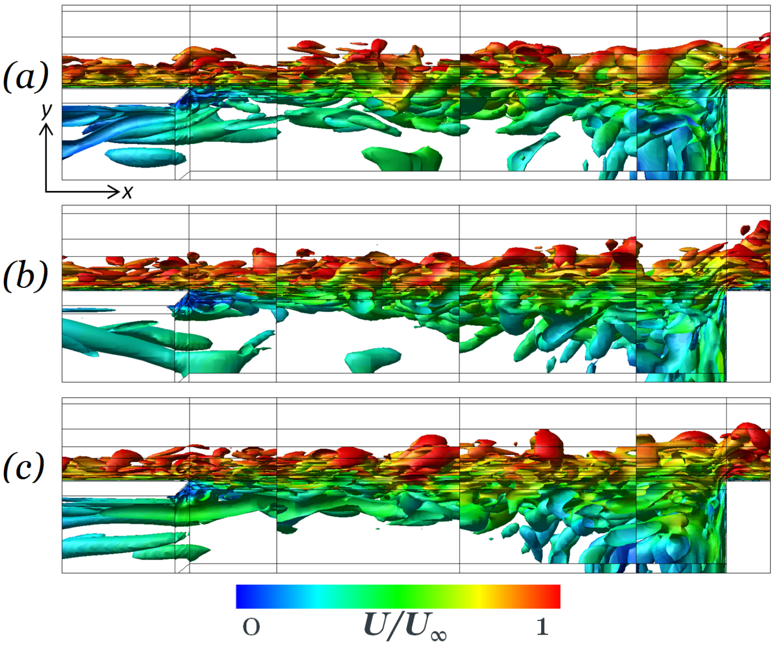

Figure 9.71: Iso-contours of instantaneous Q-criterion, coloured by velocity magnitude, side view; (a) δ/L_{open} = 0.064; (b) δ/L_{open} = 0.058; (c) δ/L_{open} = 0.053

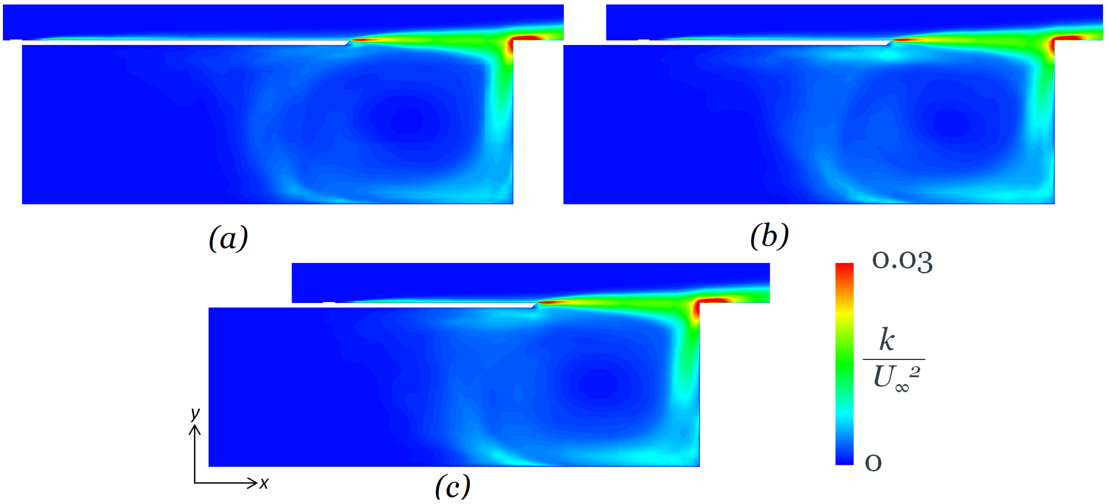

Figure 9.72: Contours of turbulent kinetic energy; (a) δ/L_{open} = 0.064; (b) δ/L_{open} = 0.058; (c) δ/L_{open} = 0.053

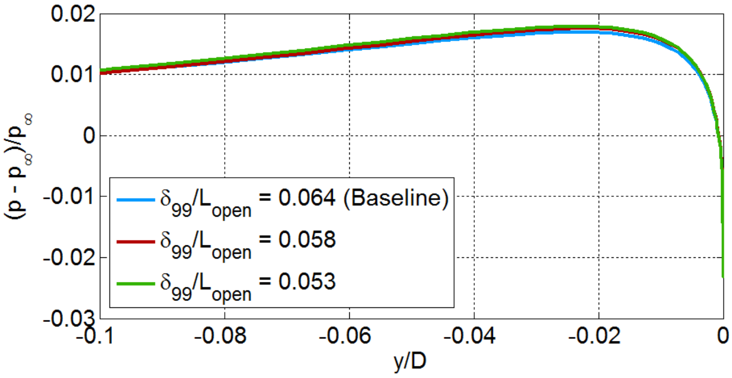

Figure 9.73: Comparison of mean pressure on the upper downstream wall of the cavity

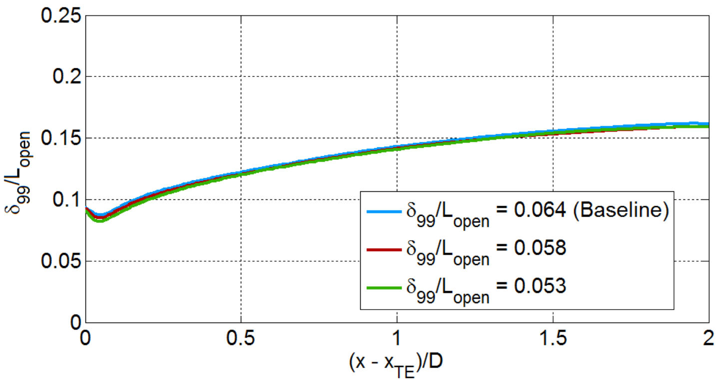

Figure 9.74: Comparison of mean boundary layer growth on the plate downstream of the cavity

9.6.4 Inside the Cavity

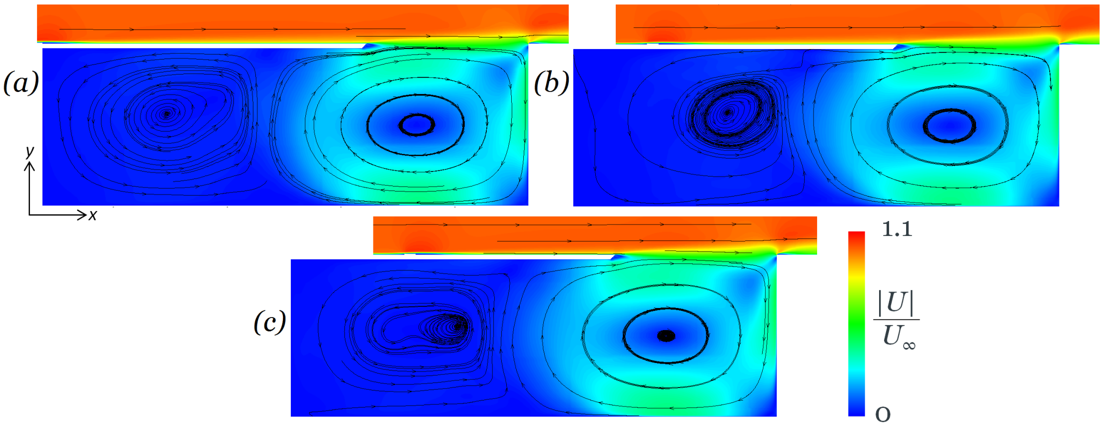

Figure 9.75: Contours of mean velocity magnitude, with streamlines; (a) $\delta/L_{open} = 0.064$; (b) $\delta/L_{open} = 0.058$; (c) $\delta/L_{open} = 0.053$

Consistent with the observations in the shear layer region, the flow field inside the cavity was found to be very similar in all three cases. The mean velocity fields are compared in Figure 9.75. The size of the two vortices, and the velocity magnitudes in the open-section vortex, are the same in all cases. Similar observations were made from the mean and RMS pressure fields.

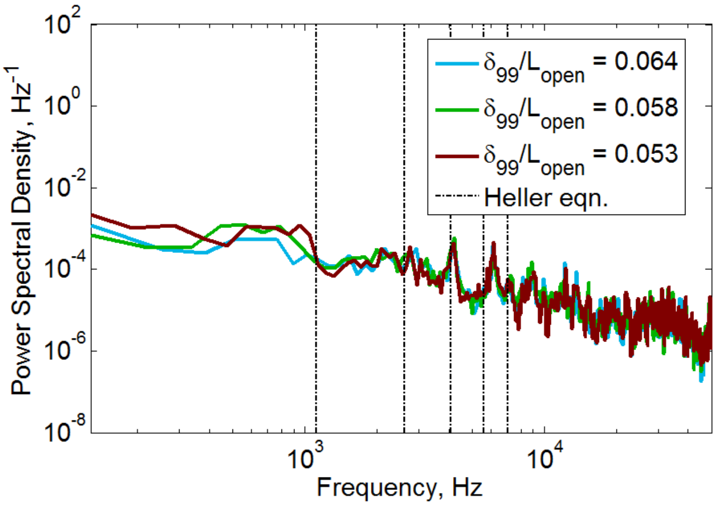

Figure 9.76: PSDs of pressure at monitor Point 21 (n the underside of the cavity cover, at 0.05D upstream of x_{LE}, as shown in Figure 8.3)

The turbulent kinetic energy field (Figure 9.72) showed similar levels along the downstream wall, floor, and the upstream side of the open-section vortex. A small difference was observed in the region of k just upstream of x_{LE}, where the band of kinetic energy swept around the open-section vortex impinges on the underside of the cavity cover. A comparison of the pressure monitors from this region is shown in Figure 9.76. The simulations with the thinner boundary layer have slightly larger humps at around 0.9-1kHz, possibly a low-frequency modulation of the dominant tonal peak at 4kHz. The dominant tones at 4, 6 and 8kHz are, however, largely unaffected in terms of both frequency and amplitude.

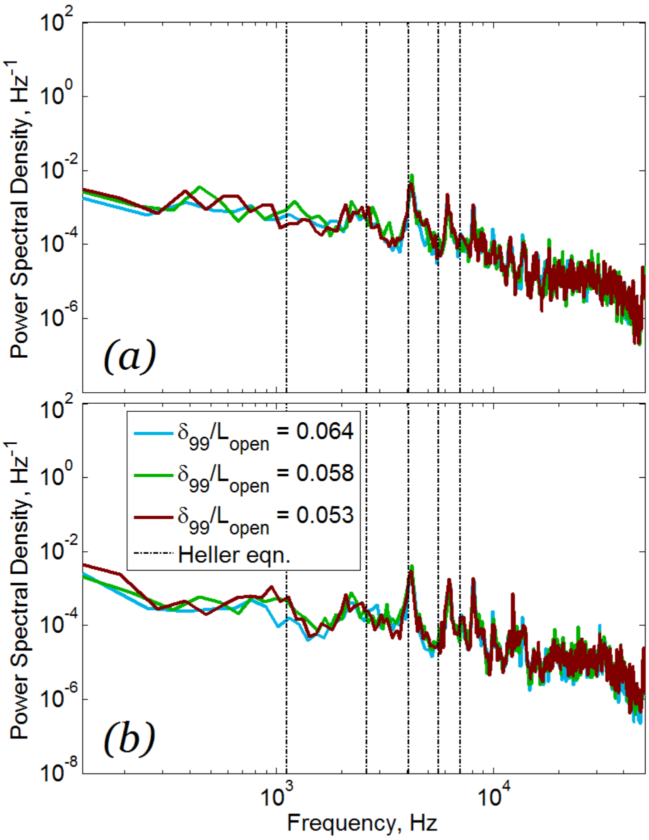

Figure 9.77: PSDs of pressure monitors from simulations with different boundary layer thicknesses; (a) at Point 16, near the downstream bottom corner; (b) at Point 17, near the upstream top corner of the covered section. Locations are as shown in Figure 8.3.

The same can be said for all the other pressure monitors inside the cavity; examples are shown at Point 16 (near the downstream bottom corner) and at Point 17 (near the upstream top corner of the covered section) in Figure 9.77. The dominant tones at 4, 6 and 8kHz, with a smaller tone at 2kHz, are evident in all cases, with similar relative amplitudes. The same lengthwise acoustic modes are therefore developing inside the cavity, independant of the changes in the upstream boundary layer.

9.6.5 Conclusion

Comparing upstream boundary layer thicknesses of $\delta/L_{open} = 0.064$, 0.058, 0.053, the mean flow in the shear layer was found to be almost identical. In terms of the aeroacoustic response, similar dominant tones at 4, 6 and 8kHz were observed in all cases. It may therefore be concluded that the boundary layer thickness, over the range considered, does not affect the resonance characteristics of this partially-covered cavity geometry. In all cases the tonal response is dominated by the lengthwise acoustic mode inside the cavity, with a likely reinforcement from a relatively weak Rossiter mode 3 developing in the shear layer, as discussed in the baseline case. The development of acoustic-mode resonance inside the cavity is determined primarily by the geometry of the cavity, so any small differences in the shear layer would not be expected to have a signficant effect on this mechanism. In this case there was also very little difference observed in the shear layer from the boundary layer thickness.

9.7 Summary

Simulations were successfully performed using LES on a wall-resolved turbulent boundary layer upstream of a partially-covered cavity, and the sensitivity of the simulation to various parameters was tested. The results were compared to the baseline spanwise-periodic configuration (from Section 8.2) where the turbulent boundary layer structures were found to reduce the development of resonance in the shear layer, and the tonal response was dominated by acoustic-mode resonance in the lengthwise direction. Regarding the sensitivity of the simulation to the modelling method, which is of interest to inform future numerical work in this area, the following observations were made:

- With a laminar boundary layer, a higher-mode resonance was observed in the shear layer, especially in the upstream half. The shear layer transitioned to turbulence, and by the trailing edge the two flow fields were fairly similar. The pressure spectra inside the cavity were fairly similar to the upstream-turbulent case.
- Changing the turbulence modelling methodology from LES to DES allowed strong and coherent resonant shear layer vortical structures to develop, at a mode coupling with the dominant lengthwise acoustic mode (still $N_x = 2$). The dominant tone frequency was therefore unchanged, but the amplitude of the acoustic mode was significantly increased. This was attributed to the coherent development of the $m = 3$ mode in the shear layer, which in turn is attributed to the absence of the 'jittering' from resolved upstream turbulent-boundary-layer structures.

In terms of the physical aspects of the flow field, the sensitivity of the aeroacoustic response to various aspects of the geometry were investigated, in order to inform future design optimisation efforts. From this study, the following conclusions were drawn:

- In the absence of the covered section, with the same upstream boundary layer, a square cavity simulation was also found to develop mainly length-wise acoustic-mode resonance.
- Changes to the geometry of the covered section lip were tested for LES and DES. For the LES, switching from a slanted to a blunt lip was found to only affect the local flow in the upstream shear layer for LES. With DES, though, the flow was found to be much more sensitive to the geometry in this region. This is due to the unsteadiness caused by the interaction between the lip vortex and the shear layer separation. The LES is not as sensitive due to the fact that unsteady flow is entering the shear layer regardless, from the upstream turbulent boundary layer.
- Reducing the upstream boundary layer thickness from $\delta/L_{open} = 0.064$ to 0.058 and 0.053 was observed to have no significant effect on the flow field.

Chapter 10

Conclusions and Future Work

10.1 Conclusions

Both DDES and wall-resolved LES were applied to partially-covered cavity configurations, and the features of the flow field were investigated, as well as the sensitivity to many simulation modelling parameters. Guidelines were developed for the use of LES. From a physical perspective, the sensitivity of the partially-covered cavity to changes in the geometry were tested, as was the effect of adding different landing gear components. From a numerical modelling perspective, the effect caused by simplifications in the span-direction boundary condition, and in the turbulence modelling method, were also assessed.

Computationally, guidelines were successfully developed for using wall-resolved LES to model a test case of a zero-pressure-gradient flat plate boundary layer. The in-house SotonCAA code, using the Shear-Improved Smagorinsky model of Leveque et al [91], was able to produce an accurate wall-resolved turbulent boundary layer simulation without inflow perturbations, by using the step-tripping method of Berland et al [46]. The SISM model was found to give a significant improvement in the performance over the standard Smagorinsky model, without any observable increase in the computational effort. The effect of grid and timestep resolutions were tested, and recommendations developed. The wall shear stress was under-predicted, but the mean and RMS profiles in outer scaling agree well with DNS and experiments. For the purpose of developing physically realistic turbulent boundary layer flow structures to feed upstream of a body of interest, as will be very useful for future studies on landing gear flows, these settings should be quite sufficient. Therefore, the objective of developing an efficient LES methodology for resolving a turbulent boundary layer was addressed.

The physical unsteady characteristics of the simplified nose landing gear bay (and of the interactions with the rear doors and central strut) were then explored. The main case considered was a partially-covered cavity with the front 2/3 covered, at $M_\infty = 0.25$. From all simulations, it was found that this cavity develops Rossiter modes across the shear layer. The frequencies were well predicted by the standard equations based on the open-section length, unaffected by the additional covered section upstream. Inside the cavity, two counter-rotating vortices were observed. The additional length does affect the development of acoustic modes inside the cavity; and under certain conditions, a coupling can occur between a lengthwise acoustic mode and a shear layer mode. Using DDES, the interaction between the cavity and the rear doors, and the main central strut, was modelled. It was found that in both cases, higher modes were produced than with the clean cavity. This effect was attributed to the other components imposing small-scale, high-frequency fluctuations on the shear layer: the rear doors create small-scale pressure waves from the flow separation around the front of the doors; and the strut causes a secondary shear layer resonance loop across the smaller distance upstream of the strut. The effect of the upstream boundary layer thickness and condition, and small variations in the geometry of the cavity cover, were also tested using LES. Therefore, the research objective of exploring the unsteady characteristics of the cavity flow field was achieved.

The sensitivity of the cavity simulation to the span boundary condition, and the sensitivity to the turbulence modelling method (especially in terms of the resolved upstream boundary layer turbulence), were both also successfully explored. Their effects on the modelled cavity flow field were found to be inter-related. Using periodic boundary conditions in the span, DES analysis was found to be problematic; the shear layer vorticity structures were correlated in the span even with the span width L_z equal to the depth D, and the flow field did not vary systematically or consistently with L_z, as the $L_z/D = 1$ case was significantly different in many respects compared to the two shorter span widths. Due to this behaviour, it cannot be concluded definitively as to which span width is the best. This is attributed to the limitations of this setup. The combination of a spanwise-uniform incoming boundary layer (due to the RANS modelling upstream), with the periodic-span boundary condition, allows the vortex structures to retain a strong level of coherence in the span direction, as has been observed in past studies from other applications (e.g [67]). However, when LES was used and the small-scale upstream boundary-layer turbulence was resolved, largely consistent behaviour was observed between $L_z/D = 0.25$ and 1, with both simulations producing shear layer structures which were decorrelated in the span. It can be concluded that these flow features are representative of the quasi-2D characteristics of the flow, with $L_z/D = 1$ giving a better prediction of the mean pressure inside the cavity, but $L_z/D = 0.25$ giving a fairly good first estimate of the mean velocity field and tonal response, for a fraction of the computational cost.

This consistency with span width was attributed to the resolved upstream boundary layer, which introduces smaller, uncorrelated structures upstream of the shear layer. Therefore, it is recommended that when using periodic span boundary conditions (e.g. to examine the quasi-2D characteristics of the cavity flow field), DES should be considered less reliable due to the inconsistent trends with the span width. Also, comparing DES and LES with the same span width ($L_z/D = 0.25$), the resolution of the upstream boundary layer from the LES was found to produce significant differences in the mean flow field and the amplitudes of tonal responses. Therefore, LES is particularly recommended for use in cavity flow simulations with periodic span boundary conditions.

Comparing periodic boundary conditions in the span against solid no-slip side walls, where the width $W = D$, the solid side walls were found to have a significant effect on the flow field both using DES and LES. From both turbulence modelling methods, the introduction of the side walls was found to change the dominant shear layer modes to modes 1 and 2, which are not coupled with any lengthwise acoustic modes, indicating that the acoustic modes are weakened. The shear layer imposed pressure fluctuations inside the cavity at the corresponding frequencies, growing in amplitude towards the upstream (covered) section of the cavity. Based on these changes, it is recommended that the side walls should be resolved where possible in this type of cavity geometry, as they do have an effect on the flow field.

The side walls were also found to break the excessive coherence in the spanwise direction from the DES, so that the overall characteristics of the flow field are more similar between the DES and the LES than when using periodic-span boundary conditions. In this case, therefore, the DES can be considered a reasonable first approximation to the cavity characteristics. However the resolved boundary layer turbulence in the LES is still a significant factor in determining the pressure amplitudes and some other aspects of the flow field, due to the jittering effect on the shear layer resonant vortex structures, so LES is still recommended where computational resources permit.

Overall, this work constitutes a significant expansion of the current understanding of cavity flows, as the combination of this partially-covered geometry, this Mach number range, and fully accurate wall-resolved turbulence have not, to the author's knowledge, previously been investigated.

10.2 Publications

The analysis of the effect on side walls on the covered cavity geometry using DDES, as described in Section 5.7, has been submitted and presented at the 46th AIAA Fluid Dynamics Conference in June 2016:

S. Premachandran, Z. Hu and X. Zhang, "*Computational Analysis of Partially-Covered Cavity With and Without Side Walls*," in 8^{th} *AIAA Flow Control Conference*, no. AIAA-2016-3174, 2016.

Two additional AIAA Journal papers are currently planned:

- Investigation of the separate effects of the main strut, and the open rear doors, on a partially-covered cavity geometry (based on the DDES simulations described in Chapter 6).
- Simulation of the partially-covered cavity using wall-resolved LES with realistic incoming boundary layer turbulence, including analysis of the sensitivity of the cavity flow to the incoming boundary layer thickness and condition (based on the LES simulations described in Chapter 9).

10.3 Future Work

This analysis raised a few questions which would be interesting points of investigation for another member of this research team. From the LES cavity simulations, a more direct comparison between the laminar and turbulent upstream boundary layers could be assessed by matching the upstream boundary layer thicknesses (δ/L_{open}), instead of the upstream development lengths, as was done here. Also, since the introduction of the side walls was found to have a significant effect on the flow field, it would be informative to repeat some of the comparisons from Chapter 9 on a geometry with side walls, as computational resources permit. Of particular interest would be the condition of the boundary layer (laminar vs. turbulent) and the sensitivity to boundary layer thickness. For application to nose landing gear geometries, the plate upstream of the cavity might be modified to incorporate curvature with very little difficulty.

The tendency of the LES cavity with side walls to contain acoustic modes, while the DES of the cavity with side walls did not, is also interesting. Whether this is due to the turbulence modelling method, or the boundary layer thickness, could be determined by performing a DES on the same geometry and mesh as was used for the LES cavity with side walls.

The next step in extending this analysis would be to apply the LES methodology and settings described here to a more complex flow field, such as with the strut, to investigate the interaction between the turbulent boundary layer/shear layer and those additional geometric features. It should also be feasible to extend the current geometry back up to model scale (depending on the available computing resources) if necessary, to check the effect of scale with the LES analysis, and for comparison with experimental studies.

Appendix A

Scale and Boundary Layer Thickness Effects with DES

In this Appendix, the DES results from the smaller-scale LES section (Section 9.3) is compared against DES simulation results from Section 5.6. Both simulations use the same partially-cavity configuration and a quarter-span ($L_z/D = 0.25$) perodic-span setup. The geometries differs in two ways: the cavity scale is reduced by a factor of 4, and the upstream development length (relative to the cavity dimension) is reduced. (The upstream geometry also contains the small step, although that is not likely to have a significant effect here, as the boundary layer is turbulent regardless with the DES treatment.) As discussed previously, it is expected based on past studies that the scale reduction should not have a significant effect on the flow field. Therefore any differences observed between these two simulations can most likely be attributed to the boundary layer thickness.

The larger-scale geometry had a boundary layer thickness of $\delta/L_{open} = 0.095$, which is well above the cutoff observed in [30] for shear layer resonance. Howver, resonant Rossiter modes were still observed. This indicates that the difference in δ/L_{open} between the DES and the LES is not the cause of the DES having shear layer resonance; and it may therefore be deduced from this that the supression of the resonance in the LES is attributable to the 'jittering' effect of the boundary layer vortex structures (as discussed in Section 2.4.5, e.g [18]).

The frequency content of some of the pressure monitors is compared between the two geometries in Figure A.1 for the shear layer. At point 1, the larger geometry did not show the high-frequency spectral hump observed in the present geometry. Figure A.2 compares the velocity field in the region of x_{TE}, and it is seen that there is a difference in the lip recirculation bubble, likely caused by the much thicker boundary layer in the larger-scale case. The lip bubble sits lower and closer to the lip surface, and therefore has less of an interaction with the separating shear layer. At the cavity trailing edge (Figure A.3), both cases show the flow impinging just below the trailing edge and forming a small recirculation region downstream. Plotted on an $X-Y$ scale adjusted for D, the larger-scale cases shows a thicker shear layer (due to the thicker upstream boundary layer), and a slightly larger downstream recirculation region.

Downstream in the shear layer, and inside the cavity (Figure A.4), both simulations show

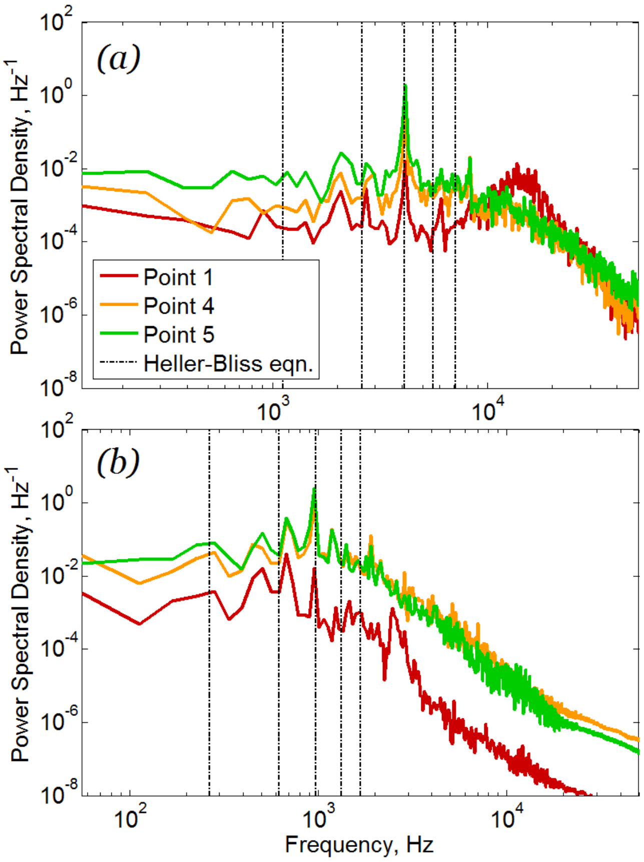

Figure A.1: PSDs of pressure at monitors in the shear layer from DES: (a) DES for cavity with $D = 0.0285$m, $\delta/L_{open} = 0.049$; (b) DES for cavity with $D = 0.12$m, $\delta/L_{open} = 0.095$. Point locations are as shown in Figure 8.3

strong peaks at Rossiter mode 3, which in both cases is very close to the $N_x = 2$ acoustic mode frequency. Both simulations also show a smaller peak at a frequency corresponding to the $N_x = 1$ mode. Comparison of the p_{RMS} contours (Figure A.5) confirms the presence of the same dominant $N_x = 2$ acoustic mode (visualized by the vertical bands of high p_{RMS} inside the cavity, which represent the antinodes of the standing waves). These bands are at the same locations in both simulations, although the smaller geometry (thinner boundary layer) has peak p_{RMS} inside the cavity around 60% higher, suggesting a stronger acoustic mode. In the shear layer, howver, the p_{RMS} shape and levels are very similar. The overall similiarity of the RMS pressure fields and the dominant modes indicate that the same coupling between acoustic and shear layer modes is occurring in both simulations. Therefore for this DES setup, the differences in scale and in boundary layer thickness have no effect in terms of the dominant tonal response.

Considering some of the secondary tones, however, there are some differences between the two simulations. The large-scale geometry (with the thicker boundary layer), showed smaller peaks at Rossiter modes 1 and 2, (especially inside the cavity), which were not observed in the smaller scale. There is also a peak at $f \approx 1920$Hz, which is close to both the $N_x = 4$ acoustic mode and the $m = 6$ Rossiter mode (1890Hz and 2030Hz respectively). Since this tone is stronger than the other high-frequency tones, there may be a secondary acoustic-mode/Rossiter-mode coupling occurring at this frequency. No

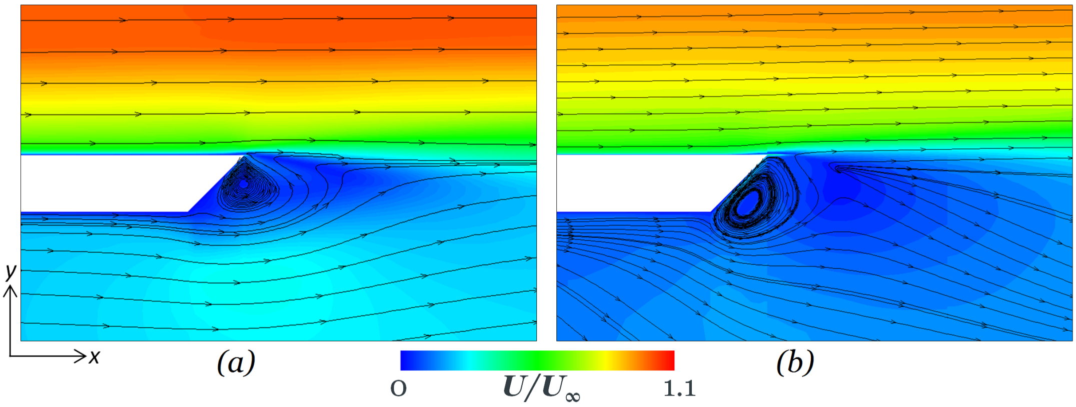

Figure A.2: Velocity contours close-up at x_{LE}: (a) DES for cavity with $D = 0.0285$m, $\delta/L_{open} = 0.049$; (b) DES for cavity with $D = 0.12$m, $\delta/L_{open} = 0.095$

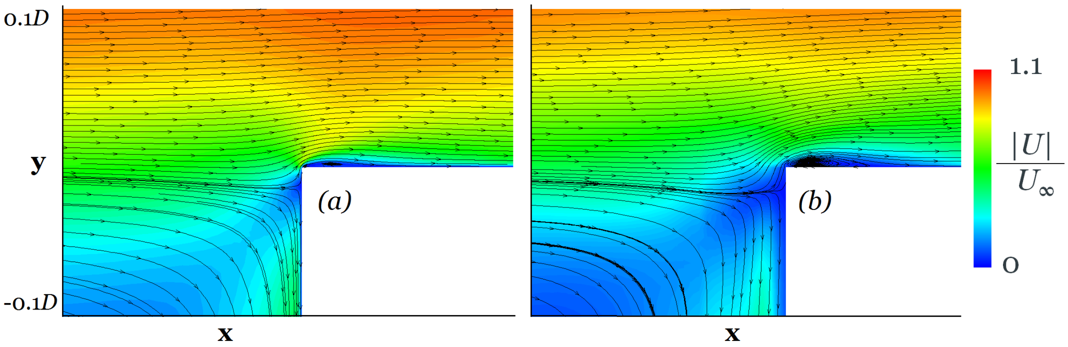

Figure A.3: Velocity contours close-up at x_{TE}: (a) DES for cavity with $D = 0.0285$m, $\delta/L_{open} = 0.049$; (b) DES for cavity with $D = 0.12$m, $\delta/L_{open} = 0.095$

other high-frequency modes were clearly distinguishable in this simulation. The smaller geometry (with the thinner boundary layer), also exhibited a peak at $N_x = 4$, but also had significant tones at $N_x = 3$ and $N_x = 6$. It cannot definitively be concluded whether these differences are more due to scale or to boundary layer thickness, but since past studies have found Re to be relatively unimportant and boundary layer thickness to be significant, it is likely to be the latter.

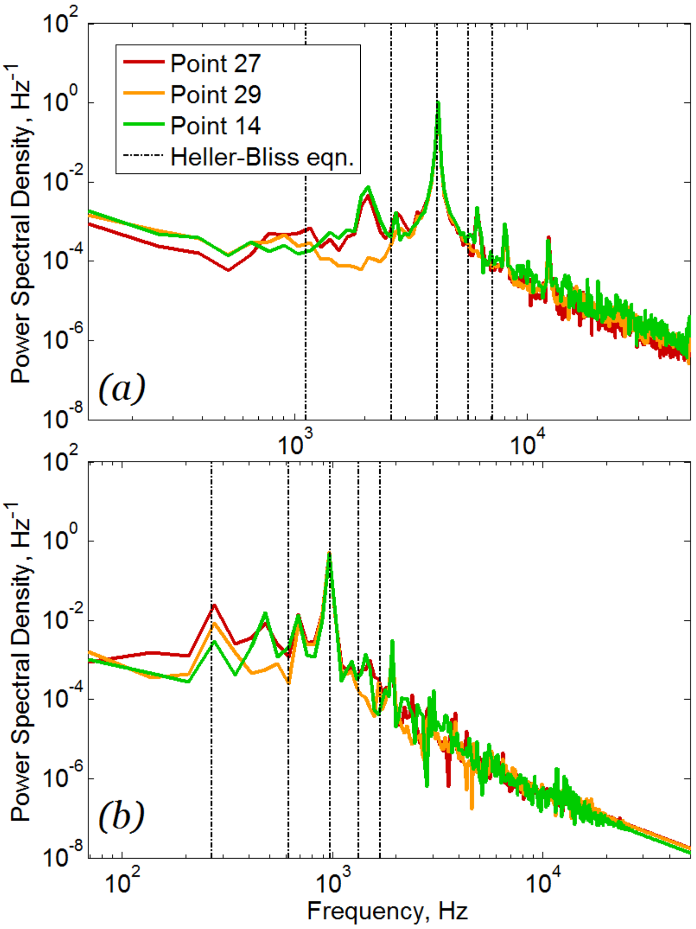

Figure A.4: PSDs of pressure at monitors inside the cavity from DES: (a) DES for cavity with $D = 0.0285$m, $\delta/L_{open} = 0.049$; (b) DES for cavity with $D = 0.12$m, $\delta/L_{open} = 0.095$. Point locations are as shown in Figure 8.3.

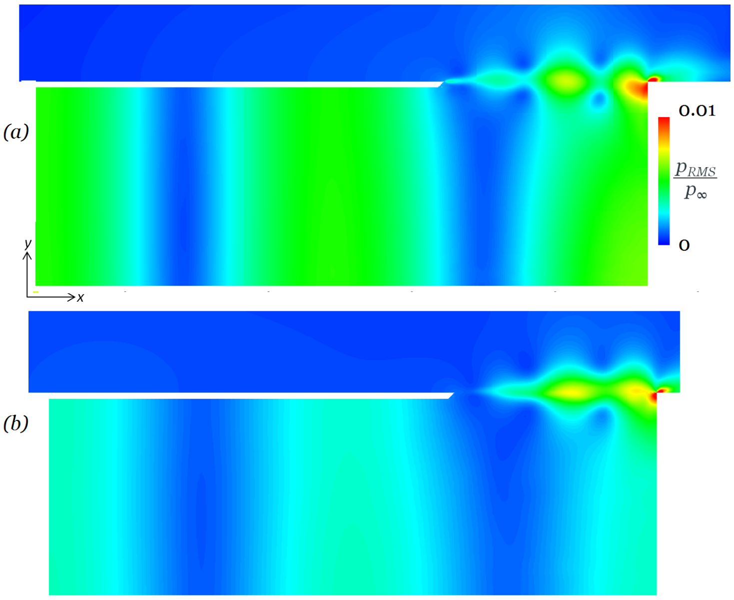

Figure A.5: RMS pressure contours from DES: (a) DES for cavity with $D = 0.0285$m, $\delta/L_{open} = 0.049$; (b) DES for cavity with $D = 0.12$m, $\delta/L_{open} = 0.095$

.

Bibliography

[1] C. M. Winkler, A. J. Dorgan, and R. Langtry, "Grid Sensitivity of the Rudimentary Landing Gear Using Unstructured Finite Volume Methods." AIAA Paper 2012-2288, 2012.

[2] W. Dobrzynski, "Almost 40 Years of Airframe Noise Research: What Did We Achieve?," *Journal of Aircraft*, vol. 47, pp. 353–367, mar 2010.

[3] The Boeing Company, "Growth in Airport Noise Restrictions." http://www.boeing.com/assets/pdf/commercial/noise/restrictions.pdf [Online; last accessed 05-Feb-2014], 2011.

[4] M. R. Khorrami, D. P. Lockard, W. M. J. Humphreys, and M. M. Choudhari, "Preliminary analysis of acoustic measurements from the NASA-Gulfstream airframe noise flight test." AIAA Paper 2008-2814, 2008.

[5] F. Li, M. R. Khorrami, and M. R. Malik, "Unsteady Simulation of a Landing-Gear Flow Field." AIAA Paper 2002-2411, 2002.

[6] M. Remillieux, "Aeroacoustic Study of a Model-Scale Landing Gear in a Semi-Anechoic Wind-Tunnel," 2007.

[7] W. Liu, J. Wook Kim, X. Zhang, D. Angland, and B. Caruelle, "Landing-gear noise prediction using high-order finite difference schemes," *Journal of Sound and Vibration*, vol. 332, no. 14, pp. 3517–3534, 2013.

[8] W. Dobrzynski, M. Pott-Pollenske, D. Foot, and M. Goodwin, "Landing gears aerodynamic interaction noise," in *Proceedings of European Congress on Computational Methods in Applied Sciences and Engineering*, pp. 115–135, Multi-Science, 2004.

[9] P. R. Spalart, M. L. Shur, M. K. Strelets, and A. K. Travin, "Initial noise predictions for rudimentary landing gear," *Journal of Sound and Vibration*, vol. 330, no. 17, pp. 4180–4195, 2011.

[10] R. Langtry and P. Spalart, "DES investigation of a baffle device for reducing landing-gear cavity noise." AIAA Paper 2008-13, 2008.

[11] B. S. Lazos, "Mean Flow Features Around the Inline Wheels of Four-Wheel Landing Gear," *AIAA Journal*, vol. 40, pp. 193–198, feb 2002.

[12] M. Chainey, “A350 XWB Landing Gear Bench Entry Into Service.” http://www.a350xwb.com/x-tra/photo-gallery [Online; last accessed 05-May-2014], 2013.

[13] Y. Guo, K. J. Yamamoto, and R. W. Stoker, “Experimental Study on Aircraft Landing Gear Noise,” *Journal of Aircraft*, vol. 43, pp. 306–317, mar 2006.

[14] S. Lawson and G. Barakos, “Review of numerical simulations for high-speed, turbulent cavity flows,” *Progress in Aerospace Sciences*, vol. 47, pp. 186–216, apr 2011.

[15] U. Oza, Z. Hu, and X. Zhang, “Effect of Cavity Flow on Landing Gear Aerodynamic Loads.” AIAA Paper 2015-2288, 2015.

[16] R. J. Fattah, Z. Hu, and D. Angland, “Aeroacoustics of a Landing Gear Door.” AIAA Paper 2013-2259, may 2013.

[17] L. Larchevêque, P. Sagaut, and O. Labbé, “Large-eddy simulation of a subsonic cavity flow including asymmetric three-dimensional effects,” *Journal of Fluid Mechanics*, vol. 577, p. 105, 2007.

[18] K. Chang, G. Constantinescu, and S.-O. Park, “Analysis of the flow and mass transfer processes for the incompressible flow past an open cavity with a laminar and a fully turbulent incoming boundary layer,” *Journal of Fluid Mechanics*, vol. 561, pp. 113–145, 2006.

[19] M. Giles, “Trends in HPC : hardware complexity and software challenges.” UK Turbulence Consortium Annual Review, 2013.

[20] M. G. Smith and L. C. Chow, “Validation of a Prediction Model for Aerodynamic Noise from Aircraft Landing Gear.” AIAA Paper 2002-2581, 2002.

[21] W. Dobrzynski, L. C. Chow, M. Smith, A. Boillot, O. Dereure, and N. Molin, “Experimental assessment of low noise landing gear component design,” *International Journal of Aeroacoustics*, vol. 9, no. 6, pp. 763–786, 2010.

[22] D. H. Neuhart, M. R. Khorrami, and M. M. Choudhari, “Aerodynamics of a Gulfstream G550 Nose Landing Gear Model.” AIAA Paper 2009-3152, 2009.

[23] L. Chow and J. Higgins, “Reduction of airframe noise from landing gear,” *Air & Space Europe*, vol. 2, no. 6, 2000.

[24] W. M. Dobrzynski, B. Schöning, L. C. Chow, C. Wood, M. Smith, C. C. Seror, and L. Choi Chow, “Design and testing of low noise landing gears,” *International Journal of Aeroacoustics*, vol. 5, pp. 233–262, sep 2006.

[25] W. Humphreys and T. Brooks, “Noise spectra and directivity for a scale-model landing gear,” *International Journal of Aeroacoustics*, vol. 8, no. 5, pp. 1–22, 2009.

[26] Z. Xiao, J. Liu, K. Luo, J. Huang, and S. Fu, “Investigation of Flows Around a Rudimentary Landing Gear with Advanced Detached-Eddy-Simulation Approaches,” *AIAA Journal*, vol. 51, pp. 107–125, jan 2013.

[27] C. K. W. Tam and P. J. W. Block, “On the tones and pressure oscillations induced by flow over rectangular cavities,” *Journal of Fluid Mechanics*, vol. 89, no. 02, p. 373, 1978.

[28] S. B. Pope, *Turbulent flows.* Cambridge University Press, 2000.

[29] P. Schlatter, Q. Li, G. Brethouwer, A. V. Johansson, and D. S. Henningson, “Simulations of spatially evolving turbulent boundary layers up to Reθ=4300,” *International Journal of Heat and Fluid Flow*, vol. 31, no. 3, pp. 251–261, 2010.

[30] K. K. Ahuja and J. Mendoza, “Effects of cavity dimensions, boundary layer, and temperature on cavity noise with emphasis on benchmark data to validate computational aeroacoustic codes,” 1995.

[31] X. Gloerfelt, C. Bogey, C. Bailly, and D. Juve, “Aerodynamic Noise Induced by Laminar and Turbulent Boundary Layers over Rectangular Cavities.” AIAA 2002-2476, 2002.

[32] P. A. Monkewitz, K. A. Chauhan, and H. M. Nagib, “Self-consistent high-Reynolds-number asymptotics for zero-pressure-gradient turbulent boundary layers,” *Physics of Fluids*, vol. 19, no. 11, 2007.

[33] Q. Ye, F. F. J. Schrijer, and F. Scarano, “On Reynolds Number Dependence of Micro-ramp-Induced Transition,” in *18th International Symposium on the Application of Laser and Imaging Techniques to Fluid Mechanics*, (Lisbon, Portugal), 2016.

[34] P. Schlatter, R. Örlü, Q. Li, and G. Brethouwer, “Turbulent boundary layers up to Re= 2500 studied through simulation and experiment,” *Physics of fluids*, 2009.

[35] J. Chicheportiche and X. Gloerfelt, “Effect of a turbulent incoming boundary layer on noise radiation by the flow over cylindrical cavities.” AIAA Paper 2011-2862, 2011.

[36] P. Schlatter and R. Örlü, “Turbulent boundary layers at moderate Reynolds numbers: inflow length and tripping effects,” *Journal of Fluid Mechanics*, vol. 710, pp. 5–34, 2012.

[37] P. R. Spalart, “Direct simulation of a turbulent boundary layer up to Re = 1410,” *Journal of Fluid Mechanics*, vol. 187, no. December, pp. 61–98, 1988.

[38] X. Wu and P. Moin, “Direct numerical simulation of turbulence in a nominally zero-pressure-gradient flat-plate boundary layer,” *Journal of Fluid Mechanics*, vol. 630, p. 5, 2009.

[39] I. Marusic and G. J. Kunkel, “Streamwise turbulence intensity formulation for flat-plate boundary layers,” *Physics of Fluids*, vol. 15, no. 8, p. 2461, 2003.

[40] S. Pröbsting, F. Scarano, M. Bernardini, and S. Pirozzoli, “On the estimation of wall pressure coherence using time-resolved tomographic PIV,” *Experiments in Fluids*, vol. 54, no. 7, p. 1567, 2013.

[41] P. Sagaut, E. Garnier, E. Tromeur, L. Larcheveque, and E. Labourasse, “Turbulent inflow conditions for Large-Eddy-Simulation of compressible wall-bounded flows,” *AIAA journal*, vol. 42, no. 3, 2004.

[42] X. Gloerfelt and J.-C. Robinet, “A silent inflow condition for the study of boundary layer noise.” AIAA Paper 2013-2247, may 2013.

[43] W. Van Der Velden, A. Van Zuijlen, A. De Jong, and H. Bijl, “on the Estimation of Spanwise Pressure Coherence of a Turbulent Boundary Layer Over a Flat Plate,” in *6th European Conference on Computational Fluid Dynamics (ECFD VI)*, (Barcelona), 2014.

[44] M. Klein, A. Sadiki, and J. Janicka, “A digital filter based generation of inflow data for spatially developing direct numerical or large eddy simulations,” *Journal of Computational Physics*, vol. 186, no. 2, pp. 652–665, 2003.

[45] Z. T. Xie and I. P. Castro, “Efficient generation of inflow conditions for large eddy simulation of street-scale flows,” *Flow, Turbulence and Combustion*, vol. 81, no. 3, pp. 449–470, 2008.

[46] J. Berland and X. Gloerfelt, “Investigation of noise radiation from a turbulent boundary layer.” AIAA Paper 2008-2802, 2008.

[47] C. Tam, “Intensity, spectrum, and directivity of turbulent boundary layer noise,” *The Journal of the Acoustical Society of America*, vol. 57, no. 1, pp. 25–34, 1975.

[48] P. Chappell, “Aerodynamics and aero-acoustics of rectangular planform cavities Part II: Unsteady flow and aero-acoustics.” ESDU Report 04023, Endorsed by The Royal Aeronautical Society, 2005.

[49] N. E. Murray and B. J. Jansen, “Effect of Door Configuration on Cavity Flow Modulation Process,” *AIAA Journal*, vol. 50, pp. 2932–2937, dec 2012.

[50] D. Bliss and R. Hayden, “Landing gear and cavity noise prediction.” NASA Contractor Report CR-2714, 1976.

[51] J. Rossiter, “Wind-tunnel Experiments on the Flow over Rectangular Cavities at Subsonic and Transonic Speeds.” Technical Report, Her Majesty’s Stationery Office, 1964.

[52] A. Roshko, “Some measurements of flow in a rectangular cutout.” NACA Technical Note No. 3488, 1955.

[53] N. Murray, E. Sallstrom, and L. Ukeiley, “Properties of subsonic open cavity flow fields,” *Physics of Fluids*, vol. 21, no. 9, 2009.

[54] G. Ashcroft and X. Zhang, “Vortical structures over rectangular cavities at low speed,” *Physics of Fluids*, vol. 17, no. 1, 2005.

[55] L. Sun, Y.; Nair, A.; Taira, K.; Cattafesta, L.N.; Brès, G.A.; Ukeiley, "Numerical Simulations of Subsonic and Transonic Open-Cavity Flows," in *7th AIAA Theoretical Fluid Mechanics Conference*, (Atlanta, Georgia), 2014.

[56] K. Chang, G. Constantinescu, and S.-O. Park, "Assessment of Predictive Capabilities of Detached Eddy Simulation to Simulate Flow and Mass Transport Past Open Cavities," *Journal of Fluids Engineering*, vol. 129, p. 1372, 2007.

[57] S. M. Grace, W. G. Dewar, and D. E. Wroblewski, "Experimental investigation of the flow characteristics within a shallow wall cavity for both laminar and turbulent upstream boundary layers," *Experiments in Fluids*, vol. 36, no. 5, pp. 791–804, 2004.

[58] M. Nishimura, T. Goto, and A. Kimura, "Study on Reducing Aerodynamic Random Noise from a Cavity." AIAA Paper 2008-2847, 2008.

[59] S. A. Syed and K. a. Hoffmann, "Numerical Investigation of 3-D Open Cavity with & without Cover Plates." AIAA Paper 2009-551, 2009.

[60] H. Heller, D. Holmes, and E. Covert, "Flow-induced pressure oscillations in shallow cavities," *Journal of sound and Vibration*, 1971.

[61] J. Malone, M. Debiasi, J. Little, and M. Samimy, "Analysis of the spectral relationships of cavity tones in subsonic resonant cavity flows," *Physics of Fluids*, vol. 21, no. 5, 2009.

[62] M. A. Kegerise, E. F. Spina, S. Garg, and L. N. Cattafesta, "Mode-switching and nonlinear effects in compressible flow over a cavity," *Physics of Fluids*, vol. 16, no. 3, p. 678, 2004.

[63] L. Shaw, H. Bartel, and J. McAvoy, "Acoustic environment in large enclosures with a small opening exposed to flow," *Journal of Aircraft*, vol. 20, no. 3, pp. 250–256, 1983.

[64] X. Gloerfelt, "Cavity noise," in *von Karman Lecture Notes on Aerodynamic Noise from Wall-Bounded Flows*, pp. 1–169, 2009.

[65] H. W. Bartel and J. M. McAvoy, "Cavity Oscillation in Cruise Missile Carrier Aircraft." AFWAL-TR-81-3036, Lockheed-Georgia Company, Structures Technology Division, Marietta, Georgia, 1981.

[66] W. Koch, "Acoustic Resonances in Rectangular Open Cavities," *AIAA Journal*, vol. 43, no. 11, pp. 2342–2349, 2005.

[67] G. a. Brès and T. Colonius, "Three-dimensional instabilities in compressible flow over open cavities," *Journal of Fluid Mechanics*, vol. 599, pp. 309–339, 2008.

[68] X. Gloerfelt, C. Bogey, and C. Bailly, "Numerical evidence of mode switching in the flow-induced oscillations by a cavity," *International Journal of Aeroacoustics*, vol. 2, no. 2, pp. 193–217, 2003.

[69] D. N. Heo, J. W. Kim, and D. J. Lee, "Study on Noise Characteristics of an Open Cavity with Cross-Correlation Anaysis." AIAA Paper 2003-3104, 2003.

[70] K. Takeda and C. Shieh, "Cavity Tones by Computational Aeroacoustics," *International Journal of Computational Fluid Dynamics*, vol. 18, pp. 439–454, aug 2004.

[71] Z. Li and A. Hamed, "Effect of sidewall boundary conditions on unsteady high speed cavity flow and acoustics," *Computers and Fluids*, vol. 37, no. 5, pp. 584–592, 2008.

[72] C. W. Rowley, T. Colonius, and A. J. Basu, "On self-sustained oscillations in two-dimensional compressible flow over rectangular cavities," *Journal of Fluid Mechanics*, vol. 455, pp. 315–346, 2002.

[73] P. Chappell, "Aerodynamics and aero-acoustics of rectangular planform cavities Part I : Time-averaged flow," 2009.

[74] W. Kang and H. J. Sung, "Experimental study of self-sustained oscillations in low Mach number turbulent cavity flows," in *7th International Symposium on Particle Image Velocimetry*, (Rome, Italy), 2007.

[75] M. Gharib and A. Roshko, "The effect of flow oscillations on cavity drag," *Journal of Fluid Mechanics*, vol. 177, pp. 501–530, 1987.

[76] V. Sarohia, "Experimental investigation of oscillations in flows over shallow cavities," *AIAA Journal*, vol. 15, no. 7, pp. 984–991, 1977.

[77] A. Hazir, D. Casalino, and R. Denis, "Lattice-Boltzmann Simulation of the Aeroacoustic Properties of Round Cavities." AIAA Paper 2014-2894, 2014.

[78] Kolossos, "A380 Undercarriage." http://en.wikipedia.org/wiki/Undercarriage_arrangements [Online; last accessed 11-Jun-2014], 2014.

[79] D. J. Wittich, A. B. Cain, and E. J. Jumper, "Strong flow-acoustic resonances of rectangular cavities," *International Journal of Aeroacoustics*, vol. 10, pp. 277–294, jun 2011.

[80] D. Heo and D. Lee, "Numerical Investigation of the Cover-Plates Effects on the Rectangular Open Cavity." AIAA Paper 2001-2127, 2001.

[81] N. Delprat, "Rossiter's formula: A simple spectral model for a complex amplitude modulation process?," *Physics of Fluids*, vol. 18, no. 7, 2006.

[82] H. Versteeg and W. Malalasekera, *An introduction to computational fluid dynamics; the finite volume method*, vol. M. Essex, United Kingdom: Pearson Education Limited, 2nd ed., 2007.

[83] A. Travin, M. Shur, M. Strelets, and P. Spalart, "Detached-eddy simulations past a circular cylinder," *Flow, Turbulence and Combustion*, pp. 293–313, 1999.

[84] P. R. Spalart, "Young-Person's Guide to Detached-Eddy Simulation Grids," Tech. Rep. July, NASA, CR-2001-211032, 2001.

[85] P. Spalart, W. Jou, M. Strelets, and S. Allmaras, “Comments on the feasibility of LES for wings, and on a hybrid RANS/LES approach,” *Advances in DNS/LES*, vol. 1, pp. 4–8, 1997.

[86] P. R. Spalart, M. L. Shur, M. K. Strelets, and A. K. Travin, “Towards noise prediction for rudimentary landing gear,” *Procedia Engineering*, vol. 6, pp. 283–292, jan 2010.

[87] P. R. Spalart, “On the precise implications of acoustic analogies for aerodynamic noise at low Mach numbers,” *Journal of Sound and Vibration*, vol. 332, no. 11, pp. 2808–2815, 2013.

[88] U. Piomelli, “Large-eddy simulation: achievements and challenges,” *Progress in Aerospace Sciences*, vol. 35, pp. 335–362, may 1999.

[89] D. P. Rizzetta, M. R. Visbal, and G. A. Blaisdell, “A time-implicit high-order compact differencing and filltering scheme for large-eddy simulation,” *International Journal for Numerical Methods in Fluids*, vol. 693, pp. 665–693, 2003.

[90] G. Bres, J. Nichols, S. Lele, and F. Ham, “Towards best practices for jet noise predictions with unstructured large eddy simulations.” AIAA Paper 2012-2965, 2012.

[91] E. Lévêque and F. Toschi, “Shear-improved Smagorinsky model for large-eddy simulation of wall-bounded turbulent flows,” *Journal of Fluid Mechanics*, vol. 570, pp. 1–11, 2007.

[92] L. S. Hedges, a. K. Travin, and P. R. Spalart, “Detached-Eddy Simulations Over a Simplified Landing Gear,” *Journal of Fluids Engineering*, vol. 124, no. 2, p. 413, 2002.

[93] N. Georgiadis, D. Rizzetta, and C. Fureby, “Large-eddy simulation: current capabilities, recommended practices, and future research,” *AIAA Journal*, vol. 48, no. 8, pp. 1772–1784, 2010.

[94] S. Krajnović, R. Lárusson, and B. Basara, “Superiority of PANS compared to LES in predicting a rudimentary landing gear flow with affordable meshes,” *International Journal of Heat and Fluid Flow*, vol. 37, pp. 109–122, oct 2012.

[95] M. M. Metzger and J. C. Klewicki, “A comparative study of near-wall turbulence in high and low Reynolds number boundary layers,” *Physics of Fluids*, vol. 13, no. 3, pp. 692–701, 2001.

[96] M. Breuer, N. Jovičić, and K. Mazaev, “Comparison of DES, RANS and LES for the separated flow around a flat plate at high incidence,” *International journal for numerical methods in fluids*, vol. 388, no. September 2002, pp. 357–388, 2003.

[97] J. Boudet, J. Caro, L. Shao, and E. Lévêque, “Numerical studies towards practical large-eddy simulation,” *Journal of Thermal Science*, vol. 16, no. 4, pp. 328–336, 2007.

[98] D. Vatsa, M. Khorrami, and J.-r. Carlson, "Aeroacoustic simulation of a nose landing gear in an open jet facility using FUN3D." AIAA Paper 2012-2280, 2012.

[99] F. Vuillot, F. Houssen, E. Manoha, S. Redonnet, and J. Jacob, "Applications of the CEDRE unstructured flow solver to landing gear unsteady flow and noise predictions." AIAA Paper 2011-2944, 2011.

[100] P. R. Spalart, S. Deck, M. L. Shur, K. D. Squires, M. K. Strelets, and A. Travin, "A new version of detached-eddy simulation, resistant to ambiguous grid densities," *Theoretical and Computational Fluid Dynamics*, vol. 20, no. 3, pp. 181–195, 2006.

[101] R. J. Fattah and Z. Hu, "Aerodynamic and Aeroacoustic Effects From a Landing Gear Door 18 month MPhil / PhD transfer thesis," Tech. Rep. September, 2012.

[102] R. J. Fattah, *The noise generation by a main landing gear door.* Phd thesis, University of Southampton, 2015.

[103] M. Wang, R. Fattah, D. Angland, and X. Zhang, "High-Order Hybrid Cell-Centered Method for Computational Aeroacoustics." 2015-3279, 2015.

[104] M. Wang, D. Angland, X. Zhang, and R. J. Fattah, "High-Order Numerical Simulations of An Isolated Landing Gear Wheel with A Hub Cavity." AIAA Paper 2016-2902, 2016.

[105] J. Gill, R. Fattah, and X. Zhang, "Evaluation and Development of Non-Reflective Boundary Conditions for Aeroacoustic Simulations." AIAA Paper 2015-2677, 2015.

[106] G. Ashcroft and X. Zhang, "Optimized prefactored compact schemes," *Journal of Computational Physics*, vol. 190, no. 2, pp. 459–477, 2003.

[107] S. K. Lele, "Compact finite difference schemes with spectral-like resolution," *Journal of Computational Physics*, vol. 103, no. 1, pp. 16–42, 1992.

[108] J. Li, F. Li, and E. Qin, "A fully implicit method for steady and unsteady viscous ow simulations," *International Journal for Numerical Methods in Fluids*, vol. 163, no. 127, pp. 147–163, 2003.

[109] J. W. Kim, "High-order compact filters with variable cut-off wavenumber and stable boundary treatment," *Computers & Fluids*, vol. 39, pp. 1168–1182, aug 2010.

[110] O. Vasilyev, T. Lund, and P. Moin, "A general class of commutative filters for LES in complex geometries," *Journal of Computational Physics*, vol. 104, pp. 82–104, 1998.

[111] W. Liu, *Numerical investigation of landing gear noise.* PhD thesis, University of Southampton, 2011.

[112] P. Sagaut, S. Deck, and M. Terracol, *Multiscale and Multiresolution Approches in Turbulence.* 2006.

[113] C. Moreno, *Turbulence, Vibrations, Noise and Fluid Instabilities. Practical Approach.* No. January, 2010.

[114] P. R. Spalart and C. L. Rumsey, "Effective Inflow Conditions for Turbulence Models in Aerodynamic Calculations," *AIAA Journal*, vol. 45, no. 10, pp. 2544–2553, 2007.

[115] A. Jameson and W. Schmidt, "Some recent developments in numerical methods for transonic flows," *Computer Methods in Applied Mechanics and Engineering*, vol. 51, no. 1-3, pp. 467–493, 1985.

[116] S. Richards, X. Zhang, X. Chen, and P. Nelson, "The evaluation of non-reflecting boundary conditions for duct acoustic computation," *Journal of Sound and Vibration*, vol. 270, no. 3, pp. 539–557, 2004.

[117] N. Georgiadis, K. Lenahan, and M. Vyas, "Turbulent Flat Plate : Study 2." http://www.grc.nasa.gov/WWW/wind/valid/fpturb/fpturb02/fpturb02.html [Online; last accessed 19-Jun-2014], 2011.

[118] Z. Hu, C. L. Morfey, and N. D. Sandham, "Wall Pressure and Shear Stress Spectra from Direct Simulations of Channel Flow," *AIAA Journal*, vol. 44, no. 7, pp. 1541–1549, 2006.

[119] J. Y. Zhu, Z. W. Hu, and D. J. Thompson, "Flow simulation and aerodynamic noise prediction for a high-speed train wheelset," *International Journal of Aeroacoustics*, vol. 13, no. 7, pp. 533–552, 2014.

[120] G. Brès, D. Freed, M. Wessels, S. Noelting, and F. Pérot, "Flow and noise predictions for the tandem cylinder aeroacoustic benchmark," *Physics of Fluids*, vol. 24, no. June 2011, pp. 1–25, 2012.

[121] G. A. Brès, M. Wessels, and S. Noelting, "Tandem cylinder noise predictions using lattice boltzmann and Fowcs Williams-Hawking Methods." AIAA Paper 2010-3791, 2010.

[122] E. Achenbach, "Distribution of local pressure and skin friction around a circular cylinder in cross-flow up to Re = 5 10 6 ," *Journal of Fluid Mechanics*, vol. 34, no. 04, p. 625, 1968.

[123] O. Inoue, "Note on multiple-frequency forcing on mixing layers," *Fluid Dynamics Research*, vol. 16, no. 2-3, pp. 161–172, 1995.

[124] F. Nicoud and F. Ducros, "Subgrid-scale stress modelling based on the square of the velocity gradient tensor," *Flow, Turbulence and Combustion*, vol. 62, no. 3, pp. 183–200, 1999.

[125] S. Deck, P. É. Weiss, M. Pamiès, and E. Garnier, "Zonal Detached Eddy Simulation of a spatially developing flat plate turbulent boundary layer," *Computers and Fluids*, vol. 48, pp. 1–15, 2011.

[126] M. L. Shur, P. R. Spalart, M. K. Strelets, and A. K. Travin, “A hybrid RANS-LES approach with delayed-DES and wall-modelled LES capabilities,” *International Journal of Heat and Fluid Flow*, vol. 29, no. 6, pp. 1638–1649, 2008.

[127] T. S. Lund, X. Wu, and K. D. Squires, “On the Generation of Turbulent Inflow Conditions for Boundary Layer Simulations,” *Journal of Computational Physics*, vol. 140, pp. 233–258, 1998.

[128] L. P. Purtell, P. S. Klebanoff, and F. T. Buckley, “Turbulent boundary layer at low Reynolds number,” *Physics of Fluids*, vol. 25, pp. 802–811, 1981.

[129] U. Piomelli and E. Balaras, “Wall-layer models for large-eddy simulations,” *Annual review of fluid mechanics*, 2002.

[130] G. E. Box, G. M. Jenkins, and G. C. Reinsel, *Time Series Analysis - Forecasting and Control*. 1994.